Universitat Autònoma de Barcelona

Theoretical Study of Spin Dynamics in Two-Dimensional Quantum Materials

Marc Vila Tusell

Institut Català de Nanociència i Nanotecnologia

Universitat Autònoma de Barcelona

Facultat de Ciències

Departament de Física

Programa de Doctorat en Física
Tesi Doctoral

Theoretical Study of Spin Dynamics in Two-Dimensional Quantum Materials

Author:

Marc Vila Tusell

Supervisors:

ICREA Prof.
Stephan Roche

Dr. Aron W. Cummings

ICREA Prof.
Sergio O. Valenzuela

Tutor:

Prof. Carles Navau Ros

November 2020

Als meus amics, amigues, familiars, companys i companyes de vida;
a tothom a qui he estimat en aquests 27 anys.

ACKNOWLEDGEMENTS

I would like to start by thanking all my colleagues at ICN2. I only started this PhD because I always liked spins, and because Stephan motivated me since the first day I met him. But this 4-year-journey wouldn't have been the same if I hadn't felt ICN2 a comfortable place. José, Aron, Stephan, Eduardo, Stephen, Kenan, Bruna, Armando, Aleandro, Pablo, Luis from my group, and many people from other groups at ICN2, specially María, Marc and Antonio. I am thankful for the opportunities I've had to travel to different countries and participate in several conferences because I've met wonderful people, I've learned other cultures and I've had lots of fun. I also would like to thank all the non-scientist workers because if it weren't for them, I simply could not be working on physics in my office: Andrés, Raquel, Inma, Sandra, Àlex, Ana, Anabel, among all the other people at ICN2, and Jordi and Ainhoa who do not work here anymore. I am also grateful to have been part of the ICN2 ping-pong and pádel community, it was a lot of fun!

Continuing with the people above, I want to specially thank Stephan, Aron and José. Stephan, you have been a continuous source of motivation and taught me how to succeed in the science world. Aron, it's been a pleasure learning from you and working with you; your patience and serenity are extraordinary. José, thank you for being my friend, not only you helped me solve numerous physical problems, but also I enjoyed all the conversations about non-science stuff. Certainly, this thesis wouldn't be what it is now without them.

I'd like also to thank Prof. Riichiro Saito-sensei and Nguyen-san for their hospitality during my stay at Tohoku University in Sendai, Japan, and also Vitor Pereira and Chuang-Han in my short stay in Singapore.

Ara li toca al torn a la gent amb qui convisc dia a dia. Champs (David i Rita), em va encantar poder tornar a viure amb vosaltres al tornar de Londres i sobretot de compartir

hores i hores de jocs de taula al vostre costat. Agrair als meus amics d'Hostalric i no d'Hostalric per totes les estones viscudes durant aquests 27 anys, en especial a en Josep, Marçal i Llaura. No m'oblido del senyor del barret, que tot i que fa molt que no el veig, també me l'estimo molt.

Vull mencionar també a la meva família, que tot i que no ens hem pogut veure gaire últimament, m'agrada molt passar estones amb ells: Mama, Papa, Xavi, Anna, Ignasi, Gemma, Mael, Rita, Maia. I també en Garp, la Gata Mare, la Cua Llarga, la Cua Torta, en Potes Blanques i l'Ufanós.

I finalment, a la meva petita família: Mònica, Dora, Catan, Bambú. Sort en tinc de poder estar cada dia amb vosaltres, us estimo molt. Gràcies per donar-me tot el que em feia falta per poder fer i escriure la tesis. Que per cert, guess what, ja l'he acabada!

També a la gent que he conegut a Sant Celoni durant l'any que hi vaig viure, a la gent de Teatre (que bé que ens ho passem), i a Mr. Grill, per ensenyar-me com sentir-me be físicament i descansar la ment.

Com que això és l'última cosa que estic escrivint abans de dipositar la tesis (per fi!), és probable que em deixi a algú. Si és el cas, afegeix-te a la llista!

Coming back to the ICN2, I'd like to thank the ones that have assisted me during these months of writing. My thesis supervisors: Stephan, Aron and Sergio; my UAB tutor, Carles Navau; the officer from the physics department, Francesc Poblet; and the PhD coordinator, Jordi Mompart; and also the researchers that agreed to be part of my evaluation committee: Xavier, Enrique, Mair, Elsa, Bernd. Finally, I'd like to acknowledge the funding agencies that have allowed me to work on what I want: el Convenio de Colaboración entre Fundació Institut Català de Nanociència i Nanotecnologia y la Obra Social "la Caixa": "Programa Internacional de Becas "la Caixa"-Severo Ochoa", the European Unions Horizon 2020 research and innovation programme under grant agreement No 696656 and the European Unions Horizon 2020 research and innovation programme under grant agreement No 785219.

ABSTRACT

The field of spintronics aims at using the spin degree of freedom of the electron to store, transport and manipulate information in next-generation electronic devices. While storing information as a magnetization in ferromagnets has already found great applications in magnetic-based memories, communicating and processing spins in nonmagnetic materials is a more challenging task because the spin in these materials is not a conserved quantity. A central aspect of spintronics is to determine the nature and strength of spin-orbit coupling (SOC) phenomena. On the one hand, SOC allows the manipulation of spins with electric fields, which is appealing for practical applications; but on the other hand it increases the rate of spin relaxation. A great variety of materials has been scrutinized in the last decades, including metals, semiconductors and two-dimensional electron gases, with both strong or weak SOC. With the discovery of graphene in 2004 and the rise of the field of two-dimensional materials, a myriad of new compounds with appealing properties have opened novel possibilities for spintronics.

In this thesis, I use quantum transport methodologies to simulate spin dynamics in devices made of two-dimensional materials. The first part of the thesis focuses on spin transport in graphene, while the second part deals with charge-to-spin interconversion effects and topological phenomena in low-symmetry transition metal dichalcogenides (TMDs). The Landauer-Büttiker formalism has been employed, as implemented in the open-source Kwant package, to simulate different kinds of electronic devices, including nonlocal spin valves. In graphene, I reveal that the full geometry of nonlocal spin valves should be taken into account when analyzing experiments in the diffusive regime when the spin transport is very efficient; otherwise spin diffusion lengths might be underestimated. Furthermore, I predict the experimental outcome of a Hanle spin precession measurement when the material quality drives the system towards a (quasi)ballistic transport regime, a regime that is not captured by the typical spin diffusion theory used to interpret exper-

iments. For TMDs, I show that the low symmetry present in some phases of this class of materials directly affects their spin texture, which in turn impacts the spin transport, as well as charge-to-spin interconversion processes such as the spin Hall effect. The spin polarization of electrons in these TMDs displays a momentum invariant (persistent) spin texture fixed in a direction along the yz plane, and as a result, anisotropic spin relaxation is found. The spin Hall effect exhibits an unconventional component, with spin accumulation generated in the plane, which together with the conventional out-of-plane polarization, forms an oblique or canted spin Hall effect. Near the band gap region, the charge-to-spin interconversion efficiency reaches values as large as $\sim 80\%$ and, when the Fermi level is placed in the topologically nontrivial gap, a canted quantum spin Hall effect is predicted. The corresponding topologically protected edge states are robust to disorder and carry spins polarized in the same direction as the persistent spin texture found at the bottom of the conduction bands. The findings presented in this thesis open a new perspective to predict and scrutinize spin transport in high-quality graphene devices and topological, low-symmetry two-dimensional materials.

CONTENTS

CHAPTER 1

INTRODUCTION

The continuous miniaturization of silicon-based complementary metal-oxide-semiconductor (CMOS) devices faces fundamental physical limits and engineeering problems as their components reach the size of a few nanometers [266, 282]. To overcome these issues, research on other architectures, materials or even completely different approaches to computer logic extensively began in the last decades [195]. Examples of such proposals include using resonant tunneling diodes as building blocks [141], molecular electronics [46, 110, 182], two-dimensional material-based electronics [87, 196], spintronics [12,39,122,179,287], neuromorphic computing [224,314] or quantum computation [88,161].

Among the aforementioned routes, spintronics (or spin electronics) aims at using the electron's spin in addition to (or instead of) the electron's charge in order to store, process and communicate information. The addition of the spin degree of freedom could result in several advantages such as low-power consumption, faster data processing speed or increased integration densities compared to conventional charged-based semiconductors [287]. It is said that the field started with the discovery of giant magnetoresistance (GMR) in the late 80's [13, 28], a phenomenon where the electrical resistance of two magnetic layers (separated by a nonmagnetic one) dramatically depends on their relative magnetization orientation, allowing in this way the realization of two disting states (high or low resistance) and hence carrying binary information ("0" or "1"). This effect, together with tunneling magnetoresistance, has been widely exploited in storage devices in modern computers such as hard disk drives or magnetoresistive random access memories (MRAM) [27, 287], and its impact has been so large than the Nobel prize in physics was awarded in 2007 to the physicist that discovered the GMR.

Since that first step, the number of materials used in spintronics increased to not only metals and ferromagnets, but also to semiconductors, insulators, superconductors

and topological materials, either being magnetic or nonmagnetic [12, 74]. In addition, numerous phenomena have been discovered, like the spin and quantum spin Hall effects [26, 112, 138, 139, 192, 234, 235, 243, 303], spin-transfer torque [23, 30, 217, 245], spin-orbit torque [42, 177, 185], spin Seebeck effect [272], spin-pumping [47, 270], persistent spin textures [232] or hidden spin polarizations [304], among others. Such a combination of materials and effects sparked the emergence of new fascinating fields within spintronics such as spin-orbitronics (based on the spin-orbit coupling (SOC)) [178], skyrmions [75, 193], antiferromagnetic spintronics [14, 135] or topological spintronics [206, 212, 247]. However, most of these achievements have been in fundamental science and it is not yet clear how these phenomena can be successfully applied to areas other than information storage, such as for example information processing in an active logic device [12].

Therefore, today the challenging task of spintronics is to communicate and process information, as storing is already accomplished. In simple terms, we can understand that communicating refers to transporting spin from one place to another, while processing entails manipulating the spin orientation or its trajectory in a controlled manner. Thus, since all these actions require a change in the spin over space or time, we can also refer to them as *spin dynamics*. Many of the phenomena described above are spin dynamics phenomena, which highlights the large efforts done by the research community in recent years to find a way to communicate and process spin.

One of the fundamental aspects regarding spin dynamics, as well as a limiting factor for further applications, is the fact that the spin angular momentum is not, in general, a conserved quantity. This is because an arbitrary spin state is not an eigenstate of the Hamiltonian that describes the electronic structure of a material (except for spins aligned along the magnetization axis of a ferromagnet). Therefore, a spin eventually changes its polarization after some time or length (i.e. the spin relaxes), defining in this way a spin relaxation time (τ_s) or length (λ_s)[1] and imposing an upper limit in time and length over which the spin information can be preserved. The same can be applied when referring to an ensemble of spins initially polarized in the same direction: after some time or length, the average polarization vanishes. Spintronics is based on the fact that different spin orientations may result in different outputs for the same physical effect, and hence the spin is what carries the information instead of the electron's charge. If, however, the spin is not conserved, then the information is lost, rendering a spin-based memory or logic device unusable.

This suggests that a clear path for improving spin communication is to enhance the spin relaxation time [287]. There exist different spin relaxation mechanisms [67, 122], but in general, magnetism and large SOC together with charge scattering are mechanism that

[1] τ_s and λ_s are also called spin lifetime and spin diffusion length, respectively.

cause spin relaxation[2]. The less perturbed the spin is, the larger the spin relaxation time and length, and consequently, typical materials for spin transport are nonmagnetic and comprised of light elements with small SOC [67, 122].

The main mechanisms of spin relaxation arise from charge scattering in the diffusive regime of transport. Hence, it is commonly speculated that in the ballistic regime, where no scattering occurs, the spin can be preserved for a much longer time. In fact, the first proposal for a spin field-effect transistor by Datta and Das in 1990 [55] was based on a ballistic transport channel for the spin. However, fabricating a ballistic conductor over large distances in conjunction with all other device components (e.g. gates, metallic contacts, insulating layers, etc.) is a formidable task. Consequently, not much progress has been made in spin dynamics in ballistic devices [154, 205].

Before introducing the important concept of spin injection and detection, it is instructive to enumerate the distinct ways electrons and spins flow in a material. In the simple but useful two-current model [122, 189], the conductivity of electrons can be separated into two independent contributions, one for each spin. If $n_\uparrow$ and $n_\downarrow$ are the charge densities associated with up and down spins in their corresponding quantization axis, respectively, then the charge and spin densities, $n = n_\uparrow + n_\downarrow$ and $s = n_\uparrow - n_\downarrow$, quantify the amount of charge and net spin, respectively. Similarly, one can define the charge and spin currents, I_c and I_s, that measure the flow of charge and spin densities. Based on this picture, different scenarios are possible, as depicted in Figure 1.1. In nonmagnetic materials, the number of up and down electrons is the same, and therefore $I_c \neq 0$ and $I_s = 0$. In materials with different spin population, like in ferromagnets, the two spin contributions of the current are unequal and hence $I_c \neq 0$ and $I_s \neq 0$. However, there is a special case when up and down spins have the same contribution but flow in opposite directions (see right panel in Figure 1.1), in which $I_c = 0$ and $I_s \neq 0$. The first situation is known as unpolarized charge current; the second one is dubbed spin-polarized current and the latter is called pure spin current. Due to the common usage of these terms, the unpolarized charge current is simply called charge current and the name spin current is also used to refer to the pure spin current scenario. Long-lasting pure spin currents are highly desirable in spintronics because they carry zero charge current and therefore heat dissipation due to Joule heating is expected to be absent. This provides a great motivation for the electronics industry since heat dissipation in microchips is one of the major challenges to overcome.

In addition to spin relaxation, another fundamental issue for spin communication is how to generate the spins in the transport material and how they are later detected to

[2]Hyperfine interaction is also a spin relaxation mechanism, but is not the most relevant in the solids we are going to study.

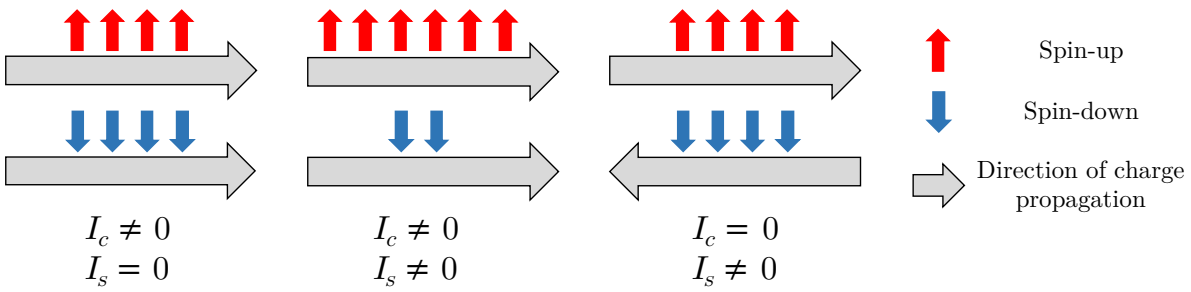

Figure 1.1: From left to right: (unpolarized) charge current, where spin-up and spin-down electrons flow in the same direction and $n_\uparrow = n_\downarrow$; spin-polarized current, where spin-up and spin-down electrons flow in the same direction and $n_\uparrow \neq n_\downarrow$; and (pure) spin current, where $n_\uparrow = n_\downarrow$ and spin-up and spin-down electrons flow in opposite directions.

'read' the spin information [67]. Since nonmagnetic compounds do not possess a net spin polarization, a nonequilibrium spin accumulation or density is what is transported, manipulated and measured. The principal ways to create spins in nonmagnetic materials include transport, optical and resonance methods [122]. Transport methods are attractive for applications as they allow for all-electrical devices compatible with current CMOS technologies. In particular, the electrical spin injection method has been widely employed [67,122,131]. This method consists of connecting a ferromagnet to the nonmagnetic material and driving current through it, resulting in the formation of a nonequilibrium spin density due to the flow of a spin-polarized current. Ferromagnetic (FM) electrodes are also commonly used as detectors as their chemical potential is sensitive to the nonequilibrium spin accumulation present in the nonmagnetic material [131,132]. However, the efficiency of spin injection and detection is to a first order proportional to the polarization of the ferromagnets, defined as $P = s/n$, which is usually of the order of 10 to 50%. Also, utilizing ferromagnetic materials complicates the device fabrication process and might introduce magnetic contaminants that can decrease the spin lifetime.

To overcome such problems, the spin Hall effect (SHE) and the inverse spin Hall effect (ISHE) may be used [61,62,112,243,244,303][3]. The spin Hall effect converts a charge current into a transverse pure spin current by deflecting spins with opposite polarization in opposite directions. In contrast, the inverse spin Hall effect converts a pure spin current into an electrical current. Thus, with the combination of both effects, one could in principle generate, transport, and detect spin information purely electrically, without the need for magnetic materials. The SHE and ISHE can arise from a variety of mechanisms [278], but the common and important ingredient is the presence of spin-orbit coupling. The figure of merit characterizing the efficiency of such charge-to-spin interconversion

[3]Another pair of phenomena, called spin galvanic and inverse spin galvanic effects were also proposed to inverconvert charge and spin [64,81].

(CSI) is the spin Hall angle (SHA), and materials with large SHA with preferably long λ_s have long been sought for their use as building blocks of active spintronics devices.

Looking at both spin relaxation and the spin Hall effect, one can easily see a fundamental problem regarding material choice. On the one hand, small SOC is needed to allow spin communication, but on the other hand, large SOC is required for efficient charge-to-spin interconversion. Therefore, although progress in obtaining materials with large spin relaxation times or SHA has been made separately, the difficult task at hand is to find materials suitable for both spin transport and manipulation. Alternatively, one could combine different materials, each performing a different function. However, this adds complexity to the device fabrication as well as an extra design variable, the interface physics between different materials. Overall, it is clear that material science together with a good understanding of physics is paramount to engineer useful active spin-based devices.

While conventional materials used for spin transport and manipulation are semiconductors and metals [67, 122, 288]; quantum materials [90] such as superconductors [171], topological semimetals [246, 256] and topological insulators [109, 206] have gained great attention in recent years due to their unique properties. For instance, topological insulators offer the possibility to carry dissipationless spin currents with the quantum spin Hall effect [26, 139, 192, 235] while also presenting large SHA [56, 68, 146, 184, 221]. However, probably the biggest advance with respect to novel materials for spintronics is the advent of two-dimensional (2D) materials [5, 10, 170].

The discovery of graphene, a monolayer of carbon atoms arranged in a honeycomb lattice [198], and other two-dimensional compounds soon after [199], expanded all areas of research with the fascinating possibility of exploring truly 2D materials. In spintronics, graphene was quickly identified as an excellent material for spin transport as its low spin-ortbit coupling and hyperfine interaction [115, 138, 186, 300] suggested long spin relaxation times. Nonetheless, experiments in nonlocal spin valves, the most common device geometry to study spin transport in 2D materials, showed that the spin lifetimes were orders of magnitude smaller than the theoretical expectations [66, 83, 117, 268, 313]; and since then great efforts have been made by the community to understand and improve spin transport in this material [10, 101, 219, 220]. In parallel, a vast array of 2D materials such as transition metal dichalcogenides (TMDs), 2D magnets, phosphorene, silicene or hexagonal boron nitride, also show great potential for active spin logic devices and CSI [5, 10, 170]. Moreover, the stacking of multiple 2D materials forming van der Waals heterostructures [86, 200] further broadened the spectrum of possible phenomena and applications, as combining two materials may give rise to new properties absent in the individual layered compounds. Likewise, owing to the high surface area of 2D ma-

terials, the properties of a material (either as a substrate or forming a van der Waals heterostructure) can be partially induced in another one by just placing them in close contact; this is known as the proximity effect [317]. These concepts are illustrated in Figure 1.2, where a few of the many 2D materials are depicted and stacked on top of each other.

One of the reasons for the large impact of 2D materials is the fact that they can realize some properties that were not possible before with bulk or thin film materials. Graphene is a primary example of this, in which electrons behave as massless Dirac fermions [197], something that was never observed before in a condensed matter system. As far as spintronics is concerned, continuous improvements in device fabrication have allowed for ballistic charge transport in graphene with mean free paths reaching hundreds of nanometers at room temperature and even tens of micrometers when the temperature is decreased [16, 17, 283]. These achievements give hope to fabricate, at last, a ballistic spin channel for efficient spin communication. To date, spin transport has been limited to the diffusive regime (either in conventional or in two-dimensional materials), and thus not much theory exists on how to analyze spin transport experiments in the ballistic regime, and in particular how to characterize the spin relaxation time and spin relaxation mechanisms.

Another natural question to ask is whether there are 2D materials with good spin Hall

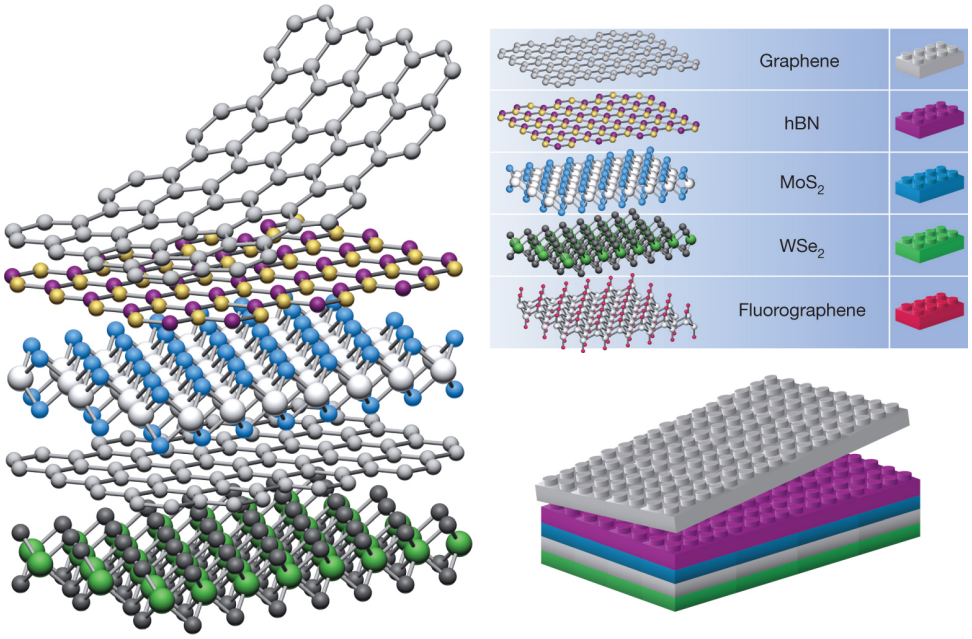

Figure 1.2: Schematics of some of the existing two-dimensional materials and how they can be stacked on top of each other and stabilized due to van der Waals interactions. Reprinted by permission from Springer Nature Customer Service Centre GmbH: Nature Publishing Group, *Nature*, Ref. [86], copyright (2013).

angles. In this regard, various crystal phases of TMDs, with formula MX_2 (M =transition metal atom; X =calchogen) have been predicted to exhibit a large SHE [73,311] owing to their large spin-orbit coupling [214,315]. Very recently, experiments reported the generation of large charge-to-spin interconversion by the SHE in multilayers of low-symmetry $MoTe_2$ and WTe_2 [227, 251, 307, 308]. In parallel, same nonlocal measurements of spin transport extracted anomalously long spin relaxation lengths ($\lambda_s \sim 1\,\mu$m) in $MoTe_2$ at room temperature [251], as well as an unconventional SHE that produces spins colinear with the charge current [227,251][4]. These novel results suggest that this class of materials holds great potential for spintronics. It is worth noting that the so-called 1T′ and $1T_d$ phases of $MoTe_2$ and WTe_2 are classified as type-II Weyl semimetals [130, 168, 249, 255], and when they are thinned towards the monolayer limit become topological insulators [214]. However, little is known about the impact of their topology on CSI, nor their combination of a large SHA together with a supposedly long spin relaxation length.

[4]The symmetries of typical metals and semiconductors where the SHE is studied restrict the spin polarization of the spin current to be perpendicular to both the charge and the spin current.

1.1 Objectives and outline

The objective of this thesis is expanding the theoretical knowledge in these two current challenges:

- Understanding the crossover from diffusive to ballistic spin transport in ultraclean graphene devices as well as the main spin relaxation mechanisms in such clean limit.
- Exploring spin transport and charge-to-spin interconversion in two-dimensional low-symmetry transition metal dichalcogenides.

To this end, in this thesis I will present numerical calculations to simulate realistic spin transport experiments. The thesis is organized as follows.

Chapter 1 introduces the field of spintronics, some of the current unresolved problems and the potential of two-dimensional materials to overcome them.

Chapter 2 establishes the fundamental theoretical concepts of spin dynamics such as spin-orbit coupling, spin relaxation, charge-to-spin interconversion and the role of topology in spintronics. It also introduces more deeply the field of 2D spintronics, especially the state-of-the-art of graphene and TMDs.

In Chapter 3, the theoretical and numerical methodologies for studying spin dynamics are presented. This includes the description of the electronic structure and spin textures with tight-binding models. The basics of the quantum transport Landauer-Büttiker formalism [54] are outlined as well as its implementation in the open-source Kwant package [94]. Finally, I show how to set up the spin transport devices for the simulations.

Chapters 4 and 5 present the main results of this thesis. In the former, I study graphene nonlocal spin valve devices. Such devices are widely used to infer the spin relaxation times and lengths of materials as they separate charge and spin currents [125, 131, 132]. First, I simulate such devices in the diffusive regime of transport in order to validate the implementation, and then I vary the degree of disorder to tune the mean free path and achieve ballistic transport. From explicit calculations of all voltages and transmission probabilities, I show that in the diffusive regime the nonmagnetic electrodes limit spin transport in the graphene channel when the spin relaxation length is comparable to the device size. Being unaware of this effect may result in an underestimation of the spin relaxation length when the typical formulas are used. In the crossover from diffusive to ballistic transport, I explicitly demonstrate that the spin diffusion formulation fails in both the ballistic and quasiballistic regimes (defined as a transition regime between diffusive and ballistic transport) and I explain the numerical results with alternative analytical formulas and clear physical arguments. This new formulation of spin transport will be crucial for the analysis of future ultra-clean spintronic devices, both for extracting

correct values of spin diffusion lengths in diffusive transport and in guiding experiments in the (quasi)ballistic regime.

In Chapter 5, I simulate nonlocal spin valves in $MoTe_2$ to study the spin relaxation lengths and also the spin Hall effect by calculating the spin accumulation at the sample boundaries. The spin polarization of the conduction bands presents a persistent spin texture canted in the yz plane, which is responsible for a spin relaxation anisotropy between the different spin orientations. Furthermore, I demonstrate the presence of an unconventional SHE with both out-of-plane and in-plane spin polarization, as found in experiments [227, 251], and derive a formula to extract the spin Hall angles. The spin Hall angle reaches unprecedented values as large as $\approx 80\%$ with reasonably long λ_s in the range of $10 - 100$ nm. Both quantities scale in the same way with varying carrier density, suggesting that these materials can be good for both spin communication and manipulation. Importantly, I reveal that the origin of the relative magnitudes of the spin textures, spin relaxation lengths and the SHAs for each spin component are dictated by the specific crystal symmetries of such TMDs. Finally, I simulate the spin transport in the topological gap of WTe_2. I find that the unconventional SHE transforms into a canted quantum spin Hall effect, in which the spin polarization of the topological edge states deviates from the common z-polarized spins into an angle in the yz plane, as in the bulk bands, dictated by the symmetries of the crystal. The new spin polarization found in both the spin Hall effect and the quantum spin Hall effect, together with the large spin diffusion lengths and spin Hall angles, open new avenues for utilizing the spin degree of freedom to transport and process information in topological, low-symmetry two-dimensional materials.

Chapter 6 draws the conclusions of the thesis and present and outlook for future research directions.

CHAPTER 2

FUNDAMENTALS OF SPIN DYNAMICS IN TWO-DIMENSIONAL MATERIALS

2.1 Physics of spin dynamics

In this section, I review some of the principal physical phenomena involved in spin dynamics.

2.1.1 Spin-orbit coupling

The spin-orbit coupling or spin-orbit interaction couples an electron's spin with its orbital angular momentum, and is a fundamental concept in spintronics. It is at the root of many phenomena such as the SHE, spin-orbit torques and spin relaxation, among others. The physical origin of the SOC is relativistic in nature, as it appears directly in the Dirac equation with the term

$$\mathcal{H}_{\mathrm{SOC}} = -\frac{e\hbar}{4m_0^2c^2\sqrt{1-v^2/c^2}}\left(\nabla V \times (\boldsymbol{p}+e\boldsymbol{A})\right)\cdot \boldsymbol{s}_\sigma, \tag{2.1}$$

where $\hbar$ is the reduced Planck constant, c is the speed of light in vacuum, V is the electrostatic potential, $\boldsymbol{p} = m_0\boldsymbol{v}$ is the linear momentum with m_0 and $|\boldsymbol{v}| = v$ the rest mass of the electron and its velocity, respectively, e is the electron's charge and $\boldsymbol{A}$ the vector potential due to a magnetic field. The term $\boldsymbol{s}_\sigma = (s_x, s_y, s_z)$ is a vector containing the Pauli matrices and relates to the spin angular momentum operator as $\mathbf{S} = \frac{\hbar}{2}\boldsymbol{s}_\sigma$. To understand the meaning of the term above, it is useful to set $\boldsymbol{A} = 0$ and rewrite it as

$$\mathcal{H}_{\mathrm{SOC}} = \frac{e\hbar}{2m_0}\frac{\boldsymbol{E}\times\boldsymbol{v}}{2c^2\sqrt{1-v^2/c^2}}\cdot\boldsymbol{s}_\sigma = \mu_{\mathrm{B}}\boldsymbol{B_0}\cdot\boldsymbol{s}_\sigma. \tag{2.2}$$

Here, $\mu_B = e\hbar/2m_0$ is the Bohr magneton, $\boldsymbol{B_0} = \frac{\boldsymbol{E}\times\boldsymbol{v}}{2c^2\sqrt{1-v^2/c^2}}$ is the magnetic flux density according to Einstein's relativity theory and $\boldsymbol{E} = -\nabla V$ is the electric field. One can clearly see that the SOC Hamiltonian can be expressed as a Zeeman interaction between the electron's spin and a magnetic field $\boldsymbol{B_0}$, whose origin is the orbital motion of electrons. This can be seen more clearly by considering an atom, which is usually described as a static nucleus with orbiting electrons. However, in the rest frame of the electron it is the nucleus that orbits, and the electron feels a magnetic field due to this moving positive charge. Consequently, the spin-orbit coupling describes an intrinsic magnetic field (SOC field), arising due to the orbital motion of electrons, that interacts with the electron's spin.

Depending on the system, the SOC can manifest in different ways. For instance, in atomic physics, one can write the magnetic field using the Biot-Savart law in terms of the radius of the electron orbit and its velocity, which allows the magnetic field to be expressed in terms of the quantum mechanical orbital angular momentum operator, $\mathbf{L}$. This results in a SOC of the form

$$\mathcal{H}_{\mathrm{SOC}} \propto \mathbf{L} \cdot \mathbf{S}, \tag{2.3}$$

highlighting the fact that $\boldsymbol{B_0}$ is related to the orbital motion of electrons. In general, the strength of the spin-orbit coupling interaction is proportional to the atomic number, so the heavier the element, the larger the SOC. In solids, equation (2.3) takes different forms depending on the symmetries of the system. For example, the Dresselhaus SOC [57] or the Rashba SOC [34] may appear when inversion symmetry is broken due to the crystal structure or an external electric field. Such spin-orbit interactions are very important in spintronics because they allow to manipulate spins via an electric field-induced magnetic field.

2.1.2 Spin texture of Bloch bands

The spin texture or spin polarization of the bands is given by the expectation value of the spin operator applied to the Bloch wave functions. As it will be seen in Chapter 5, this quantity is fundamental to understand spin transport and relaxation. For a given k, the spin texture at band n is:

$$\langle s_n^\alpha(k)\rangle = \frac{\hbar}{2}\langle n,k|s_\alpha|n,k\rangle, \tag{2.4}$$

where s_α is the spin Pauli matrix with $\alpha = x, y, z$. Usually, the different components of the spin polarization are related to each other via the norm of the spin polarization,

$|\langle \boldsymbol{s}_n(k)\rangle|$, which is equal to:

$$|\langle \boldsymbol{s}_n(k)\rangle| = \sqrt{|\langle s_n^x(k)\rangle|^2 + |\langle s_n^y(k)\rangle|^2 + |\langle s_n^z(k)\rangle|^2}. \tag{2.5}$$

It is also useful to define the k-resolved spin texture at a given energy, since an electron that scatters samples the whole Fermi surface. In this way, we define:

$$\langle s_n^\alpha(k)\rangle_E = \frac{\hbar}{2}\frac{\delta(E_n(k)-E)\langle n,k|s_\alpha|n,k\rangle}{\delta(E_n(k)-E)\langle n,k|n,k\rangle}. \tag{2.6}$$

Here, $\delta(E_n(k)-E)$ is a Dirac delta centered at the given energy E, $E_n(k)$ is the eigenvalue of band n, and the denominator normalizes the sum since otherwise the value of the spin texture would depend on the number of k-points used for the sum. Numerically, one can replace the single-valued delta by a probability distribution (a Gaussian, Lorentzian or a derivative of a Fermi-Dirac distribution are typically employed). This generates a finite broadening (e.g. $k_\mathrm{B}T$ for the Fermi-Dirac distribution) that will add the contribution of other energies to the spin texture. Nevertheless, this does not pose a problem as long as the spin texture does not change abruptly in a window of energies on the order of the broadening [1].

Unless stated otherwise, calculations of the spin texture will always be done for a single band, and therefore the subscript n can be dropped.

2.1.3 Spin relaxation

Spin relaxation is the process by which a nonequilibrium spin density decays to its equilibrium population. As commented in Chapter 1, this sets an upper limit on the time and length in which spins can carry information, which are characterized by the spin lifetime, τ_s, and the spin diffusion length, λ_s. Here, we will briefly summarize the main mechanisms of spin relaxation before focusing on how spin relaxation is studied experimentally.

Spin relaxation mechanisms

There are several mechanism of spin relaxation in solids [67,122,288]. The most typical are the ones related to semiconductors and metals, namely the Elliot-Yafet mechanism [65, 296], the D'Yakonov-Perel' mechanism [63], the Bir-Aronov-Pikus mechanism [122, 288] and the hyperfine-interaction mechanism [122, 288]. Among these, the former two have been the most used to interpret spin relaxation in 2D materials. Although distinct, they have two common ingredients: SOC and charge scattering.

[1] These broadenings can also have physical meaning. For example, the derivative of the Fermi-Dirac distribution is used to account for thermal broadening at a finite temperature.

In the Elliot-Yafet mechanism, up and down spins that would normally be independent of each other are coupled by the SOC. The result is that an electron's spin has a finite probability of flipping during a scattering event, leading to a spin relaxation time that is proportional to the momentum scattering time (τ_p), $\tau_s \propto \tau_p$. Thus, spin relaxation in this case can be thought of as a sudden process where a single spin changes its polarization upon scattering. On the other hand, the D'Yakonov-Perel' mechanism can be understood as a continuous evolution of an electron's spin. It occurs in systems where inversion symmetry is broken, and, together with SOC, leads to a spin splitting of the bands. This splitting is proportional to the induced SOC field, which usually is momentum-dependent. In this way, the SOC field produces spin precession whose direction changes at each scattering event, resulting eventually in spin dephasing of the ensemble polarization. When the scattering time is shorter than the precession time, electrons tend to maintain their spin orientation, in what is known as motional narrowing. Consequently, the spin relaxation time is inversely proportional to the momentum scattering time, $\tau_s \sim 1/\tau_p$.

Measuring spin relaxation: lateral nonlocal spin valves

Introduction Two kinds of experiments can be used to study spin relaxation in a sample [122]: experiments measuring spectroscopic features that are spin-dependent, and experiments measuring explicitly the change of the nonequilibrium spin density with time or distance. We will focus on the latter, specifically on the Hanle effect [106] in lateral nonlocal spin valves (NSV) [131], which is the standard procedure to measure spin lifetimes in 2D materials.

The NSV was developed by Johnson and Silsbee [131] and is depicted in Figures 2.1(a) and 2.1(b). The device consists of two ferromagnetic contacts[2] (the injector (F1) and detector (F2)) and at least two nonmagnetic (NM) leads (N1 and N2). They are placed on top of a nonmagnetic sample (N), whose spin transport properties are to be characterized, separated by distances on the order of micrometers. The order of the leads is important: the FM contacts are in the middle whereas the nonmagnetic ones are at opposite ends of the device. We can distinguish three sections in the device: the closed circuit where a charge current I_0 is driven between F1 and N1; the channel where spins propagate over the distance L between F1 and F2 (see Figure 2.1(a)); and the open circuit where voltage is measured between F2 and N2. Probably the most fundamental aspect of a NSV is the fact that the voltage is measured far from the path of charge current, thus the name *nonlocal* spin valve and *nonlocal* voltage, V_{nl}.

One of the key aspects that makes NSV so practical is that they can separate spin from charge signals. Charge-related backgrounds, which may appear in two-terminal devices

[2]Contacts can also be called electrodes or leads.

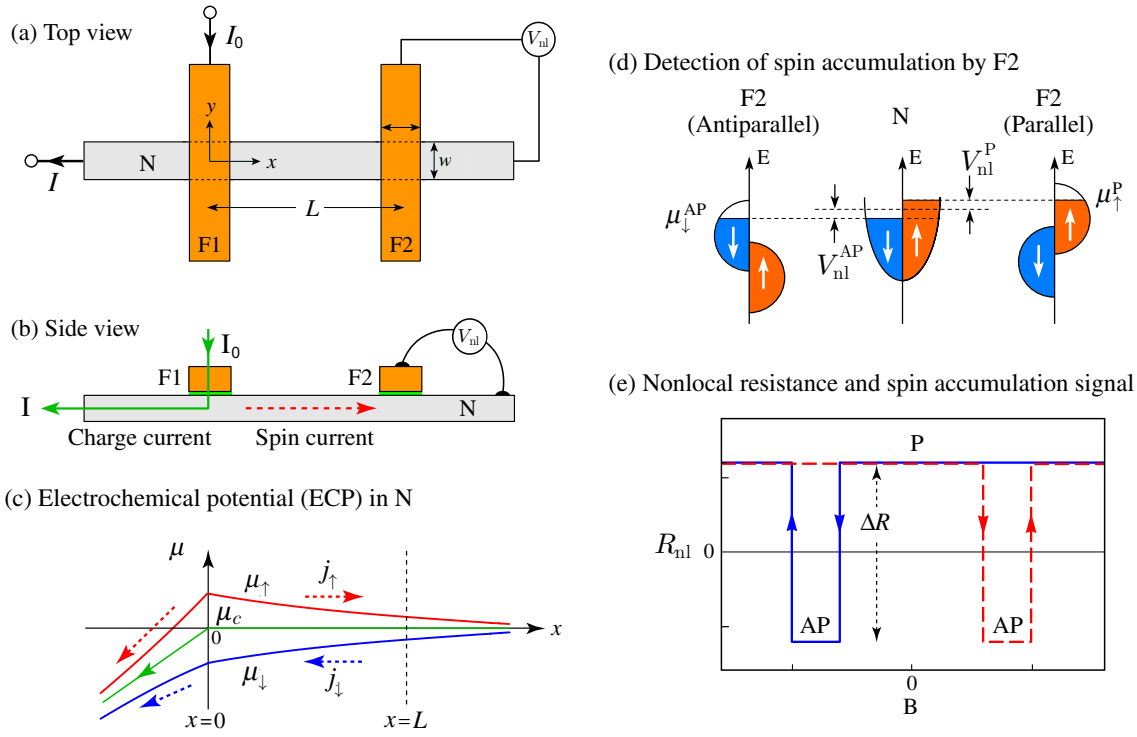

Figure 2.1: (a) Top view of a lateral nonlocal spin valve. Two ferromagnets (F1, F2) are placed on top of a nonmagnetic material of width w, separated by a distance L. A current I_0 is driven from F1 to the left side of the device and a voltage $V_{\rm nl}$ is measured between F2 and the right part of the sample. (b) Side view of the NSV. The application of a charge current in the left generates a spin current diffusing to the right. The ferromagnets are separated from the sample by tunnel barriers (green) to prevent spin absorption. (c) Charge and spin electrochemical potential profiles in the sample. Green, red and blue denotes charge, spin-up and spin-down ECP, respectively. (d) Schematics showing how the spin-dependent ECP of F2 aligns with the nonequilibrium spin density of the nonmagnet. (e) Experimental signature of a NSV. When the relative polarization direction of the injector and detector is parallel, $R_{\rm nl} > 0$. When the magnetic field flips one of the FM electrodes so their polarization is antiparallel, $R_{\rm nl} < 0$. Figure extracted from Ref. [258]: *Spin current, spin accumulation and spin Hall effect*, Saburo Takahashi and Sadamichi Maekawa (2008), Science and Technology of Advanced Materials, copyright © National Institute for Materials Science, reprinted by permission of Taylor & Francis Ltd, http://www.tandfonline.com on behalf of © National Institute for Materials Science.

where spin is transported via a spin-polarized current, might mask the spin-dependent effects. In a NSV, the way the voltage and currents are set up plays a crucial role in achieving good spin sensitivity. Different combinations are possible, but a simple and common configuration is the following: while a voltage is applied between F1 and N1 (which is grounded), contacts F2 and N2 are left floating since they are used as voltage probes. In this way, the left side of the device is closed and current flows between F1 and N1, but to the right of the injector the circuit is open, so electrical current does not flow towards F2 nor N2. However, as explained below, pure spin current does flow from F1 to the right.

Before delving further into the processes occurring in a NSV, it is important to introduce the concept of spin electrochemical potential (ECP), since this is what is probed by the FM detector, and its relationship with the spin density. Similar to the charge and spin densities, we can use the spin-dependent electrochemical potentials, $\mu_{\uparrow/\downarrow}$, to define a charge ECP, $\mu_c = \frac{\mu_\uparrow + \mu_\downarrow}{2}$, and a spin ECP, $\mu_s = \mu_\uparrow - \mu_\downarrow$[3]. Furthermore, the spin-dependent Einstein relation states that $\sigma_{\uparrow/\downarrow} = e^2 N_{\uparrow/\downarrow} D_{\uparrow/\downarrow}$, where $\sigma_{\uparrow/\downarrow}, N_{\uparrow/\downarrow}, D_{\uparrow/\downarrow}$ are the spin-dependent electrical conductivity (or sheet conductivity in two-dimensions), the spin-dependent density of states and the spin-dependent spin diffusion coefficient, respectively. Noting that a small change of density is related to a variation in electrochemical potential as $\delta n_{\uparrow/\downarrow} = N_{\uparrow/\downarrow} \delta\mu_{\uparrow/\downarrow}$, we obtain, by using the Einstein relation,

$$\delta n_{\uparrow/\downarrow} = \frac{\sigma_{\uparrow/\downarrow}}{e^2 D_{\uparrow/\downarrow}} \delta\mu_{\uparrow/\downarrow} = \frac{\sigma}{2e^2 D_s} \delta\mu_{\uparrow/\downarrow}, \tag{2.7}$$

where we have used the formulas $\sigma_\uparrow = \sigma_\downarrow = \sigma/2$ and $D_\uparrow = D_\downarrow = D_s$ that apply to nonmagnetic materials ($\sigma = \sigma_\uparrow + \sigma_\downarrow$ is the total electrical conductivity and D_s the spin diffusion coefficient or constant). By subtracting the up and down components, we get:

$$\delta \boldsymbol{s} = \frac{\sigma}{2e^2 D_s} \delta \boldsymbol{\mu}_s. \tag{2.8}$$

Here, we have explicitly accounted for the fact that the spin density and the spin electrochemical potential are vectors ($\boldsymbol{s} = (s^x, s^y, s^z)$ and $\boldsymbol{\mu}_s = (\mu^x, \mu^y, \mu^z)$) since the spin can be polarized in any Cartesian direction. Equation (2.8) converts the spin accumulation, in units of inverse area or volume, into the spin ECP that has units of energy, and will prove useful later on when deriving the expression for the nonlocal voltage. Likewise, it is important to introduce the relation between the spin accumulation, the spin electrochemical potential and the spin current. From diffusive theory, the current density of an

[3]Sometimes a factor of 1/2 is used when defining the spin ECP, $\mu_s = \frac{\mu_\uparrow - \mu_\downarrow}{2}$. It is just a convention and both choices are widely used in the literature [67, 122, 273].

up or down spin ($J_{\uparrow/\downarrow}$) is:

$$J_{\uparrow/\downarrow} = eD_s \frac{\partial n_{\uparrow/\downarrow}}{\partial x} = \frac{\sigma}{2e} \frac{\partial \mu_{\uparrow/\downarrow}}{\partial x}, \tag{2.9}$$

and consequently, the spin current density along the x direction is[4]:

$$\boldsymbol{J}_{s,x} = (J^x_{s,x}, J^y_{s,x}, J^z_{s,x}) = eD_s \frac{\partial \boldsymbol{s}}{\partial x} = \frac{\sigma}{2e} \frac{\partial \boldsymbol{\mu}_s}{\partial x}. \tag{2.10}$$

Working principle The complete working principle of a NSV can be divided into three processes: spin injection, spin transport and spin detection. For spin injection, as just mentioned, a bias difference is imposed between F1 and the N1, so a current I_0 flows in that device region (see Figures 2.1(a) and 2.1(b)). Importantly, this current is spin-polarized, and creates a nonequilibrium spin accumulation in the sample underneath F1. The sign of this spin density is the same as the polarization of F1.

Because of a gradient in the spin accumulation, the spins diffuse to the right along the channel until they reach F2. To understand the transport and relaxation of spins in a NSV, it is insightful to view the profile of the spin accumulation or spin ECP along the device. A representative example is shown in Figure 2.1(c). The green line depicts the charge ECP, while red and blue lines show the spin-up and spin-down ECP, respectively. From the position of F1 (set at $x = 0$) to the left, both charge and spin ECPs display a slope in the profile. Such a variation of ECP with distance indicates (see equations (2.9) and (2.10)) a spin-polarized current from F1 to N1. On the other hand, from $x = 0$ to the right, the charge ECP is constant, but the spin ECPs are not. The most relevant aspect to remark from this profile is the opposite slopes of the up and down spin ECPs for $x > 0$. Not only does this mean that there is a spin current, but also that there is the same amount of spin-up and spin-down electrons flowing in opposite directions, thus canceling out the charge current (i.e. $(\mu_\uparrow - \mu_c) = -(\mu_\downarrow - \mu_c)$). Consequently, the charge ECP is constant throughout $x > 0$, as marked by the flat green curve.

Finally, the spins reach the F2 electrode and are detected by means of the so-called spin-charge coupling. This concept, developed by Silsbee [240], states that a nonequilibrium spin accumulation in a nonmagnetic material produces a spin-dependent electromotive force which can be measured as a spin-dependent voltage. This is the reason why a ferromagnetic material is needed as a detection probe, as only materials with a net spin magnetization are sensitive to such spin-dependent voltage. A schematic of this measurement process is displayed in Figure 2.1(d), in which the FM is idealized to be

[4]The spin current (density) is in fact a tensor including both the direction of the spin polarization and the direction of propagation. See List of Acronyms and useful Symbols for the different definitions used in this thesis.

100% polarized to simplify the explanation. The F2 detector can measure only spins that are aligned with its magnetization axis. In this manner, if we assume that the spin density profiles shown in Figure 2.1(c) are parallel to the detector's magnetization, F2 will detect a voltage proportional to $\mu_\uparrow$ or $\mu_\downarrow$. This voltage arises because the spin-dependent chemical potential of F2 aligns with that of the nonmagnetic sample (red or blue line in Figure 2.1(c)), thus giving $V_{\mathrm{F2}} = \mu_{\uparrow/\downarrow}/(-e)$. On the other hand, lead N2 is nonmagnetic and as such does not align with the spin-dependent ECP, but rather with μ_c. Therefore, the measured nonlocal voltage $V_{\mathrm{nl}} = V_{\mathrm{F2}} - V_{\mathrm{N2}}$ will be just $V_{\mathrm{nl}} = (\mu_{\uparrow/\downarrow} - \mu_c)/(-e)$. After the voltage is measured, it is typically normalized by the injected current I_0, defining in this way the nonlocal resistance $R_{\mathrm{nl}} = V_{\mathrm{nl}}/I_0$. [5]

An important caveat of this detection method is that the above explanation assumes that the spins do not flow into F2. The specific conditions of voltage and currents in a NSV ensure that there is no charge current flowing into F2, but do not prevent spin current from flowing between the sample and the detector. When this occurs, F2 acts as a spin sink and suppresses all the nonequilibirum spin accumulation in N, reducing in this way the value of V_{nl}. This phenomenon is known as spin absorption [67,76,122,126,218,257] and takes place when the contact resistance between F2 and the conducting channel is small. Because of the larger conductivity and smaller spin relaxation length of a ferromagnet, spins find less resistance in going into the detector than continuing propagating in the sample. In this scenario, since F2 perturbs the spin transport, V_{F2} becomes dependent on the interface resistance [257,258]. Although we just mentioned spin absorption at the F2/N interface, it applies as well to the injector, where the created spin accumulation returns back to F1 instead of diffusing along the channel. Naturally, this effect is something that needs to be avoided as it hinders spin transport and communication, and hence high-resistive tunnel barriers are normally placed between FM contacts and the sample [10,101].

Since both the injector and detector have the same polarization direction due to the magnetocrystalline (or shape) anisotropy, two different outputs of nonlocal voltage can be measured: when F1 and F2 have parallel alignment, and when F1 and F2 have antiparallel alignment. Assuming that F1 injects up-spins, a parallel measurement would correspond to measuring the $\mu_\uparrow$ component of the spin ECP. Conversely, in the antiparallel setup, $\mu_\downarrow$ is detected. By looking at the spin accumulation profile (Figure 2.1(c)), one can easily observe that the former case will lead to a positive V_{nl} ($\mu_\uparrow - \mu_c > 0$), whereas the latter one renders a negative nonlocal voltage ($\mu_\downarrow - \mu_c < 0$). A typical experimental measurement is shown in Figure 2.1(e), where V_{nl} is probed while applying an in-plane magnetic field to switch the FM polarizations. The abrupt and reversible change of sign in the nonlocal

[5] This nonlocal resistance is not a resistance in the usual sense. It can take positive and negative values and normalizes the output voltage by the input current.

voltage is a smoking gun of a true spin signal generated, transported and detected in a NSV.

Spin diffusion equations

After understanding how NSV works, the next step is to extract the spin relaxation time and length from a nonlocal resistance measurement. For that, the dynamics of spins moving along the NSV channel is modeled with the so-called spin drift-diffusion equation (also called diffusive Bloch equations) [67, 125, 131, 132], which describes the time and space dependence of the spin density. This equation reads

$$\frac{\partial \boldsymbol{s}}{\partial t} = \overline{D_s}\nabla^2 \boldsymbol{s} + \mu \boldsymbol{E}\boldsymbol{\nabla}\boldsymbol{s} + \boldsymbol{s} \times \boldsymbol{\omega} - \frac{\boldsymbol{s}}{\overline{\tau_s}}. \tag{2.11}$$

Here, μ is the carrier mobility, $\boldsymbol{E}$ the electric field applied along the channel in the NSV, $\boldsymbol{\omega} = g\mu_{\mathrm{B}}\boldsymbol{B}/\hbar$ is the Larmor precession frequency associated with an applied external magnetic field $\boldsymbol{B}$ (with g the Landé g-factor). $\overline{D_s}$ and $\overline{\tau_s}$ are tensors describing the spin diffusion coefficient and spin lifetime in each Cartesian direction for each spin component. The first term in the r.h.s of equation (2.11) describes the spin diffusion, the second term the spin drift due to an applied electric field, the third term models spin precession and the last term spin relaxation. In NSV devices, a few simplifications can be made in the equation above. First, the electric field is typically absent, as highlighted in Figure 2.1(c), which allows separation of the spin from the charge background contribution. Second, the channel in the device has a large aspect ratio, such that transport is usually assumed one-dimensional and the gradient becomes a simple derivative. Finally, the spin diffusion tensor $\overline{D_s}$ is assumed to be isotropic in both spin and direction, thus becoming a scalar. Importantly, equation (2.11) assumes diffusive transport for both spin and charge, and because of this, some authors assume that the spin diffusion constant is the same as the charge diffusion contant, D_c. However, this is still a controversial topic and a distinction between spin and charge diffusion coefficients is sometimes made [15, 67, 134]. With the above approximations, and also assuming steady state ($\frac{\partial \boldsymbol{s}}{\partial t} = 0$), one can express equation (2.11) as

$$0 = D_s\frac{\partial^2 \boldsymbol{s}}{\partial x^2} + \boldsymbol{s} \times \boldsymbol{\omega} - \frac{\boldsymbol{s}}{\overline{\tau_s}}, \tag{2.12}$$

where we have assumed that the spin transport direction is along x.

There are two experimental procedures to extract the spin lifetime. One is to track the decay of the spin accumulation with length in absence of magnetic field by using multiple FM detectors and measuring several nonlocal voltages. The other involves just one detector and what is measured is the variation of the spin accumulation with an

applied magnetic field. The latter method, called the Hanle effect [106], is generally preferred since fabricating many FM contacts with similar tunnel barriers and contact resistances is complicated. Because of the magnetocrystalline or shape anisotropy of the FM contacts, their polarization is in-plane and perpendicular to the transport direction (i.e, along y in the current case) and consequently, the injected spin density in the channel is along y too. Depending on the direction of the applied field, different components of the spin lifetime tensor can be inferred, and if the material presents spin lifetime anisotropy, that is, the spin lifetime for different spin components is not equal, a combination of measurements with several directions of the field is needed to disentangle each individual spin lifetime. Here, we will focus on the simplest and most studied case for 2D materials, which is a magnetic field perpendicular to the plane (i.e. along z) and isotropic spin lifetime. A derivation of the Bloch equations with other field directions and anisotropy can be found in Refs. [83, 216]. Taking $\boldsymbol{\omega} = (0, 0, \omega_z)$, the Bloch equation reads

$$\frac{\partial^2}{\partial x^2}\begin{pmatrix} s^x \\ s^y \\ s^z \end{pmatrix} = \begin{pmatrix} 1/\lambda_s & -\omega_z/D_s & 0 \\ \omega_z/D_s & 1/\lambda_s & 0 \\ 0 & 0 & 1/\lambda_s \end{pmatrix}\begin{pmatrix} s^x \\ s^y \\ s^z \end{pmatrix}, \tag{2.13}$$

where we have used the relation $\lambda_s = \sqrt{D_s\tau_s}$. The components of the spin density have solutions of form:

$$\begin{aligned} s^x &= -A\frac{i}{\kappa}e^{-\kappa x} + B\frac{i}{\kappa}e^{\kappa x} + C\frac{i}{\kappa^*}e^{-\kappa^* x} - D\frac{i}{\kappa^*}e^{\kappa^* x} \\ s^y &= -A\frac{1}{\kappa}e^{-\kappa x} + B\frac{1}{\kappa}e^{\kappa x} - C\frac{i}{\kappa^*}e^{-\kappa^* x} + D\frac{i}{\kappa^*}e^{\kappa^* x} \\ s^z &= Ee^{-x/\lambda_s} + Fe^{x/\lambda_s}, \end{aligned} \tag{2.14}$$

with $\kappa = \sqrt{\frac{1}{\lambda_s^2} - i\frac{\omega_z}{D_s}}$. Because of the out-of-plane magnetic field, the in-plane components of the spin density are coupled to each other, whilst the z-component is not. Nevertheless, we are only interested in s^y since this is what the detector can measure.

To solve the system of equations, boundary and/or initial conditions have to be considered. Although spin flows in the whole NSV depicted in Figure 2.1(a), equations (2.14) are usually solved only on the right side of the injector. First, it is assumed that the spin is completely relaxed at $+\infty$ and at lead N2,

$$s^x(+\infty) \to 0 \tag{2.15}$$

$$s^y(+\infty) \to 0. \tag{2.16}$$

Second, the spin current at the injection point ($x = 0$) is described by equation (2.10)

and is polarized along y, implying:

$$\frac{\partial s^x}{\partial x} = 0 \tag{2.17}$$

$$\frac{\partial s^y}{\partial x} = \frac{J^y_{s,x}}{2eD_s}, \tag{2.18}$$

where the factor of 2 appears because the right-propagating spin current at the injector is assumed to be half the value of the total injected spin-polarized current. Although these assumptions may be reasonable for most cases, we will see in Chapter 4 that other boundary conditions for equations (2.14) need to be taken into account to describe certain regimes of spin transport. Applying these conditions, one obtains:

$$s^y = -\frac{J^y_{s,x}}{2eD_s}\mathrm{Re}\left\{\frac{e^{-\kappa x}}{\kappa}\right\}. \tag{2.19}$$

To convert the spin accumulation into the nonlocal resistance, a few extra steps are required. First, we convert the spin density into the spin electrochemical potential using equation (2.8),

$$\mu^y = -\frac{eJ^y_{s,x}}{\sigma}\mathrm{Re}\left\{\frac{e^{-\kappa x}}{\kappa}\right\} = -\frac{eI_0P_i}{w\sigma}\mathrm{Re}\left\{\frac{e^{-\kappa x}}{\kappa}\right\}, \tag{2.20}$$

where we have used $J^y_{s,x} = P_iI_0/w$, with P_i and w being the injector polarization and the cross section (in three dimensions) or the width (in two dimensions) of the spin conducting channel, respectively. Then, by inspecting the spin density profile (Figure 2.1(c)), one can see that $\mu_\uparrow - \mu_c = -(\mu_\downarrow - \mu_c) = \mu_s/2$. Hence, $V_{\mathrm{nl}} = P_d\mu_s/(-2e)$, where we have introduced the polarization of the detector, P_d, to account for non-ideal ferromagnets. With these relations, the nonlocal resistance becomes:

$$R_{\mathrm{nl}} = \frac{V_{\mathrm{nl}}}{I_0} = \frac{P_iP_d}{2w\sigma}\mathrm{Re}\left\{\frac{e^{-\kappa x}}{\kappa}\right\} = \frac{P_iP_d}{2w\sigma}\mathrm{Re}\left\{\frac{e^{-x\sqrt{\frac{1}{\lambda_s^2} - i\frac{\omega_z}{D_s}}}}{\sqrt{\frac{1}{\lambda_s^2} - i\frac{\omega_z}{D_s}}}\right\}. \tag{2.21}$$

The polarization of the leads take values in the interval $[-1, 1]$, with 1 (-1) representing a fully polarized ferromagnet along the spin-up (spin-down) direction, while 0 denotes a nonmagnetic contact. Therefore, equation (2.21) shows that the sign of the nonlocal resistance depends on the relative polarization direction of the FM leads, as illustrated in Figure 2.1(e). To extract the spin diffusion time or length, one measures the dependence of the nonlocal resistance with the out-of-plane magnetic field, and fit it to equation (2.21). Tipically, the fitting parameters are the polarization, which is assumed to be the same for both electrodes ($P_i = P_d = P$) and the spin diffusion time or length. The spin diffusion coefficient is also usually fitted, although the value of the charge diffusion

constant may be used, if known. An example of a typical Hanle curve is shown in Figure 2.2(a) for different values of spin diffusion length. One advantage of this technique is the relatively low magnetic field needed to observe the Hanle oscillation, as it avoids the presence of orbital-related effects, such as Landau levels.

As commented earlier, another way to obtain the spin transport properties is by measuring the length dependence of the nonlocal resistance. Taking the limit $\omega_z = 0$, $R_{\rm nl}$ becomes

$$R_{\rm nl}(B=0) = P_i P_d \frac{\lambda_s}{2w\sigma} e^{-x/\lambda_s}, \tag{2.22}$$

which indicates that the spin accumulation decays exponentially with length. In contrast to the Hanle oscillations, a fit with equation (2.22) does not allow for the extraction of the spin diffusion coefficient. An example of such exponential decay is illustrated in Figure 2.2(b) for several values of λ_s.

To complement the derivation presented above, it is worth mentioning that there is an alternative procedure to obtain an expression equivalent to equation (2.21) [67, 125]. Diffusive theory tells us that an electron density n that satisfies the initial condition $n(x,0) = N_0\delta(x)$, evolves in time and space as a normal probability distribution [67]

$$P(x,t) = \frac{N_0}{\sqrt{4\pi D_c t}} e^{-x^2/(4D_c t)}, \tag{2.23}$$

where N_0 is the total number of electrons. If we now apply this result to the spin density along an in-plane component and consider that spins precess about an out-of-plane field

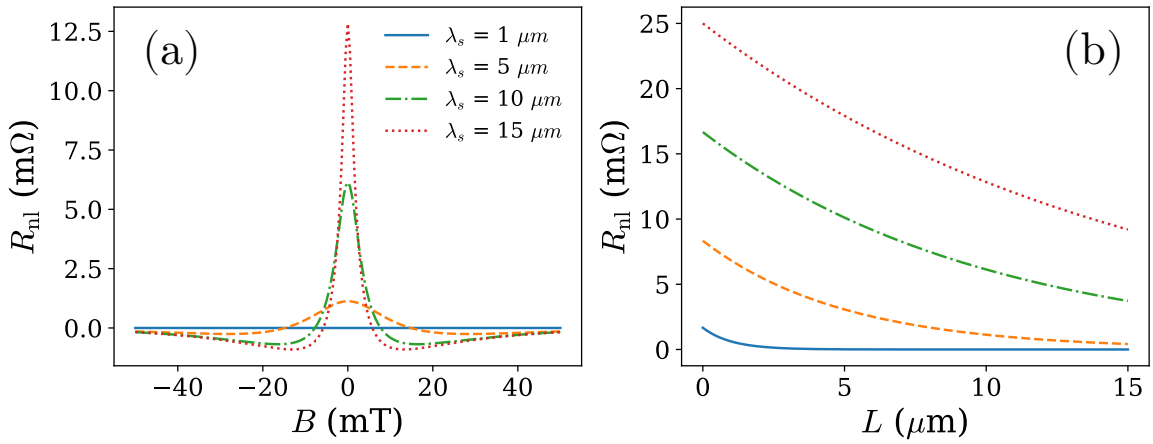

Figure 2.2: (a) Hanle curves for different values of spin diffusion length modeled with equation (2.21). The parameters used are: $L = 10$ μm, $D_s = 0.05$ m^2/s, $P_i = P_d = 1$, $\sigma = 100$ S, $w = 3$ μm . (b) Length dependence of the nonlocal resistance for different values of spin diffusion lengths modeled with equation (2.22). The parameters used are the same as in (a).

and also relax exponentially with time, one obtains [67]:

$$s_y(x,t) \sim \frac{N_0}{\sqrt{4\pi D_s t}} e^{-x^2/(4D_s t)} \cos(\omega_z t) e^{-t/\tau_s} = P(x,t)\cos(\omega_z t) e^{-t/\tau_s}. \tag{2.24}$$

To relate this to the spin accumulation underneath the FM detector (and therefore to R_{nl}), we need to integrate over all possible transport times so we account for all spins reaching the detector,

$$R_{\mathrm{nl}} \propto \int_0^\infty s_y(x=L,t)\mathrm{d}t = \int_0^\infty P(x=L,t)\cos(\omega_z t) e^{-t/\tau_s}\mathrm{d}t = \tag{2.25}$$

$$= \int_0^\infty \frac{N_0}{\sqrt{4\pi D_s t}} e^{-L^2/(4D_s t)} \cos(\omega_z t) e^{-t/\tau_s}\mathrm{d}t. \tag{2.26}$$

It can be easily verified numerically that equations (2.21) and (2.25) are equivalent. The advantage of this equation over equation (2.21) is that one can directly see what physical effects are taking place. Namely, a spin density that diffuses ($P(x,t)$), precesses ($\cos(\omega_z t)$) and relaxes (e^{-t/τ_s}). It is to be noted that the combination of precession and diffusion reduces the magnitude of the nonlocal signal. Although all spins precess coherently with frequency ω_z, the diffusive motion makes the spins reach the detector at different times, and therefore with different spin polarization. Importantly, this is just a dephasing process and is independent of spin relaxation.

In this section, we have presented two procedures to obtain an equation describing the spin dynamics (diffusion, rotation and relaxation) of spins. In Chapter 4 we will make use of both approaches to derive other equations suitable for describing NSV in unconventional spin transport regimes.

2.1.4 Charge-to-spin interconversion

The interconversion of the charge and spin degrees of freedom is another key ingredient for realizing active spintronic devices. Here, we define CSI to those phenomena that involve the generation of spin (charge) currents due to the transport of charge (spin). In this category, we include the SHE and ISHE [61, 62, 112, 143, 238, 243, 274, 290, 303]; and so-called inverse spin galvanic effect (ISGE) and spin galvanic effect [64, 81, 142, 239]; and motion of magnetic textures (skyrmions) [75, 193], magnetic domain walls [210, 265, 297], and magnons [44, 45, 136] induced by (spin-polarized) charge currents. In this thesis, we will focus only on nonmagnetic materials where the CSI is driven by the spin-orbit coupling, and specifically on the SHE and ISHE, which are described in the following. For completeness, we also briefly explain the inverse spin galvanic effect and its inverse in this section.

The SHE and ISHE produce, respectively, a spin current from a transverse charge current, and a charge current from a transverse spin current, both phenomena being related to each other via the Onsager reciprocal relations. Two main types of SHE can be distinguished, namely, the intrinsic SHE [243] and the extrinsic SHE [61, 62, 112, 303]. In the intrinsic SHE, the spin-orbit coupling inherent to the lattice generates an anomalous spin-dependent velocity (with equal magnitude but opposite direction) transverse to the charge current and proportional to the so-called Berry curvature (see section 2.1.5). In this way, the resulting total velocity of a k-state at band n becomes [83, 291]:

$$\boldsymbol{v}_n(k) = \frac{1}{\hbar}\boldsymbol{\nabla} E_n(k) - \frac{e}{\hbar}\boldsymbol{E} \times \boldsymbol{\Omega}_n(k). \tag{2.27}$$

Here, E_n is the energy of the electron at band n, e is the electron charge, $\boldsymbol{E}$ is the electric field and $\boldsymbol{\Omega}_n(\boldsymbol{k})$ is the Berry curvature of band n. The second term in equation (2.27) thus generates a velocity that is perpendicular to the applied electric field. Conversely, in the extrinsic SHE, it is the SOC induced by localized impurities that produce spin-dependent scattering leading to a transverse spin current. Both effects are illustrated in Figure 2.3(a). The symmetries of the lattice or the local impurities (and hence the SOC Hamiltonian) dictate the relative direction of the spin polarization (s_α) with respect to the charge and spin currents. Typically, charge current, spin current and spin polarization are perpendicular to each other (i.e. $I_c \perp I_s \perp s_\alpha$). However, this is not rooted in a fundamental constrain, and less restrictive combinations of the aforementioned quantities can be allowed provided some lattice symmetries are broken, as in the case of low-symmetry TMDs discussed in section 2.2.2. Such effects will be the basis of the results in Chapter 5.

In the SHE, one can define the charge-to-spin conversion efficiency for spins generated along the α direction as

$$\theta_{ij}^{\alpha} = \frac{J_{s,i}^{\alpha}}{J_{c,j}}, \tag{2.28}$$

where $J_{s,i}^{\alpha}$ is the spin current density flowing in the i direction, $J_{c,j}$ is the charge current density along j, and θ_{ij}^{α} is the so-called spin Hall angle (SHA). Because of the reciprocity between the SHE and ISHE, the SHA takes the inverse form in the ISHE and defines the efficiency of spin-to-charge conversion. For disordered systems in the diffusive regime, the spin Hall angle can also be defined as the ratio of the spin Hall conductivity (SHC), σ_{ij}^{α}, and the longitudinal charge conductivity, σ_{jj}:

$$\theta_{ij}^{\alpha} = \frac{\sigma_{ij}^{\alpha}}{\sigma_{jj}}. \tag{2.29}$$

This formula is useful for numerical calculations as both conductivities can be easily

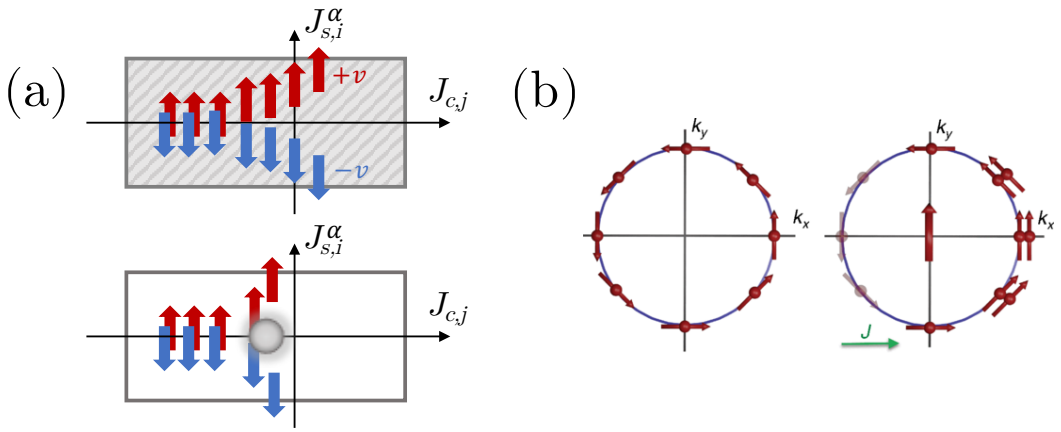

Figure 2.3: (a) Schematics of the spin Hall effect produced by intrinsic (top) and extrinsic (down) mechanisms. In the intrinsic SHE, spin-up and spin-down electrons in a charge current density flowing along j, $J_{c,j}$, acquire opposite transverse velocities from a uniform SOC in the material (denoted as a shaded gray background), resulting in a transverse spin current density along i, $J_{s,i}$. In the extrinsic SHE, up and down electrons scatter in opposite transverse directions due to an impurity with SOC. (b) Spin polarization or texture of a Rashba system, without (left) and with (right) an applied in-plane electric field. The electric field shifts the Fermi surface, resulting in a net spin density. Reprinted figure with permission from Ref. [244]. Copyright (2015) by the American Physical Society, https://doi.org/10.1103/RevModPhys.87.1213.

computed with the Kubo-Bastin formula (see next section and section 3.2.2).

While the SHE generates pure spin currents, the ISGE produces a spin density or accumulation s^{α} from the application of a charge current. Likewise, its reciprocal effect, the spin galvanic effect, converts a spin density into a charge current. The origin of the ISGE resides again in the SOC, specifically in how the Fermi surface and the spin texture of the bands are displaced upon the application of an electric field (i.e. a drift charge current). For the ISGE to occur, the spin texture of the bands needs to arise from a broken inversion symmetry, as in the case of Rashba SOC [244]. Figure 2.3(b) shows the ISGE in one of the chiral Rashba bands. When the electric field is absent, the total spin polarization at the Fermi surface is zero. However, an in-plane electric field along the x direction displaces the Fermi surface and as a result there are more filled states with positive wavevector than negative wavevector. Because of the spin-momentum locking of the Rashba SOC, a spin density in the y direction develops, s^{y}, which can further spread as a spin current. In the literature, the inverse spin galvanic effect is also called current-induced spin polarization or Rashba-Edelstein effect [64].

2.1.5 Topology in spintronics

In condensed matter physics, topology is used to classify distinctive phases of matter. The quantum Hall effect [148] revealed that the insulating phase of a two-dimensional electron gas subjected to a strong magnetic field is topologically different than a typical band insulator. Insulating materials can be classified according to a topological invariant [107], which is associated to an integer number that depends on the different topological phases. These classifications allows us to distinguish materials possessing nontrivial topology (as in the quantum Hall state) from trivial ones. One of the main consequences of topology is that small perturbations and smooth variations of the Hamiltonian, induced for instance by disorder, leave unaffected the topological invariant, which is related to a measurable quantity (such as the Hall resistance). To modify the topological order, a transition from the two inequivalent insulators must occur. In other words, the band gap must close and reopen again, with the consequence that at the transition point the system becomes metallic. This has the direct implication that at the interface of two topologically different materials, nontrivial metallic state emerges [100, 107, 108]. Importantly, its propagation is chiral (i.e. it flows along only one direction) and it is resilient to disorder because the nontrivial insulator is very robust against perturbations. This relation between the topology of a bulk crystal and the manifestation of gapless edge states is known as bulk-boundary correspondence [107].

The first topological invariant used to describe the quantum Hall effect was the Chern number, $\mathcal{C}$. Its value is related to the number of gapless states propagating along the edge as well as to the magnitue and quantization of the Hall conductivity [267],

$$\sigma_{xy} = \mathcal{C}\frac{e^2}{h}, \tag{2.30}$$

with $\mathcal{C} = \frac{1}{2\pi}\int_{\mathrm{BZ}} \boldsymbol{\Omega}(k) \cdot \mathrm{d}^2\boldsymbol{k}$. The quantity $\boldsymbol{\Omega}$ is the Berry curvature and has many implications for the electronic properties of electrons [291]. The Berry curvature can be calculated as the sum of the partial Berry curvature of each occupied band with the Kubo formula as follows [69, 215, 291, 299]. For a 2D Brillouin zone in the xy plane, $\mathrm{d}^2\boldsymbol{k} = \mathrm{d}^2k\,\hat{\boldsymbol{z}}$ such that only $\Omega_z\hat{\boldsymbol{z}}$ needs to be considered, and one has [291]

$$\Omega_z(k) = \Omega_{xy}(k) = \sum_n f_n \Omega_{n,xy}(k), \tag{2.31}$$

with

$$\Omega_{n,xy}(k) = -2\hbar^2 \sum_{n\neq m} \mathrm{Im}\left\{\frac{\langle nk|v_x|mk\rangle\langle mk|v_y|nk\rangle}{(E_n(k)-E_m(k))^2}\right\}. \tag{2.32}$$

Here, n and m are band indices, $|nk\rangle$ is a Bloch eigenstate with energy E_n, f_n is the

distribution function of electrons and $v_i = \frac{1}{\hbar}\frac{\partial E_n(k)}{\partial k_i}$ is the velocity operator, with $i = x, y$. Equation (2.32) measures a topological property of the electronic spectrum, which derives from an invariant of a correlation function between velocity operators [151].

In 2005, Kane and Mele proposed a different topological classification for time-reversal-invariant systems [139], the $\mathbb{Z}_2$ invariant (equivalent to the later on defined spin Chern number, $\mathcal{C}_s$ [234]), in which spin-orbit coupling, instead of a real magnetic field, leads to a nontrivial topological phase. This state of matter is called a topological insulator and in two dimensions exhibits the quantum spin Hall effect (QSHE) [26, 138, 192, 234, 235]. Because of the nontrivial bulk topology, the quantum spin Hall (QSH) regime must also display in-gap states localized at the sample boundary. In this scenario, however, each spin state propagates along opposite directions (see Figure 2.4), forming therefore a pair of *helical* edge states carrying a pure spin current, in contrast with the chiral nature seen in the quantum Hall regime. This picture can also be understood as the motion of a Kramers pair, with opposite chirality owing to time-reversal symmetry [98, 138].

The topology of the QSHE implies that these spin-polarized helical channels are robust against disorder and imperfections in the material, and therefore propagate ballistically. Consequently, these modes hold great potential in spintronics, as they can in principle be used to carry spin currents over long distances. Because of the intrinsic one-dimensional (1D) nature of the edge states, only forward and backward scattering of electrons is possible. However, backscattering is only allowed if the spin is flipped during the scattering

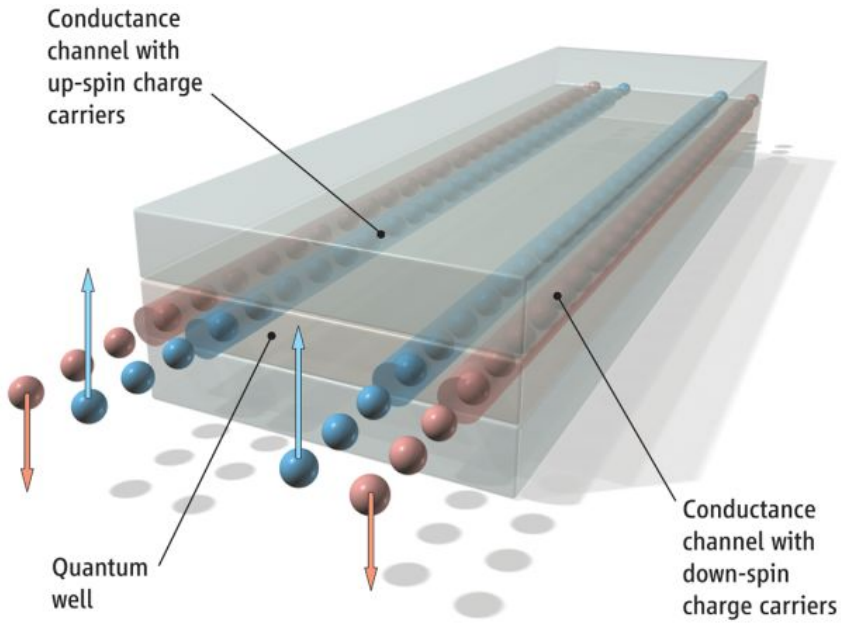

Figure 2.4: Illustration of the helical transport carried by the spin-polarized edge states of the quantum spin Hall effect in a HgTe quantum well. From [152]. Reprinted with permission from AAAS.

event, as the state that propagates in the opposite direction has opposite spin. In other words, time-reversal-symmetry must be broken to destroy the ballistic transport in the QSHE. Because of that, it is said that these gapless modes are *topologically protected* against disorder that preserves time-reversal-symmetry, while magnetic fields and magnetic impurities are detrimental to such long-range ballistic propagation. An exception would be the case of very strong nonmagnetic interactions that couple edge states from opposite edges through the bulk. In a ribbon geometry, if spin-up electrons move from left to right along one edge, they are counterpropagating in the opposite edge. Therefore, if the material is not wide enough, connecting these states could be induced by nonmagnetic disorder, yielding backscattering in absence of time-reversal symmetry breaking.

While the QSHE exhibits a vanishing Hall conductivity, the spin Hall conductivity is finite inside the gap. However, the SHC is quantized to an integer value defined by the spin Chern number only when the spin is conserved [139, 234][6]. The elements of the SHC tensor can be calculated in a similar way to the Hall conductivity using the α-spin Berry curvature as [69]

$$\sigma_{xy}^{\alpha} = \frac{e^2}{h}\frac{1}{2\pi}\int_{\mathrm{BZ}}\sum_{n} f_n \Omega_{n,xy}^{\alpha}(k)\,\mathrm{d}^2k, \tag{2.33}$$

with

$$\Omega_{n,xy}^{\alpha}(\boldsymbol{k}) = -2\hbar^2\sum_{n\neq m}\mathrm{Im}\left\{\frac{\langle nk|\frac{1}{2}\{s_\alpha, v_x\}|mk\rangle\langle mk|v_y|nk\rangle}{(E_n(k)-E_m(k))^2}\right\}. \tag{2.34}$$

Here we have chosen to define the spin Berry curvature with the Pauli matrix, resulting in the spin Hall conductivity with units of e^2/h. Thus, the value of the SHC defined in equation (2.33) indicates the number of helical channels propagating along the sample edges. We note, however, that other units are found in the literature [191, 234].

Figure 2.5 gives an example of the band structure of a Kane-Mele quantum spin Hall insulator together with the SHC and conductance expected in the bulk and ribbon geometry, respectively. The bulk bands (i.e. with periodic boundary conditions and thus no edge termination) seen in Figure 2.5(a) are gapped. The corresponding SHC, shown in Figure 2.5(b), displays a finite and quantized value of $2e^2/h$ precisely in the gap region, proving the existence of the QSHE with conserved spins. An important remark is that the SHC decays outside the gap but is still finite. This feature will play an important role in describing the results in Chapter 5. If this system is indeed a 2D topological insulator, its band structure should display in-gap states when the system is cut into a quasi-1D ribbon. This is in fact the case in Figure 2.5(c): two pairs of degenerate bands with opposite velocity (one for each spin) appear in the band gap region. Although such states are helical and carry a pure spin current, if a bias voltage is applied in a

[6] Although the nontrivial topological phase can remain even without spin conservation [139, 234].

two-terminal setup, the conductance will show a value of $2e^2/h$ due to two right- (or left-) propagating modes (one spin at each edge). Figure 2.5(d) illustrates exactly this situation. In the gap, the total conductance is quantized to $2e^2/h$, while the conductance of the spin-up and spin-down channels is equal to e^2/h.

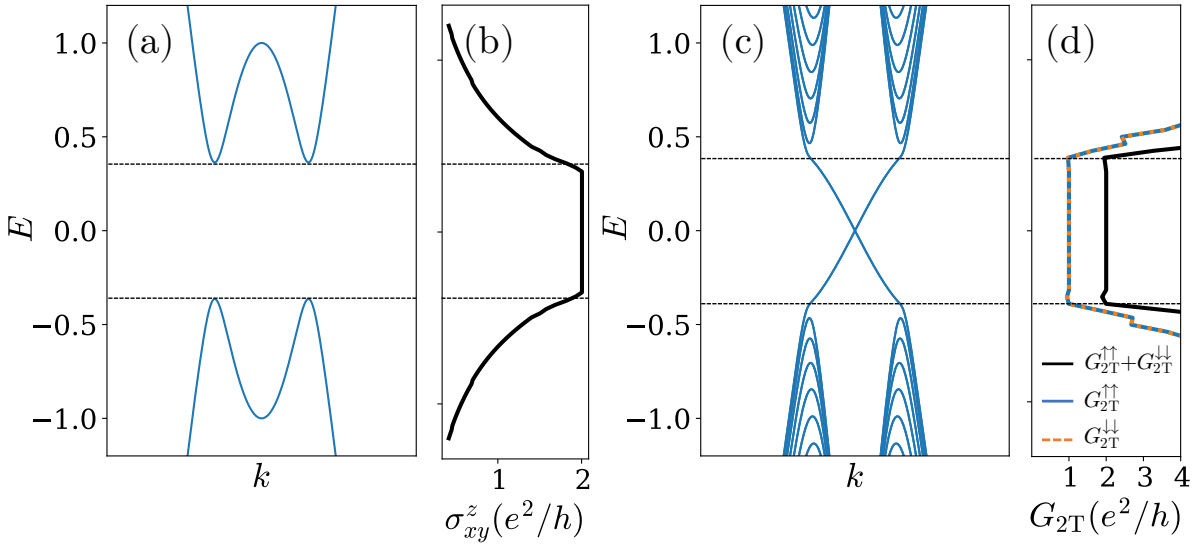

Figure 2.5: (a) Bulk band structure of the Kane-Mele QSH insulator. (b) Spin Hall conductivity of the system in (a), showing a quantized value in the gap. (c) Band structure of the Kane-Mele QSH insulator of a quasi-1D system. Helical in-gap states appear as a consequence of having a finite system. (d) Two-terminal conductance, G_{2T}, of the system in (c), showing a total two-terminal conductance of $2e^2/h$ (and of e^2/h for each spin component) for all energies in the gap. The horizontal dashed lines denote, in all plots, the extension of the band gap.

Since the spin Hall conductivity is not directly experimentally accessible (in contrast to the charge conductivity or the spin Hall angle obtained by measuring currents and voltages in a device), experiments usually rely on the observation of a plateau of conductance of $2e^2/h$ to determine the existence of the QSHE. However, the QSHE has another unique fingerprint in multi-terminal devices that can be used to unambiguously detect it [222]. The theory behind such effect is given by the Landauer-Büttiker formalism and is explained in Appendix F.

Finally, we note that the field of topological insulators and topological matter is extremely vast, including for example topological insulators in three dimensions [80, 305] or with higher-order topology [231].

2.2 State-of-the-art in two-dimensional spintronics

In this section, we focus on the recent developments of the fields relevant for this thesis. Namely, the progress on graphene spin transport and the transition towards ballistic spin communication, and the spin transport characteristics and charge-to-spin interconversion in low-symmetry TMDs.

2.2.1 Graphene

The potential of graphene as a conducting spin channel stems from its small spin-orbit coupling ($\sim \mu$eV) and hyperfine interaction [92,101,116,153,186,286], which should result in long spin relaxation times and lengths. Indeed, the first theoretical studies predicted τ_s exceeding the μs range [66, 118, 313], which is orders of magnitude larger than in typical metals and semiconductors [122]. These estimates were based on traditional mechanisms of spin relaxation in metals and semiconductors, namely the Elliott-Yafet and D'yakonov-Perel' mechanisms. The typical scattering events considered in these calculations are collisions with charged impurities [66, 313], ripples [79, 116, 118, 277], phonons [66, 79, 202, 277, 313] and other electrons [313]. However, from the experimental side, early measurements of graphene nonlocal spin valves revealed a large discrepancy with the theoretical expectations, with $\tau_s < 1$ ns [11, 96, 134, 194, 268, 269, 316], remaining orders of magnitude shorter than earlier predictions. This intriguing difference between theory and experiment initially suggested that the traditional application of Elliott-Yafet and D'yakonov-Perel' mechanisms may not be fully appropriate for graphene. As a result, several mechanisms, either from extrinsic sources or intrinsically from graphene, have been proposed to explain this discrepancy.

The first graphene NSVs consisted on exfoliated graphene with FM contacts directly on top [102] or with tunnel barriers [268]. It was rapidly seen that the quality and homogeneity of the tunnel barrier was extremely important in order to prevent spins sinking and decrease spin relaxation [103]. Consequently, a lot of efforts were made in that direction and it was found that the contact resistance between graphene and the FM contacts was equally relevant [211, 280, 281]. This was accompanied by theoretical models that included contact-induced spin relaxation by the FM electrodes in the spin diffusion equation [6, 120, 121, 174, 201, 253, 254]. Another source of extrinsic spin relaxation, scattering by magnetic impurities (likely originating during the device fabrication), was experimentally [172] and theoretically [149, 252] studied. In parallel, the use of hexagonal boron nitride (hBN) as a substrate or protective layer, in addition to other improvements of device fabrication, revealed an increase of spin lifetimes up to 12 ns due to the protection of graphene from contaminants and better interface quality [58–60, 95, 137, 241]. Figure

2.6 illustrates the evolution of all these improvements in material growth and fabrication techniques that have established graphene as an excellent spin transport material.

Although these results already made clean graphene a suitable platform for achieving longer coherent spin propagation than in typical metals or semiconductors, τ_s remained several orders of magnitude below the initial theoretical predictions [66, 118, 313], a puzzling result which remains open to discussion and interpretation [219, 220]. Thus, other sources of (intrinsic) spin relaxation, that are unique to graphene, were proposed. The role of the hyperfine interaction between the nucleus and electrons was proven negligible because of the low abundance of ^{13}C and the weak hyperfine coupling in graphene [286]. Ripples and corrugation, where local curvature increases the effective spin-orbit coupling, or gauge fields, were also investigated [118, 202, 277]. However, calculations of this phenomenon in experimentally-relevant situations revealed spin lifetimes in the range of hundreds of ns up to μs, indicating that this mechanism is not likely to be a limiting factor in experiments to date. Finally, another mechanism, known as spin-pseudospin coupling, predicted the increase of spin dephasing near the graphene Dirac point due to the entanglement of these degrees of freedom [271], resulting in spin lifetimes on the order of the nanosecond range [276].

All these works suggest that the extrinsic effects on spin transport can be eventually avoided by increased sample quality and device fabrication, while intrinsic mechanisms such spin-pseudospin coupling could represent the upper limit of spin lifetime in the ultraclean limit. Nevertheless, enhanced spin transport is not the only improvement from such better device quality. The increased mean free path up to tens of micrometers at lower temperatures [16, 17, 283] has also resulted in ballistic charge transport in the μm range. Therefore, it is expected that spin propagation becomes ballistic too provided such long mean free paths are reached in nonlocal spin valves.

Ballistic spin transport research has been limited to theoretical works and only few experiments on two-dimensional electron gases (2DEGs) have been carried out due to the short mean free paths (in comparison with graphene) of just a few μm at most [31, 169, 205]. Many of the theoretical contributions have focused on either one of these two following aspects: ballistic spin injection from a ferromagnet into a nonmagnetic conductor [40, 155] and the modulation of spins by the Rashba SOC in a ballistic two-terminal channel [128, 165, 187] to realize the Datta-Das spin transistor [55]. An important result from these works that may be relevant for NSVs is the prediction of increased spin accumulation when spins are injected in a material with spin diffusion length shorter than the mean free path [40]. In fact, this work explained the results from a few experiments in 2DEGs where signs of ballistic spin transport were detected [31, 169, 205]. However, in these studies the width of the FM leads was equal or larger than the channel length,

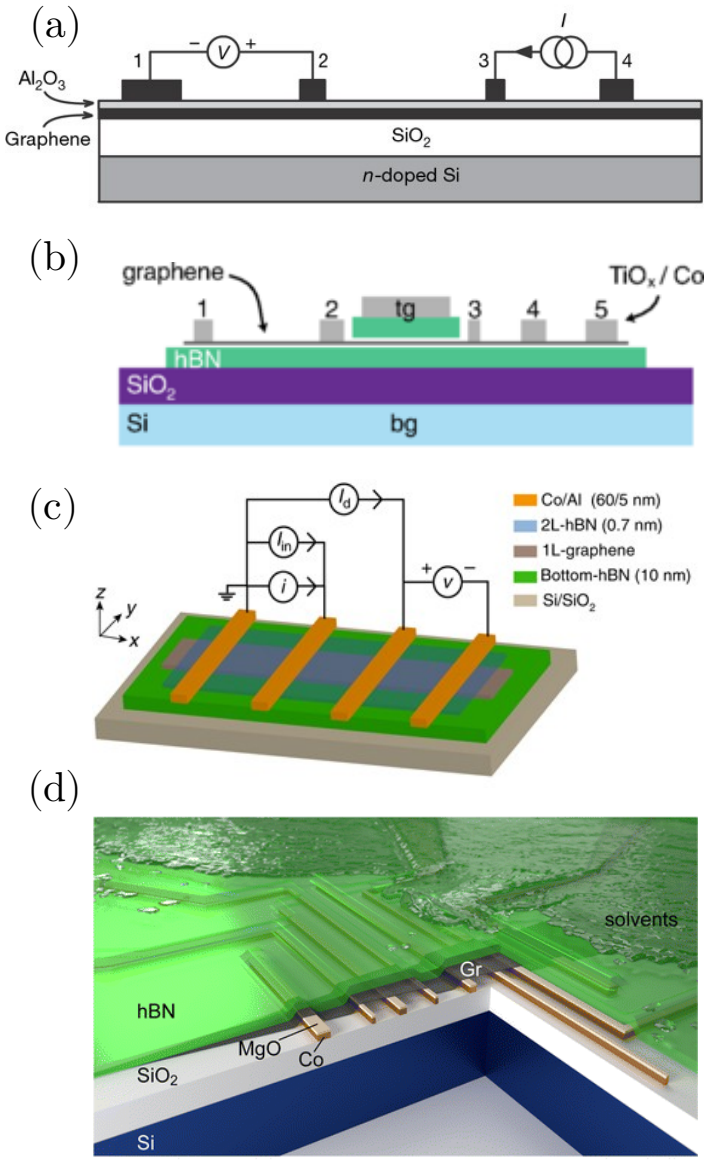

Figure 2.6: (a) First NSV made of graphene. Tunnel barriers made of Al_2O_3 were used. (b) NSV with hBN-encapsulated graphene, where the top hBN covers the transport channel only. (c) NSV with hBN-encapsulated graphene, where the top hBN covers the transport channel and is also the tunnel barrier between graphene and the FM electrodes. (d) Inverted NSV where graphene is deposited on top of the electrodes and then hBN is used to cover the whole device, protecting graphene from residues and solvents needed during the fabrication procedure. Figures reprinted with permission from: (a) Spinger Nature Customer Service Centre GmbH: Nature Publishing Group, *Nature*, Ref. [268], copyright (2007). (b) Ref. [95]. Copyrighted (2014) by the American Physical Society, https://doi.org/10.1103/PhysRevLett.113.086602. (c) Ref. [97], with license https://creativecommons.org/licenses/by/4.0/. (d) Reprinted with permission from [58]. Copyright (2016) American Chemical Society.

so all ballistic effects were attributed to spin injection (rather than spin transport or precession) in the region underneath the FM contacts.

Nonetheless, a few works did study spin transport in nonlocal geometries or mechanisms of spin relaxation unique from the ballistic regime. Tang *et. al.* [262] performed semiclassical Monte Carlo simulations of nonlocal spin valves in a ballistic channel. Scattering was present during spin injection and detection, leading to spin dephasing with magnetic field due to different paths taken by the electrons to travel along the channel. However, the dependence of the signal with varying disorder strength as well as the limits of diffusive or completely ballistic transport were not investigated. On the other hand, Zainuddin *et. al.* [301] performed Landauer-Büttiker simulations of a NSV in the ballistic regime, but they primarily focused on the modulation of the signal with the Rashba SOC and the effect of the Hanle precession and spin relaxation was barely studied.

A common generality in all these articles is the assumption of a finite spin relaxation length in the ballistic regime without specifying the spin relaxation mechanism, which is not obvious since the typical D'Yakonov-Perel' or Elliot-Yaffet mechanisms should not apply. This issue was finally investigated in Ref. [51], where the authors showed that spins can relax during ballistic transport if spins precess at different frequencies during propagation. This phenomenon could occur in a system where SOC leads to an energy-dependent spin splitting (and thus into an energy-dependent precession frequency) and electrons occupy a distribution of energies due to e.g. thermal broadening. This work, however, was based on bulk transport calculations and thus it is not clear how this mechanism can impact a nonlocal transport experiment.

Finally, another common feature of all studies based on quantum transport calculations is the fact that none of them focused on the diffusive regime. The reason is likely to be the large computational time required to average over many disorder configurations in order to capture the randomness present in diffusive transport. This has an important consequence, which is that a global picture of the crossover from diffusive to quasiballistic and to ballistic transport regimes has not yet been deeply investigated. Furthermore, characterizing the quasiballistic regime is specially important for providing experimental guidance, as it is the most likely scenario to be found in a real device, as opposed to the fully ballistic transport.

2.2.2 Transition metal dichalcogenides

Transition metal dichalcogenides are layered materials with formula MX_2, with M being a transition metal atom and X a chalcogen atom. Their weak van der Waals interlayer interaction allows one to exfoliate them in two-dimensional crystals, down to a monolayer crystal [199]. Different crystal structures are stable depending on the elements composing

the material. Two common structures are the hexagonal (2H in bulk and 1H in two-dimensions) and the tetragonal (1T) phases [43, 180], which are illustrated in Figure 2.7(a). The 1T phase (central panel in Figure 2.7(a)) can be distorted into a monoclinic structure, the 1T′ phase (space group $P2_1/m$), which contains a mirror plane, a two-fold screw rotation axis, and an inversion center in both the bulk and the monolayer. This 1T′ can be further distorted into a very similar structure, the so-called $1T_d$ phase (space group $Pmn2_1$), but with different symmetry operations. In the bulk, it possesses a mirror plane, a two-fold screw rotation axis and a glide mirror with both operations involving a translation in the out-of-plane direction. However, in two-dimensions, the lack of tranlational symmetry in the perpendicular direction results in the absence of both the screw-rotation axis and the glide plane, leaving the $1T_d$ phase with only a single mirror plane [251, 295]. This reduction of symmetry with dimensionality is depicted in Figures 2.7(b) and 2.7(c).

TMDs have received a lot of attention for their potential in spintronics and topological transport due to their strong SOC inherent from the heavy atoms. In the hexagonal phase, SOC produces a spin splitting of the valence band on the order of hundreds of meV and locks the spin polarization of these bands with the valley degree of freedom [292], allowing one to selectively excite up or down spins by the chirality of circularly polarized light [35, 176, 302]. On the other hand, the 1T′ and $1T_d$ phases accommodate the interesting class of Weyl semimetal candidates MX_2 (M = Mo, W; X = S, Se, Te) [130, 168, 249, 255, 294], which have been advanced as platforms for realizing exotic phenomena such as topological superconductivity [71, 213, 229], non-linear Hall effect [140, 173, 242, 295, 306], anisotropic spin Hall transport [311] or out-of-plane spin-orbit torque [175]. When thinned towards the monolayer limit, they transition from the Weyl semimetal phase characteristic of the bulk to the quantum spin Hall regime [41, 72, 129, 214, 237, 264, 289] with strain-tunable topological gap [309].

Recently, large charge-to-spin interconversion generated by the spin Hall effect has been reported in multilayers of $MoTe_2$ and WTe_2 [227, 251, 307, 308] with indication of long spin diffusion lengths on the order of micrometers [251]. The efficiency of the SHE is determined by the spin Hall angle θ_{xy}^{α} which indicates the percentage of spin current produced by a driving charge current; θ_{xy}^{α} depends on the magnitude of SOC and is typically no more than a few percent at room temperature in heavy metals [244]. Usually, the stronger the SOC, the shorter the spin diffusion length is, so achieving long λ_s concurrently with large SHA is a long-standing challenge for spintronics. To date, the best trade-off obtained with heavy metals amounts to $\lambda_s\theta_{xy}^{\alpha} \sim 0.1$–$0.2$ nm [113, 123, 160, 228, 244]. Interestingly, hints of unconventional SHE have been detected in 1T′ [227] and $1T_d$ phases of $MoTe_2$ multilayers [251] as well as $1T_d$-WTe_2 multilayer [307]. This is not surprising

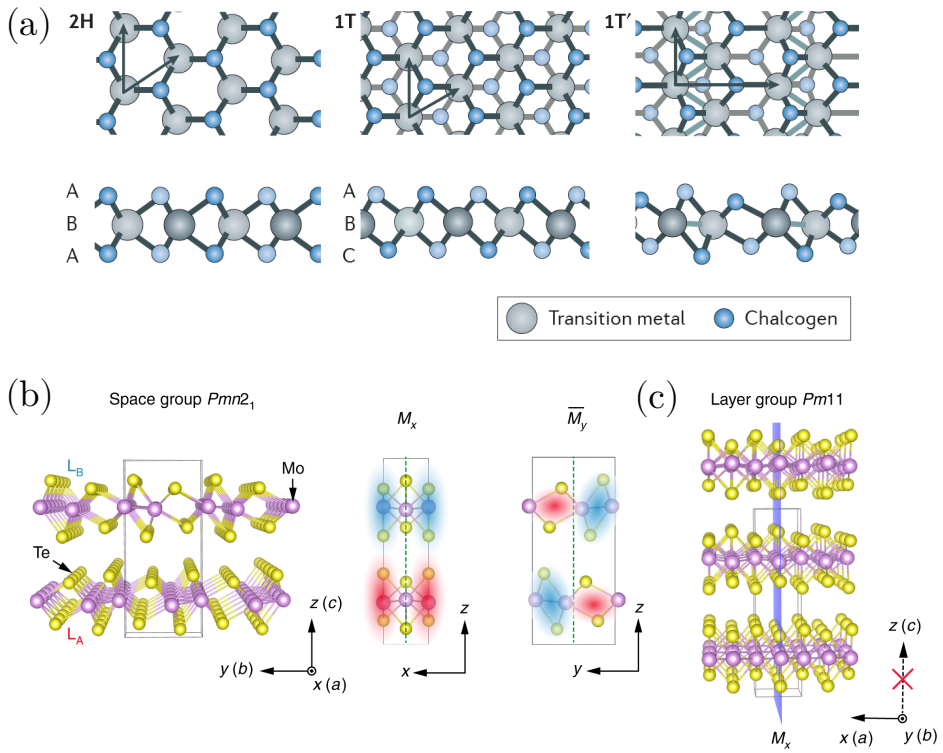

Figure 2.7: (a) Crystal structure of different TMD pahses. Top and bottom rows correspond to a top and side view, respectively. From left to rigth: hexagonal structure (2H), rhombohedral (1T) and monoclinic (1T′). (b) Crystal structure of bulk 1Td-$MoTe_2$, possessing a mirror symmetry in the yz plane (M_x) and a glide mirror symmetry ($\overline{M}_y$) along the perpenidcular z direction. (c) In two-dimensions, 1Td-$MoTe_2$ only has M_x due to the lack of translational symmetry along the z direction. Figures reprinted with permission from: (a) Spinger Nature Customer Service Centre GmbH: Nature Publishing Group, *Nature Reviews Materials*, Ref. [180], copyright (2017). (b) Spinger Nature Customer Service Centre GmbH: Nature Publishing Group, *Nature Materials*, Ref. [251], copyright (2020).

since, in contrast to bulk crystals of $1T_d$, the absence of the glide mirror symmetry in few-layer slabs is expected to generate additional nonzero components of the spin Hall conductivity tensor, resulting in spin current with polarization collinear with the charge current [251]. Indeed, Figures 2.8(a) and 2.8(b) show, respectively, the components σ^z_{xy} and σ^z_{xz} of the SHC tensor of bulk $1T_d$-$MoTe_2$. While a the former is nonzero, the latter is absent, as the symmetries present in the bulk crystal do not allow the spin polarization to be parallel to the charge current. However, the situation changes when the SHC is calculated for a 5-layer slab (Figures 2.8(c) and 2.8(d)), in which both components become finite. In Appendix C, we give a more detailed explanation of why elements of the SHC tensor become finite upon breaking certain symmetries. Moreover, we also provide all the elements of the SHC for both bulk and layer $1T'$ and $1T_d$ phases. Interestingly, while the unconventional components of the SHC only appear in 2D for the $1T_d$ phase, the different symmetries of the $1T'$ phase allow them to appear in the bulk.

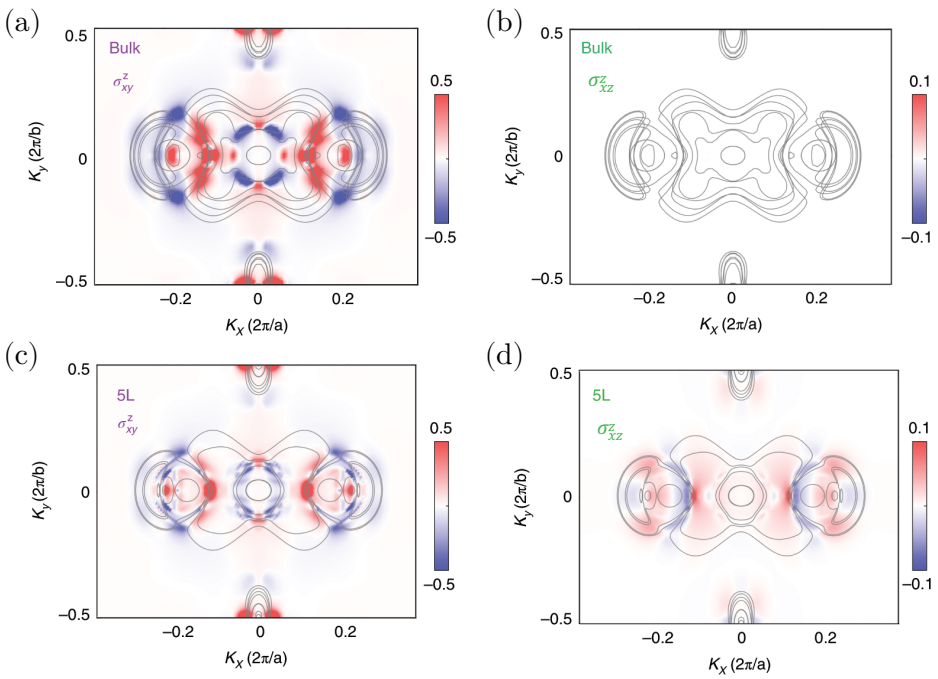

Figure 2.8: Spin Hall conductivity of bulk (a, b) and 5-layer (c, d) $1T_d$-$MoTe_2$ for the conventional (a, c) and unconventional (b, d) component. The unconventional element of the SHC tensor is only allowed in the 2D limit. Reproduced by permission from Spinger Nature Customer Service Centre GmbH: Nature Publishing Group, *Nature Materials*, Ref. [251], copyright (2020).

Spin Hall materials that do not have the restriction of mutually perpendicular charge current, spin current and spin polarization are very attractive as they bring more flexibility in the design of spintronic devices as well as for spin torque applications [175]. These materials would be even more promising if they possessed large spin relaxation lengths,

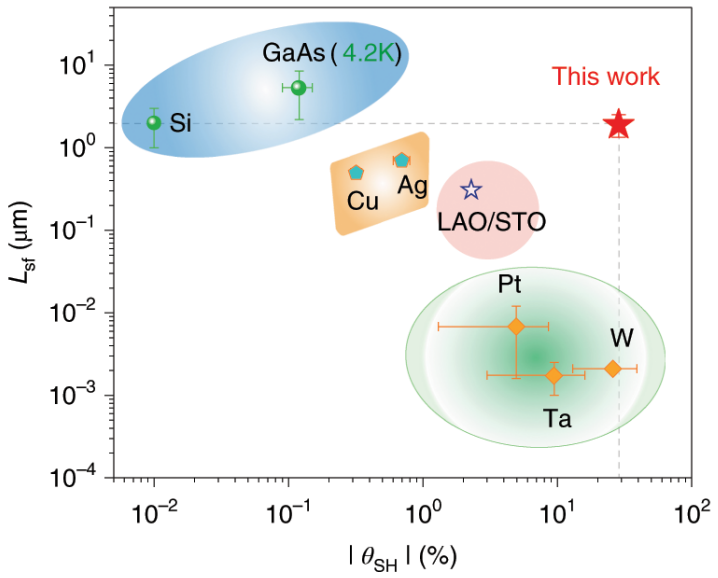

Figure 2.9: Ashby plot of spin diffusion length and spin Hall angle of common spin Hall materials. $MoTe_2$ in Ref. [251] was found to posses large λ_s and θ^{α}_{xy}. Reprinted by permission from Spinger Nature Customer Service Centre GmbH: Nature Publishing Group, *Nature Materials*, Ref. [251], copyright (2020).

usually incompatible with strong SOC. Nevertheless, Song *et. al.* have estimated spin diffusion lengths in few-layer $1T_d$-$MoTe_2$ on the order of micrometers together with large SHAs [251]. When compared to other spin Hall materials (Figure 2.9), low-symmetry TMDs appear to be superior spintronic materials with large charge-to-spin interconversion efficiencies, $\lambda_s\theta^{\alpha}_{xy}$.

In addition to the spin Hall effect, monolayers of such low-symmetry TMDs were predicted to be 2D topological insulators exhibiting the quantum spin Hall effect [214]. Such predictions have been recently confirmed experimentally by several groups [41,72,129,237, 264, 289], with most of the experiments being carried out in WTe_2. In contrast to other quantum spin Hall materials where the QSHE was observed only at milikelvin temperatures [152, 222], the effect in WTe_2 persists up to 100 K [289], establishing these TMDs as great candidates for utilizing the QSHE in applications. Figures 2.10(a) and 2.10(b) show the band structure and edge states of 1T′ TMDs and the measured quantization of the two-terminal conductance distinctive of the QSHE.

The prototypical models of the QSHE are based on z-polarized spins [24, 138]. However, if we combine the results of the unconventional spin Hall effect with the presence of topological helical edge states, we may ask ourselves the following question: what is the effect of the symmetry reduction of monolayer TMDs on the QSHE? To date, little is known about the imprint of the inherently low symmetry in the quantum spin

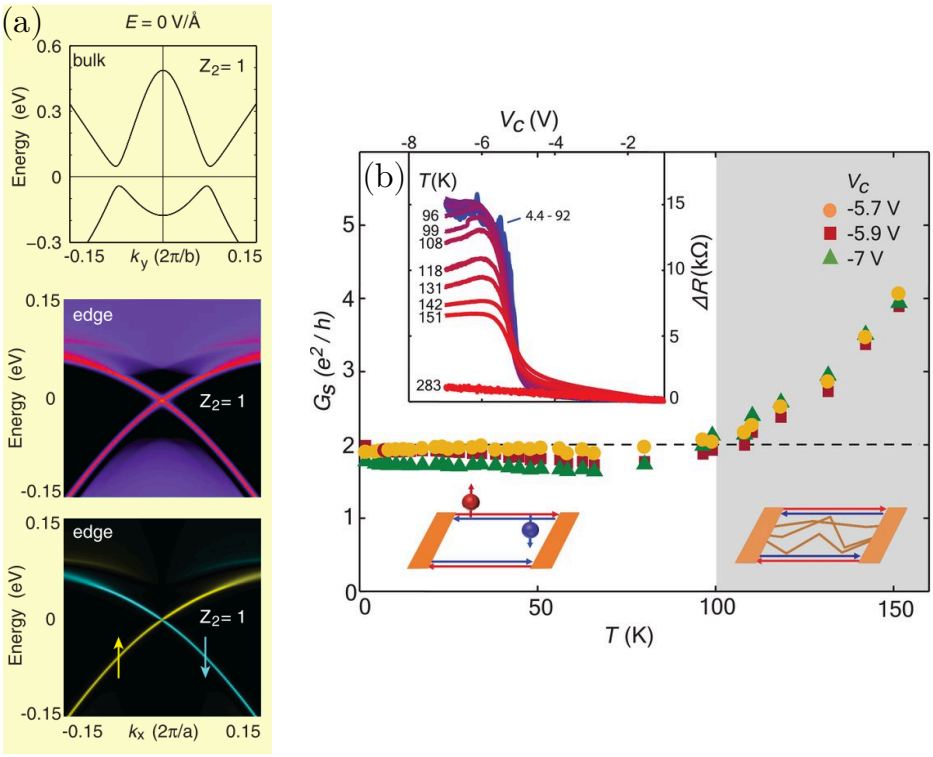

Figure 2.10: (a) Top, middle and bottom panel correspond to the band structure, edge density of states and spin texture of the edge modes, respectively, for 1T′-MoS_2. (b) Two-terminal conductance of in-gap states of 1T′-WTe_2 as a function of temperature. Different colors represent different gate voltages. Inset: Voltage-dependence of the two-terminal conductance at various temperatures. Figures from: (a) Ref. [214], reprinted with permission from AAAS. (b) Ref. [289], reprinted with permission from AAAS.

Hall regime. Correlations and substrate effects were found to induce localization of edge modes [203], and resilient in-plane spin-states [52], but the impact of low symmetries and the possibility of multiple spin Hall components in the QSHE remains to be determined.

CHAPTER 3

QUANTUM TRANSPORT METHODOLOGIES FOR SPIN TRANSPORT

Numerical simulations are an important tool to study physical and chemical properties of materials and, with the continuous improvement of modern computers, realistic calculations can be carried out even on a laptop. Although computer simulations imply approximating a real material to a set of physical equations, they offer unique advantages. One can calculate properties without performing an experiment and thus it is possible to make predictions about uncharacterized materials, undiscovered physical effects or obtain microscopic insights into physical phenomena that experiments cannot unveil.

In this thesis, I aim at describing spin transport in electronic devices made of two-dimensional materials. In other words, I am not only interested in the intrinsic properties of a material, but also in the effects arising from the application of voltages and currents with metallic leads. In this manner, I am able to simulate a mesoscopic transport experiment and predict, at least qualitatively, the output of experimental measurements in the laboratory. Among the theoretical frameworks of charge and spin transport [69, 78, 288], the Landauer-Büttiker (LB) formalism is very well suited to carry out these types of simulations.

This chapter addresses all methodological aspects needed to prepare, simulate and interpret spin transport in mesoscopic devices made of 2D materials such as graphene or TMDs. In section 3.1, the different methods available and used to obtain the Hamiltonians and the electronic structure are presented. Such quantum mechanical description of the electrons is needed in the LB formalism and is essential to capture the physics of the spin transport. Section 3.2 reviews the theory of the LB formalism and the Kubo-Bastin formula, presents the Kwant code [94] that performs the LB calculations, and describes

the theoretical modeling of the devices, including how to set up a NSV in Kwant.

3.1 Electronic structure modeling

The knowledge of the Hamiltonian and consequently of the electronic structure (also referred to as band structure or energy dispersion) is paramount to quantum transport as it provides the information of the energy levels of electrons in solids. There are different levels of approximation in computing band structures, ranging from all-electron, first principles methods to single-orbital, $\mathbf{k}\cdot\mathbf{p}$ models. The simulations performed in this thesis are done in large real-space systems, aiming at describing realistic materials. This means that employing high-level methods such as first-principles or *ab-initio* calculations that accounts for many of the orbitals in an atom would be too time-consuming and memory-demanding. Therefore, the typical procedure is to describe the electronic structure with a simple Hamiltonian in a tight-binding (TB) form which reproduces well that of high-level methods for a particular range of energies. Thus, as long as the transport calculations are carried out in this range of energies, the results should be reasonably reliable.

In what follows, we briefly describe the fundamentals of *ab-initio* density functional theory (DFT), which will be used to benchmark the tight-binding models of graphene and TMDs.

3.1.1 Density Functional Theory

First principles or *ab-initio* calculations are a method to compute quantum mechanical properties of materials without needing any sort of parametrization or knowledge of that given compound. Different levels of approximation exist within first principles methods, from mean-field, one-particle theories such as DFT, to *GW* or dynamical mean-field theory that accounts more explicitly for many-body interactions. Nevertheless, DFT is a very extended method for calculating band structures since it is faster and often good enough for describing most materials.

In DFT, a system of interacting electrons is mapped onto a system of non-interacting ones described by the Kohn-Sham equations, in which the energy is a functional of the electron density [48, 127]. These equations are solved in a variational manner until the energy is minimized and the ground-state electron density is found. In the Kohn-Sham equations, the so-called exchange-correlation functional takes into account the many-body interactions, and because its exact form is not known, different levels of approximation exist based on the type of such functional.

The DFT calculations carried out in this thesis for the low-symmetry TMDs are

performed using the VASP package [156–158] with the PBE exchange-correlation functional [208]. More details of the simulations can be found in previous works [38,251,295]. From the DFT calculations, a tight-binding model was interpolated in the Wannier basis via Wannier90 [188] and applied for calculating the spin texture.

3.1.2 Tight-binding models

In the following, we introduce the tight-binding models of graphene and TMDs in their $1T_d$ and $1T'$ phases. We also compare them to the DFT band structures and show the features arising in the electronic structure when the systems are cut into a 1D ribbon.

Graphene

2D graphene tight-binding and DFT fit Graphene is made of a monolayer of carbon atoms arranged in a honeycomb lattice, as pictured in Figure 3.1(a). The honeycomb structure is a triangular or hexagonal lattice with a basis of two atoms, which are commonly labeled as A and B sublattices. The lattice vectors $(\mathbf{a}_1, \mathbf{a}_2)$ read

$$\mathbf{a}_1 = a(\frac{\sqrt{3}}{2}, \frac{1}{2}), \qquad \mathbf{a}_2 = a(\frac{\sqrt{3}}{2}, -\frac{1}{2}), \tag{3.1}$$

where $a = \sqrt{3}a_c$, with $a_c = 1.42$ Å being the carbon-carbon distance. The reciprocal lattice, with its Brillouin zone shown in Figure 3.1(b), is also hexagonal with reciprocal lattice vectors

$$\mathbf{b}_1 = b(\frac{1}{2}, \frac{\sqrt{3}}{2}), \qquad \mathbf{b}_2 = b(\frac{1}{2}, -\frac{\sqrt{3}}{2}) \tag{3.2}$$

that satisfy $\mathbf{a}_i \cdot \mathbf{b}_j = 2\pi\delta_{ij}$, with $b = 4\pi/(\sqrt{3}a)$. Importantly, the high-symmetry points at the vertices of the Brillouin zone are the so-called K and K′ points (red dots in Figure 3.1(a)), with coordinates:

$$\mathrm{K} = \frac{4\pi}{3a}(\frac{\sqrt{3}}{2}, \frac{1}{2}), \qquad \mathrm{K}' = \frac{4\pi}{3a}(\frac{\sqrt{3}}{2}, -\frac{1}{2}). \tag{3.3}$$

The s, p_x and p_y orbitals of carbon hybridize forming σ-type bonds whereas electrons in the p_z orbital are delocalized and form a π bond that contributes to electronic transport. Hence, the graphene tight-binding model is usually comprised of a single p_z orbital in each sublattice and one can write the wave function as a linear combination of periodic Bloch functions,

$$\Psi(\mathbf{k}, \mathbf{r}) = c_A(\mathbf{k})p_z^A(\mathbf{k}, \mathbf{r}) + c_B(\mathbf{k})p_z^B(\mathbf{k}, \mathbf{r}), \tag{3.4}$$

where $|c_A(\mathbf{k})|^2$ ($|c_B(\mathbf{k})|^2$) is the probability of finding the electron in sublattice A (B),

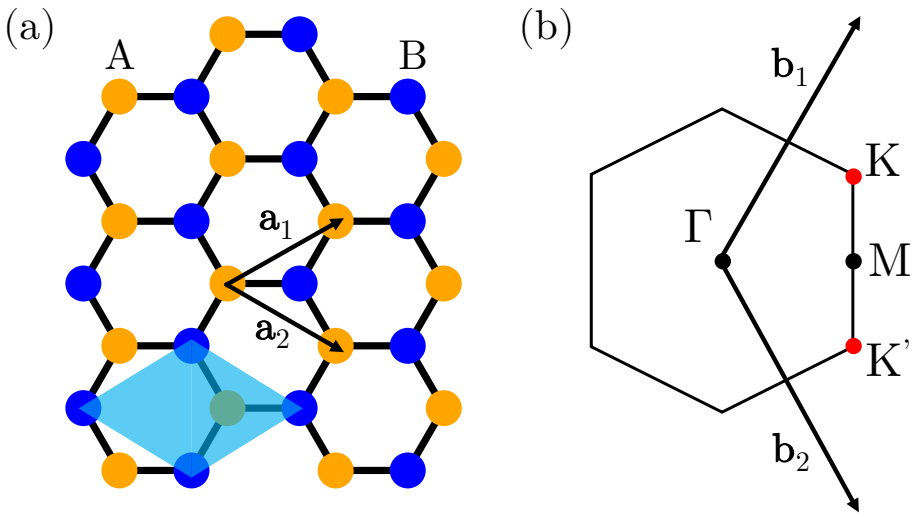

Figure 3.1: (a) Crystal structure of graphene. Orange (blue) atoms correspond to the A (B) sublattice of the honeycomb lattice. The shaded cyan region denotes the rhombohedral unit cell. (b) First Brillouin zone of the honeycomb lattice with the corresponding high-symmetry points.

and $p_z^A(\mathbf{k},\mathbf{r})$ and $p_z^B(\mathbf{k},\mathbf{r})$ are Bloch functions of the p_z orbitals in the A and B sublattice, respectively. Taking these two sublattice states as a basis, the typical real-space tight-binding Hamiltonian of graphene is given by [20, 36, 78]

$$\mathcal{H} = \epsilon_0 \sum_i c_i^\dagger c_i + t \sum_{\langle i,j \rangle} c_j^\dagger c_i. \tag{3.5}$$

The first term is the on-site energy (with magnitude ϵ_0) that dictates the position of the Fermi level and $c_i^\dagger$ (c_i) is the creation (annihilation) operator of an electron at atom or site i. The second term is the nearest-neighbor hopping between different sublattices with t the strength of the transfer integral between neighboring π orbitals, and $\langle i,j \rangle$ denotes nearest-neighbor hopping. Further next-nearest-neighbor hoppings can be included, but are not essential to capture the low-energy dispersion. By taking the Fourier transform of equation (3.5), one arrives at the Hamiltonian

$$\mathcal{H}(\mathbf{k}) = \begin{pmatrix} \epsilon_0 & tf(\mathbf{k}) \\ tf(\mathbf{k})^* & \epsilon_0 \end{pmatrix}, \tag{3.6}$$

with $f(\mathbf{k}) = 1 + e^{-i\mathbf{k}\cdot\mathbf{a}_1} + e^{-i\mathbf{k}\cdot\mathbf{a}_2}$. Then, by solving the Schrödinger equation, the energy spectrum has the form ($\pm$ stands for conduction and valence band dispersion, respec-

tively)

$$E(k_x, k_y) = \pm t|f(\mathbf{k})| = \pm t\sqrt{1 + 4\cos\left(\frac{\sqrt{3}k_x a}{2}\right)\cos\left(\frac{k_y a}{2}\right) + 4\cos^2(\frac{k_y a}{2})}. \tag{3.7}$$

By comparing such energy dispersion to DFT calculations, one finds that $\epsilon_0 = 0$ and $t \in [-2.6, -3.1]$ [78], indicating that the Fermi level lies at the charge neutrality point located at K and K′. As sees from Figure 3.2(a), a nearest-neighbor tight-binding model suffices to reproduce the DFT bands at low energies near the Fermi level. Adding extra hoppings results in a modification of the linear dispersion, known as trigonal warping, as well as in electron-hole asymmetry [78].

If equation (3.6) is expanded near these K and K′ points as $\mathbf{k} \to \mathrm{K}^{(\prime)} \pm \mathbf{q}$, the Hamiltonian resembles that of electrons described by the relativistic massless Dirac equation, $H_K = \hbar v_F \boldsymbol{\sigma} \cdot \mathbf{q}$, where $\boldsymbol{\sigma} = (\sigma_x, \sigma_y, \sigma_z)$ is a vector containing the Pauli matrices acting on the sublattice degree of freedom and $v_F = \sqrt{3}ta/(2\hbar)$ is the Fermi velocity, which is approximately 300 times smaller than the speed of light. This result is of high importance to understand the exceptional electronic properties of graphene such as Klein tunneling [78, 144] or high electron mobility [36, 53]. Moreover, this low-energy Hamiltonian is symmetric around K and K′, forming a cone-shaped linear energy dispersion known as a Dirac cone (see Figure 3.2(b)). Because of the degeneracy of K and K′, these regions are called valleys, defining in this way a valley degree of freedom for electrons (or holes).

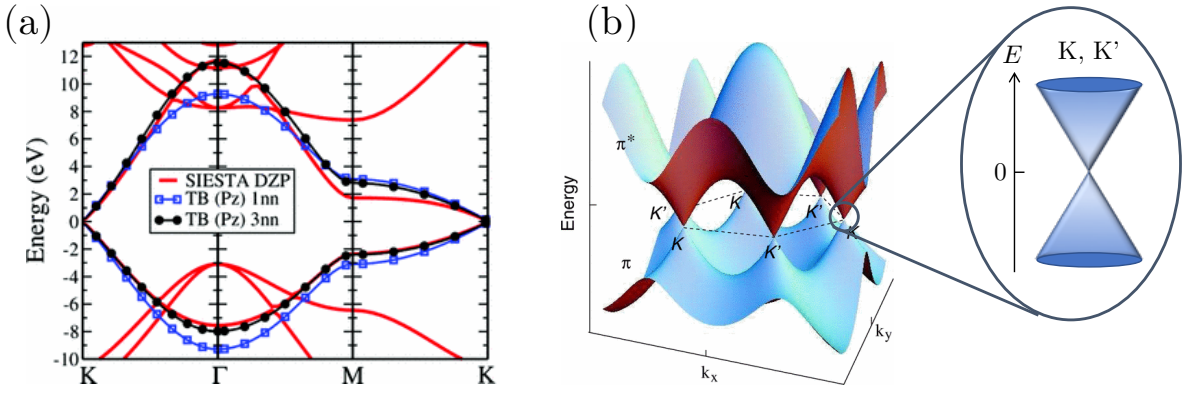

Figure 3.2: (a) DFT (red) and tight-binding (blue and black) band structure of graphene. Graphene tight-binding models inluding only nearest-neighbor hoppings and up to third-nearest-neighbor hoppings are shown in blue and black, respectively. Reprinted figure with permission from Ref. [167]. Copyright (2012) by the American Physical Society, 10.1103/PhysRevB.86.075402. (b) Three-dimensional band structure of graphene, with an schematic showing the linear dispersion of the Dirac cones at K and K′. Adapted figure with permission from Ref. [93]. Copyright (2011) by the American Physical Society, 10.1103/RevModPhys.83.1193.

The fact that the sublattices A and B can be described by Pauli matrices allows one to treat them as mathematically equivalent to spins, and for this reason the term (lattice) pseudospin is often used to refer to the sublattice degree of freedom. Likewise, the K and K′ valleys can be treated in the same way, thus defining a so-called valley pseudospin.

Graphene nanoribbons The above description of graphene applies to 2D graphene; however, any material forming a device has a finite size with edges and boundaries. Stripes of very narrow graphene are called graphene nanoribbons (GNRs), and due to their finite width, finite size effects appear in the electronic structure [49]. Strictly speaking, graphene nanoribbons are quasi-1D graphene, where one direction preserves translational symmetry whereas the other does not. Depending on the crystalline orientation that is periodic, nanoribbons are classified as armchair graphene nanoribbons (aGNR) or zigzag graphene nanoribbons (zGNR), as shown in Figures 3.3(a) and 3.3(b). The fact that the system considered is quasi-1D implies that the unit cell is no longer made by only two atoms, but by 2N atoms (N atoms from each sublattice) comprising the width of the ribbon. Such N number of A-B atom pairs is used to label the GNR: for example, the structures ploted in Figures 3.3(a) and 3.3(b) correspond to a 9-aGNR and 6-zGNR, respectively.

Since spin transport experiments deal with large graphene samples that are effectively 2D, and we want to model realistic experimental conditions, we want to remove any

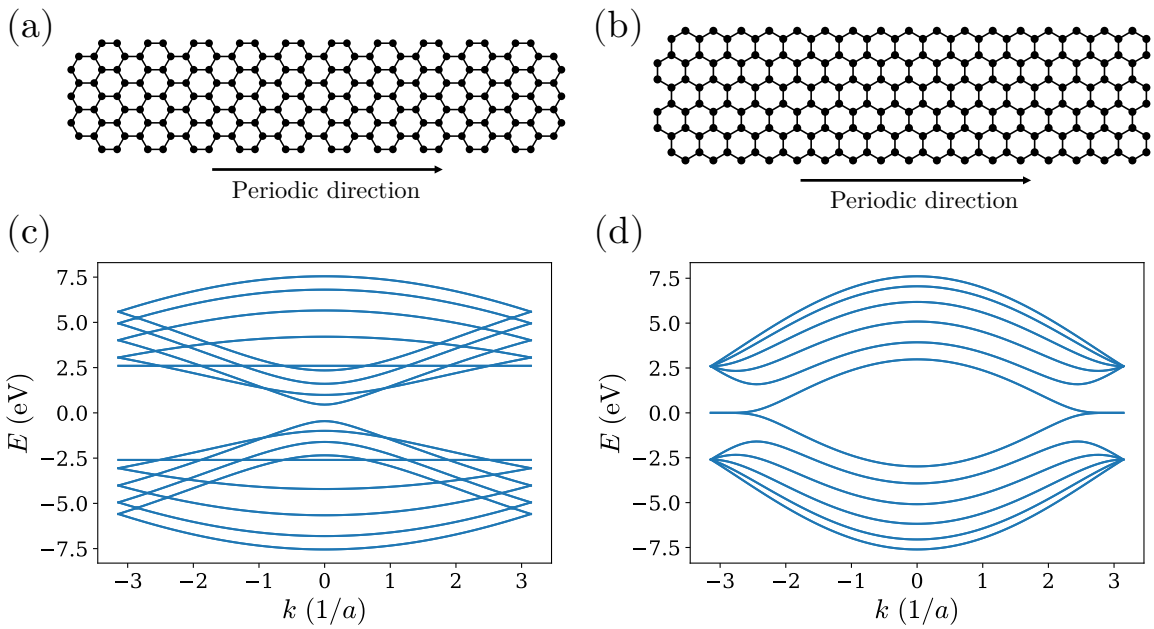

Figure 3.3: (a) Structure of a 9-aGNR with its band structure shown in (c). (b) Structure of a 6-zGNR with its band structure shown in (d).

quasi-1D feature whenever possible. Nevertheless, it is important to understand the peculiarities in the electronic structure of GNRs so as to identify their effects in the LB simulations. The tight-binding model of equation (3.5) can be used to describe both types of GNR; one only needs to consider the termination of the ribbon appropriately when connecting the atoms with the hoppings. In this way, the band structures of the 9-aGNR and 6-zGNR are plotted in Figures 3.3(c) and 3.3(d), respectively.

The first difference to notice with respect to 2D graphene is the appearance of subbands, arising from the confinement in the transverse direction of the ribbon. More importantly, since the system is quasi-1D, the Brillouin zone has changed, and the K and K′ points are folded at Γ for aGRN and at $\pm 2\pi/(3a)$ for the zGNR, as seen in Figures 3.3(c) and 3.3(d). The usage of a nearest-neighbor only tight-binding model presents certain limitations when compared to DFT calculations. For aGNRs, DFT always predicts them to be semiconductors, whereas equation (3.5) renders aGNRs gapless for specific ribbon widths. zGNRs always appear metallic in the TB model owing to the presence of two zero-energy modes whose real-space projection is localized at the ribbon edges. Meanwhile, in DFT it was found that correlation and magnetism at the edges make the system semiconducting as well. All these limitations can be overcome by using a more complete tight-binding model that accounts for up to third-nearest-neighbor hoppings and adds a mean-field Hubbard term [104]. However, as stated above, we focus on 2D graphene physics where it is not necessary to use such a rigorous model.

Disorder, magnetism and SOC

Electronic disorder The tight-binding model mentioned above describes well pristine graphene. However, real materials are more complex. First of all, device fabrication techniques may generate defects in the graphene lattice or contaminants on top of it, and the presence of a substrate and charge inhomogeneities at the interface produces electron-hole puddles, which are electrostatic potential fluctuations within the graphene plane [181]. These imperfections produce elastic scattering of electrons in graphene, and have been shown to be the main factor limiting the mean free path [3,53,119]. Therefore, it is necessary to include some sort of elastic scattering in the TB model of equation (3.5). Although vacancies and puddles can be implemented in the tight-binding (by removing atoms [68] and adding long-range potential profiles [4,276], respectively), here we chose to use Anderson potential disorder to define the mean free path [166,279]. In this thesis we are not focused on studying the consequences of a specific realistic disorder in graphene, but just to be able to tune the mean free path from ballistic to diffusive regime (see section 3.3.4), and Anderson disorder is the simplest way to do so. The tight-binding

form of Anderson disorder is given by

$$\mathcal{H}_A = \sum_i U_i c_i^\dagger c_i, \tag{3.8}$$

where $U_i \in [-U/2, U/2]$ is a potential added at each site i with values randomly chosen from a uniform distribution.

Magnetic exchange Zeeman splitting can occur in the electronic energy levels when an external magnetic field is applied or when a magnetic material is placed in close contact (e.g. as a substrate) with graphene [298]. Since graphene has the pseudospin degree of freedom, it can occur that different graphene sublattices experience different exchange fields, $\boldsymbol{B}_i$, with $i = \mathrm{A}, \mathrm{B}$. In this way, the corresponding TB term to be added to equation (3.5) is

$$\mathcal{H}_Z = \mu_\mathrm{B} \sum_i \sum_{ss'} c_{is}^\dagger [\boldsymbol{s}_\sigma \cdot \boldsymbol{B}_i]_{ss'} c_{is'}. \tag{3.9}$$

Here, μ_B is the Bohr magneton, $\boldsymbol{s}_\sigma = (s_x, s_y, s_z)$ is a vector containing the Pauli matrices acting on the real spin, and the summation runs over the spin index s and both sublattices. To understand the effect of such sublattice-dependent exchange field, it is useful to write $\boldsymbol{B}_{ex} = \frac{\boldsymbol{B}_A + \boldsymbol{B}_B}{2}$ and $\boldsymbol{B}_{s-ex} = \frac{\boldsymbol{B}_A - \boldsymbol{B}_B}{2}$. The first term produces the typical Zeeman splitting of up and down spins, whereas the second one creates a sublattice-dependent exchange field with opposite spin-splittings in each sublattice. While an external magnetic field only induces a nonzero $\boldsymbol{B}_{ex}$ because $\boldsymbol{B}_A = \boldsymbol{B}_B$, a magnetic substrate, either ferromagnetic [99] or antiferromagnetic [114], usually allows for both terms to appear.

Spin-orbit coupling Albeit small, SOC in graphene is responsible for spin relaxation. In addition, different substrates, adatoms and symmetry breaking can induce extra SOC terms that otherwise are absent in freestanding graphene. In this thesis, although we will not make use of SOC-induced spin relaxation (see *Rashba SOC* below), we will still briefly describe the TB of such SOC terms as they are important to understand the state-of-the-art of spin relaxation in graphene and graphene heterostructures.

Intrinsic and Valley-Zeeman SOC. According to the symmetries of graphene, the intrinsic atomic SOC arising from the coupling of the orbital and spin angular momentum manifests in tight-binding as a spin-conserving, next-nearest-neighbor hopping [115, 138, 150, 153, 186, 300],

$$\mathcal{H}_\mathrm{SOC} = \frac{i}{3\sqrt{3}} \sum_{\langle\langle i,j \rangle\rangle} \sum_{ss'} \lambda_I^i \nu_{ij} c_{i,s}^\dagger [s_z]_{ss'} c_{j,s'}. \tag{3.10}$$

Since a next-nearest-neighbor couples atoms with the same pseudospin, we can define a

sublattice resolved intrinsic SOC, λ_I^i, with $i = \mathrm{A}, \mathrm{B}$. In equation (3.10), $\nu_{ij} = \pm 1$ with $+1$ (-1) for a hopping counterclockwise (clockwise), and s_z is a Pauli matrix. As similarly done for the exchange field, we can define $\lambda_I = \frac{\lambda_I^A + \lambda_I^B}{2}$ and $\lambda_{VZ} = \frac{\lambda_I^A + \lambda_I^B}{2}$. The former is typically called intrinsic SOC and opens a topological gap of size $2\lambda_I$ in K and K′ [92,138], whereas the latter is the so-called valley-Zeeman SOC that produces an exchange field with opposite signs at K and K′ [91].

Rashba SOC. When the inversion symmetry $z \to -z$ is broken due to for example the presence of a substrate, adatoms or a gate voltage, an electric field perpendicular to the graphene plane develops and generates a finite Rashba SOC [92, 150, 153, 186], which in TB appears as a spin-mixing, nearest-neighbor hopping,

$$\mathcal{H}_{\mathrm{R}} = \frac{2i}{3} \sum_{\langle i,j \rangle} \sum_{ss'} \lambda_R c_{i,s}^{\dagger} [(\boldsymbol{s}_\sigma \times \hat{\boldsymbol{l}}_{ij}) \cdot \hat{\boldsymbol{z}}]_{ss'} c_{j,s'}. \tag{3.11}$$

Here, λ_R is the strength of the Rashba SOC, $\hat{\boldsymbol{l}}_{ij}$ is a vector pointing from site i to j, and $\hat{\boldsymbol{z}}$ is a unit vector along the z direction. Rashba SOC spin-splits the bands and locks the effective spin-orbit field ($\boldsymbol{B}_{\mathrm{SOC}}$) perpendicular to the momentum of the electron, producing an in-plane helical spin texture. Therefore, in a diffusive 2D system, when the momentum is randomized, so is the effective spin-orbit field However, in a quasi-1D system, the Fermi surface is not circular because the k_y component is quantized (if periodicity is along x). This leads to two consequences: a net spin-orbit field along y that remains even when momentum is randomized, and different spin relaxation rates in the diffusive regime for spins pointing along x and y. This is a direct consequence of the quasi-1D nature of the GNR and cannot be easily solved, and it is the reason why Rashba SOC, although quite common in the literature [67, 101, 122], is not used in this thesis to study spin relaxation with the LB formalism in graphene.

Staggered potential For completeness, we also mention the so-called staggered potential, which usually appears in graphene tight-binding models when inversion symmetry is broken due to different potentials in the A and B sublattices,

$$\mathcal{H}_{\Delta} = \sum_i \Delta \xi_i c_i^{\dagger} c_i. \tag{3.12}$$

Here, Δ is the staggered potential and $\xi_i = +1$ (-1) when $i = \mathrm{A}$ $(i = \mathrm{B})$. The effect of this Hamiltonian is to open a topologically-trivial gap of magnitude 2Δ at K and K′.

Transition metal dichalcogenides

4-band tight-binding model Whereas graphene's tight-binding model is widely known and used, only a few models describing the low-symmetry TMDs exist in the literature, and they all slightly differ from one another [9,164,190,203,214,236,293,295]. Because of that, we derive a tight-binding model of these materials and fit it to DFT calculations (see section 3.1.1) to obtain the tight-binding parameters. Low-symmetry TMDs encompass the 1T′ and $1T_d$ phases of MX_2, with M = Mo, W and X = S, Se, Te [180,214], which are 2D topological insulators in the monolayer limit [214]. Their crystal structure is shown in Figure 3.4(a), with a rectangular unit cell. Therefore, in contrast to graphene, the real-space tight-binding description of such low-symmetry TMDs will be mapped onto a rectangular lattice with lattice parameters $a_x\hat{\boldsymbol{x}}$ and $a_y\hat{\boldsymbol{x}}$. This unit cell has a rectangular Brillouin zone, as pictured in Figure 3.4(b).

We begin by describing a 4-band $\mathbf{k}\cdot\mathbf{p}$ model based on the symmetries of 1T′ and $1T_d$ MX_2 monolayers, belonging to the space groups $P2_1/m$ and $Pmn2_1$, respectively. Both phases possess mirror symmetry in the yz plane (M_x) but only 1T′ has inversion symmetry $\mathcal{I}$. We consider the point group symmetry C_{2h} of the 1T′ phase and additional

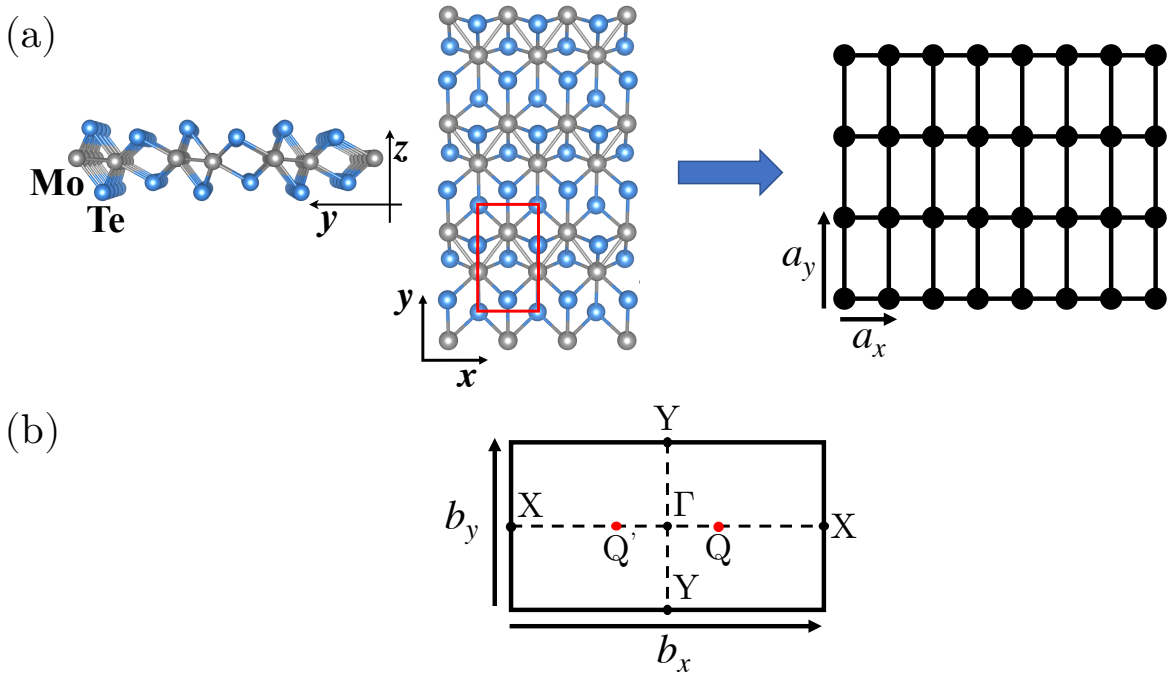

Figure 3.4: (a) Crystal structure of $1T_d$-$MoTe_2$, with a red rectangle denoting the unit cell. The arrow denotes how the tight-binding of such low-symmetry TMD is mapped into a rectangular lattice. (b) First Brillouin zone of the rectangular lattice shown in (a) with the corresponding high-symmetry points.

terms are added to reduce it to $1T_d$.

The low-energy band structure of $1T_d$-$MoTe_2$ is shown in Figure 3.5(a), together with the irreducible representations (irreps) at Γ. Our 4-band $\mathbf{k}\cdot\mathbf{p}$ model will capture the states near Γ. For the C_{2h} point group, we choose two irreps for the $p_y\,(B_u)$ and $d_{yz}\,(A_g)$ orbitals, as they form the valence and conduction bands, respectively [1] [214]. This allows us to assign τ_z as the inversion operator (I) for this basis, where $\boldsymbol{\tau} = (\tau_x, \tau_y, \tau_z)$ is a vector of Pauli matrices acting on the orbital space (p_y and d_{yz}). The parabolic conduction and valence bands can be expressed as $m_p k^2 \tau_0 + (m_d k^2 + \delta)\,\tau_z$, where $m_p - m_d$ and $m_p + m_d$ are effective masses of p_y and d_{yz}, and δ is the strength of band inversion at Γ. Away from Γ, any generic k-points have time-reversal $\mathcal{T} = is_y K$ symmetry, where $\mathcal{T}^2 = -1$ for a spinor. At $k_x = 0$, states have the mirror symmetry $M_x = is_x \otimes \tau_0$; at $k_y = 0$, states have the rotational symmetry $C_{2x} = IM_x = is_x \otimes \tau_z$. By considering these symmetries, the Hamiltonian with additional symmetry-allowed terms up to first order in k is

$$\begin{aligned}\mathcal{H}_{kp}(k_x, k_y) &= m_p k^2 \tau_0 + \left(m_d k^2 + \delta\right)\tau_z + \beta k_y s_0 \otimes \tau_y \\ &\quad + \Lambda_x k_y s_x \otimes \tau_x + \Lambda_y k_x s_y \otimes \tau_x + \Lambda_z k_x s_z \otimes \tau_x \\ &\quad + \eta s_0 \otimes \tau_x, \end{aligned} \tag{3.13}$$

where the third term $\propto \beta$ in the first line gives the crystalline anisotropy between x and y. Terms Λ_α in the second line are the spin-orbit coupling terms for spin-α, and the last term breaks the inversion symmetry, describing in this way either $1T'$ $(\eta = 0)$ or $1T_d$ $(\eta \neq 0)$ TMDs.

To map H_{kp} onto a rectangular lattice, the k-vectors are restored back to periodic functions via the expansions $\sin(k) \approx k + O(k^3)$ and $\cos(k) \approx 1 - k^2/2 + O(k^4)$. Using $\sin(k) = \left(e^{ik} - e^{-ik}\right)/2i$ and $\cos(k) = \left(e^{ik} + e^{-ik}\right)/2$, the tight-binding model can be written down according to the phase $Ce^{i\mathbf{k}\cdot\mathbf{a}}$, where $\mathbf{a} = a_x\hat{\boldsymbol{x}} + a_y\hat{\boldsymbol{y}}$. Thus,

$$\begin{aligned}\mathcal{H}_k(k_x, k_y) &= m_p\left[4 - 2\cos(k_x a_x) - 2\cos(k_y a_y)\right]\tau_0 + \left(m_d\left[4 - 2\cos(k_x a_x) - 2\cos(k_y a_y)\right] + \delta\right)\tau_z \\ &\quad + \Lambda_x \sin(k_y a_y)\, s_x \otimes \tau_x + \Lambda_y \sin(k_x a_x)\, s_y \otimes \tau_x + \Lambda_z \sin(k_x a_x)\, s_z \otimes \tau_x \\ &\quad + \beta \sin(k_y a_y)\, s_0 \otimes \tau_y + \eta s_0 \otimes \tau_x. \end{aligned} \tag{3.14}$$

[1] As explained below, the two irreps need to have opposite parity at Γ to describe the topological gap.

In the second quantization representation, H_k becomes

$$\begin{aligned}\mathcal{H} = &\sum_{i,s}(\Delta + 4m_d + \delta)c^\dagger_{i,s}c_{i,s} - \sum_{\langle ij\rangle,s}(m_p + m_d)c^\dagger_{i,s}c_{j,s} \\ &+ \sum_{i,s}(\Delta - 4m_d - \delta)d^\dagger_{i,s}d_{i,s} - \sum_{\langle ij\rangle,s}(m_p - m_d)d^\dagger_{i,s}d_{j,s} \\ &- \sum_{\langle ij\rangle,s}\frac{\beta}{2}(\hat{\boldsymbol{l}}_{ij}\cdot\hat{\boldsymbol{y}})\,c^\dagger_{i,s}d_{j,s} + \sum_{i,s}\eta c^\dagger_{i,s}d_{i,s} \\ &- \sum_{\langle ij\rangle}\sum_{ss'}\frac{i}{2}(\boldsymbol{\Lambda}_{ss'}\times\hat{\boldsymbol{l}}_{ij})\cdot(\hat{\boldsymbol{y}}+\hat{\boldsymbol{z}})c^\dagger_{i,s}d_{j,s'}. \end{aligned} \tag{3.15}$$

Here, $c^\dagger_{i,s}(c_{i,s})$ and $d^\dagger_{i,s}(d_{i,s})$ are the creation (annihilation) operators of an electron in the p_z and d_{yz} orbitals at the i-th position with spin s. As in the graphene tight-binding model, the symbol $\langle i,j\rangle$ denotes summation over the nearest-neighbors of site i, with $\hat{\boldsymbol{l}}_{ij}$ being a unit vector connecting site i with its nearest neighbor in j and $\hat{\boldsymbol{y}}$ ($\hat{\boldsymbol{z}}$) is a unit vector pointing in the y (z) direction. The spin-orbit coupling terms are included in $\boldsymbol{\Lambda}_{ss'} = (\Lambda_x s_x, -\Lambda_y s_y, \Lambda_z s_z)$. Finally, Δ is a constant energy shift (also absorbing the factor $4m_p$ from equation (3.14)) to match the Fermi level from the DFT results.

Finally, Anderson disorder and magnetic exchange fields can also be included with the following TB terms:

$$\mathcal{H}_A = \sum_i U_i c^\dagger_{i,s}c_{i,s} + \sum_i U_i d^\dagger_{i,s}d_{i,s}, \tag{3.16}$$

$$\mathcal{H}_Z = \mu_\mathrm{B}\sum_i\sum_{ss'} c^\dagger_{is}[\boldsymbol{s}_\sigma\cdot\boldsymbol{B}_i]_{ss'}c_{is'} + \mu_\mathrm{B}\sum_i\sum_{ss'} d^\dagger_{is}[\boldsymbol{s}_\sigma\cdot\boldsymbol{B}_i]_{ss'}d_{is'}. \tag{3.17}$$

It should be noted that the Anderson disorder is applied equally to both orbitals, so for the same site i, the same value of U_i is assigned. Likewise, the Zeeman field acts in the same manner on both orbitals.

DFT fit Next, we fit equation (3.14) to the DFT calculations of $1\mathrm{T_d}$-$MoTe_2$ and $1\mathrm{T_d}$-WTe_2. We have focused on the $1\mathrm{T_d}$ phase in DFT calculation because the $1\mathrm{T}'$ counterpart exhibits practically the same features except for showing no spin-split bands (as a consequence of preserving inverion symmetry). In this manner, we can generally describe both phases depending on whether we set $\eta = 0$ or not. The fits presented here include not only the band dispersion, but the spin splitting and importantly, the spin texture (see section 2.1.2). The band dispersion is enough if one is interested in charge transport, but the spin splitting and especially the spin texture are crucial since they dictate the magnitude and orientation of the spin-orbit field, thus being crucial for spin transport [250].

For example, in graphene/TMD heterostructures, different tight-binding Hamiltonians may describe the same band dispersion but with strikingly different spin textures [83]. Consequently, neglecting the spin texture might result in incorrect parametrization of the TB model.

The bands and spin splitting of $1T_d$-$MoTe_2$ can be seen in Figure 3.5(b). From DFT, one observes that there are two electron pockets (from Γ to X and near Y) and one hole pocket at Γ. However, the hole pocket and the electron pocket at Y present a very small Fermi surface and hence it is expected that the states along the $\Gamma - X$ path dominate the transport properties. The k-point where the conduction band minimum occurs along such $\Gamma - X$ path is sometimes called the Q point (marked with a red dot in Figure 3.4). The tight-binding reproduces well this band, both in dispersion and in magnitude of the spin splitting. We note that our model does not capture the topmost valence band, but rather the second topmost band. However, such topmost valence band (with irreducible representation B_g) is not important to model the band inversion and nontrivial topology, as we need bands with opposite parity at Γ to that end [80]. On the other hand, the DFT and TB results for $1T_d$-WTe_2 (Figure 3.5(c)) show a band gap in the band dispersion, with the topmost valence band not crossing the Fermi level. These fits indicate that our 4-band model is capable of describing both $MoTe_2$ and WTe_2. Although it is true that the topmost valence band of $MoTe_2$ may contribute to transport when the Fermi levels lies in the conduciton band, we note that the absence or presence of a band gap in monolayers of $1T_d$-$MoTe_2$ is still a controversial issue both in DFT calculations (results are very sensitive to the exchange-correlation functional and lattice parameters) [147, 214, 255, 284] and in experiments [145, 207, 250, 259, 263], and even if the gap is closed, it can be opened using strain engineering [309]. Hence, our 4-band model is sufficient to describe $MoTe_2$ since it models well the conduction band near the Fermi level and correctly reproduces the nontrivial topology and band inversion. Extensions to an 8-band model could help describe better the topmost valence band [164, 190, 203] but would also prevent their deployment in large-scale transport calculations due to the higher computational cost associated with having more orbitals in the model.

Next, we present the comparison of the spin texture calculated with the 4-band model and DFT. For $MoTe_2$, two distinct energies are shown: at the Fermi level ($E = 0$) and near the bottom of the conduction band ($E = -100$ meV). For WTe_2, since the Fermi level is very close to the conduction band minimum, we just show the comparison at the Fermi level. A broadening of $T = 300$ K using the derivative of the Fermi-Dirac distribution has been applied. The results are presented in Figure 3.6, where the spin textures of both conduction bands are shown. For all cases, our tight-binding model correctly reproduces the DFT features, namely, a spin texture pointing mainly along

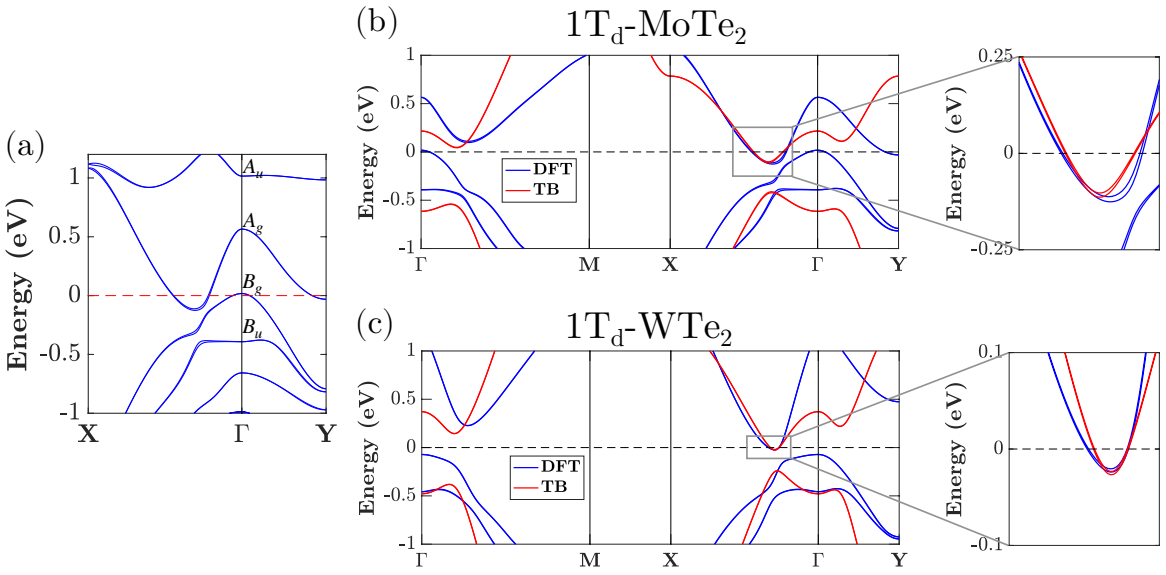

Figure 3.5: (a) DFT band structure of monolayer $1T_d$-$MoTe_2$ and the irreducible representation of states near Γ. (b) Comparison of band structure of monolayer $1T_d$-$MoTe_2$ obtained from DFT (blue) and 4-bands tight-binding model (red). (c) Same as in (c) but for $1T_d$-WTe_2. For all three plots, the horizontal dashed line at energy $E = 0$ denotes the position of the Fermi level.

y and z with small x contribution and with opposite signs for each band. The fitted parameters for both $MoTe_2$ and WTe_2 are listed in Table 3.1.

TMD ribbons Because equation (3.15) is to be used in a ribbon geometry, it is instructive to calculate the band structure of the quasi-1D TMD. The bands of a $1T_d$- and $1T'$-$MoTe_2$ ribbon periodic along the x direction with width $w = 50$ nm are shown in Figures 3.7(a) and 3.7(b). Similar results are found for WTe_2. The k-path runs from X to Γ to X, and therefore the two conduction band minimum appear at Q and its time-reversal-symmetric point at Q′.

One key difference between the two low-symmetry phases is the band splitting, arising from the conservation or absence of inversion symmetry. Indeed, the $1T_d$ phase breaks inversion symmetry (characterized by $\eta = 5.4$ meV) whereas the $1T'$ phase does not.

Table 3.1: DFT-fitted parameters for the 4-band tight-binding model (equations (3.13) - (3.15)); units are in meV.

Material	m_p	m_d	δ	β	η	Λ_x	Λ_y	Λ_z	Δ
$MoTe_2$	-67.1	-417.0	415.3	432.3	5.4	94.8	159.2	-89.6	-467.8
WTe_2	-105.0	-544.9	424.8	449.4	1.7	59.1	77.7	-115.9	-473.2

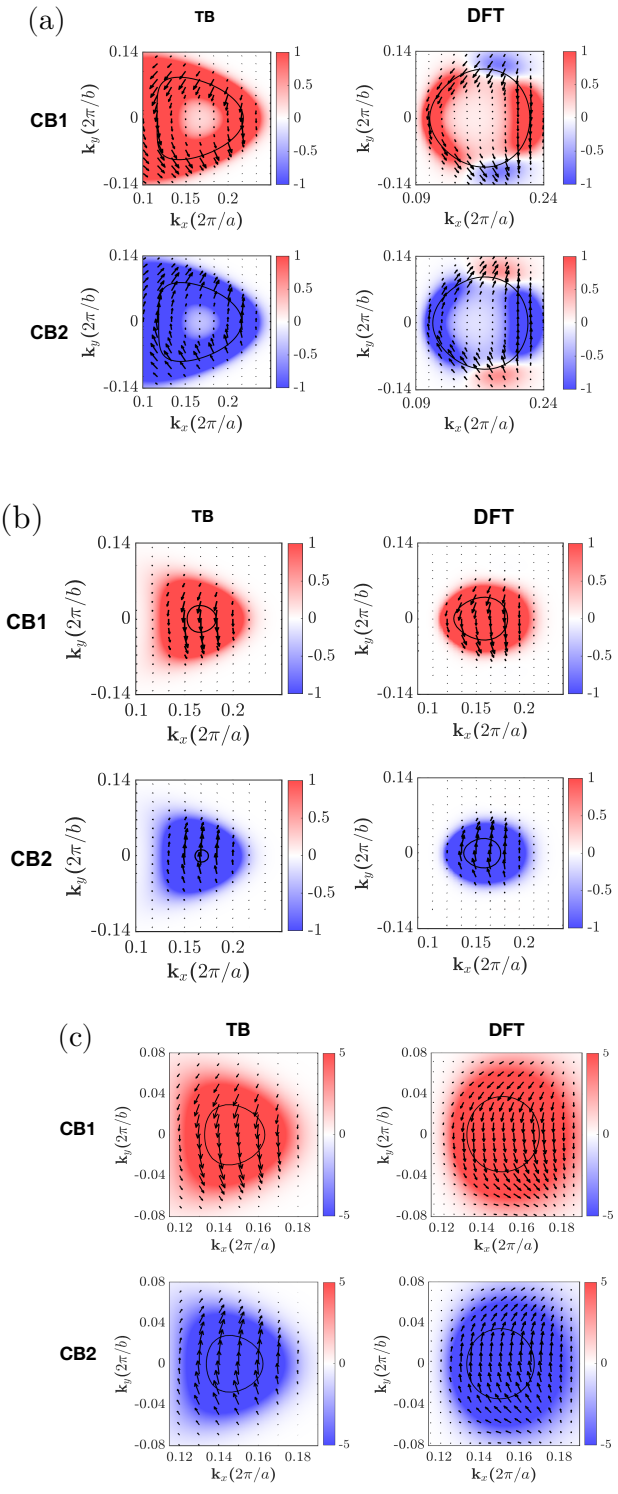

Figure 3.6: (a) Spin texture of $1T_d$-$MoTe_2$ at the Fermi level ($E = 0$) computed with the tight-binding model (left) and DFT (right) for the two conduction bands (CB1, CB2) and broadening of ≈ 26 meV. (b) Same as (a) but at $E = -100$ meV. (c) Same as (a) but for $1T_d$-WTe_2.

Such splitting manifests even in the in-gap states, shown in orange in Figure 3.7. These bands arise due to the nontrivial topology and carry counter-propagating spin-polarized states, localized at the sample boundary, and give rise to the QSHE [214].

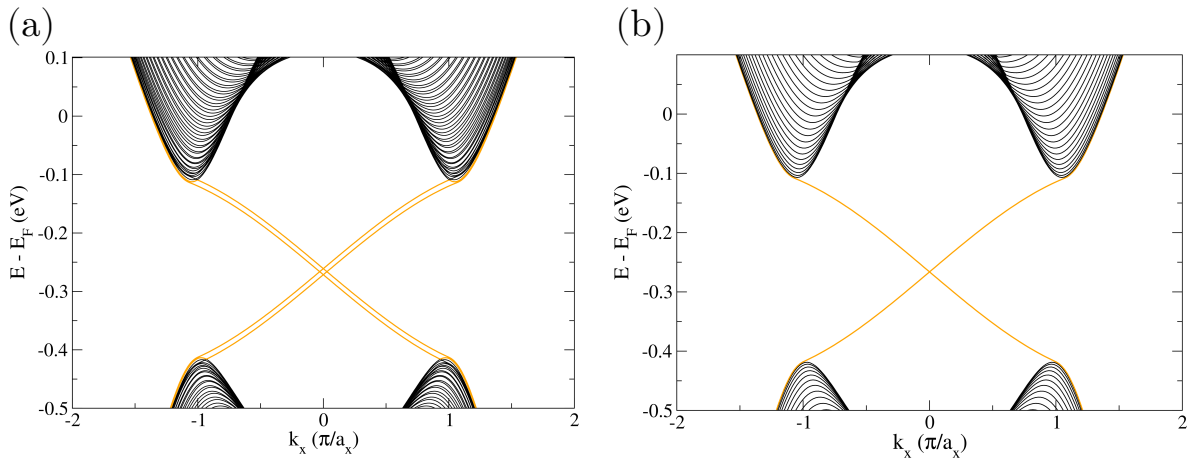

Figure 3.7: (a) Band structure of a $1T_d$-$MoTe_2$ ribbon with finite width $w = 50$ nm in the y direction. Orange bands depict the topological edge states. (b) Same as (a) but for $1T'$-$MoTe_2$.

3.2 Quantum transport

With the knowledge of the Hamiltonian of our system, we now can compute observables such as conductances, voltages or current densities by means of quantum transport methods. The theoretical background of the Landauer-Büttiker formalism will be reviewed first, with the subsequent introduction of the Kubo-Bastin formula to compute the spin Hall conductivity with real-space methods. Then, we introduce the Kwant code and explain how to model nonlocal devices such as nonlocal spin valves so as to extract experimentally relevant quantities.

3.2.1 Landauer-Büttiker formalism

In the Landauer-Büttiker formalism, the electrical current in a conductor is expressed in terms of the transmission probability. The relationship between current and transmission probabilities was first introduced by Landauer [162,163], and later on Büttiker expanded the formulas to describe multi-terminal devices [32, 33]. Since then, this formulation has been extensively used in describing transport in mesoscopic systems [54]. In this section, we will briefly review the two-terminal formulas for current and conductance and then proceed to the generic case of multi-terminal devices and how the transmission probabilities are computed using the scattering matrix approach.

The Landauer formula

Let us consider a quasi-1D conductor contacted by two electrodes, as sketched in Figure 3.8(a), forming a two-terminal (2T) device. Because of the confinement along the transverse direction, the band structure of the conductor is made by a finite number of subbands or transverse modes, M, as shown in Figure 3.8(b) (here we do not assume spin degeneracy). The wider the conductor is, the smaller is the energy separation between subbands and the higher the number of modes at a certain energy. The left and right electrodes, or lead p and lead q in this example, act as reservoirs and consequently are assumed to have a greater number of modes than the conductor ($M_p > M$ and $M_q > M$). This assumption often also implies that the contacts are reflectionless, meaning that there is not backscattering when electrons travel from the conductor to the contact.

The Landauer formula for the electric current reads

$$I_{qp} = \frac{e}{h} \int f_p(E, \mu_p) M_p(E) T_{qp}(E) - f_q(E, \mu_q) M_q(E) T_{pq}(E) \mathrm{d}E. \tag{3.18}$$

Here, $f_p(E, \mu_p)$ and $f_q(E, \mu_q)$ are the Fermi-Dirac distributions in lead p and q, respectively, with μ_p and μ_q the ECP of each lead. In addition, T_{qp} (T_{pq}) is the transmission

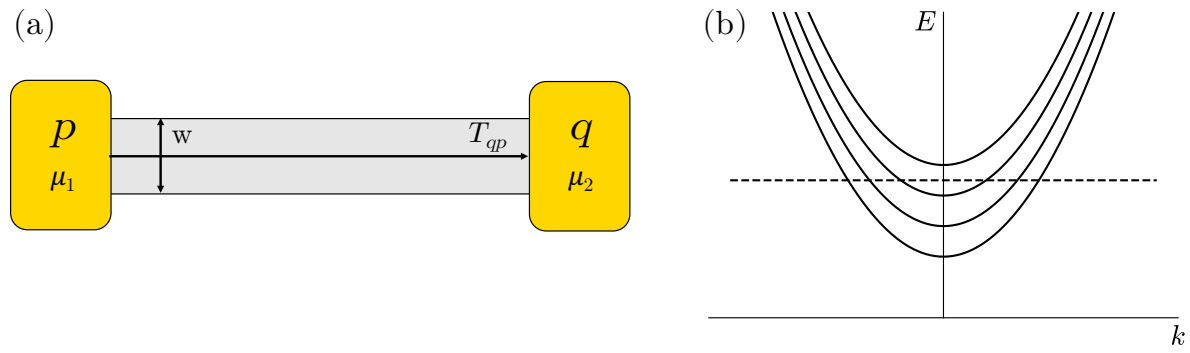

Figure 3.8: (a) Sketch of a two-terminal device, where leads p and q are attached to a quasi-1D conductor with width w. The transmission T_{qp} is related to the current flowing in the device. (b) Schematic of the band dispersion of a quasi-1D system, in which several subbands or transverse modes are present. The dashed line shows the Fermi level, which cuts through three left- and right-propagating modes.

probability per mode (thus it has values between 0 and 1) that an electron injected from lead p (lead q) goes trough the conductor and reaches lead q (lead p), which it is a paramount quantity in the LB formalism. It can be shown that in the absence of inelastic scattering [54], $M_p(E)T_{qp}(E) = M_q(E)T_{pq}(E)$, and hence

$$I_{qp} = \frac{e}{h}\int M_p(E)T_{qp}(E)[f_p(E,\mu_p) - f_q(E,\mu_q)]\mathrm{d}E. \tag{3.19}$$

This equation says that if contacts p and q are in equilibrium, that is, $\mu_p = \mu_q = E_\mathrm{F}$ (with E_F the Fermi level), there is no current flowing. For small variations from that, for example when a small bias voltage is applied, such that $M_p(E)T_{qp}(E)$ is approximately constant over the interval $\mu_p - \mu_q$, the linear response regime can be used. In this way, expanding f_p and f_q near E_F, we obtain

$$I_{qp} = \frac{e}{h}\int M_p(E)T_{qp}(E)(\mu_p - \mu_q)\left(-\frac{\partial f_0}{\partial E}\right)\mathrm{d}E, \tag{3.20}$$

with f_0 being the Fermi-Dirac distribution at equilibrium (centered at $\mu = E_\mathrm{F}$). Working in linear response allows us to define the concept of two-terminal conductance, G_{qp} or $G_{2\mathrm{T}}$, that relates the current with the voltage difference between leads, $V_{qp} = (\mu_p - \mu_q)/|e|$, as

$$G_{qp} = \frac{I_{qp}}{V_{qp}} = \frac{e^2}{h}\int M_p(E)T_{qp}(E)\left(-\frac{\partial f_0}{\partial E}\right)\mathrm{d}E. \tag{3.21}$$

In addition to the linear response regime, if low temperature is considered such that

$\left(-\frac{\partial f_0}{\partial E}\right) \to \delta(E - E_{\rm F})$, we arrive at

$$\begin{aligned} I_{qp} &= \frac{e}{h} \int M_p(E) T_{qp}(E)(\mu_p - \mu_q)\delta(E - E_{\rm F}) {\rm d}E \\ &= \frac{e}{h} M_p(E_{\rm F}) T_{qp}(E_{\rm F})(\mu_p - \mu_q) \end{aligned} \tag{3.22}$$

$$G_{qp} = \frac{e^2}{h} M_p(E_{\rm F}) T_{qp}(E_{\rm F}) = G_0 \overline{T}_{qp}. \tag{3.23}$$

Equation (3.23) is the linear-response, low-temperature, two-terminal conductance and will be widely employed throughout this thesis. Before proceeding to the the case of multi-terminal conductors, a few technical remarks are in order. We have introduced the unit of conductance, $G_0 = e^2/h$, which is often defined as $2e^2/h$. The factor of 2 arises due to the inclusion of the spin degree of freedom and spin degeneracy. However, if bands are spin-split, as they will be in many cases in this thesis because of SOC or magnetic fields, then each spin subband must be counted independently. Also, we have replaced $M_p T_{qp}$ by the transmission function $\overline{T}_{qp}$. Many times, not all modes from lead p have the same transmission probability to reach lead q, so we cannot define a unique T_{qp}. Instead, $\overline{T}_{qp}$ accounts for the transmission probability of each mode n in lead p to arrive to each mode m in lead q:

$$\overline{T}_{qp} = \sum_{n \in p}^{M_p} \sum_{m \in q}^{M_q} T_{mn}. \tag{3.24}$$

The transmission probability T_{mn} has values ranging between 0 and 1, with 1 meaning a perfect transmission from mode n to mode m. Two main effects exist that decrease the value of the transmission. One is electron scattering inside the sample, which produces backscattering or reflection of the electrons and decreases the transmission probability. The other factor is associated with the fact that both leads have a higher number of modes than the conductor; this imposes a maximum number of modes capable of being transmitted. For instance, if both contacts have 20 modes, but the conductor only 5, then the total maximum transmission will be 5 (assuming ballistic transport in the conductor), indicating that many modes do not have a perfect tranmission. This "bottleneck" effect is known as contact resistance since it appears because of the mode mismatch between the leads and the conductor. Thus, the associated conductance is

$$G_{qp} = \frac{e^2}{h} M. \tag{3.25}$$

This is the *maximum* value of conductance, determined by the total number of modes in the *conductor*, and corresponds to the case of totally ballistic transport. Therefore, even in the absence of scattering inside the sample, a finite resistance exists, called contact

resistance $G_c^{-1} = h/(e^2 M)$. Another effect also associated with the contact resistance exists, and may further decrease the conductance. If the band dispersion of the leads and the conductor differs, their energy levels mismatch at the interface, resulting in backscattering of lead modes at the interface, and thus not populating all modes M in the channel. As a consequence, $G_{qp} < G_c$. In this way, the contact resistance can be generally written as $G_c^{-1} = Ah/(e^2 M)$, with $A \geq 1$ being some parameter quantifying the effect of such mode mismatch. Importantly, when $A = 1$, the contact resistance is minimum and is called the Sharvin resistance [29, 225]

$$R_S = G_S^{-1} = \frac{h}{e^2 M}. \tag{3.26}$$

Therefore, the upper bound of the two-terminal conductance is the Sharvin conductance G_S (or equation (3.25)), and this value is reduced by decreasing the transmission probability, either by introducing scattering in the conductor or by mode mismatch at the lead-conductor interface.

The Büttiker formula

Next, we extend equations (3.22) and (3.23) to multi-terminal geometries, such as the one depicted in Figure 3.9. In a two-terminal device, all the current that is injected by lead p, I_p, is absorbed by lead q, so we can write $I_p = I_{qp}$ and calculate it using $I_{qp} = G_{qp} V_{qp}$. For more than 2 electrodes, I_p is simply the sum of currents from lead p to all other leads,

$$I_p = \sum_q I_{qp} = \sum_q (G_{qp} V_p - G_{pq} V_q) = \sum_q G_{qp}(V_p - V_q), \tag{3.27}$$

where we have used the relation $\sum_q G_{qp} = \sum_q G_{pq}$ that ensures that the current is zero in equilibrium. In contrast, $G_{pq} \neq G_{qp}$ in general.

As an example that will prove useful for investigating nonlocal spin valves later on, let us apply equation (3.27) to the four-terminal device shown in Figure 3.9. Because there are 4 leads, we have a system of 4 linear equations:

$$I_1 = G_{21}(V_1 - V_2) + G_{31}(V_1 - V_3) + G_{41}(V_1 - V_4) \tag{3.28a}$$
$$I_2 = G_{12}(V_2 - V_1) + G_{32}(V_2 - V_3) + G_{42}(V_2 - V_4) \tag{3.28b}$$
$$I_3 = G_{13}(V_3 - V_1) + G_{23}(V_3 - V_2) + G_{43}(V_3 - V_4) \tag{3.28c}$$
$$I_4 = G_{41}(V_4 - V_1) + G_{42}(V_4 - V_2) + G_{43}(V_4 - V_3). \tag{3.28d}$$

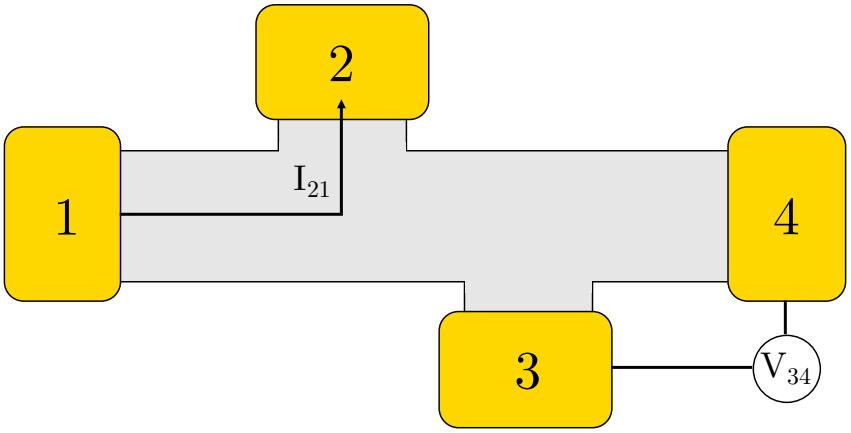

Figure 3.9: Sketch of a multi-terminal device consisting of a conductor contacted to more than two leads. In this example, current flows from lead 1 to 2, and a voltage is measured between leads 3 and 4.

In matrix form, we can rewrite them as

$$\begin{pmatrix} I_1 \\ I_2 \\ I_3 \\ I_4 \end{pmatrix} = \begin{pmatrix} G_{21}+G_{31}+G_{41} & -G_{21} & -G_{31} & -G_{41} \\ -G_{12} & G_{12}+G_{32}+G_{42} & -G_{32} & -G_{42} \\ -G_{13} & -G_{23} & G_{13}+G_{23}+G_{43} & -G_{43} \\ -G_{14} & -G_{24} & -G_{34} & G_{14}+G_{24}+G_{34} \end{pmatrix} \begin{pmatrix} V_1 \\ V_2 \\ V_3 \\ V_4 \end{pmatrix}, \tag{3.29}$$

or in compact notation,

$$\mathbf{I} = \mathbf{G} \cdot \mathbf{V}, \tag{3.30}$$

where $\mathbf{G}$ is referred to as the conductance matrix. Once each pair of two-terminal conductance G_{qp} is known, we can calculate the current at each lead if we assume a value for each voltage in $\mathbf{V}$, or calculate the voltage at each lead if we know how the current is driven in the device. To illustrate this, let us consider the device configuration drawn in Figure 3.9. There, a current I is driven between lead 1 and lead 2 only, and voltage is measured between probes 3 and 4, which are left floating so no current flows in them. We are interested in the nonlocal resistance

$$R_{\mathrm{nl}} = \frac{V_{34}}{I_{21}} = \frac{V_3 - V_4}{I_1} = \frac{V_3 - V_4}{-I_2} = \frac{V_3 - V_4}{I}. \tag{3.31}$$

It is worth noting that the four currents are not independent. As stated earlier, $\sum_q G_{qp} = \sum_q G_{pq}$ so no current flows in equilibrium, and this leads to the Kirchoff's law $I_1+I_2+I_3+I_4 = 0$. Hence, the four equations above are not linearly independent, and we can delete one current component and one row of $\mathbf{G}$. Likewise, since currents depend on voltage differences and not on absolute values, we can ground one of the leads, set that voltage

to zero and in this manner delete the corresponding column of $\mathbf{G}$. Given that the drain electrode is lead 2, we choose $V_2 = 0$, although this is arbitrary. With $\mathbf{I} = (I, -I, 0, 0)$ we obtain:

$$\begin{pmatrix} I \\ 0 \\ 0 \end{pmatrix} = \begin{pmatrix} G_{21} + G_{31} + G_{41} & -G_{31} & -G_{41} \\ -G_{13} & G_{13} + G_{23} + G_{43} & -G_{43} \\ -G_{14} & -G_{34} & G14 + G_{24} + G_{34} \end{pmatrix} \begin{pmatrix} V_1 \\ V_3 \\ V_4 \end{pmatrix}, \tag{3.32}$$

where we have chosen to delete the I_2 component to remove both the second row and column of $\mathbf{G}$. Since usually $G_{qp} \neq G_{pq}$, the analytical solution for $\mathbf{V}$ is too cumbersome to be shown here. In fact, usually one solves the above equations numerically to obtain each voltage value and compute the nonlocal resistance with equation (3.31).

The scattering matrix approach

Thus far we have sho that in order to obtain the currents, voltages and conductances in the LB formalism, one needs to calculate the transmission function accounting for the transmission probability that a mode n in lead p arrives at mode m in lead q. In the following, we describe how these transmissions are calculated.

For a fixed energy E, the scattering matrix, or S-matrix, relates the wave function (WF) of modes entering the scattering region (SR) or device (incoming WF) to the wave function of modes exiting the scattering region (outgoing WF), and its matrix elements are related to the transmission and reflection probabilities. The probability that a mode n transmits from lead p to another mode m in lead q is $T_{mn} = |t_{mn}|^2$, where t is the transmission amplitude. Likewise, a mode can be reflected back to the same lead with reflection probability $R_{nn} = |r_{nn}|^2$, with r being the reflection amplitude. In this way, the elements of the scattering matrix are composed of $s_{mn} = t_{mn}$ and $s_{nn} = r_{nn}$.

Let us consider the simple case of a two-terminal device with one mode per lead, as shown in Figure 3.10. The S-matrix and and wave functions can be written as [55]

$$\begin{pmatrix} \psi_n^{\text{out}} \\ \psi_m^{\text{out}} \end{pmatrix} = \begin{pmatrix} r_{nn} & t_{nm} \\ t_{mn} & r_{mm} \end{pmatrix} \begin{pmatrix} \psi_n^{\text{in}} \\ \psi_m^{\text{in}} \end{pmatrix}. \tag{3.33}$$

The vector multiplying the S-matrix is composed of WFs that enter the scattering region, $\psi_{n,m}^{\text{in}}$, and they can be reflected back or transmitted through the conductor. The combination of reflection and transmission of modes form the outgoing WFs that go from

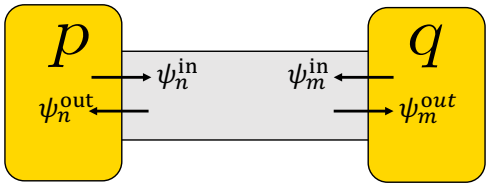

Figure 3.10: Sketch of a two-terminal device, where leads p and q, with modes n and m, respectively, are attached to a quasi-1D conductor. The wave function associated with each mode can be classified as incoming (i.e. going from the lead to the SR, $\psi^{\text{in}}_{n,m}$) or outgoing (i.e. going from the SR to the lead, $\psi^{\text{out}}_{n,m}$).

the SR to the leads, $\psi^{\text{out}}_{n,m}$. This is seen by writing out the matrix equation above

$$\psi_n^{\text{out}} = r_{nn}\psi_n^{\text{in}} + t_{nm}\psi_m^{\text{in}} \tag{3.34a}$$

$$\psi_m^{\text{out}} = t_{mn}\psi_n^{\text{in}} + r_{mm}\psi_m^{\text{in}}. \tag{3.34b}$$

For the general case of multi-terminal devices with many modes per lead, the reflection and transmission amplitudes become matrices, r_{pp} and t_{qp}, whose elements are $s_{n'n}$ and s_{mn}, respectively (note that now there can be reflection between two modes belonging to the same lead, $r_{n'n}$). These matrices include all the possible reflection and transmission amplitudes between all modes in p and q. Thus, the size of t_{qp} (r_{pp}) is $M_q \times M_p$ ($M_p \times M_p$). Consequently, the size of the S-matrix is $M_T \times M_T$, where $M_T = \sum_p M_p$ is the total number of modes obtained by summing all modes in each lead. We illustrate this matrix representation in Figure 3.11(a).

Finally, we can obtain the transmission function $\overline{T}_{qp} = \sum_{n\in p}^{M_p}\sum_{m\in q}^{M_q} T_{mn}$ (equation

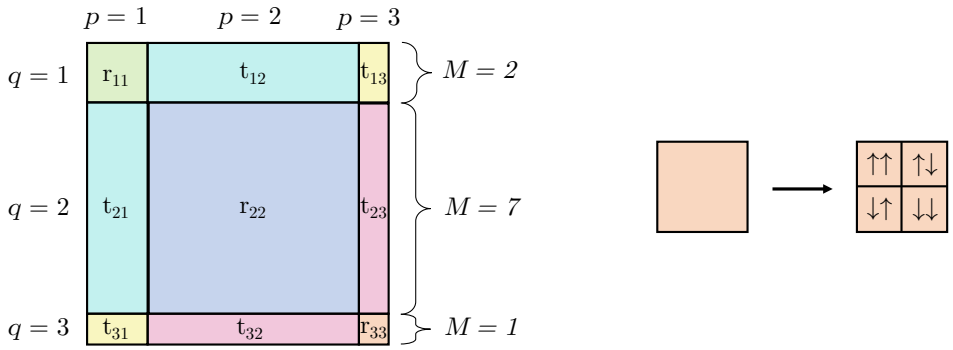

Figure 3.11: Left: illustrative representation of the matrix elements of the scattering matrix. This S-matrix describes a system with 3 leads with different number of modes: $M_1 = 2$, $M_2 = 7$, $M_3 = 1$. Therefore, the S-matrix is a 9×9 matrix. Right: Division of an element s_{mn} into 4 spin sectors.

(3.24)) from the S-matrix as

$$\overline{T}_{qp} = \mathrm{Tr}[t_{qp}^{\dagger} t_{qp}]. \tag{3.35}$$

When the spin-degree of freedom is included, we can further subdivide each transmission and reflection amplitude s_{mn} into spin sectors, as shown in Figure 3.11(b). Equation (3.35) automatically takes this into account to obtain the total transmission from p to q. However, it is also possible to write the total transmission as a sum of transmissions of each spin sector:

$$\overline{T}_{qp} = \overline{T}_{qp}^{\uparrow\uparrow} + \overline{T}_{qp}^{\uparrow\downarrow} + \overline{T}_{qp}^{\downarrow\uparrow} + \overline{T}_{qp}^{\downarrow\downarrow}, \tag{3.36}$$

with $\overline{T}_{qp}^{ss'} = \mathrm{Tr}[t_{qp}^{ss'\dagger} t_{qp}^{ss'}]$ being the transmission of modes with spin s' of lead p to the modes in lead q having spin s. The cases $\overline{T}_{qp}^{\uparrow\uparrow}$ and $\overline{T}_{qp}^{\downarrow\downarrow}$ preserve the spin, while $\overline{T}_{qp}^{\uparrow\downarrow}$ and $\overline{T}_{qp}^{\downarrow\uparrow}$ denote spin mixing. The spin-mixing components are zero in absence of magnetic field and SOC, but might become finite when these interactions are present in the Hamiltonian.

So far we have shown the relation of the transmission coefficients with the S-matrix. To actually compute the scattering matrix and its elements, two distinct methods exist: the non-equilibrium Green's function method via the Fisher-Lee relation [77], and the wave function method [94]. Since Kwant utilizes the latter, we will restrict ourselves to this approach in the following.

We start by defining the Hamiltonian of both the scattering region and the leads and solve the Schrödinger equation. Without loss of generality, we restrict ourselves to the case of a single lead since multiple leads can be mapped onto a single lead [94, 124]. A schematic of this system is depicted in Figure 3.12. The Hamiltonian of the SR is described by H_S, with size $N_S \times N_S$. Here, N_S is the number of orbitals used to describe the SR, and in a tight-binding representation it corresponds to the number of lattice sites times the degrees of freedom (such as spin or orbital) per site. Whereas the scattering region is finite, the lead is semi-infinite. Therefore, the description of a lead is made by a unit cell which is repeated periodically along a translationally-invariant direction. As shown in Figure 3.12, each unit cell is labeled by an index j, which starts with $j = 1$ in the unit cell contiguous to the SR and increases as the unit cell is repeated away from the SR. Because of the periodicity, the Bloch theorem can reduce the infinite Hamiltonian of the lead to the Hamiltonian of one unit cell, H_L, with size $M \times M$, where M is the total number of modes in the lead. V_L denotes the coupling from j to $j+1$, while $V_L^{\dagger}$ is the hopping from $j+1$ to j. Likewise, the SR couples to the lead $j = 1$ with the terms V_{LS} and $V_{LS}^{\dagger}$. Hence, in the basis in which the leads are ordered from infinity to $j = 1$ and

then the scattering region, we can write the following total Hamiltonian:

$$H = \begin{pmatrix} \ddots & V_L & & \\ V_L^\dagger & H_L & V_L & \\ & V_L^\dagger & H_L & V_{LS} \\ & & V_{LS}^\dagger & H_S \end{pmatrix} \tag{3.37}$$

To obtain the elements of the scattering matrix, we need to solve M systems of equations, one per each mode n in the lead. Such system of equations is the coupling between H_S and only the first unit cell of the lead (due to the transnational symmetry of H_L). Because the unit cell $j = 1$ couples with $j = 2$, we just need to consider the last three rows of equation (3.37), which results in the following Schrödinger equation:

$$\begin{pmatrix} H_L - E & V_L & 0 \\ V_L^\dagger & H_L - E & V_{LS} \\ 0 & V_{LS}^\dagger & H_S - E \end{pmatrix} \begin{pmatrix} \Psi_{n,E}(2) \\ \Psi_{n,E}(1) \\ \Psi_{n,E}^S \end{pmatrix} = 0, \tag{3.38}$$

where $\Psi_{n,E}^S$ is the wave function in the SR due to the propagating mode n in the lead at energy E and $\Psi_{n,E}(j)$ is the scattering wave function of mode n in the j-th unit cell in the

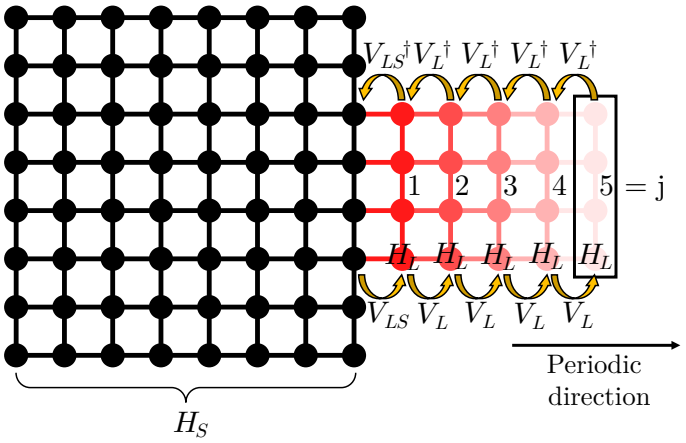

Figure 3.12: Schematic of a lead (red lattice) connected to a scattering region (black region). The lead is composed of a unit cell (marked with a rectangle) that is repeated infinitely along a periodic direction. The position of each unit cell with respect to the SR is indicated by an index j, with $j = 1$ the closest unit cell to the SR and increasing up to $j \to \infty$ as the unit cell is repeated away from the SR. The Hamiltonian of each unit cell is H_L and the hopping between j $(j + 1)$ to $j + 1$ (j) is V_L $(V_L^\dagger)$. Likewise, the coupling between the scattering region and the first unit cell is V_{LS} and its conjugate transpose. Finally, the Hamiltonian of the scattering region is H_S.

lead at energy E. Since all the quantities are going to be calculated at a fixed energy, we drop the index E hereafter in all wave functions. The scattering WF is a state composed of the incoming and outgoing wave functions[2] (the WFs depicted in Figure 3.10) in the following way [94, 124]:

$$\Psi_n(j) = \psi_n^{\text{in}}(j) + \sum_m^M s_{mn}\psi_m^{\text{out}}(j), \tag{3.39}$$

where $\psi_n^{\text{in/out}}(j)$ is the incoming/outgoing wave function at the unit cell j and has the form of a Bloch state,

$$\psi_n^{\text{in/out}}(j) = e^{ikja}u_n^{\text{in/out}}, \tag{3.40}$$

with k and a being the crystal momentum of mode n at energy E and the lattice constant along the periodic direction, respectively. Combining both equations, the scattering wave function can be expressed as

$$\Psi_n(j) = e^{ikaj}(u_n^{\text{in}} + \sum_m^M s_{mn}u_m^{\text{out}}). \tag{3.41}$$

The periodic function $u_n^{\text{in/out}}$ is nothing else than the eigenvector of the Hamiltonian of the infinite lead. Therefore, it satisfies the Schrödinger equation,

$$\left[(H_L - E) + V_L e^{-ika} + V_L^\dagger e^{ika}\right] u_n = 0. \tag{3.42}$$

By calculating the group velocity of each eigenstate, we can then make the distinction between u_n^{in} and u_n^{out} depending on whether the velocity is negative or positive, respectively. This is because the positive direction of the periodic direction is taken to be from the SR to infinity, independent of the relative orientation of the leads with the Cartesian axes. By examining equation (3.41), the scattering WF of mode n can be understood as the sum of the incoming WF of this n mode and all possible outgoing m states originating from the scattering from n to m, with probability $|s_{mn}|^2$. This must not be confused with the outgoing WF of mode n: $\psi_n^{\text{out}}(j) = \sum_m^M s_{nm}\psi_m^{\text{in}}(j)$.

[2] Actually, the so-called bound or evanescent states also contribute to the scattering wave function [94, 124]. These states are localized in the SR and decay exponentially in the leads. Importantly, these states do not contribute to transport and consequently are omitted here without affecting the final result in order to keep the explanation consise and free from excessive information that may obscure the derivation.

We proceed by recasting equation (3.38) as a linear system of equations,

$$(H_L - E)\Psi_n(2) + V_L\Psi_n(1) = 0 \tag{3.43a}$$

$$V_L^\dagger\Psi_n(2) + (H_L - E)\Psi_n(1) + V_{LS}\Psi_n^S = 0 \tag{3.43b}$$

$$V_{LS}^\dagger\Psi_n(1) + (H_S - E)\Psi_n^S = 0, \tag{3.43c}$$

where only the last two equations are actually needed to obtain the coefficients of the S-matrix. By using equation (3.41), one arrives at

$$V_L^\dagger e^{ik2a}(u_n^{\text{in}} + \sum_m^M s_{mn}u_m^{\text{out}}) + (H_L - E)e^{ika}(u_n^{\text{in}} + \sum_m^M s_{mn}u_m^{\text{out}}) + V_{LS}\Psi_n^S = 0 \tag{3.44a}$$

$$V_{LS}^\dagger e^{ika}(u_n^{\text{in}} + \sum_m^M s_{mn}u_m^{\text{out}}) + (H_S - E)\Psi_n^S = 0. \tag{3.44b}$$

Next, we group the common terms of u_n^{in} and u_m^{out} in the first equation and use equation (3.42) to arrive at

$$-V_L(u_n^{\text{in}} + \sum_m^M s_{mn}u_m^{\text{out}}) + V_{LS}\Psi_n^S = 0 \tag{3.45a}$$

$$V_{LS}^\dagger e^{ika}(u_n^{\text{in}} + \sum_m^M s_{mn}u_m^{\text{out}}) + (H_S - E)\Psi_n^S = 0, \tag{3.45b}$$

which can be rewritten as

$$\begin{pmatrix} -V_L\sum_m^M u_m^{\text{out}} & V_{LS} \\ V_{LS}^\dagger e^{ika}\sum_m^M u_m^{\text{out}} & H_S - E \end{pmatrix} \begin{pmatrix} s_{1n} \\ \vdots \\ s_{Mn} \\ \Psi_n^S \end{pmatrix} \begin{pmatrix} V_L u_n^{\text{in}} \\ -V_{LS}^\dagger e^{ika}u_n^{\text{in}} \end{pmatrix}. \tag{3.46}$$

This is the matrix operation that needs to be computed, and as a result, the elements s_{mn} and Ψ_n^S are obtained (note that u_n^{in} and u_m^{out} are obtained from equation (3.42)). Because there are M coefficients and Ψ_n^S is a vector of size N_S, the total number of equations to solve is $M + N_S$. Yet, this procedure needs to be repeated a total of M times, as only a single column of the S-matrix is obtained after solving equation (3.46) for a given n.

3.2.2 Kubo-Bastin formula for the spin Hall conductivity

In section 2.1.5, we provided a formula to compute the spin Hall conductivity, equation (2.33). Here, we introduce an equivalent formula in which the velocity operators are

written in real space, which allows one to break the periodicity of the Hamiltonian by e.g. introducing Anderson potential disorder. The elements of the SHC tensor can be calculated in the linear response regime using the Kubo-Bastin formula [18],

$$\sigma_{ij}^{\alpha} = -2\hbar\Omega \int_{-\infty}^{E_{\mathrm{F}}} dE \,\mathrm{Im}\left(\mathrm{Tr}\left[\delta(E-H)J_{s,i}^{\alpha}\frac{dG^{+}}{dE}J_{j}\right]\right), \tag{3.47}$$

where Ω is the volume of the sample, J_j is the j-th component of the charge current density operator and is defined in a localized tight-binding basis by [69]

$$J_j = \frac{ie}{\Omega\hbar}[H, R_j], \tag{3.48}$$

with R_j the jth-component of the position operator. The operator $J_{s,i}^{\alpha}$ is the spin current density operator, which is defined in terms of the current density as $J_{s,i}^{\alpha} \equiv \{J_i, s_\alpha\}/2$. The spectral operators $\delta(E-H)$ and $G^{+} \equiv \lim_{\eta\to 0} 1/(E-H+i\eta)$ are the Dirac delta and retarded Green's function, respectively, and are approximated numerically by using the kernel polynomial method [285]. More details about the numerical real-space implementation can be found in Refs. [50, 69, 82, 83]. In a similar manner, the longitudinal charge conductivity, σ_{jj}, can also be obtained by replacing $J_{s,i}^{\alpha}$ by J_j in equation (3.47). With both the spin and charge conductivities, the spin Hall angle can be obtained as $\theta_{ij}^{\alpha} = \sigma_{ij}^{\alpha}/\sigma_{jj}$.

3.2.3 The Kwant package

Kwant [94] is an open-source python package that makes use of other scientific-based python libraries, such as NumPy [204] and SciPy [133], to carry out Landauer-Büttiker calculations on tight-binding Hamiltonians. In this section, we briefly outline the main aspects of Kwant that are related to this thesis, and we refer to the original article for an in-depth explanation of the program [94].

One of the unique features of Kwant is its objective of being both flexible and user-friendly, so that a wide range of systems can be studied while the user focuses on the physics instead of algorithm implementation, while at the same time being efficient and fast in solving the scattering problem. To achieve this seemingly complicated task, Kwant's workflow is divided in two steps. The first one is the creation of a Kwant system, that is, formulating the tight-binding model that describes the scattering region and the leads. Because this is a task where the user has to interact with the code the most, the program uses a high-level language (e.g. Python) to facilitate the tight-binding implementation. The second step is solving equation (3.46) or any other operation to compute other physical quantities. To achieve high efficiency, the program uses carefully

optimized Python algorithms as well as routines written in Cython and C/C++, like the so-called nested dissection algorithm implemented in sparse linear algebra libraries, such as MUMPS [7]. These processes are run internally and automatically, without needing the users' commands.

Kwant allows one to create systems of any arbitrary form and with any number of leads. As an example, we show in Figure 3.13 a triangle-shaped scattering region with three leads connected to it along different directions. As commented in the previous section, the leads are semi-infinite; this is denoted by the fading red color. The the tight-binding sites are represented by the dotted circles, whereas the lines connecting them are the hoppings. In Kwant, each site has two attributes, the so-called family and tag. The family represents the sublattice degree of freedom in a unit cell, or in crystallographic terms, the basis applied to each lattice site to form a crystal. Within a family, a unique tag is associated to each site, so it can be identified. In fact, the way the values of onsite and hopping energies are implemented is by mapping every tag to a value. A very useful resource is that these values are not restricted to numbers, but they can be a function or even a matrix. This becomes really helpful when working with spinful systems, as one can simply use the term $\mu_{\mathrm{B}} B s_z$ (with s_z a Pauli matrix) as an onsite term to model the Zeeman exchange field.

The lead is an important part of a Kwant system since its scattering wave functions dictate the transmission through the scattering region. Likewise, the interface between both regions is fundamental, and this interface is formed when Kwant "attaches" the lead to the SR. In Kwant, attaching a lead means adding hoppings connecting the lead

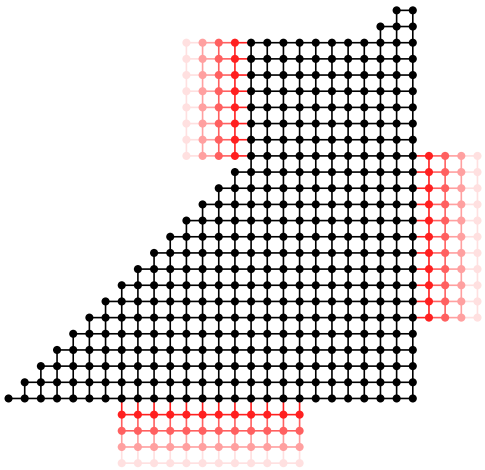

Figure 3.13: Example of a Kwant system. The black (red) region denotes the scattering region (leads). The leads extend to infinity, as illustrated by the fading red color.

to the scattering region, forming in this way the matrix V_{LS} entering in equation (3.37). By default, the added hoppings are the lead's hoppings, but this does not have to be the case, and can be defined manually if necessary.

With regard to the numerical solving procedure of Kwant, it is worth noting that the scaling of the computational time for a system of length L and width W is of order $O(LW^2)$ [94]. This contrasts with the $O(LW^3)$ scaling of Green's function-based methods typically used in the Landauer-Büttiker formalism. This faster computation comes at the expense of a higher memory requirement, and hence the typical limitation in terms of system size is the memory demand. Nonetheless, with computers commonly available nowadays, Kwant is able to simulate systems with millions of orbitals.

As explained before, the main outputs of Kwant are the scattering matrix and the wave function inside the scattering region. From these, several physical observables can be obtained. In this thesis, we will calculate the conductance, the (spin) density response function and the (spin) current response function:

- The linear response, low-temperature conductance is computed with equation (3.23), $G_{qp} = G_0 \overline{T}_{qp}$.

- The (charge) density response function calculates the electron density at each site i of the scattering region, n_i, per unit energy or bias, V_b, due to the incoming WFs of lead p:

$$n_{p,i} = \frac{\delta n_i}{\delta V_b} = \sum_n^{M_p} {\psi^S_{n,p,i}}^\dagger \psi^S_{n,p,i}, \tag{3.49}$$

  where $\psi^S_{n,p,i}$ is the wave function of the scattering region at site i due to an incoming mode n. We can also introduce the spin density response function as

$$s^\alpha_{p,i} = \frac{\delta s^\alpha_i}{\delta V_b} = \sum_n^{M_p} {\psi^S_{n,p,i}}^\dagger s_\alpha \psi^S_{n,p,i}, \tag{3.50}$$

  with s^α_i being the spin density at site i and s_α once again the Pauli matrix with $\alpha = x, y, z$. We note that this quantity is not restricted to be a spin density, but rather the density of the degree of freedom described by the Pauli matrix.

- The (charge) current response function computes the local or bond current (i.e. between two sites i and j) per unit energy or bias due to the incoming WFs of lead p:

$$I_{c;p,ij} = \frac{\delta I_{c;ij}}{\delta V_b} = \mathrm{i} \sum_n^{M_p} \left({\psi^S_{n,p,j}}^\dagger H^\dagger_{ij} \psi^S_{n,p,i} - {\psi^S_{n,p,i}}^\dagger H_{ij} \psi^S_{n,p,j} \right), \tag{3.51}$$

where H_{ij} is the matrix element $\langle i|H|j\rangle$. Similarly, we can also define a spin current response function with the following expression:

$$I^{\alpha}_{s;p,ij} = \frac{\delta I^{\alpha}_{s,ij}}{\delta V_b} = \mathrm{i}\sum_{n}^{M_p} \left({\psi^S_{n,p,j}}^{\dagger} H^{\dagger}_{ij} s_\alpha \psi^S_{n,p,i} - {\psi^S_{n,p,i}}^{\dagger} s_\alpha H_{ij} \psi^S_{n,p,j} \right). \tag{3.52}$$

We note that both the charge and spin bond currents are vectorial quantities with the same dimension as the lattice (e.g. a 2D system will have an x and y component of the bond currents).

From these 4 response functions, we can also define the *total* densities and bond currents in the device. Taking the spin bond current as an example, but noting that the following expression applies to the other quantities as well, we can write

$$I^{\alpha}_{s;ij} = \sum_{p} I^{\alpha}_{s;p,ij} V_p, \tag{3.53}$$

where the sum runs over all leads p in the device and V_p is the voltage at that lead. This expression is very useful in multiterminal devices to understand how the current flows as a result of a specific set of current and voltage conditions in the leads, given by equation (3.30). For a two-terminal device, because one of the leads can be grounded, equation (3.52) is recovered.

Finally, Kwant can also compute other quantities such as the band structure of the leads using their translational symmetry. From that, the wave functions (u_n in equation (3.42)), momenta and velocities are obtained at a given energy. Moreover, Kwant can also add periodic boundary conditions in the transverse direction of the scattering region to calculate its 2D band structure.

3.3 Implementation of nonlocal devices in Kwant

In this section we will put together the notions of the previous sections to implement tight-binding models of nonlocal spin valves in Kwant. We can divide the process in four steps:

- Building a two-terminal device.
- Attachment of the ferromagnetic leads.
- Optimization of parameters and geometry.
- Tuning the transport regime: localized, diffusive, quasiballistic or ballistic.

In the following, we describe the physics and technical aspects of such steps, but before proceeding, let us standardize the notation that will be used for a NSV from this point on. The geometrical aspects and lengths, as well as the notation for the leads, are shown in Figure 3.14. The scattering region is depicted with a black lattice, the nonmagnetic leads with a red lattice, and the FM contacts, whose polarization is represented by arrows, with red squares positioned on top of the SR. Following the numbered notation of leads used in section 3.2.1, the leads N1, F1, F2 and N2 will be labeled as leads 1, 2, 3 and 4, respectively. In addition, we will name them according to their function, so leads 1, 2, 3 and 4 will be referred to as drain, injector, detector and reference, respectively.

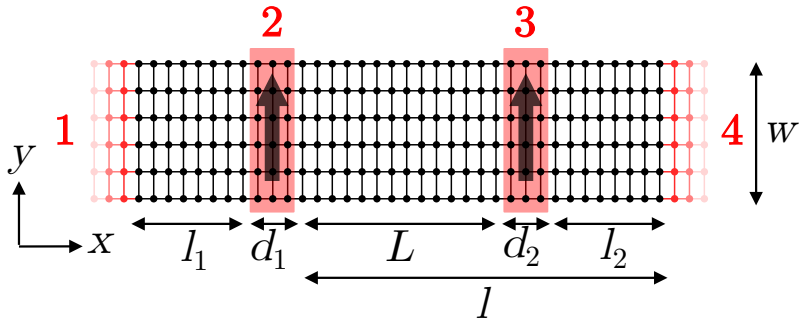

Figure 3.14: Schematics of the nonlocal spin valve. Black (red) regions denote the device (leads). Leads 1 and 4 are nonmagnetic, and leads 2 and 3 are ferromagnetic, with the polarization represented by the arrow direction. L is the injector-detector distance; w is the channel width; d_1 and d_2 are the width of leads 2 and 3, respectively; l_1 and l_2 are the separation between leads 1 and 2, and between 3 and 4, respectively; and $l = L + d_2 + l_2 \approx L + l_2$.

3.3.1 Building a two-terminal device

We can understand a NSV as a two-terminal device in which two extra FM leads are attached from the top. Thus, the first step is to ensure that the TB model is well implemented in a 2T setup so the transport in the NSV is correct. The TB model is implemented in the scattering region as described in section 3.2.3 and two leads are attached at opposite ends of the device, as shown in Figure 3.15. The TB of the leads does not need to be the same as the one in the SR as long as it has more modes than the SR for all energies. However, we choose to utilize the same TB as the scattering region because in this manner we can use the band dispersion of the leads that we obtain with Kwant to extract information about the scattering region (such as the number of propagating modes). Moreover, if the bands of the lead are faithful to the material we want to describe, the SR will then also be correctly modeled. To validate the correct implementation of the models, we compare Kwant's output to some known results. For graphene, we calculate the bands of the semi-infinite leads, as mentioned at the end of section 3.2.3, and compare them with the bands obtained from the tight-binding model of graphene nanoribbons (which gives the band structures of Figures 3.3(c) and 3.3(d)). For the TMD models, we calculate the 2D or bulk band structure of the scattering region and compare it with the bands obtained from equation (3.14).

Furthermore, these two contacts will play the role of the nonmagnetic contacts of the NSV. One could argue that this is not the most realistic setup for the NSV, as the NM contacts are also placed on top of the sample in experiments, as schematically shown in Figure 3.15. However, as explained in more detail later, using top leads generates additional contact resistances difficult to quantify. In addition, in this setup the scattering region ends sharply, causing backscattering of electrons and likely generating quantum interferences in the ballistic regime. Since we want to study the effects of the transition from diffusive to ballistic spin transport in the nonlocal resistance, we try to avoid any additional contribution to R_{nl} coming from unknown contact resistances and extra interference patterns. This could be examined later on when trying to replicate identical experimental conditions after understanding the main physical aspects.

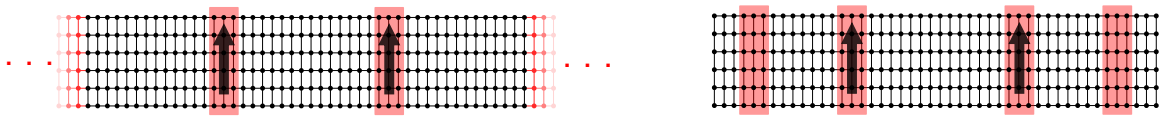

Figure 3.15: Two possible ways to attach the nonmagnetic leads to the scattering region. On the left, they are attached from the side of the sample, and on the right, they are attached from the top in the same way as the FM leads.

3.3.2 Attachment of the ferromagnetic leads

The most difficult technical aspect of building a NSV is the implementation of the ferromagnetic contacts. Because Kwant is very flexible, there are different ways to achieve this; here we describe the method used in this thesis. The implementation of FM leads consists of two parts: the modeling of the ferromagnetism and the attachment to the scattering region.

As far as the magnetism is concerned, rather than using a giant exchange field in the lead's Hamiltonian (as in real ferromagnets), a spin-dependent hopping, $t_\perp^s$, at the interface between the leads and the sample is used to filter a desired spin component. This means that the lead's Hamiltonian is not modified at all even though we are effectively modeling a FM contact. The form of this interfacial spin-dependent hopping is [94, 301]

$$t_\perp^s = \frac{1}{2} t_\perp (s_0 + P s_\alpha), \tag{3.54}$$

where s_0 is the identity matrix, s_α the α-spin Pauli matrix, $P \in [-1, 1]$ models the FM polarization and $t_\perp$ is the hopping amplitude. Using this method instead of applying a Zeeman field to the lead's Hamiltonian has the advantage that one can easily tune the polarization.

If $P = 1$ and $s_\alpha = s_z$, we obtain $t_\perp^s = \begin{pmatrix} t_\perp & 0 \\ 0 & 0 \end{pmatrix}$, showing that only spin-up electrons can transmit to this lead. Similarly, if $P = -1$, we revert the polarization and only spin-down electrons can flow through the interface: $t_\perp^s = \begin{pmatrix} 0 & 0 \\ 0 & t_\perp \end{pmatrix}$. Recalling equation (3.36), if both the injector and detector have $P = 1$, the transmission function will read $\overline{T}_{32} = \overline{T}_{32}^{\uparrow\uparrow}$. It is interesting to note that the transmission function from lead 4 to 2 is not exactly the same as the one from 2 to 4: the former has the form $\overline{T}_{24} = \overline{T}_{24}^{\uparrow\uparrow} + \overline{T}_{24}^{\uparrow\downarrow}$ whereas the latter is $\overline{T}_{42} = \overline{T}_{42}^{\uparrow\uparrow} + \overline{T}_{42}^{\downarrow\uparrow}$. For polarizations along x and y, the hopping acquires off-diagonal elements in spin space, indicating nonzero up-to-down and down-to-up transmission probabilities. This is expected since we use the z direction as the basis of the spin space, and hence x and y spins are a linear combination of z-up and z-down spins.

In regard to the attachment, similar to real devices, the FM leads are attached from the top. In this case, however, the FM leads are not connected to the SR, but instead to an interfacial layer placed above the SR, as illustrated in Figure 3.16. The reason for that is that when leads attach to the scattering region, they attach using the lead's hopping. Because at the SR-lead interface we need to define another hopping, equation (3.54), we can attach the lead to the interfacial layer and then manually define the spin-

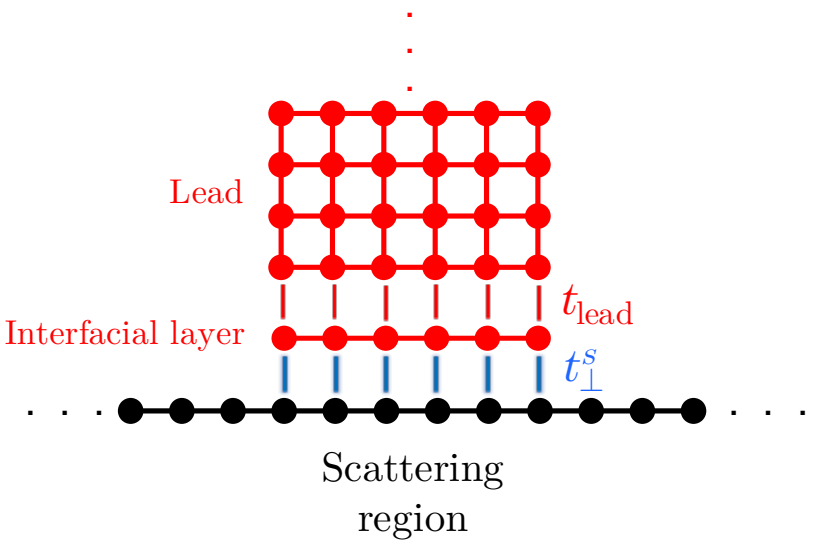

Figure 3.16: Schematic of the attachment of the FM lead to the scattering region. The lead attaches to an interfacial layer, whose coupling $t_{\perp}^{s}$ between the scattering region is spin-dependent.

dependent hopping from the layer to the SR. The hoppings within this interfacial layer and to the lead can be the same of those of the lead, so effectively this layer has the same physical behavior as the lead. However, within Kwant's classification, this layer belongs to the scattering region and not to the lead. This adds complexity to this implementation because while Kwant automatically connects a lead with the scattering region, it does not do that between two regions of the SR (the interfacial layer and the SR itself). To do so, the *kd*-tree algorithm from SciPy is employed, which searches the nearest sites of the SR for each site in the interfacial layer [94].

Next, we present a few tests to validate the correct implementation of the FM leads and the precession of spins due to the magnetic field. To that end, we compute the transmissions between the injector and detector and the nonlocal resistance for different combinations of FM polarization and magnetic fields, without disorder, in a graphene NSV. Since the purpose of these simulations is just to test the implementation, unrealistically small sizes (and hence unrealistically large magnetic fields) have been used to speed up the calculation.

Figure 3.17 displays the total and spin-dependent transmission functions (recall equation (3.36)) between leads 2 and 3 in two distinct situations: the lead polarization points along z while a finite magnetic field is applied along y, and the opposite case where the leads are polarized along y and the field has only a z component. Furthermore, both parallel and antiparallel magnetic configurations of the leads are presented. When spins are injected in the z direction, for parallel (antiparallel) alignment we expect only $\overline{T}_{32}^{\uparrow\uparrow}$

($\overline{T}_{32}^{\downarrow\uparrow}$) to contribute to the total transmission. Indeed, Figures 3.17(a) and 3.17(b) show exactly that. In contrast, when the leads are y-polarized, the spin-dependent hopping (equation (3.54)) includes both diagonal and off-diagonal components, indicating that all spin-dependent transmission functions are responsible for the total transmission. In Figures 3.17(c) and 3.17(d) we observe exactly this, with all spin-dependent transmissions having the same value since there is not any spin mixing in the scattering region. Furthermore, the values of the transmission when changing from parallel alignment to antiparallel are correct: in the parallel configuration (Figures 3.17(a) and 3.17(c)), the transmission is maximum at $B = 0$, while it is completely 0 when the leads are antiparallel (Figures 3.17(b) and 3.17(d)).

To understand the trend of the transmission function with the magnetic field, it is necessary to know how many and which modes contribute to transport. Therefore, we plot in Figure 3.17(e) the band structure of lead 1, and since it has the same Hamiltonian as the scattering region, we are in fact plotting the energy dispersion that an infinite scattering region would have. The calculations are performed at $E = 1$ eV, thus only one mode with Fermi velocity v_{F} contributes to transport. Because only one mode is present and the transport is completely ballistic, it is reasonable to expect that the transmission will have a sine or cosine dependence with B as a consequence of a single coherent precession frequency. In fact, it is insightful to calculate the magnetic field needed for a state with constant velocity to precess 2π for a fixed length (in our case, the channel length L). Combining $|\omega| = \gamma B = \frac{g\mu_{\mathrm{B}}}{\hbar} B$, $\omega = 2\pi/T$ and $v = L/T$, we obtain

$$B_{2\pi} = \frac{2\pi\hbar v_{\mathrm{F}}}{g\mu_B L}. \tag{3.55}$$

Plugging in the channel length for the calculations ($L = 100$ nm) and the Fermi velocity of the mode at $E = 1$ eV, we obtain $B_{2\pi} = 295$ T, which agrees with the period displayed by the transmission functions in Figure 3.17. Importantly, at periods of $B = B_{2\pi}/2$, the spin has rotated 180° and hence the transmission becomes minimum (maximum) for the parallel (antiparallel) setup.

In addition to the transmission, the effect of the polarization and magnetic field is tested on the nonlocal resistance. Figure 3.18(a) shows Hanle curves for the same device and energy as in Figure 3.17 when the two FM are in parallel or antiparallel alignment, as well as when either electrode is set to be nonmagnetic. Both parallel and antiparallel cases present the same oscillatory period with magnetic field (marked with a vertical dashed line) as the transmission functions. Also, at zero field, the parallel alignment shows maximum R_{nl}, whereas for antiparallel leads the nonlocal resistance is minimum. Here, however, the minimum value is not 0 but has the same magnitude as the parallel

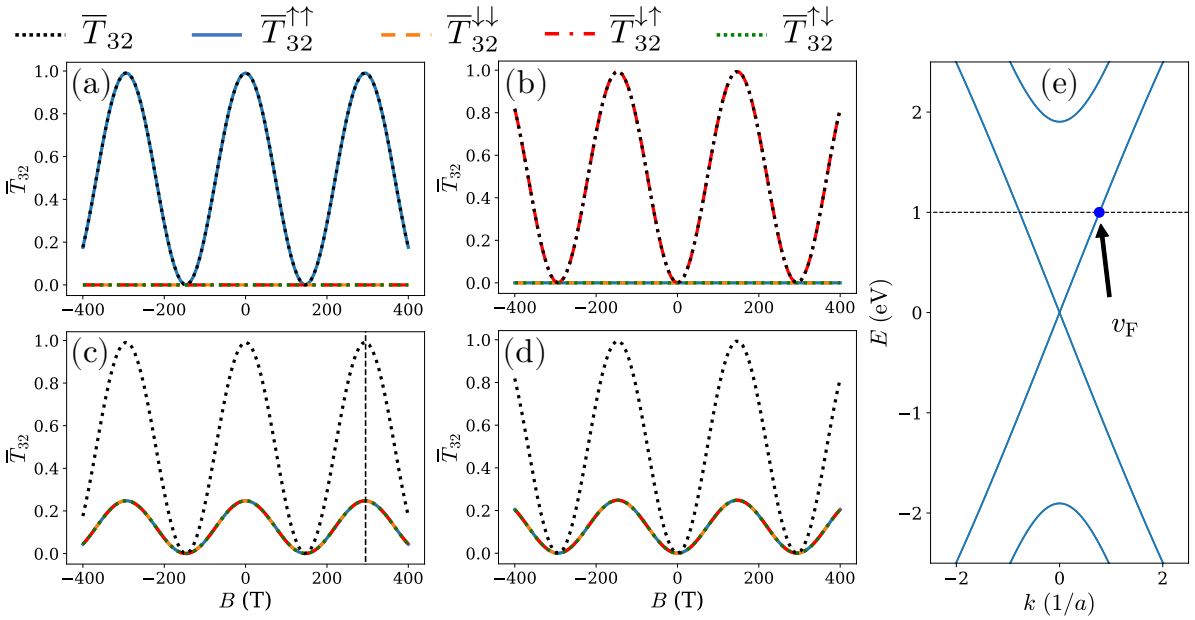

Figure 3.17: (a-d) Total and spin-dependent transmission functions from lead 2 to lead 3. In (a) and (b), the FM leads are z-polarized and the magnetic field is applied along y, while in (c) and (d) the FM leads are y-polarized and the magnetic field is applied along z. Panels (a) and (c) correspond to a parallel alignment of the leads, while (b) and (d) to an antiparallel configuration. (e) Band structure of a 5-aGNR; the dashed line indicates the energy at which the calculation is performed, and the blue dot the k-state carrying the current with Fermi velocity v_F. The vertical dashed line in (c) shows the magnetic field required for the k-state to rotate 2π for a fixed L. The device has the dimensions $w = 0.5$ nm, $d_1 = d_2 = 1$ nm, $l_1 = l_2 = 2$ nm and $L = 100$ nm.

case with a negative sign, in agreement with the theory of nonlocal detection explained in Chapter 2 (see equation (2.21)). The results change when one of the two electrodes is set to be nonmagnetic by setting $P = 0$ in equation (3.54). In either case, the nonlocal signal is 0 independently of the magnetic field, also in agreement with what is expected in a NSV.

A final remark about the magnetic field dependence is in order here. One has to be careful when the energy at which the nonlocal resistance is calculated is close to another subband, as illustrated in Figures 3.18(b) and 3.18(c). For small fields, the precession frequency is given by a single Fermi velocity as only band 1 in Figure 3.18(b) propagates. However, when the Zeeman splitting is large enough, one of the spin-split states of band 2 also adds contribution to the transport. As a consequence, the precession frequency varies due to different Fermi velocities and the magnitude of $R_{\rm nl}$ increases because there are more modes carrying the current.

We note that all these tests have been performed with a single transverse mode. For multi-mode transport, the qualitative results are similar but the effect of the magnetic

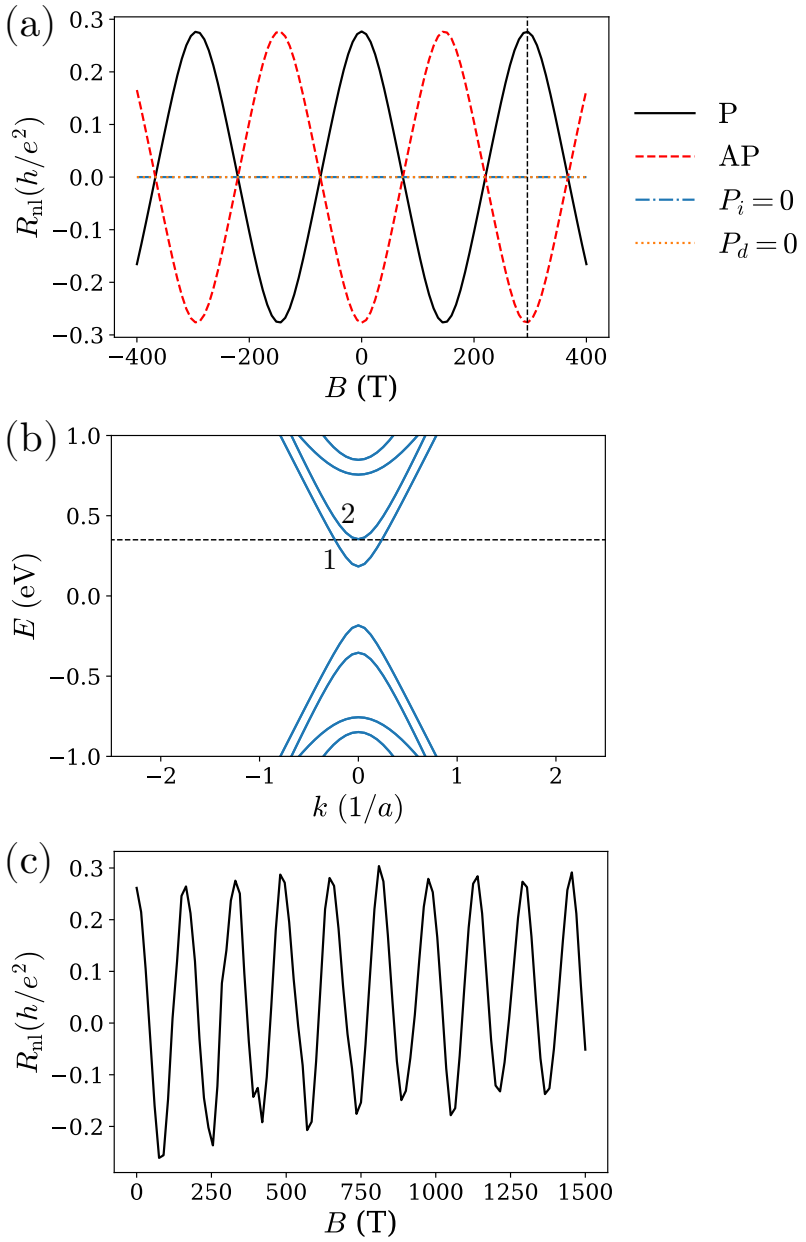

Figure 3.18: Hanle curves ($R_{\rm nl}$ vs B) for parallel (solid black) and antiparallel (dashed red) configuration of the FM electrodes, for the injector being nonmagnetic (dot-dashed blue) and for the detector being nonmagnetic (dotted orange). The energy and device geometry is the same as in Figure 3.17. The vertical dashed line shows the magnetic field required for the k-state to rotate 2π for a fixed L. (b) Band structure of a 25-aGNR; the dashed line indicates the energy at which the calculation is performed. The bands crossing the dashed line and right above it are labeled as bands 1 and 2, respectively. (c) Hanle curve of the 25-aGNR shown in (b). For low fields, only band 1 contributes to the nonlocal signal and precession, but at high fields, the Zeeman splitting lowers band 2 in energy and contributes as well to transport. As a result, the magnitude of $R_{\rm nl}$ does not present a single precession frequency.

field is more difficult to analyze because multiple precession frequencies are present, as just shown in this latter example. We will examine this case again in Chapter 4 with more realistic parameters.

3.3.3 Optimization of parameters and geometry

Once the physics of the NSV is well reproduced, the different parameters need to be optimized. These include the interfacial hopping (equation (3.54)) and the length scales in the device, namely, the device width, w; the width of the injector and detector, d_1 and d_2, respectively; the separation between the injector and the drain, l_1; the separation between the detector and the reference electrode, l_2; and the channel length, L. We also define the distance between the injector and the reference lead, $l = L + l_2$, which will prove useful in Chapter 4. Knowing the effects of all these parameters on the NSV is very important since it allows us to optimize the computational cost of the simulations and understand which features in the nonlocal signal are artifacts and which ones are comparable to experiments.

We begin with the strength ($t_\perp$) and polarization (P) of the interfacial hopping, which do not affect the computational time, but can have a great impact on the magnitude of the nonlocal resistance. Physically, the hopping amplitude $t_\perp$ can be related to the contact or interface resistance between the scattering region and the FM leads. It is well known that both the interface resistance and the polarization affect the value of $R_{\rm nl}$ [257, 258], and to avoid spin sinking by the FM leads, large contact resistances are needed. In this limit, one obtains the widely used formulas given by equations (2.21) and (2.22). In our case, we also want to prevent spin sinking, as we are interested in the spin relaxation in the nonmagnetic material. It turns out that using large contact resistance is not the only way to achieve so, but utilizing perfectly polarized ferromagnets (i.e. $P = \pm 1$) also allows for a non-invasive effect of the FM leads [258]. The explicit effects of the interface resistance and FM polarization on the nonlocal resistance will be presented later in Chapter 4 and Appendix A, where we extend equations (2.21) and (2.22) using less restrictive boundary conditions in solving the spin diffusion equations. Here, we show the presence or absence of spin sinking in a NSV by calculating the bond spin current with different values of $t_\perp$ and P. This visual and direct calculation will aid us in choosing the correct values of $t_\perp$ and P to be used in modeling NSV.

Figure 3.19 displays the total charge and spin bond currents flowing in a clean graphene NSV calculated with equation (3.53), in addition to a sketch of the geometry of the NSV. We performed 4 calculations with large and small values of $t_\perp$ and P, namely, $t_\perp = t$ and $t_\perp = t/10$ (with t being the graphene nearest-neighbor hopping, see equation (3.5)) and $P = 1$ and $P = 0.4$. It is seen that the charge current flows

only in the left side of the device (in agreement with the theory of NSV, see Chapter 2), between the injector and the drain electrodes. This result is found to be independent of the parameters used. On the other hand, the bond spin current does depend on the parameters, and flows from the injector to both left and right ends of the device. It can be seen that when the polarization is perfect, $P = 1$, the magnitude of $t_\perp$ does not qualitatively change the flow of the spin current. In contrast, when $P = 0.4$, only when we select a large interface resistance (i.e. a small interfacial hopping), do the spins reach all the way to lead 4. When the hopping is large, the spin current ends at the detector, indicating that spin sinking is taking place.

Based on these results, the most convenient choice of parameters is a small hopping and a large polarization. However, we also found that the shape of the Hanle curve was sometimes sensitive to the value of $t_\perp$. For the graphene tight-binding model, if $t_\perp$ was too small, the nonlocal resistance was suppressed while $t_\perp = t$ and $t_\perp = t/10$ gave similar results. On the other hand, for the TMD model, larger values of hopping suppressed the signal. Therefore, after some numerical convergence tests, we chose $t_\perp = t$ and $t_\perp = 25$ meV (smaller than the other hoppings, see Table 3.1) for graphene and TMDs, respectively.

Next, we describe the impact of each length scale on both the computation time and their physical implications for spin transport in a NSV. Regarding the physical effects, the width of the device mainly varies the number of modes in the scattering region for a fixed energy. As will be explained below, a wider device is desired as it allows one to obtain diffusive transport for a larger range of distances, in contrast to narrow channels where electrons transition almost directly from ballistic to localized transport. The width also changes the number of modes in the leads, although this does not matter substantially because the only requirement is that they possess an equal or greater number of modes than the scattering region, and this is always accomplished[3]. The distances d_1 and d_2, in addition to also modifying the number of modes in leads 2 and 3, can have a spurious effect on the shape of the Hanle signal if they are large enough. Both the injection and detection of spins occur at the entire surface beneath these contacts. This means that if the magnetic field is strong enough so the spins precess considerably within a length $\sim d_{1,2}$, the injected or detected spins will not present a single polarization but rather a distribution. Consequently, the magnitude of the nonlocal signal is suppressed, in agreement with other theoretical works [301]. The different lengths of the device (L, l_1 and l_2) determine how much distance the electrons and spins propagate. Section 3.3.4 explains how the variation of these parameters can be utilized to choose the transport

[3]Because leads 1 and 4 have the same band structure as the SR, and leads 2 and 3 have a larger unit cell than that from leads 1 and 4, resulting in a larger number of modes.

regime. In practice, however, only L is varied because l_1 and l_2 can have spurious effects on the nonlocal signal. This effect is actually not trivial and will be revisited in detail in Chapter 4.

In regards to the scaling of the computation time with the different length scales in the system (see Figure 3.14), w, d_1 and d_2 are the lengths that scale less efficiently. This is because by increasing w, both the scattering region and the unit cells of all leads increase, resulting in a larger size of the matrices in equation (3.46). The scaling is particularly bad

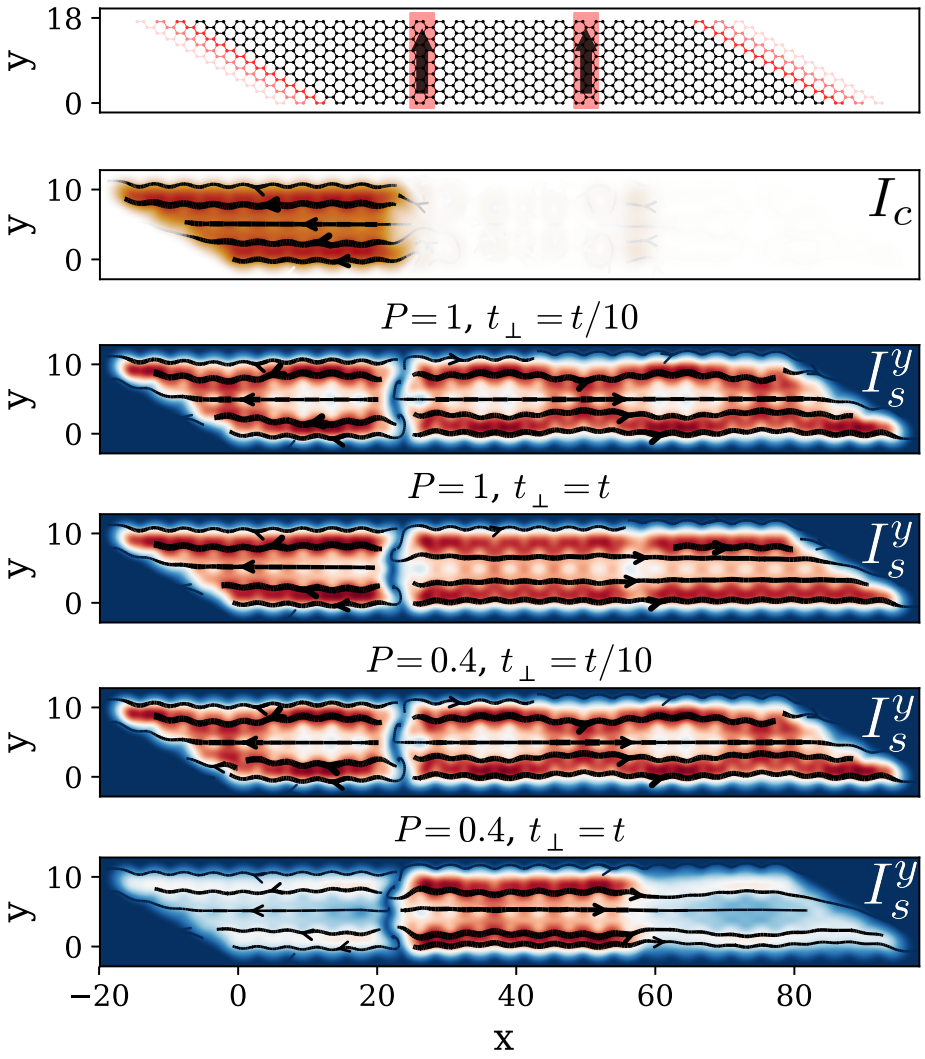

Figure 3.19: Charge and spin bond currents in a 15-aGNR NSV. From top to bottom: schematic of the NSV geometry, total charge bond current (abbreviated as I_c) and total spin-y bond current (abbreviated as I_s^y) calculated with equation (3.53). The spin bond currents are computed with different values of injector and detector polarizations (P) and interfacial hopping ($t_\perp$). The arrows denote the direction of the current, and their thickness and the background color its magnitude: orange (white) and red (blue) show large (small) charge and spin currents, respectively.

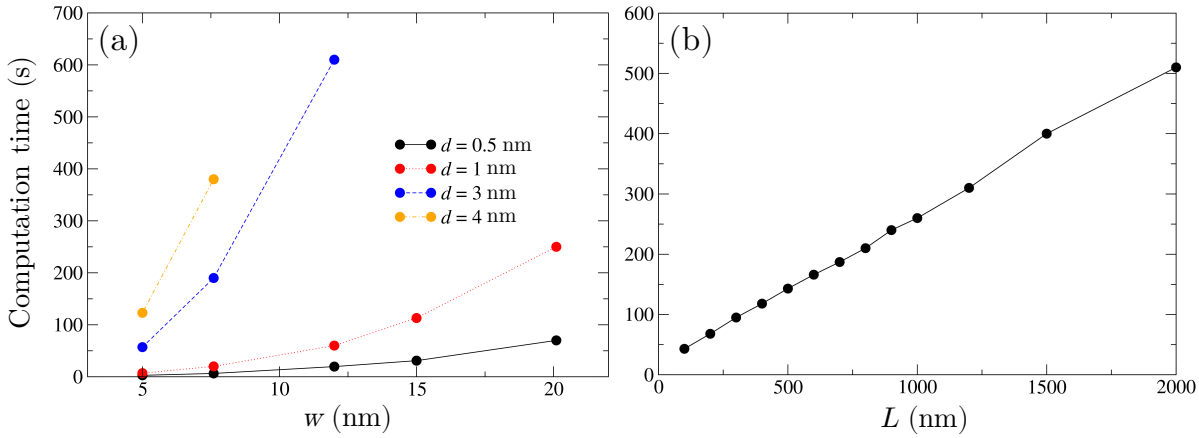

Figure 3.20: (a) Computation time of R_{nl} in a graphene NSV for a single energy and magnetic field versus device width w for different values of the FM leads' width ($d_1 = d_2 = d$). The other device parameters are $l_1 = l_2 = 4$ nm and $L = 20$ nm. (b) Computation time of R_{nl} for a single energy and magnetic field versus channel length L. The other device parameters are $l_1 = l_2 = 10$ nm, $d_1 = d_2 = 1$ nm and $w = 7.6$ nm.

for the FM leads, since their unit cell is proportional to $wd_{1,2}$ due to their rectangular cross section. In Figure 3.20(a), we present an example of how the computation time scales with w for fixed $d_1 = d_2 = d$. The important conclusion is the fact that if we want to simulate a wide NSV, the FM leads need to be extremely narrow; otherwise the cost becomes prohibitive very fast. Fortunately, the same conclusion about d_1 and d_2 was found above when discussing the physical implications of varying the FM width. On the other hand, the scaling of L is more favorable, as expected since new orbitals are added only to the scattering region whereas the leads are left unaffected. As expected from a Landauer-Büttiker calculation, the increase of computation time with L is linear, and is shown in Figure 3.20(b). A similar trend was found for l_1 and l_2, also expected since these parameters just increase the total length of the device.

3.3.4 Tuning the transport regime

After the simulations of NSVs are physically correct and can be performed with a reasonable amount of time, the final aspect is to tune the regime of charge and spin transport, that is, localized, diffusive, quasiballistic or ballistic. Being in one regime or another is dictated by the relative values of the mean free path (l_e), localization length (l_{loc}) [2, 8] and the dimensions of the device. Both l_e and l_{loc} depend on the energy, device width (both quantities also affect the number of modes) and strength and type of disorder [166].

When a given length x is larger than l_{loc}, the electrical conductivity σ decays with increasing x, with a functional form that depends on the type of localization [70, 78]. On the opposite end of the spectrum, when $l_e \gg x$, that is, electrons have barely scattered,

the transport is ballistic. In this case, the conductivity increases linearly with length. On the other hand, if $l_e \ll x < l_{\text{loc}}$, there are many scattering events and the transport is diffusive. In this situation, the conductivity is independent of x and is related to the conductance G through the typical textbook formula $G = \sigma \frac{w}{x}$, with w being the cross section or width of a three-dimensional (3D) or 2D conductor, respectively [54, 78]. The transition between ballistic to diffusive is continuous and smooth, and therefore when $l_e \sim x$ a distinct qualitative regime, dubbed quasiballistic transport, occurs in which some scattering has taken place. The conductance, on the other hand, can be described by the formula $G = \frac{M}{1+x/l_e} G_0$ [19, 78].

These four regimes are depicted in Figure 3.21, where σ as a function of the system length is plotted. The plot shows the linear, constant and decay of σ with increasing length. Such a plot is very convenient as one can visually tell the range in which the transport is diffusive just by looking at the conductivity plateau. From a 2T conductance simulation with varying channel length, the conductivity is obtained as $\sigma = G_{2\text{T}} \frac{x}{w}$ [248].

Very importantly, in NSVs there are several length scales, as shown in Figure 3.14, comprising the distance between each pair of leads. This might make achieving the diffusive regime for the whole device complicated. If the window of diffusive regime is not very large, it could happen that from the injector to drain the transport is quasiballstic, diffu-

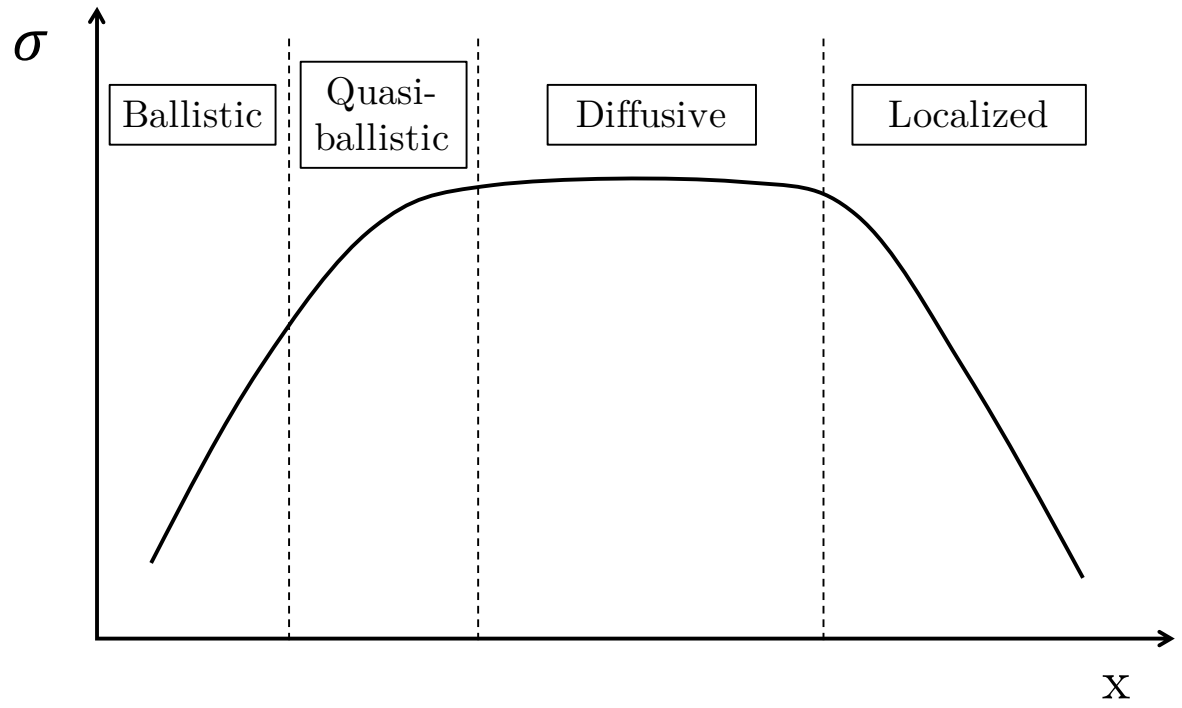

Figure 3.21: Schematic dependence of the conductivity σ as a function of a system's length for a fixed strength of disorder (i.e. mean free path and localization length).

sive from injector to detector, and localized from drain to the reference lead. Therefore, the task here is to maximize the "diffusive window" by varying the energy, device width and Anderson strength. However, a few aspects need to be considered. For instance, increasing w usually helps in obtaining a larger range of diffusive transport (as it more closely resembles a 2D system), but this comes at the expenses of a higher computational cost. Also, the energy dependence of l_e and l_{loc} depends on the energy dispersion of the transverse modes for a specific device width. In other words, the number of modes changes with energy and hence so do the transport properties (e.g. the more modes in the scattering region, the stronger the disorder effects), leading to an energy-dependent "diffusive window".

Finally, in addition to identifying the diffusive regime through a plateau of the conductivity, it is also useful to directly calculate the values of the mean free path and the localization length. For the former, the length dependence of the two-terminal conductance is fitted to [19, 78]

$$G_{2\mathrm{T}} = \frac{M l_e}{x} G_0, \tag{3.56}$$

but only in the lengths corresponding to a conductivity plateau of σ. Consequently, the plot of σ versus x needs to be done prior to fitting. Furthermore, we can also extract a precise value of the conductivity by fitting with the formula

$$G_{2\mathrm{T}} = \frac{\sigma w}{x}. \tag{3.57}$$

This that implies the following relationship holds: $M l_e = \sigma w$, with σ in units of G_0. To obtain l_{loc}, if the conductance decays exponentially with length, we can fit it to $\langle \ln(G_{2\mathrm{T}}/G_0) \rangle \sim -x/l_{\mathrm{loc}}$ [166], where $\langle \cdots \rangle$ denotes averaging over disorder configurations. Again, the fit must be done only in the region where localization occurs, that is, when the plateau of σ in Figure 3.21 ends. It is worthwhile to validate the fits by using the Thouless relationship [19, 49] that relates l_e and l_{loc} in quasi-1D systems. For time-reversal-symmetric systems and spin conservation, it reads $l_{\mathrm{loc}} = l_{\mathrm{e}} \left(\frac{\frac{M}{2}-1}{2} + 1 \right) = l_{\mathrm{e}} \left(\frac{M+2}{4} \right)$, whereas for time-reversal-symmetric systems with spin-mixing it takes the form $l_e(M-1)$ [19].

CHAPTER 4

NONLOCAL SPIN DYNAMICS IN THE CROSSOVER FROM DIFFUSIVE TO BALLISTIC TRANSPORT IN GRAPHENE

This Chapter focuses on the simulation of nonlocal spin transport in graphene NSVs using the Landauer-Büttiker formalism. We intend to provide a global picture of how the diffusive spin transport, typically studied in experiments, evolves towards a (quasi)ballistic regime when the material becomes cleaner.

4.1 Diffusive regime conditions

As explained in section 3.3.4, in order to determine the charge transport regime, the mean free path l_e and localization length l_{loc} need to be estimated. To that end, we calculate the two-terminal transmission of a device modeled by the graphene tight-binding model (equation (3.5)) with Anderson disorder (equation (3.8)). We choose a metallic armchair ribbon with width $w = 20.1$ nm (164-aGNR) so it resembles more the band structure of 2D grapehen [275], Anderson disorder of U=1.04 eV and Fermi level $E_{\mathrm{F}} = 0.4$ eV for which there are M=18 total propagating modes (i.e. 9 per spin). As shown in the following, these parameters allow to minimize l_e whereas l_{loc} remains the larger length scale of the system.

In Figure 4.1, we plot $\langle \ln(G_{2\mathrm{T}}/G_0) \rangle$ and $G_{2\mathrm{T}}$ versus channel length. From the first quantity we extract $l_{\mathrm{loc}} = 880$ nm by fitting with the downscaling law $\langle \ln(G_{2\mathrm{T}}/G_0) \rangle \sim -x/l_{\mathrm{loc}}$ for $x > 1000$ [166]. Here, the average has been performed over 200 disordered realizations. From the Thouless relationship $l_{\mathrm{loc}} = l_e \left(\frac{M+2}{4}\right)$, a mean free path of $l_e = 176$ nm is inferred. To further validate this approach, the 2T conductance in the diffusive regime is also fitted with the formula $G_{2\mathrm{T}} = e^2/h \times M l_e/x$ in the region $500 < x < 1000$, from which $l_e \sim 117$ nm, in good agreement with the estimation from the Thouless

relationship. The diffusive regime is also concomittant to a plateau of the conductivity [78] (see Figure 4.1 inset), computed using $\sigma = G_{2\mathrm{T}}\frac{x}{w}$, and which extends approximately from a few mean free paths till the localization length.

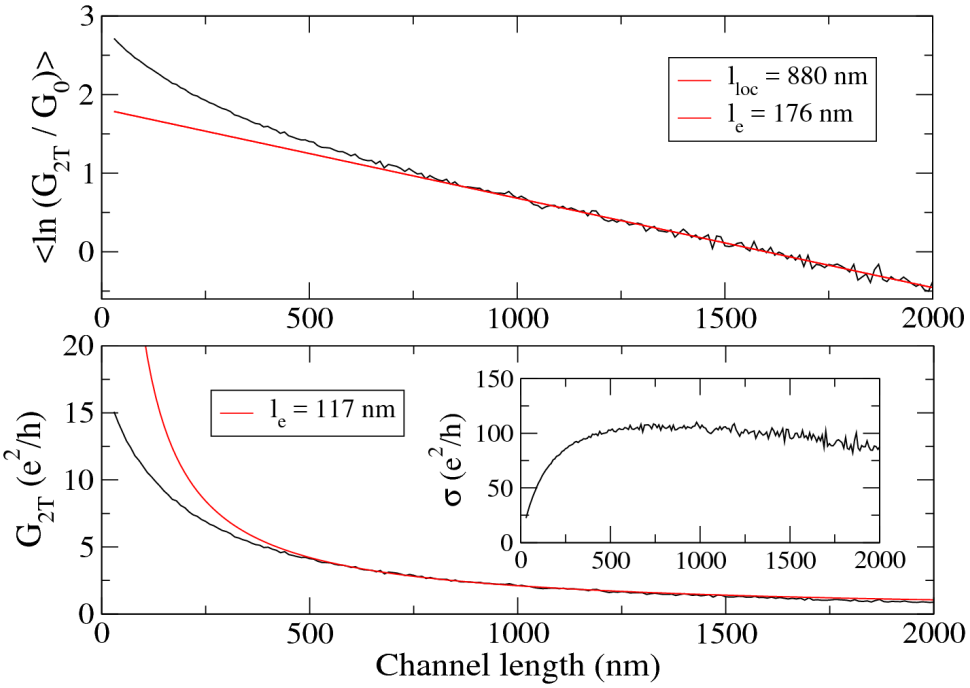

Figure 4.1: 2T conductance scaling of a graphene device (average made over 200 disorder configurations). Top panel shows the logarithmic fit to extract l_{loc} and l_e, while the bottom panel gives the direct fit of l_e. Inset: conductivity versus channel length.

4.2 Diffusive spin relaxation: new insights

We proceed to study the behavior of graphene NSVs using the Landauer-Büttiker formalism to the device setup in Figure 4.2. The graphene layer is described in a single-π-orbital tight-binding basis, with a Hamiltonian given by

$$\mathcal{H} = t\sum_{\langle i,j\rangle} c^{\dagger}_{i\eta}c_{j\eta} + \sum_{i} U_i c^{\dagger}_{i\eta}c_{i\eta} + \mu_{\mathrm{B}}\sum_{iss'} c^{\dagger}_{is}[\boldsymbol{s}_{\sigma}\cdot\boldsymbol{B}_i]_{ss'}c_{is'} + \sum_{iss'} c^{\dagger}_{is}[\boldsymbol{s}_{\sigma}\cdot\boldsymbol{J}_i]_{ss'}c_{is'}. \tag{4.1}$$

All the terms are described in section 3.1.2, except the last one, which is a random magnetic disorder mainly affecting the spin dynamics. It is defined as a magnetic exchange coupling with strength J and random orientation at each site i, $\boldsymbol{J}_i = J[\sin(\theta_i)\cos(\phi_i), \sin(\theta_i)\sin(\phi_i), \cos(\theta_i)]$, with θ and ϕ spherical angles and $\boldsymbol{s}_{\sigma}$ the spin Pauli matrices. In general, U is taken to be much larger than J, such that U dictates the charge transport regime, whereas the spin relaxation is driven by J. Finally, we note that orbital effects of the magnetic field are neglected, but these are not relevant in experimental conditions due to the low magnetic fields typically applied.

The calculation of R_{nl} is performed by evaluating all transmission probabilities between different leads, as described in section 3.2.1. Namely, we construct the conductance matrix $\mathbf{G}$ [54] and solve the linear system $\mathbf{I} = \mathbf{G}\cdot\mathbf{V}$, where $\mathbf{I}$ and $\mathbf{V}$ are vectors including

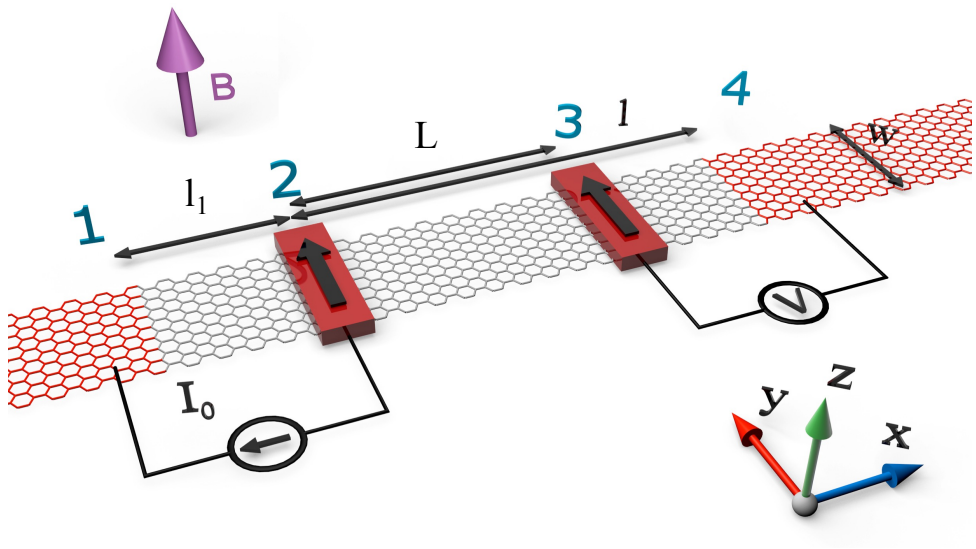

Figure 4.2: Sketch of the lateral nonlocal spin valve. Red (black) regions denote the contacts (sample). The injector and detector contacts, labeled 2 and 3 respectively, are ferromagnetic with their magnetization indicated by arrows. Contacts 1 and 4 represent the drain and reference electrodes, respectively.

the current and voltage conditions at each electrode. We fix a current I_0 from lead 2 (injector) to lead 1 (drain) while enforcing that no current flows in leads 3 (detector) and 4 (reference). This ensures zero charge current in the channel since any current going to the right from the injector will be compensated with an oppositely spin-polarized current injected by the reference lead. We also ground the drain ($V_1 = 0$) and solve the system to obtain the other voltages. The nonlocal resistance is then calculated as $R_{\rm nl} = (V_3 - V_4)/I_0$.

We first investigate spin dynamics in the diffusive regime of charge transport. We take $l_1 = 250$ nm and $l = 1000$ nm so that most of the transport occurs between l_e and $l_{\rm loc}$, and we compute $R_{\rm nl}$ vs. the channel length L at $B = 0$ for different magnetic disorder strengths J. Also, unless noted otherwise, the FM leads are fully polarized and with width $d_1 = d_2 = 1$ nm. The results are plotted in Figure 4.3. For large values of J, $R_{\rm nl}$ decays exponentially with channel length, as predicted by the typical spin diffusion formula with[1]:

$$R_{\rm nl} = \frac{P_i P_d}{2w\sigma}\mathrm{Re}\left\{\frac{e^{-L\sqrt{\frac{1}{\lambda_s^2} - i\frac{\omega_z}{D_s}}}}{\sqrt{\frac{1}{\lambda_s^2} - i\frac{\omega_z}{D_s}}}\right\}, \tag{4.2}$$

where $P_{\rm i}$ ($P_{\rm d}$) is the polarization of the FM injector (detector), $\kappa = \sqrt{\frac{1}{\lambda_s^2} - i\frac{\omega_z}{D_s}}$ with ω_z and D_s the Larmor spin precession frequency and the spin diffusion, respectively. However, as spin relaxation slows with decreasing J, the decay of $R_{\rm nl}$ becomes linear instead of exponential. Even for $J = 0$ (see Figure 4.4, solid line), corresponding to $\lambda_s \to \infty$, there is a loss of spin signal with channel length, a result not captured by equation (2.22). Conventional spin diffusion theory assumes that the spin accumulation vanishes at $x \to +\infty$, or at least at $x = l$ [67, 288]. However, this condition is violated for the lowest values of J in our simulations, and may also be the case in recent experiments for which λ_s reaches tens of μm [58].

To describe the proper length dependence of $R_{\rm nl}$, in Appendix A we solve the spin diffusion equations taking the full device geometry into account; not only are spins injected from lead 2, but leads 1 and 4 are explicitly included (lead 3 does not perturb the system). From this, $R_{\rm nl}$ becomes

$$R_{\rm nl} = \frac{P_i P_d}{2w\sigma}\mathrm{Re}\left\{\frac{[\beta\cosh(l_1\kappa) + 4\sinh(l_1\kappa)]\cdot[\beta\cosh(\kappa(L-l)) - 4\sinh(\kappa(L-l))]}{\kappa[4\beta\cosh((l_1+l)\kappa) + (8+\beta^2/2)\sinh((l_1+l)\kappa)]}\right\}, \tag{4.3}$$

where $\beta = R_{\rm c} w\sigma\kappa$ with $R_{\rm c}$ the contact resistance between leads 1 and 4 and graphene. In the case of perfectly transparent contacts, the interface resistance is not zero but dictated by the Sharvin resistance $R_S = h/(e^2 M)$ [29, 225]. If one takes the limits $\lambda_s \ll l_1, l$,

[1] This equation is the same as equation (2.21) in section 2.1.3, but is repeated here for clarity.

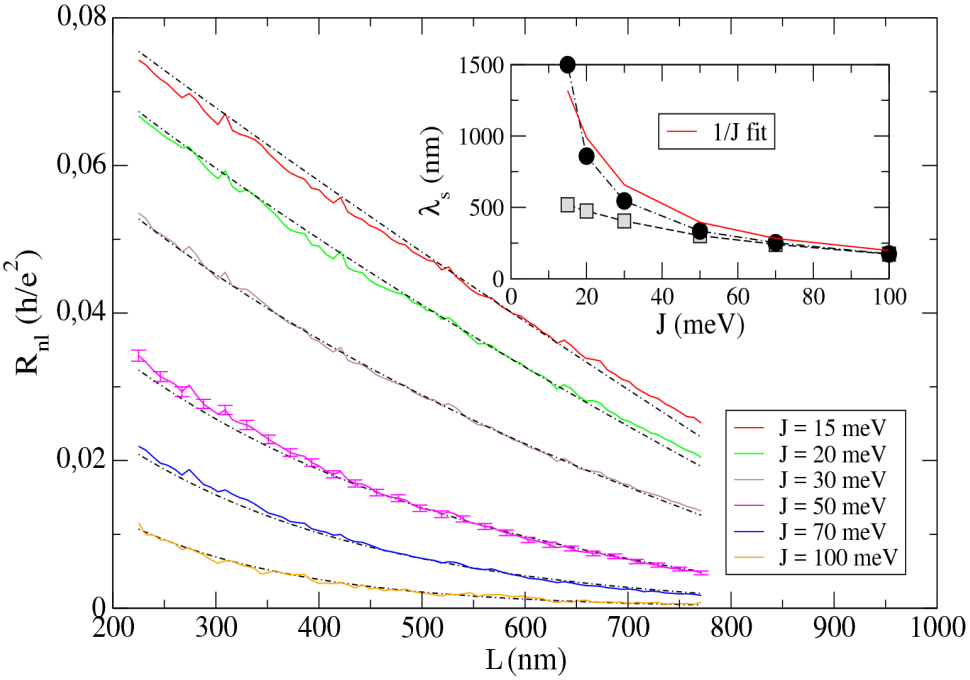

Figure 4.3: R_{nl} as a function of injector-detector distance for different strengths of magnetic disorder, with $l_e = 117$ nm. Error bars result from the averaging of several disorder configurations (> 130). All curves have similar error bars. Black dot-dashed lines are the fits using equation (4.3). Inset: comparison of λ_s extracted from equation (2.22) (gray squares) and equation (4.3) (black circles). The red line indicates $1/J$ scaling of λ_s (see Appendix B for details).

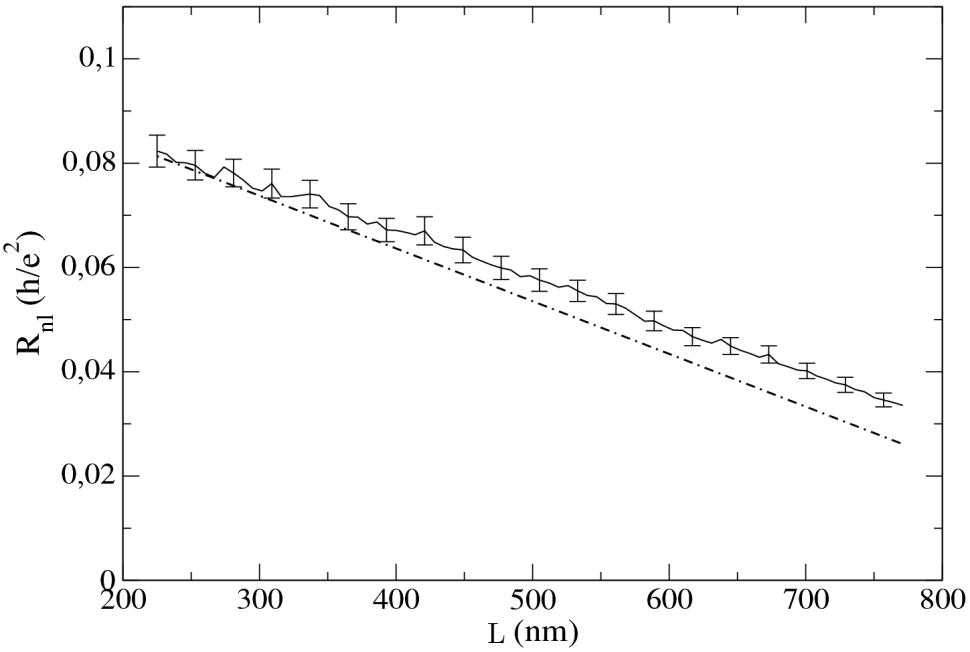

Figure 4.4: R_{nl} as a function of the channel length L for the case without spin relaxation $J = 0$ (solid line) and equation (4.4) (dot-dashed line), with $U = 1.04$ eV. Error bars result from the averaging of 50 disorder configurations.

equation (2.22) is recovered. Importantly, equation (4.3) becomes linear when $\lambda_s \to \infty$,

$$R_{\rm nl} = \frac{P_i P_d}{2w\sigma} \frac{(4R_{l_1} + R_{\rm c})(-4L + 4l + R_{\rm c} w\sigma)}{8R_{l_1} + 8R_l + 4R_{\rm c}}, \tag{4.4}$$

where $R_{l_1} = l_1/(w\sigma)$ and $R_l = l/(w\sigma)$ are the sheet resistance of the left and right device regions, respectively. The black dot-dashed lines in Figure 4.3 show the fits of the numerical results to equation (4.3), indicating that this expression is able to capture the scaling of $R_{\rm nl}$ for any value of J. Moreover, the analytical result of equation (4.4) agrees very well with the numerical calculation of $J = 0$, shown in Figure 4.4, without the need of any fitting parameter, suggesting that our formulas work well in such extreme limit.

Equation (4.4) shows that when $\lambda_s \geq l_1, l$ the nonlocal spin signal still decays with length. This decay is no longer related solely to spin relaxation but also to charge diffusion and the presence of the leads. Recall that $R_{\rm nl}$ depends on the conductance matrix $\mathbf{G}$, which consists of the transmission between *all* leads and the imposed current/voltage conditions. In the limit of long λ_s, the drain and reference electrodes act as spin sinks, fixing the value of $R_{\rm nl}$ in order to meet the conditions $I = I_0$ and $I = 0$ at leads 1 and 4, respectively. We note that this spin sinking effect occurs despite the absence of spin relaxation in the leads (they conserve spin). Rather it is the result of these leads absorbing and reinjecting spin current under the imposed boundary conditions, as the spins in the channel propagate under the influence of how the voltages and currents were set up. In other words, the condition of zero charge current in the channel forces the injection of spin-down current from lead 4 to 1 so that lead 2 can inject up-spins that diffuse towards lead 3. If lead 4 (1) is unable to inject (absorb) down-spins to (from) the system, up-spins will not be able to diffuse along the channel and $R_{\rm nl}$ will be suppressed. Therefore, lead 4 absorbs up-spins from the channel so that it can reinject down-spins; this affects the spin accumulation in the channel and reduces $R_{\rm nl}$. The fact that the spin sinking effect increases as L becomes longer is because the transmissions in the channel decay with length due to diffusive transport, incldluing the transmission from lead 4 to lead 1. This type of spin sinking contrasts with the contact-induced spin dephasing from FM leads, as mentioned in seciton 2.1.3, where it is the low contact resistance together with the low spin diffusion length in the ferromagnet that produces the spin sink [6, 120, 174].

Equation (4.4) also shows that at the reference electrode ($L = l$) $R_{\rm nl}$ is proportional to $R_{\rm c}$ to leading order. Thus, in the limit of weak spin relaxation a small $R_{\rm c}$ will suppress the nonlocal spin signal. Another consequence of long λ_s is that, as mentioned, the transmission between the drain and reference electrodes becomes crucial. In Figure 4.5(a) such effect is evidenced further by changing lead 1 from nonmagnetic to FM, which reduces $R_{\rm nl}$ by more than three orders of magnitude. This effect can be traced back to

the transmission, where the main difference between these two lead configurations is the reduction of the reference-drain transmission (T_{41}) when lead 1 becomes magnetic (see Figure 4.5(b)). This originates from the fact that now the reference contact 4 cannot inject down-spins because all other contacts are spin polarized in the opposite spin direction and cannot absorb them. This impacts directly on the amount of up-spins allowed to flow from the injector to the detector, as needs to be the same as the amount of down-spins being injected from lead 4. Consequently, the nonlocal signal drops dramatically. These results suggest not employing FM materials for leads 1 and 4 in experiments. We note that this calculation was done without spin mixing (i.e. $J = 0$) and perfectly polarized electrodes, and although finite spin relaxation or partially polarized leads will decrease such suppression of R_{nl} to a certain extent, these effects are likely to become relevant in ultraclean devices where the spin diffusion length is large.

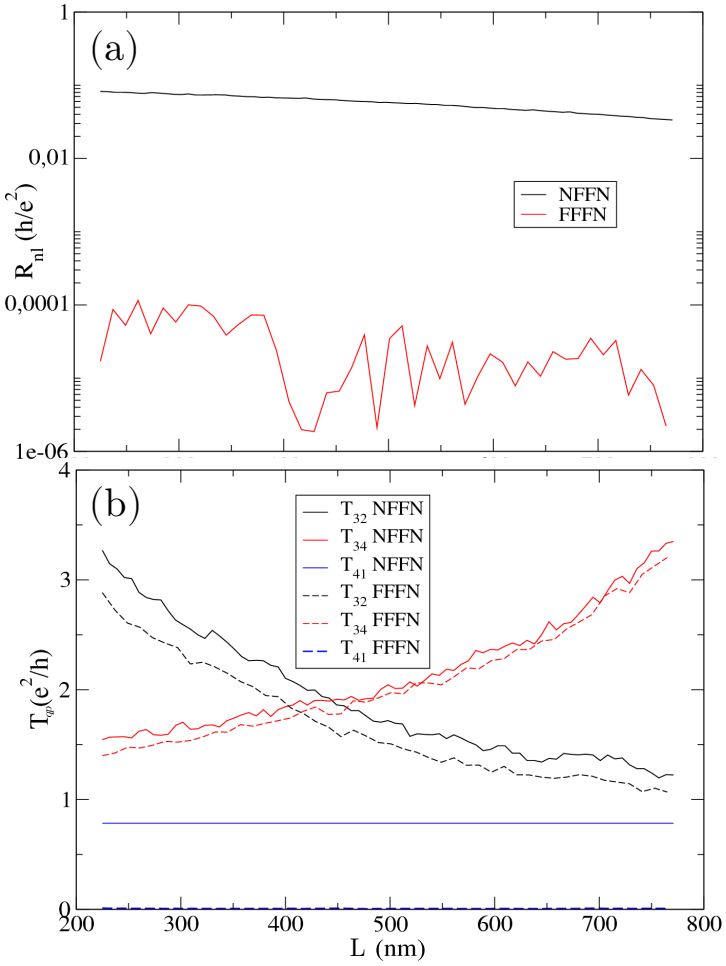

Figure 4.5: (a) R_{nl} for the normal NSV configuration (NFFN) and with setting the drain contact ferromagnetic (FFFN). (b) Transmission probability between leads as a function of the channel length L for such two lead configurations.

Another important consequence is that since equation (4.2) does not account for this extra decay induced by leads 1 and 4, this reduction is absorbed in the value of λ_s, which will be therefore underestimated by equation (4.2). This is shown in Figure 4.3 (inset), where λ_s is plotted vs. spin relaxation strength. The gray squares are extracted from fits to equation (4.2), while the black circles are from equation (4.3). The spin diffusion length is the same when $\lambda_s < l_1, l$ (large J), but for small J equation (4.2) significantly underestimates the value of λ_s. According to the theory of spin relaxation arising from exchange fluctuations (see Appendix B for details), λ_s should scale as $1/J$ [67], which is captured by the fits to equation (4.3).

We now extend the analysis to Hanle precession and plot $R_{\rm nl}$ vs. B in Figure 4.6 using a channel length of $L = 500$ nm. We note that large magnetic fields are required for computational convenience (our device is smaller than in experiments) but no spurious effect is introduced since the Zeeman splitting remains much smaller than the subband energy separation and orbital effects are excluded. The simulation data are fitted with equations (4.2) and (4.3) using $D_s = D_c = \frac{1}{2} v_{\rm F} l_e$ and the resulting λ_s are compared in Figure 4.6 (inset). Similar to Figure 4.3, in the limit of weak spin relaxation λ_s is

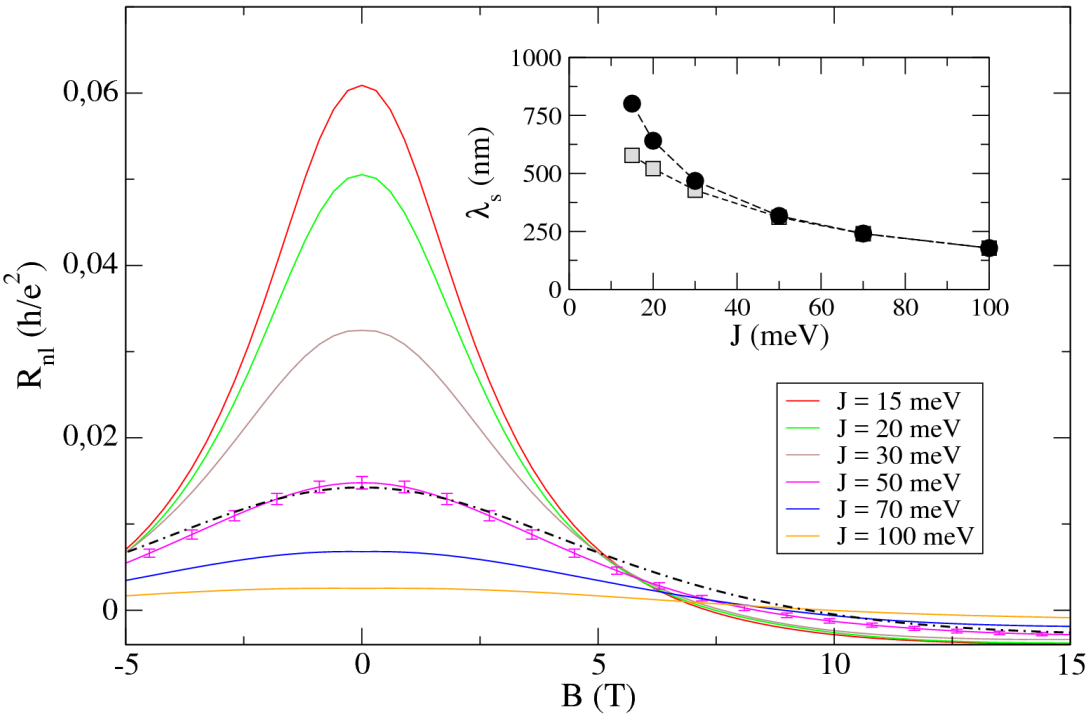

Figure 4.6: Hanle spin precession curves for different strengths of magnetic disorder, with $l_e = 117$ nm and $L = 500$ nm. Error bars result from the averaging of several disorder configurations (> 90). All curves have similar error bars. Black dot-dashed line is the fit using equation (4.3). Inset: comparison of λ_s extracted from equation (4.2) (gray squares) and equation (4.3) (black circles).

underestimated when using the conventional equation.

To estimate how strong the underestimation of λ_s may be in state-of-the-art devices, we calculate a Hanle curve with equation (4.3) using realistic parameters ($l_1 = 5$ μm, $l = 20$ μm, $L = 15$ μm, $\lambda_s = 10$ μm, $D_s = 0.05$ m^2/s) and fit it with equation (4.2). We obtain $\lambda_s = 7.26$ μm, about 25% less than the real value. More importantly, the spin lifetime ($\tau_s = \lambda_s^2/D_s$) is underestimated by nearly 100%; the real value is 2 ns while the fit gives 1.05 ns. These results thus call for a revised analysis of Hanle spin precession measurements taking into account the device geometry and our more general formula (equation (4.3)).

4.2.1 Effect of the injector and detector polarizations

To test how equation (4.3) holds when the FM polarization is finite, we simulate the length dependence of nonlocal spin valves keeping all parameters the same as in Figure 4.3 with $J = 70$ meV and varying both the injector and detector polarization from totally polarized (100%) to slightly polarized (20%). The results are shown in Figure 4.7.

One can observe that the smaller the polarization, the weaker is the nonlocal signal, fully consistent with the polarization entering as a prefactor in equation (4.3). We note that when we fit these curves (dot-dashed lines) with equation (4.3) using values of $P_\mathrm{i} = P_\mathrm{d} = 1, 0.8, 0.6, 0.4$ and 0.2, and when the polarization is small, equation (4.3)

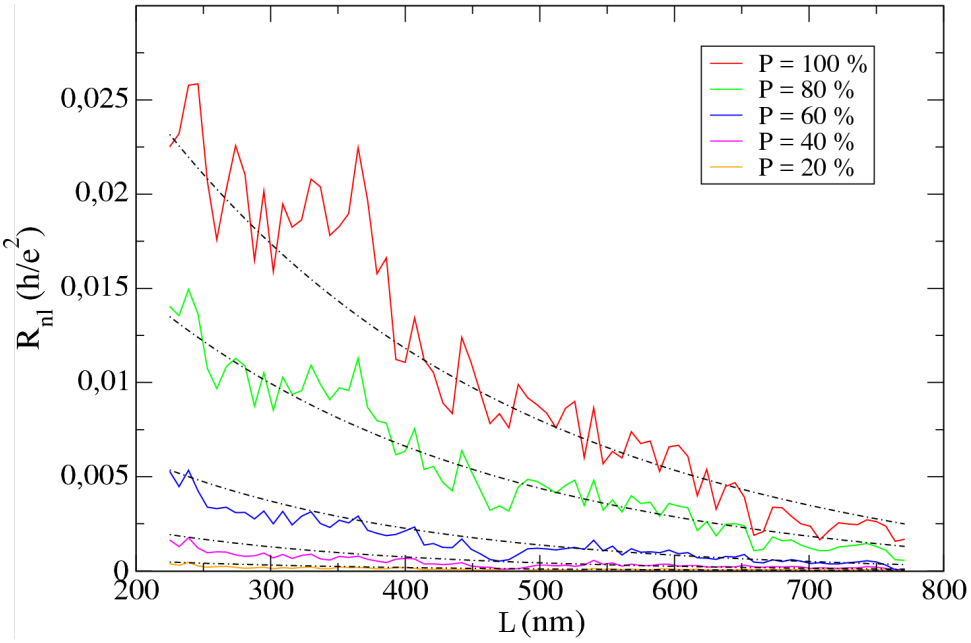

Figure 4.7: R_nl as a function of injector-detector distance for different injector and detector ferromagnetic polarization, with $l_e = 117$ nm and $J = 70$ meV. Black dot-dashed lines are the fits with equation (4.3).

clearly underestimates the spin diffusion length. The values are reported in Table 4.1.

This underestimation is expected because for low contact resistance between the electrodes and graphene, spin sinking occurs for small polarization of spin injector and detector [257, 258]. Our simulations are in the low contact resistance regime, since the used interfacial hopping is comparable to the in-plane graphene hopping. Noteworthy, this spin sinking reduces the total nonlocal spin signal, but occurs concurrently with the effects of magnetic disorder (J) and the nonmagnetic spin sinking of electrodes 1 and 4. Since equation (4.3) does not take into account the spin sinking of leads 2 and 3 (see Appendix A for details), this extra decay is not captured by the formula. Nevertheless, equation (4.3) can be applied in state-of-the-art experiments as they employ tunnel barriers that increase the contact resistance and prevent spin sinking.

Table 4.1: Extracted spin diffusion length for a given polarization of spin injector and detector.

Polarization (%)	λ_s (nm)
100	262
80	247
60	203
40	182
20	180

4.3 Quasiballistic and ballistic spin transport regimes

Finally, we examine the quasiballistic limit. When $l_e \sim L$, only a few scattering events occur during transport through the channel. This situation has been discussed for spin relaxation in ultraclean graphene [51], but little is known about its impact on Hanle measurements. We keep all simulation parameters the same as before, including the channel length $L = 500$ nm, and reduce the Anderson disorder to $U = 0.52$ eV, giving a mean free path $l_e \sim 500$ nm. The solid lines in Figure 4.8 show the Hanle curves for this quasiballistic regime, and the dashed lines show fits using equation (4.3). The behavior of $R_{\rm nl}$ is now substantially different, especially with respect to the dependence on B. The unit B_0 corresponds to the magnetic field needed for spin to precess 2π radians upon reaching the detector, $B_0 = \frac{2\pi v_{\rm F}^{\rm av}}{\gamma L}$, which is the multi-mode version of equation (3.55). Here, $\gamma = g\mu_{\rm B}/\hbar$ is the gyromagnetic ratio and $v_{\rm F}^{\rm av} = \sum_i^M v_{{\rm F},i}/M$ is the averaged Fermi velocity from all modes i with velocity $v_{{\rm F},i}$ at the Fermi level.

The first rotation of the spins occurs at $B_0 = 1$, but is followed by a dispersion of frequencies for larger B. This can be understood if we examine the origin of such oscillations. By performing a simulation in a purely ballistic regime, $U = J = 0$, we observe in Figure 4.8 (inset) that the main oscillation has the same period, but is

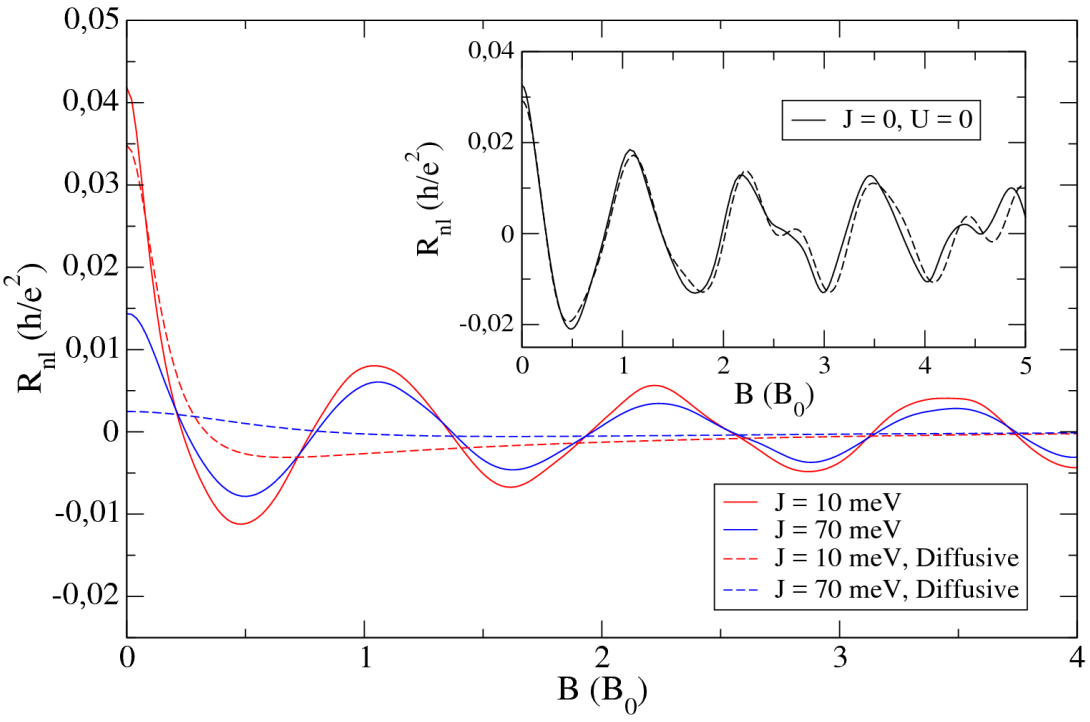

Figure 4.8: Hanle spin precession curves in the quasiballistic regime, with $l_e = 487$ nm and $L = 500$ nm. Solid lines correspond to simulations (averaged over 12 disorder configurations), while dashed lines are fits using equation (4.3). Inset: Case with $U = J = 0$, solid (dashed) line shows the simulation ($R_{\rm nl} \propto \sum_i^M \cos(\gamma BL/v_{{\rm F},i})$).

superimposed with other frequencies. This arises because the nonlocal signal is the sum of each propagating mode moving at a different velocity. To verify this, we follow Ref. [125] and express the nonlocal resistance as the sum of all contributions of electron spins i over all transport times t:

$$\begin{aligned} R_{\mathrm{nl}} &\propto \sum_{i}^{M} \int_{0}^{\infty} s_i(x=d,t)\mathrm{d}t = \\ &= \sum_{i}^{M} \int_{0}^{\infty} P_i(t)\cos\left(\gamma B t\right) e^{-t/\tau_s}\mathrm{d}t, \end{aligned} \tag{4.5}$$

where $P_i(t)$ is the probability that of an electron i injected at $x = 0$ reaches the detector at $x = L$ at time t. Importantly, the functional form of $P_i(t)$ depends on the transport regime. In the diffusive regime, it follows the normal distribution equation (2.23) [67,125], but in the purely ballistic regime (i.e. no scattering), we can write $P_i(t) = \delta(t - t_i)$, with $t_i = L/v_{F,i}$ and $v_{\mathrm{F},i}$ the Fermi velocity from mode i. Hence, the expression reads

$$\begin{aligned} R_{\mathrm{nl}} &\propto \sum_{i}^{M} \int_{0}^{\infty} \delta(t - t_i)\cos\left(\gamma B t\right)\mathrm{d}t = \\ &= \sum_{i}^{M} \int_{0}^{\infty} \delta(t - \frac{L}{v_{\mathrm{F},i}})\cos\left(\gamma B t\right)\mathrm{d}t = \qquad (4.6) \\ &= \sum_{i}^{M} \cos\left(\frac{\gamma B L}{v_{\mathrm{F},i}}\right). \qquad (4.7) \end{aligned}$$

In this way, by taking only the Fermi velocities of each mode of the system (computed with Kwant as $v_{\mathrm{F},i} = \frac{1}{\hbar}\frac{\partial E_n(k)}{k_x}$ for the modes in lead 1), the simulations are very well reproduced. From these results in the ballistic limit we can conclude that in the quasiballistic regime the scattering is weak enough for the precession to follow that of ballistic transport, but is also strong enough to average the beating pattern to one main frequency. This explains why neither equation (4.3) nor the sum of cosines is able to fit the quasiballistic Hanle curves. In fact, the difficulty in obtaining an analytical formula for the quasiballitic regime lies in the functional form of $P_i(t)$ which is no longer a Dirac delta nor a normal distribution. This difficulty in capturing the crossover from diffusive to ballistic transport in a single expression highlights the importance of brute force quantum simulations to understand such a regime.

Finally, in the limit of a 2D graphene flake, with most electrons moving at the same Fermi velocity, one would expect the signal to be determined by a single frequency. To observe this effect at low magnetic fields ($B \leq 0.5$ T), the channel length needs

to be $L \geq \frac{2\pi v_F}{\gamma B} \approx 50$ μm. We highlight the fact that this analysis can be applied to other materials as well; depending on whether there are electrons moving at the same or different Fermi velocities, one can expect single or multiple precession frequencies, respectively.

4.3.1 Detailed transition from diffusive to quasiballistic regime

Since the quasiballstic regime is a transition regime, it is important to quantify how the mean free path should compare with device geometry to identify the crossover from diffusive to the quasiballistic case. Therefore, we have performed additional simulations of Hanle curves with different values of disorder ranging between $U = 1.04$ eV (diffusive) and $U = 0.52$ eV (quasiballistic), while keeping all parameters the same as in Figures 4.6 and 4.8. We have used $U = 0.65, 0.78$ and 0.91 eV, which results in mean free paths of 312, 212 and 151 nm, respectively. We recall that the channel length is kept constant ($L = 500$ nm), as well as the magnetic disorder, for which we choose $J = 10$ meV (this value does not affect the transport regime, as seen by the same quasiballistic oscillations from both $J = 10$ meV and $J = 70$ meV in Figure 4.8).

We present these results in Figure 4.9, where we plot two Hanle curves which correspond to situations with varying mean free paths lying in between the values corresponding to Figures 4.6 and 4.8. We fit these curves with equation (4.3), although it is not able to correctly capture the oscillations of the signal for either of the curves. In the inset, we plot all Hanle curves simulated (including the ones from Figures 4.6 and 4.8). With decreasing mean free path, not only does the maximum of the oscillation begins to shift towards values $B < B_0$, indicating a transition from ballistic to diffusive regime, but also the amplitude of those oscillations decreases until they disappear for the case of $l_e = 117$ nm, which is in fact the same curve as in Figures 4.6. From these calculations, we can conclude that for our numerical model, once the mean free path becomes equal or larger than 1/3 the channel length, the spin dynamics enters a quasiballistic regime. Importantly, we recall that the quasiballistic regime defines the transition zone from a diffusive to a purely ballistic case, and thus different curves fall into this regime; for example the curves with $l_e = 151$ nm and $l_e = 487$ nm have their first precession at different B and with different amplitude, but both belong to this transition regime.

Finally, it is interesting to evaluate the effect of spin sinking produced by electrodes 1 and 4 in the ballistic regime. To that end, we simulate the length dependence of the nonlocal resistance for $J = 0$, as we did in Figure 4.4, but varying the Anderson disorder strength. We plot the results in Figure 4.10. Interestingly, we see that in all cases the decay is linear and that the spin sinking effect disappears with decreasing the disorder, up to a point where the signal is constant with length when the transport is purely ballistic

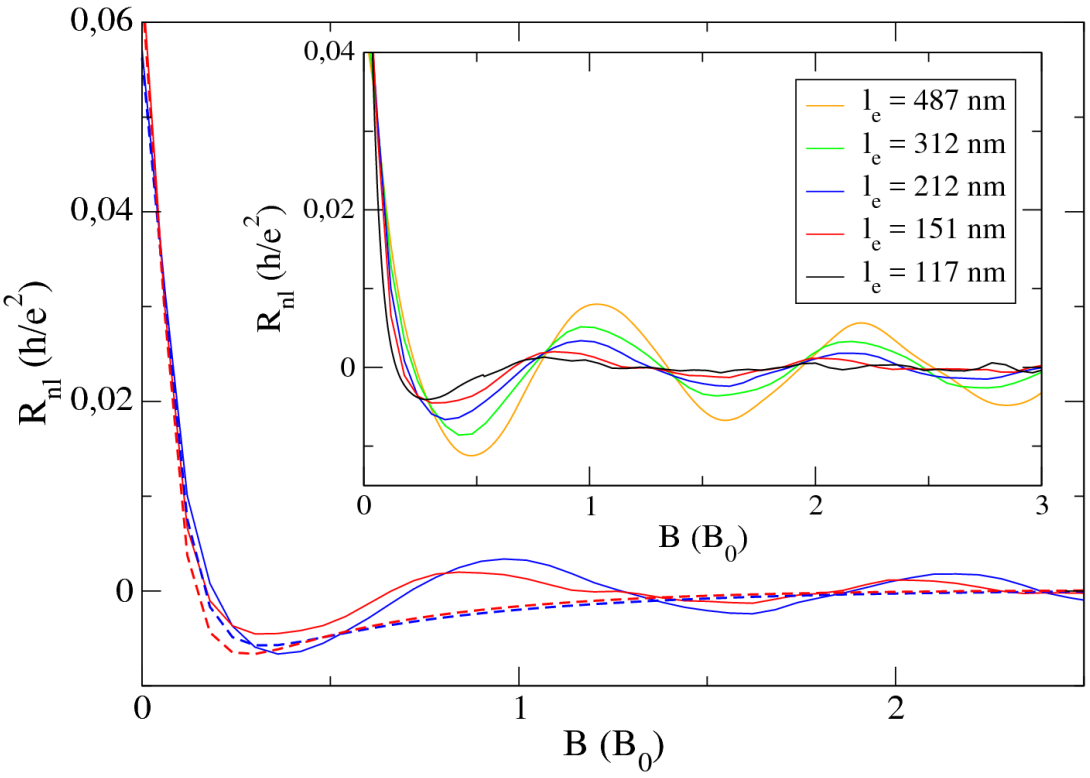

Figure 4.9: Hanle spin precession curves for different disorder strengths leading to different l_e, with $L = 500$ nm and $J = 10$ meV. Solid lines correspond to simulations (averaged over 25 disorder configurations), while dashed lines are fits using equation (4.3). Inset: more simulations with different mean free paths, showing the qualitative change of the Hanle curve when entering the quasiballistic regime. Black and orange lines correspond to the cases shown in Figures 4.6 and 4.8, respectively.

($U = 0$). Although equation (4.4) is valid only in the diffusive regime, it appears that the linear decay with channel length also occurs in the quasiballistic regime. Moreover, the fact that the spin sinking effect is absent in the ballistic regime illustrates once more that the origin of this effect resides in the transmission between leads. Now such transmissions do not depend nor decay with length, and therefore neither does the nonlocal signal.

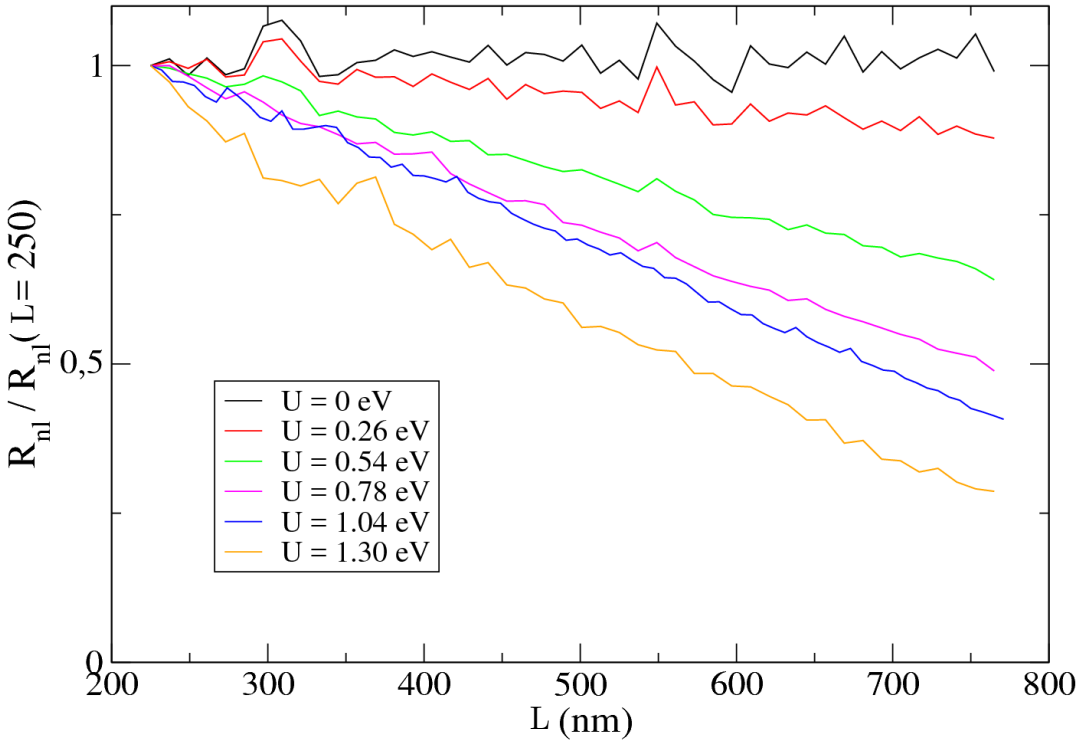

Figure 4.10: R_{nl} as a function of the channel length L for the case without spin relaxation $J = 0$ and varying the Anderson disorder strength. The results are averaged over 50 disorder configurations (all curves have similar error bars than the plot in Figure 4.4).

4.4 Conclusions

In conclusion, we have performed fully quantum simulations that provides a more global picture of nonlocal spin transport when the material quality drives the system towards the quasiballistic regime, as well as an extended theoretical frame to analyze systems with long spin diffusion lengths. In this limit, the drain and reference electrodes become the limiting factors, and one should aim for these to be nonmagnetic and optimize their contact resistance to reach the upper limit for spin information transfer. Beyond guiding future nonlocal spin transport measurements in graphene devices, the developed methods and findings should be also relevant for other types of two-dimensional materials and van der Waals heterostructures.

CHAPTER 5

SPIN DYNAMICS IN LOW-SYMMETRY TRANSITION METAL DICHALCOGENIDES

This chapter devotes to the spin dynamics of $MoTe_2$ and WTe_2, namely, spin relaxation, spin Hall effect (SHE) and quantum spin Hall effect (QSHE). The first two phenomena will be studied for $MoTe_2$ given the recent experimental findings concerning unconventional SHE and large spin diffusion lengths [227, 251]. On the other hand, since WTe_2 has received more attention in the topic of QSHE [41, 72, 129, 237, 264, 289], our simulations of this effect will focus on WTe_2.

5.1 Diffusive regime conditions

Similarly than in Chapter 4, we begin by determining the charge transport properties so we can study spin transport in the diffusive regime. We implement the real-space tight-binding model of $1T_d$-$MoTe_2$ on a rectangular lattice (equation (3.15)), add Anderson disorder (equation (3.16)), and calculate the two-terminal conductance, G_{2T}. We use the DFT values $a_x = 3.4607$ Å and $a_y = 6.3066$ Å for the lattice parameters. Unless stated otherwise, we chose the x axis as the semi-infinte transport direction so our system has a finite width w and length L as indicated in Figure 5.1.

The mean free path depends on the Anderson strength, U, but also on the energy, E, and we need to chose a wide enough device ($l_e << w$) so the system behaves more like a two-dimensional system. In addition, we found that upon varying the value of U, the mean free path varies much strongly than the spin diffusion length. This dictates our device lengths L on the order of the spin relaxation, and we tune U to achieve mean free paths much shorter than L. In this way, we can achieve diffusive transport for both charge ($l_e << L$) and spin. To that end, we use $U = 2$ eV and $w = 50$ nm.

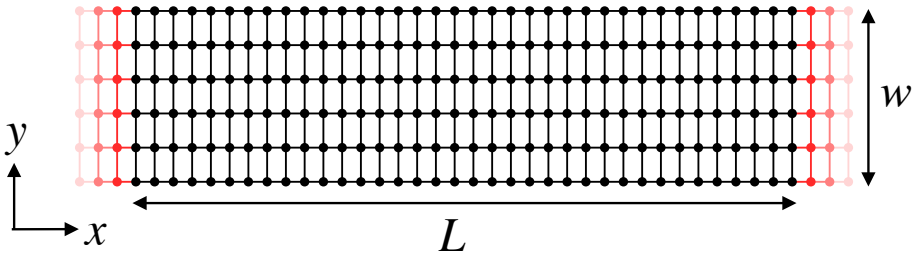

Figure 5.1: Schematics of the two-terminal device modeled with equation (3.15). Black (red) regions denote the scattering region (leads).

In contrast to Chapter 4, here we perform simulations at different energies. The range of energies studied are listed in Table 5.1, and they vary from slightly above the Fermi level until the bottom of the conduction band. In Figure 5.2 we plot the length dependence of the two-terminal conductance and conductivity for two representative energies: $E = 0$ and $E = -105$ meV. As seen from the conductivity plateaus and shaded regions, only the lengths between 25 and 55 nm are diffusive for the case $E = 0$, and between 45 and 90 nm for $E = -105$ meV. For all energies studied (see Table 5.1), the length at which the transport is diffusive varies slightly, but in general ranged from a few tens of nanometers to around 100 nm. In Table 5.1, we report the mean free paths for all energies, as well as the number of modes, M, the conductivity, σ, and the charge diffusion coefficient, D_c. Both the mean free path and the conductivity are extracted as explained in section 3.3.4 and the diffusion coefficient by $D_c = \frac{1}{2} v_{\mathrm{F}} l_e$, where v_{F} is the averaged Fermi velocity of all modes at that energy extracted from the band structure of the semi-infinite lead. For energies $E \leq -95$ meV, there are not many modes and therefore we removed the Sharvin resistance $\frac{h}{e^2 M}$ from $G_{2\mathrm{T}}$ to account properly for the bulk values of σ and l_e. As seen from Table 5.1 and Figure 5.2, the mean free path is much shorter than the crossover length to the diffusive transport and the plateau of conductivity just comprises a few tens of nanometers. This forces us identifying the "diffusive window" visually from Figure 5.2 instead of comparing l_e and l_{loc}.

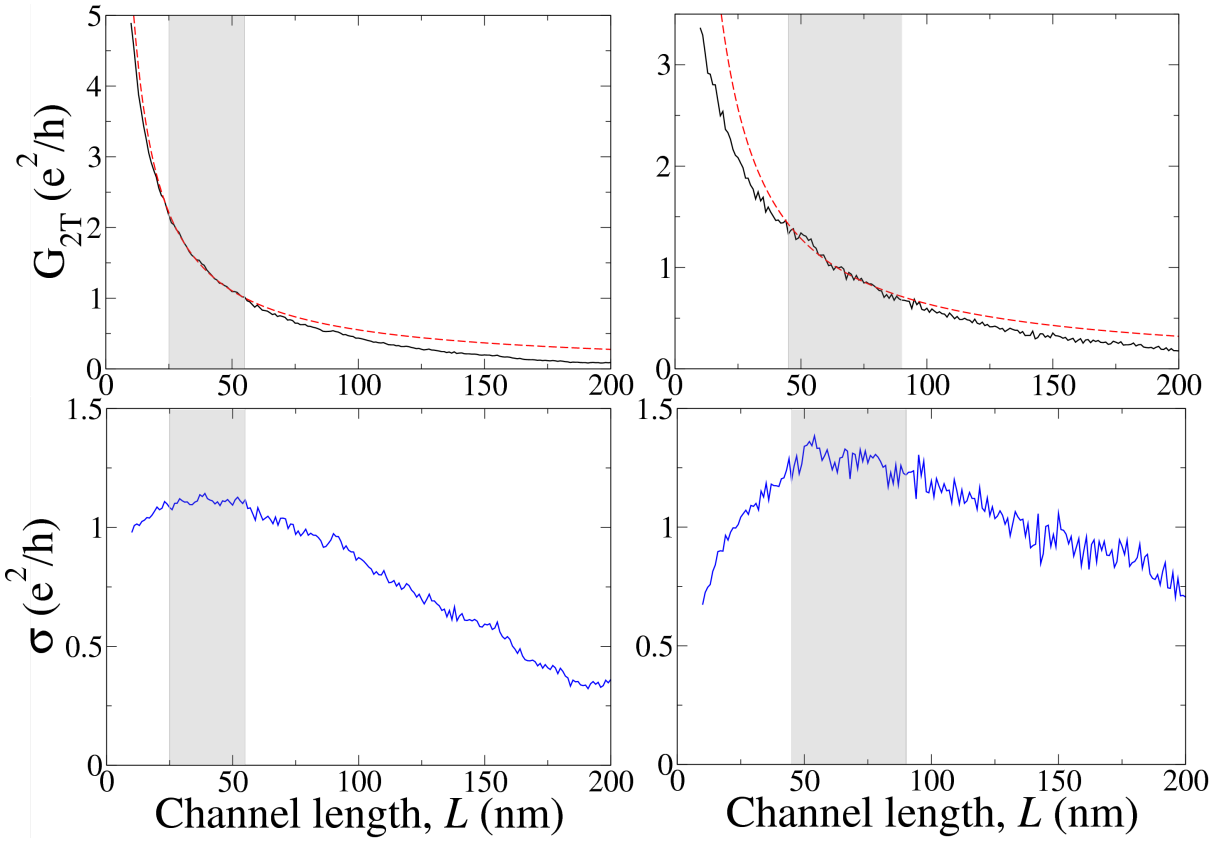

Figure 5.2: Two-terminal conductance G_{2T} (top) and electrical conductivity σ (bottom) as a function of channel length, L, of $1T_d$-$MoTe_2$ at $E = 0$ (left) and $E = -105$ meV (right). Dashed, red lines are fits with equation $G_{2T} = \frac{Ml_e}{x}G_0$ (see section 3.3.4). Shaded, gray regions denote the lengths at which the transport is diffusive, as shown by the conductivity plateaus.

Table 5.1: Values of the mean free path (l_e), number of modes in the system (M), electrical conductivity (σ) and diffusion coefficient (D_c) for different values of energy E (with respect to the Fermi level). The states at $E = -140$ meV lie in the bulk gap and arise due to the nontrivial band inversion of our model.

E (meV)	l_e (nm)	M	σ (e^2/h)	D_c (cm^2/s)
30	0.88	64	1.12	0.9
0	1.02	54	1.10	1.2
-30	1.55	42	1.30	1.5
-60	1.89	32	1.21	1.6
-80	3.00	22	1.32	2.3
-95	4.50	14	1.25	2.5
-100	6.90	10	1.38	3.4
-105	10.8	6	1.30	4.5
-110	15	4	1.20	4.8
-140	50	2	2	17

5.2 Spin relaxation

The energy dispersion and specially the spin texture will be key for the results of this Chapter. Therfore, in Figure 5.3 we plot part of the energy bands and spin texture presented earlier in section 3.1.2. The band structure near the Fermi level, E_{F}, is shown in Figure 4.2(a). The valence and conduction band extrema present a small splitting and occur at the time-reversal-symmetric Q and Q′ points. Figure 5.3(b) shows the spin texture at the Fermi level, $\langle s^{\alpha}\rangle_{E_{\mathrm{F}}}$, with two crucial observations: the existence of an approximate *persistent spin texture* (PST) through the whole Fermi contour [25,232,233] and canted spins with $\langle s^{y}\rangle_{E_{\mathrm{F}}} > \langle s^{z}\rangle_{E_{\mathrm{F}}} \gg \langle s^{x}\rangle_{E_{\mathrm{F}}}$, consistent with prior studies [236,295].

We simulate the nonlocal spin valve illustrated in the inset of Figure 5.4, where contacts 2 and 3 are ferromagnetic to allow injection and detection of spin-polarized currents [67, 125, 131]: FM electrode 2 injects a spin-polarized current I_0^{α} with spins polarized along $\alpha \in \{x, y, z\}$; this creates a spin accumulation that diffuses along the channel and is detected as a nonlocal voltage $V_{\mathrm{nl}} = V_3 - V_4$ at electrodes 3-4, located a distance L from the source and far from the path of charge current between electrodes 1-2. This effect is quantified by the nonlocal resistance $R_{\mathrm{nl}}^{\alpha} \equiv V_{\mathrm{nl}}/I_0^{\alpha}$ and the spin diffusion length for α-pointing spins, λ_s^{α}, is obtained from the decay of R_{nl}^{α} with L in the diffusive regime. As mentioned above, since the "diffusive window" change with energy, we had to choose different distances between leads for different energies. In general, $l_1 \sim 50$ nm and $l \sim 150$ nm, while the width of the FM leads is kept as narrow as possible with

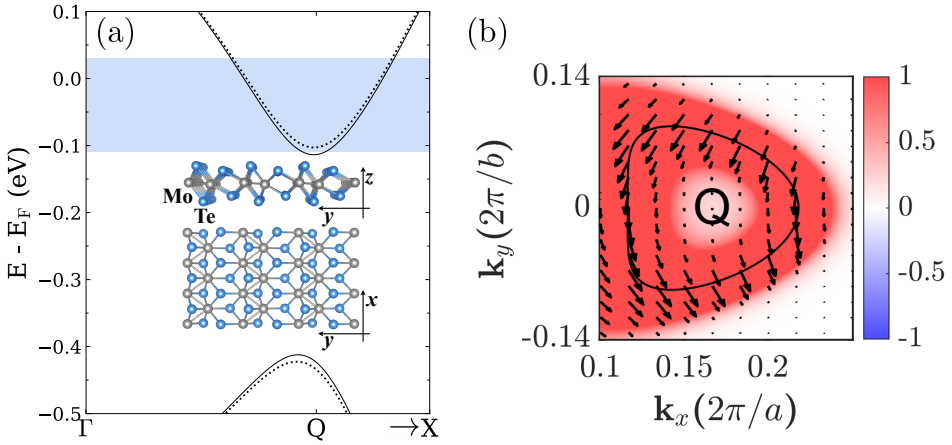

Figure 5.3: (a) Close-up of the bandstructure near E_{F} for a $1\mathrm{T_d}$-$MoTe_2$ monolayer (model of equation (3.15)). The blue-shaded region indicates the energy range covered in the spin transport calculations. Inset: monolayer crystal structure. (b) Spin texture of one of the bands of the electron pocket near Q at E_{F} (Fermi-broadened with $T = 300$ K); the solid line marks the Fermi contour, arrows depict the in-plane spin projection and the color indicates the spin projection along z.

$d_1 = d_2 = d = 1$ nm and with perfect polarization. Also, in the TMD tight-binding model (equation (3.15)) we do not need to add additional terms to produce spin relaxation, such as random magnetic disorder as we did for graphene in Chapter 4, since the intrinsic SOC of the TMD is large enough to produce significant spin relaxation.

Figure 5.4 shows $R_{\rm nl}^{\alpha}(L)$ for the three spin orientations at $E_{\rm F}$. We see clear differences in the magnitude of the nonlocal signals and their relaxation distances for different orientations of the injected spins, ranging from tens of nanometers to the sub-nanometer scale. By fitting the length dependence of $R_{\rm nl}^{\alpha}$ to equation (4.3) (dashed lines in Figure 4.3), we obtained $\lambda_s^y \approx 30$ nm and $\lambda_s^z \approx 10$ nm, while λ_s^x has a negligible value. The finite values are comparable with strong-SOC metals such as Pt, β-W or β-Ta [123, 244]. It is significant that the spin diffusion lengths follow the trend $\lambda_s^y > \lambda_s^z \gg \lambda_s^x$, in correspondence to that of the spin texture. The upper inset of Figure 5.4 shows that this hierarchy holds over the entire range of energies analyzed, from $E = 30$ meV to the band edge at ~ -110 meV. Both λ_s^y and λ_s^z increase about threefold as $E_{\rm F}$ moves towards the band

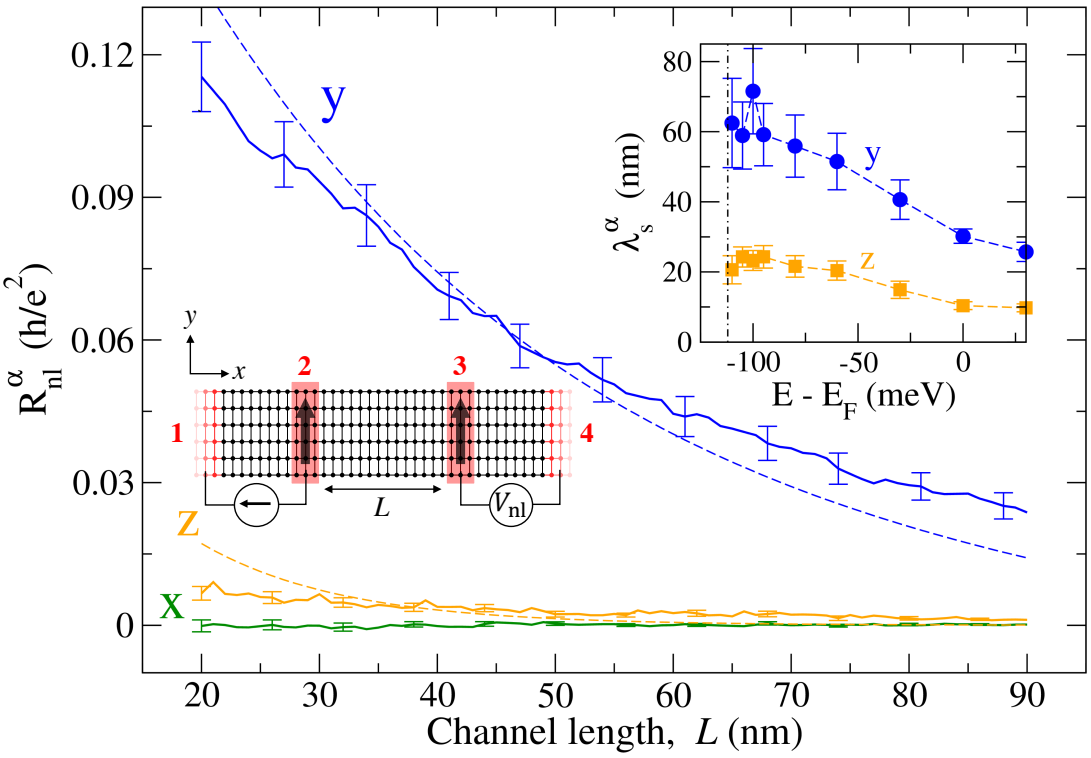

Figure 5.4: $R_{\rm nl}^{\alpha}$ (solid lines) against the channel length, L, for spins polarized along x, y and z. Error bars result from averaging over 150 disorder configurations ($w = 50$ nm). Dashed lines are fits to equation (4.3) in Chapter 4. Left inset: Scheme of the nonlocal spin valve. Black (red) regions denote the device (leads), with leads 2 and 3 being ferromagnetic. Current I_0^{α} flows from lead 2 to 1 and $V_{\rm nl}$ is measured between leads 3 and 4. Right inset: Energy dependence of $\lambda_s^{y,z}$. The dot-dashed line marks the conduction band minimum.

edge (dot-dashed line). Details of how the (persistent) spin texture impacts λ_s^α and its scaling with energy are discussed in the next section.

Once the energy lies in the gap and the transport is mediated by the topological edge states, the spin diffusion length is expected to diverge as these states are topologically protected against nonmagnetic disorder and they propagate ballistically without scattering. To explore this effect, we calculate how the nonlocal resistance varies with channel length for energies in the gap (shown as dashed lines in Figure 5.5), namely $E = -140$ meV and $E = -320$ meV. The former corresponds to an energy in the gap but relatively close to the conduction band, whereas the latter lies deep in the gap. Figure 5.6 shows the length dependence of R_{nl}^α for spins injected with polarization along x, y and z directions. For $E = -140$ meV (Figure 5.6(a)), the behaviour is similar to that of energies in the conduction band; the disorder is strong enough to perturb these edge states lying close to the bulk bands and inducing spin relaxation. Nevertheless, the obtained spin diffusion lengths are much larger than those reported for the conduction band: $\lambda_s^y = 156$ nm and $\lambda_s^z = 56$ nm. On the other hand, for $E = -320$ meV, the nonlocal resistance presents a length-independent value (i.e. no spin sinking is taking place), consistent with the onset of ballistic transport of topologically protected edge states.

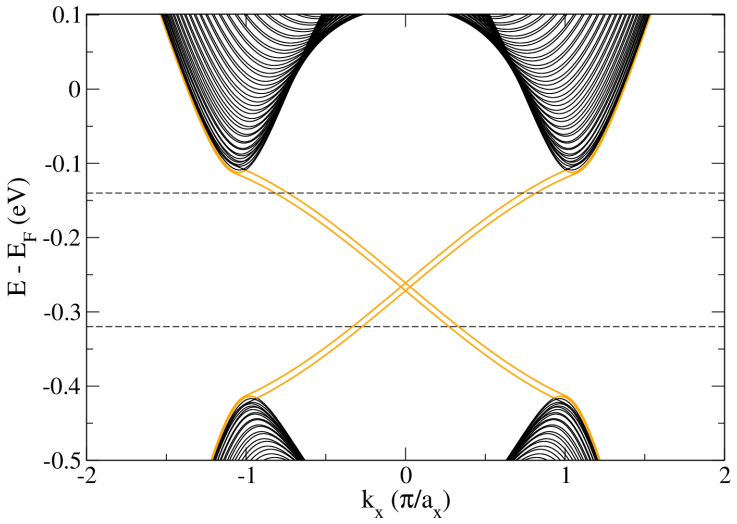

Figure 5.5: Band structure of a $1T_d$-$MoTe_2$ ribbon with finite width $w = 50$ nm in the y direction. Orange bands depict the topological edge states. Horizontal dashed lines mark the energies $E = -140$ meV and $E = -320$ meV.

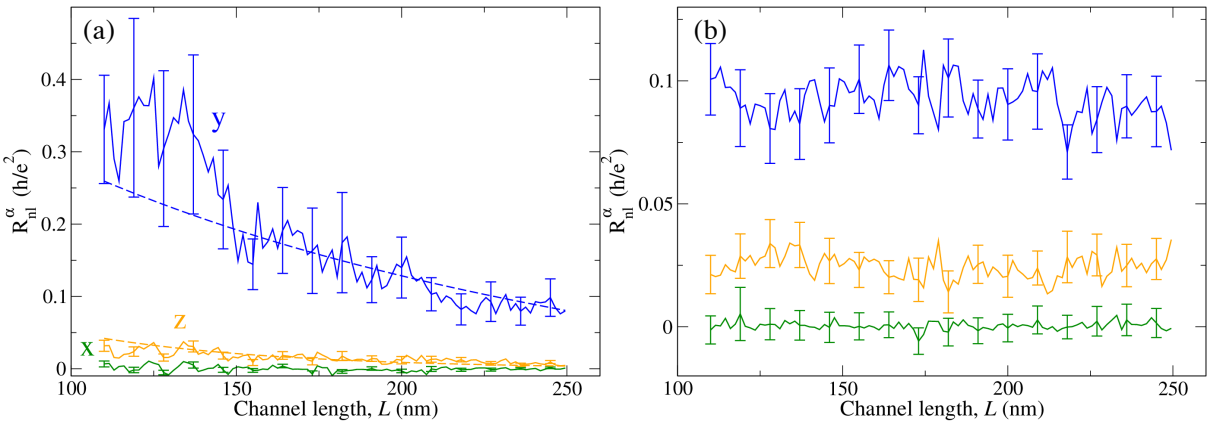

Figure 5.6: R_{nl}^{α} (solid line) as a function of channel length, L, for spins injected along x, y and z for (a) $E = -140$ meV and (b) $E = -320$ meV. Error bars result from the averaging of 50 disorder configurations. Dashed lines in (a) are fits to equation (4.3). The device lengths are $l_1 = 100$ nm, $L + l_2 = 350$ nm whereas s_1, s_2, w and the Anderson disorder is kept the same as in the calculations presented in the main text.

5.2.1 Origin of the spin diffusion length anisotropy

In general, the relaxation of spins is related to the spin texture of the eigenstates [67]. In our case, the spin texture of conducting electrons (see Figures 3.6(a) and 3.6(b) in section 3.1.2 and Figure 5.3) present two key characteristics:

- The spins mainly lie on the yz plane because the projection along x is negligible, with magnitudes obeying $\langle s^y \rangle_E > \langle s^z \rangle_E \gg \langle s^x \rangle_E$. That is, to a very good approximation, the spins are canted along one direction in the yz plane. Specifically, the spins present an angle of $\theta \sim -29°$ with respect to y and $\theta \sim 61°$ with respect to $-z$. Moreover, the y and z projections have opposite sign and the projection along x diminishes as E moves towards the bottom of the conduction band.

- The spin orientation is mostly unchanged throughout the whole Fermi contour. In other words, when "traveling" along the Fermi contour, one sees an approximately persistent spin texture [25, 232, 233] with the above-stated canting of the spins. The PST is not perfect because of the small but finite $\langle s^x \rangle_E$.

The canted spin texture contrasts with the out-of-plane spin polarization in two-dimensional centrosymmetric systems, and also with the in-plane spin-momentum locking in systems with broken inversion symmetry [83], but follows from straightforward symmetry considerations. The SOC Hamiltonian of the TMD tight-binding model derived in section 3.1.2 reads

$$\mathcal{H}_{\mathrm{SOC}} = (\Lambda_x k_y s_x + \Lambda_y k_x s_y + \Lambda_z k_x s_z) \otimes \tau_x. \tag{5.1}$$

In systems with multiple vertical mirror symmetries the coefficient Λ_z of equation (5.1) vanishes, thereby reducing equation (5.1) to a Rasha-like spin-orbit interaction with in-plane spin-momentum locking. Additionally, in this case, all the nonzero elements of the spin Hall conductivity tensor describe spins pointing out of the plane. Such symmetry-constraints are absent in $MoTe_2$ monolayers where only a mirror point symmetry M_x remains, allowing for different spin polarizations in the spin texture as well as multiple components of the spin Hall conductivity tensor, as observed below in section 5.3. More details on how the symmetry of the crystal affects the spin texture and the SHC can be found in Appendix C.

The second characteristic is crucial to understand the hierarchy we observe for the spin relaxation lengths in the diffusive regime. It is convenient to reason in terms of the natural spin quantization axis in this system, which is precisely that defined by the canting direction of the PST. The (approximate) PST here implies an (approximate) conservation of spin along the canting direction: if we describe the spin orientation with reference to a rotated coordinate system where the z' axis points along the canting direction, the Hamiltonian is (approximately) diagonal with a SOC term proportional to the spin Pauli matrix in that direction, $s_{z'}$. Consequently, when spins are injected collinear to that direction, they enter the system as spin eigenstates. Moreover, the disorder potential, being diagonal in the spin and orbital indices, does not change that - neither at the moment of injection nor during the spin transport in the material -, with the implication that those spins retain a large lifetime (in fact, if the PST were strictly exact, there would be no spin relaxation at all for collinear injection). Conversely, maximum (faster) relaxation is expected for spins injected perpendicularly to z'. The case of spins injected parallel to x is one such case, for which we obtain only numerical noise in the nonlocal spin signal. Therefore, we can correlate the trend in relaxation rate observed in the simulations with the injected spins' projection along z'. Accordingly, the hierarchy $\lambda_s^y > \lambda_s^z$ is a natural reflection of that trend: spins injected along y have a slightly larger spin diffusion length than those spins injected along z because the y direction lies ~ 30 degrees away from z' compared with ~ 60 degrees for the z direction. Furthermore, because the x component of the spin texture decreases monotonically towards the band edge, the canting direction becomes more aligned with the yz plane, resulting in the increase of both λ_s^y and λ_s^z when E approaches the bottom of the conduction band.

5.3 Spin Hall effect

The SHE is investigated by computing the spin accumulation s^α with equation (3.50) in the device illustrated in the inset of Figure 5.7. The charge current along y generates a transverse spin current parallel to x by the SHE, which results in spin accumulation at the open lateral boundaries. The efficiency of such sharge-to-spin interconversion (CSI) is characterized by the spin Hall angle (SHA), defined in equations (2.28) and (2.29) in section 2.1.4. To numerically determine the SHA, we calculate the spin accumulation response function per unit of current applied to the lead, and fit it to the solution of the spin drift-diffusion equations (see Appendix D for details):

$$\frac{s^\alpha(x)}{J_{c,y}} = -\frac{\theta^\alpha_{xy}\lambda^\alpha_s}{|e|D_s}\frac{\sinh\left(\frac{w-2x}{2\lambda^\alpha_s}\right)}{\cosh\left(\frac{w}{2\lambda^\alpha_s}\right)}, \tag{5.2}$$

where w is the device width, e the electron's charge and D_s is the spin diffusion coefficient obtained from the charge diffusion coefficient (see Table 5.1).

Figure 5.7 shows the averaged spin accumulation along the channel cross-section, $s^\alpha(x)$, for each spin orientation. In a typical SHE scenario, the electrical current, spin current, and the spin polarization are all mutually orthogonal (for this geometry, that would generate a finite s^z only). However, we observe a nonzero s^y as well. In fact, $|s^z| \sim |s^y|$, implying that the accumulated spins point *obliquely* in the yz plane, with significant projection parallel to the electrical current. Interestingly, note that the spin accumulation displays the hierarchy $s^y > s^z \gg s^x$, echoing the trend seen above for the spin texture and spin diffusion lengths.

We determine θ^α_{xy} by fitting the numerically calculated spin accumulation to equation (5.2), using the values of D_s extracted from the two-terminal conductance of this device and λ^α_s from Figure 5.4. The results are displayed in the inset of Figure 5.7. We note that while the charge conductivity along x and y is slightly anisotropic, resulting in an equally anisotropic SHA, $|\theta^\alpha_{xy}|$ and $|\theta^\alpha_{yx}|$ are still very similar (see section 5.3.2). At E_F, the SHA for spins pointing along y and z have magnitudes of $\approx 10\%$ (but opposite sign). Remarkably, both increase substantially when approaching the band edge, at which point $|\theta^y_{xy}|$ overcomes $|\theta^z_{xy}|$ with values as large as $|\theta^y_{xy}| \approx 80\%$. We also compute the SHC and the SHA with the Kubo-Bastin formula and obtain the same result both qualitatively and quantitatively (see section 5.3.2). This increase of θ^α_{xy} is attributed to hotspots of spin Berry curvature near the bottom of the electron pockets [251, 295], which directly determine the SHC/SHA magnitude [243, 261, 311]. More details about the effects of the spin Berry curvature is found in the next section. Importantly, our combined results

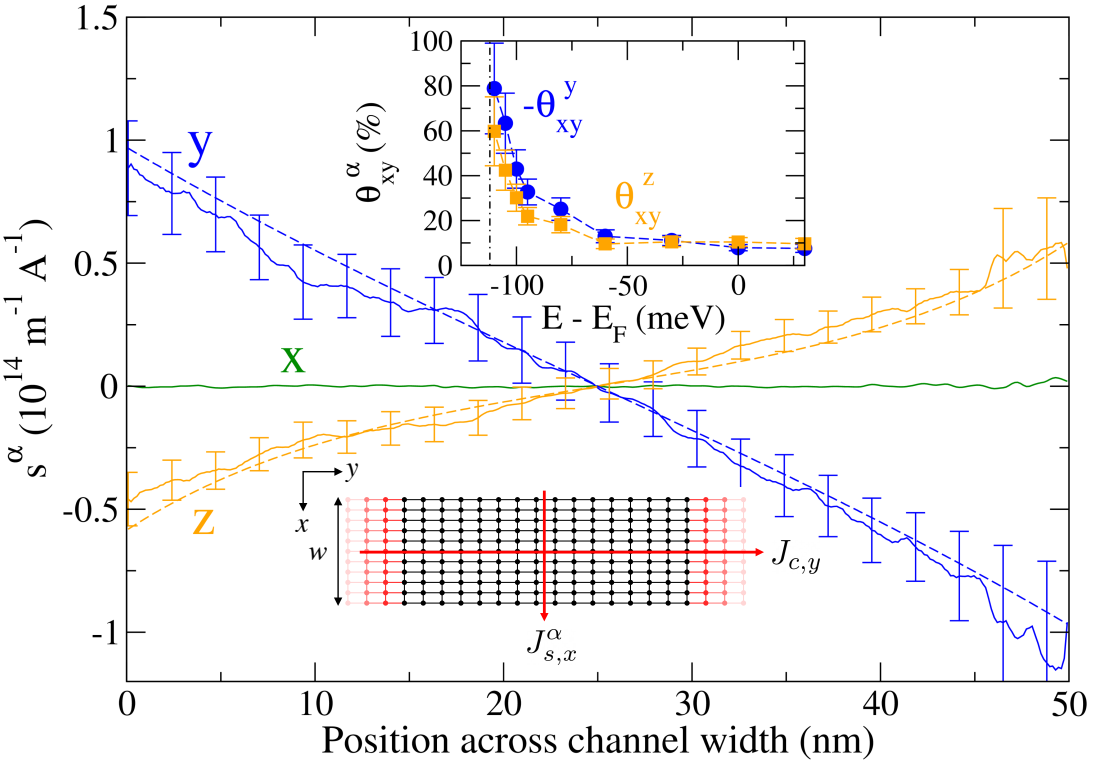

Figure 5.7: Spin accumulation (solid lines) as a function of position across the channel width, of spins along x, y and z. Error bars result from averaging over 200 disorder configurations (w=50 nm). Dashed lines are fits to equation ((5.2)). Bottom inset: Scheme of the two-terminal device, where a current flowing along y creates a spin accumulation in the x direction. Top inset: Energy dependence of the spin Hall angles, with the conduction band minimum marked by a dot-dashed line.

yield CSI efficiencies $\lambda_s^{\alpha}\theta_{xy}^{\alpha} \sim$ 1–50 nm, with larger values near the band edge and for y spins. The upper limit exceeds that of traditional SOC materials (Pt, β-W, β-Ta or Au) for which $\lambda_s^{\alpha}\theta_{xy}^{\alpha} \sim 0.1 - 0.2$ nm [123, 223, 244], and is up to 2 to 3 times larger than that induced by proximity in graphene [21, 111, 226]. Such remarkable CSI efficiency stems from the combination of large spin Berry curvature *and* the persistent spin texture near the $MoTe_2$ band edges.

5.3.1 Origin of the large spin Hall effect

The monolayer nature of TMDs and their nontrivial band topology are both important ingredients for the existence of a large and unconventional spin Hall effect (SHE). As discussed in section 2.2.2, specific symmetry reductions with respect to that of the 3D bulk form of these crystals are essential conditions for the existence of nonzero elements of the spin Hall conductivity (SHC) tensor, σ_{ij}^{α}, beyond the conventional one, i.e. σ_{xy}^{z} and its cyclic permutations; such symmetry reduction is ensured in the monolayers we

consider. This constraint is explicitly illustrated in Figure 2.8 which compares the SHC of $1T_d$-$MoTe_2$ calculated for a 3D bulk crystal with a 5-layer slab.

In this sense, having a mono- or few-layer slab is a *necessary condition* to observe the anomalous SHC components irrespective of the underlying nontrivial band topology (in contrast to the conventional component σ^z_{xy} which is finite in the 3D bulk as well). But it is *not a sufficient condition* because the magnitude of the SHC, when allowed, is determined by the spin Berry curvature (SBC, see section 2.1.5). The essential topological aspect here arises from the band inversion that occurs at the Γ point, as illustrated in the schematic of Figure 5.8.

While the spin-orbit coupling lifts the degeneracy at the Q points where the inverted pair of bands intersect, the regions near Q retain locally large spin Berry curvatures. The SBC associated with band n corresponds to the quantity described by equation (2.34) in section 2.1.5, and is plotted in Figure 5.9. For definiteness, we look here specifically at the case relevant for the anomalous component σ^y_{xy} of the SHC. Each panel of Figure 5.9 shows the k-resolved SBC in the vicinity of the Q point in the Brillouin zone, at two representative values of Fermi level: the ground-state E_F we obtain in DFT and very near the bottom of the two conduction bands ($E = -100$ meV). The important observation to make is that, as conveyed by the color scale, the magnitude of the SBC increases when E approaches the bottom of the conduction pockets (the magnitude is higher in the right plot). This is even better illustrated in Figure 5.10, where we show the same quantity,

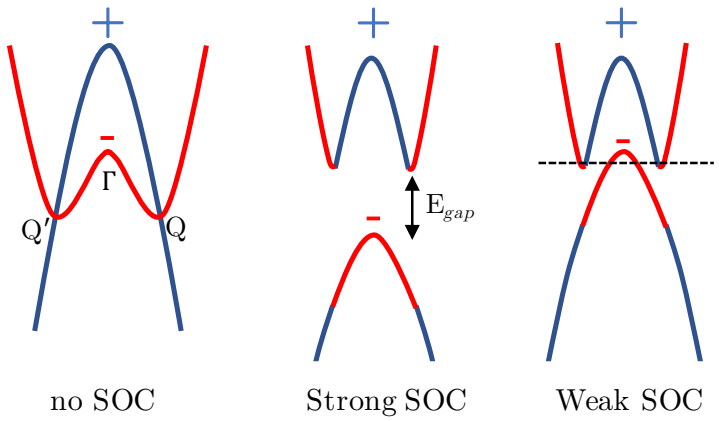

Figure 5.8: Illustration of the band inversion at the Γ point and the emergence of the electron pockets at Q and Q′ as a result of degeneracy lifting by SOC. The symbols "+" and "-" refer to the parity eigenvalues at Γ. See Figure 3.5 for the actual DFT bandstructure of $MoTe_2$ and WTe_2.

but as a function of energy along a cut with $k_y = 0$. It can be clearly seen that the magnitude of the SBC is maximal at the bottom of the conduction pockets and decreases relatively quickly to zero when we increase the energy. We refer to this behavior as SBC *hotspots* associated with the band minima.

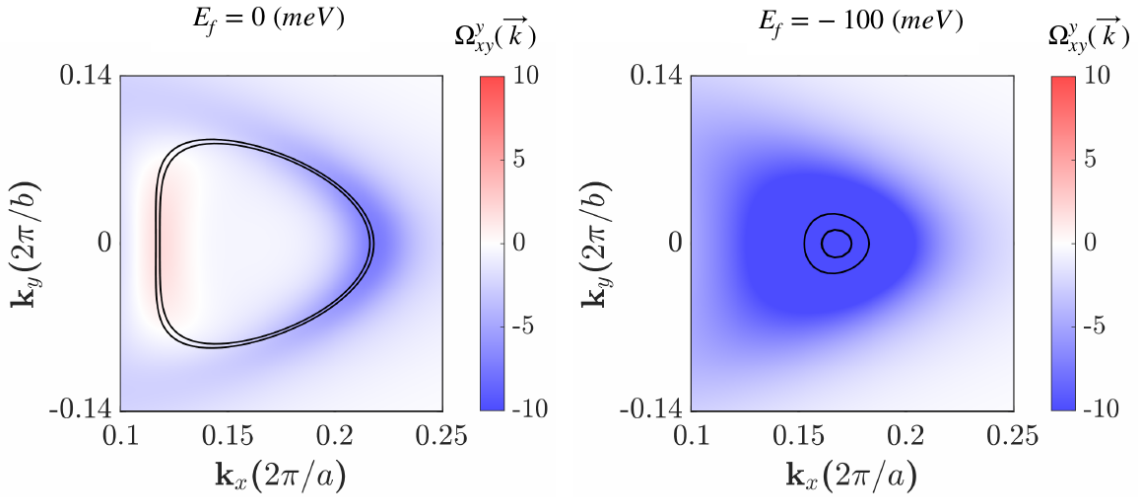

Figure 5.9: Momentum-resolved spin Berry curvature, defined in equation ((2.34)) above, near the Q point in the Brillouin zone, at two representative values of Fermi level: the ground-state E_{F} (left) and very near the bottom of the two conduction bands, $E = -100$ meV (right).

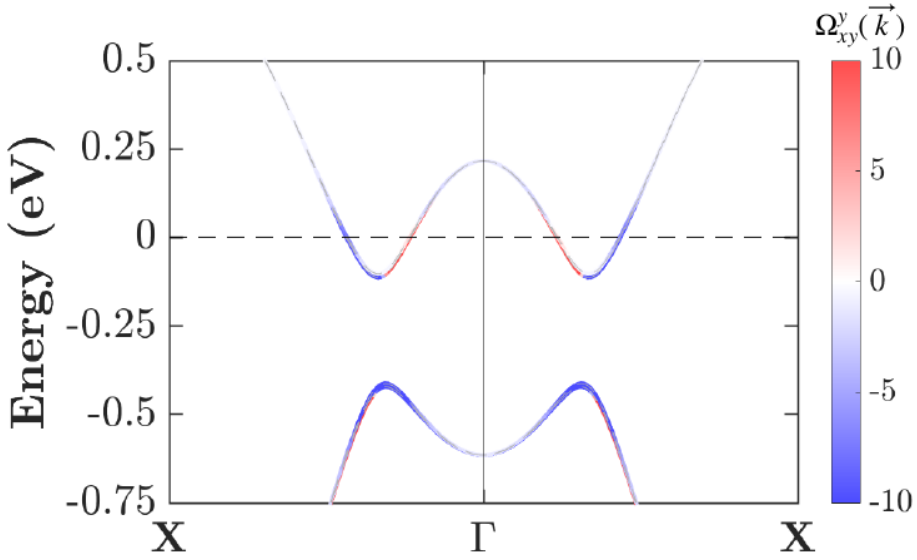

Figure 5.10: Superimposing the total spin Berry curvature (see equation ((2.34)) above; color scale) onto the TB-effective band dispersion. It progressively diminishes when moving away from the local extrema at the Q points.

5.3.2 Comparison with Kubo-Bastin simulations

The values of the SHA presented above obtained with the Landauer-Büttiker formalism are now compared with the values obtained with the Kubo-Bastin formula with the formula $\theta_{ij}^{\alpha} = \sigma_{ij}^{\alpha}/\sigma_{jj}$ (see section 3.2.2). These calculations are carried out using 1000 Chebyshev expansion moments, which is equivalent to a broadening of 10 meV for this particular system, and with a system size of $4 \times 1000 \times 1000$ orbitals.

We plot the values of the SHA as a function of the energy in Figure 5.11(a), where a good agreement is clearly seen between both quantum transport methodologies, supporting the validity of our results. Moreover, in Figure 5.11(b) we plot the ratios between the charge and spin Hall conductivities obtained with the Kubo-Bastin formula. On the one hand, there is a slight charge transport anisotropy, with the charge conductivity along y being a factor 1.2-1.6 of that of the charge conductivity along x in the energy range studied. On the other hand, the spin Hall conductivity shows an almost isotropic behavior for both spin components. These results imply that the SHA is also slightly anisotropic, with the same factor of the ratio σ_{yy}/σ_{xx}, but nevertheless $|\theta_{xy}^{y,z}|$ and $|\theta_{yx}^{y,z}|$ have the same order of magnitude.

The residual difference between the two methods seen in Figure 5.11(a) is expected due to the averaging over disorder realizations that is performed in LB calculations, in addition to a smaller system size required in the LB case with respect to Kubo-Bastin because of a higher computational cost. The LB calculations were performed for disordered systems with 22750 unit cells, while the Kubo-Bastin calculation of the SHC was performed on a clean system with 10^6 unit cells.

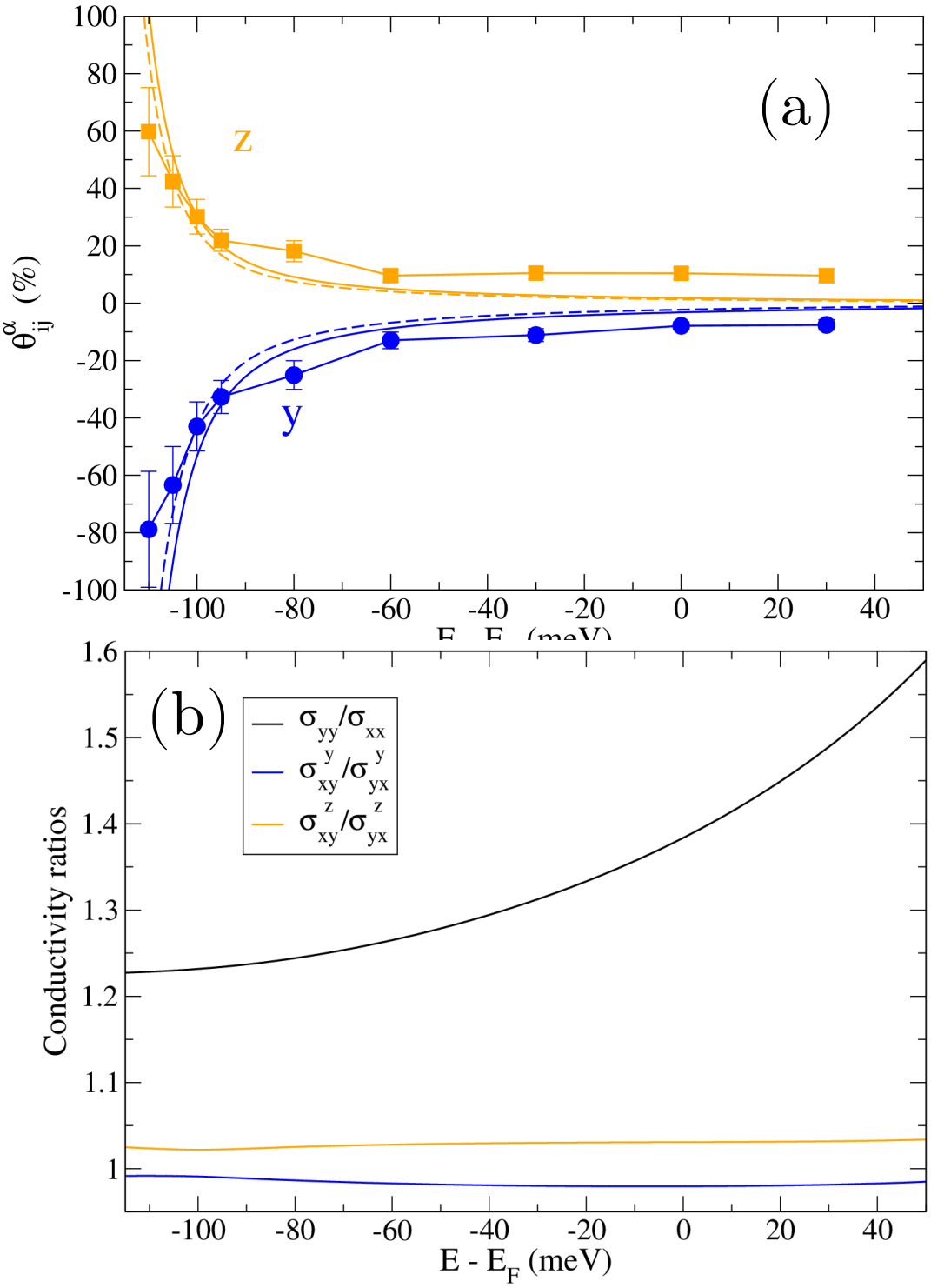

Figure 5.11: (a) Spin Hall angles as a function of energy for spins in y and in z. Solid lines with circles and squares correspond to Landauer-Büttiker calculations ($\theta_{xy}^{y,z}$). Solid (dashed) lines correspond to Kubo-Bastin calculations for $\theta_{xy}^{y,z}$ ($\theta_{yx}^{y,z}$). The positive convention for the SHA is taken when the spin current flows to the right with respect to the charge current (see Appendix D for details). (b) Ratio of charge (black) and spin Hall conductivities (orange and blue).

5.4 Detection of the oblique spin Hall effect

Such a peculiar spin response should become evident in suitably designed nonlocal spin-precession experiments [21,37,227,230]. To probe this oblique SHE, we propose the device concept pictured in the insets of Figure 5.12, which relies on the reciprocal/inverse SHE (ISHE) [244]. It consists of a Hall bar comprising a graphene channel and a transversely aligned monolayer TMD crystal.

A non-equilibrium spin accumulation is induced in the graphene channel through a FM electrode whose magnetization direction determines that of the spin density injected into graphene underneath. This generates a pure-spin current that diffuses toward — and is absorbed by — the remote TMD. It is assumed that the spin current is absorbed by the TMD at its edge and continues to follow the diffusion direction, given that the spin resistance in the TMD is two orders of magnitude lower than in graphene for $\lambda_s^y =$ 30 nm or $\lambda_s^z = 10$ nm (see Appendix E for details). By ISHE, a transverse voltage V_{ISHE} develops on the TMD, which can be measured along its length as illustrated in Figure 5.12. In experiments, the diffusing spins can be controlled by spin precession in a non-collinear magnetic field B. To capture this situation, we generalized the Bloch diffusion equations to account for anisotropic spin diffusion and calculat $V_{\mathrm{ISHE}}(B)$ using the approach described in Ref. [21] (which accurately reproduces CSI in real devices). This procedure is detailed in Appendix E. Figure 5.12 shows the precession response for two selected orientations of the TMD crystal in the limit of full absorption ($R_{\mathrm{ISHE}} \equiv V_{\mathrm{ISHE}}/I_0^y$). We observe magnitudes of R_{ISHE} nearly three orders of magnitude larger than the values reported for graphene/TMDs [21,89,111,226] and graphene/bulk-WSMs [227, 308]. This is a direct consequence of the extremely large SHA predicted here for $MoTe_2$ [1].

The essence of the experiment is that the precession response depends strongly on the crystal orientation. As evidenced in Figure 5.4, the spin relaxation in the TMD is anisotropic, and the CSI depends crucially on both the majority spin orientation and crystalline orientation. In Figure 5.12(a), the TMD's crystallographic y-axis is transverse to the spin propagation. A magnetic field parallel to z causes spins to precess in the graphene plane but, according to Figure 5.7, only the y spin projection contributes to the ISHE signal with an efficiency of $|\theta_{xy}^y|$; R_{ISHE} is symmetric with respect to the sign of B because the magnetization at the FM injector is parallel to y, resulting in the maximum signal at $B = 0$. When the field is parallel to x, the spins acquire a z component (in

[1] In experiments, R_{ISHE} also depends on the TMD's electrical resistance (see Appendix E for details) and the Fermi level, as seen in Figure 5.7. Interfacial barriers between graphene and the TMD can suppress the spin sink effect and cause a more distributed spin absorption across the TMD width, in which case the observed signal might be partially reduced.

addition to that in y), which is asymmetric with respect to B and adds a contribution to the ISHE with an efficiency of $|\theta^z_{xy}|$; because $|\theta^y_{xy}| \geq |\theta^z_{xy}|$, the signal remains roughly symmetric. In Figure 5.12(b), the crystallographic y-axis is parallel to the spin propagation. As the y and z directions are now orthogonal to the FM magnetization, the lineshapes are antisymmetric. The signal is zero at $B = 0$ and, by sweeping B from negative to positive along z (x), the spin component along y (z) changes sign. Therefore, two combined observations in this proposed experiment represent a "smoking gun" demonstration of the intrinsic oblique SHE predicted in this work: (i) $R_{\mathrm{ISHE}}(B)$ should display a different lineshape under different field orientations for a fixed TMD crystal; (ii) rotation of the crystal converts the lineshapes from predominantly symmetric to antisymmetric.

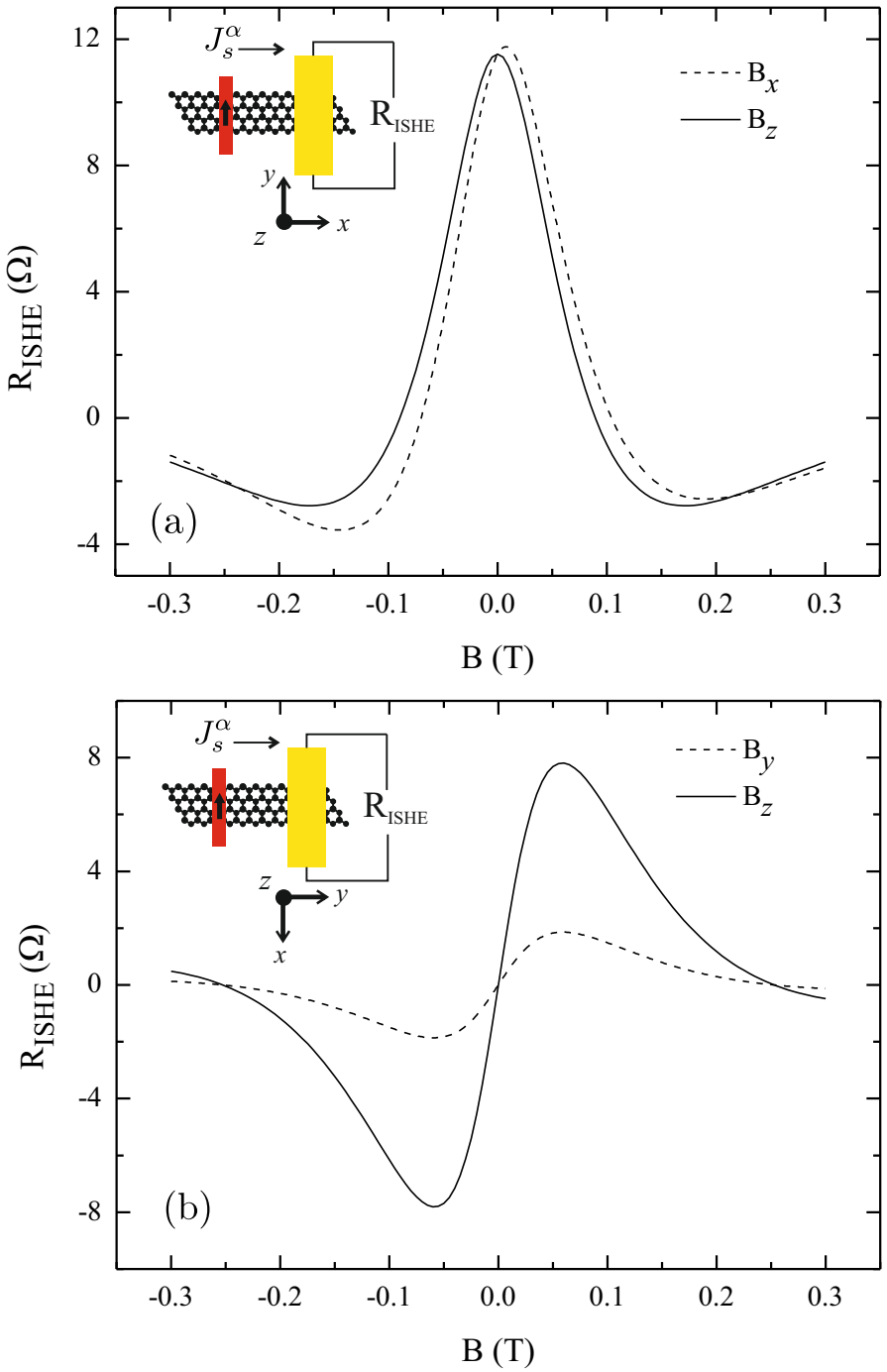

Figure 5.12: Simulated response of the inverse SHE (R_{ISHE}) to spin precession for two orientations of the TMD crystal (coordinate axes in the insets). The device geometry is shown in the insets, with the TMD depicted in yellow and the FM injector in red (magnetization indicated by an arrow). The polarization of the spin current reaching the TMD ($\boldsymbol{J}_s^\alpha$) is controlled externally with a magnetic field, B, oriented either along the graphene channel (dashed lines) or out-of-plane (solid lines). Typical experimental device dimensions were used in the simulation, as described in Appendix E.

5.5 Comparison between 1T′ and 1T$_d$ phases of MoTe$_2$

In this section, we compute the nonlocal resistance and spin accumulations for 1T′-MoTe$_2$. This is obtained by using the same model (equation (3.15)) but setting $\eta = 0$. In this way, inversion symmetry is now preserved, and the bands do not display spin splitting (see Figure 3.7(b)). All the other parameters, both from the model and from the device geometry, are kept the same.

In Figure 5.13 we plot the length dependence of the nonlocal resistance calculated in a nonlocal spin valve, and compare it to the corresponding simulation performed in the 1T$_d$ phase. We focus on two energies, one at the Fermi level $E = 0$ (Figure 5.13(a)) and the other near the band edge at $E = -105$ meV (Figure 5.13(b)). The two phases present the same scaling of the nonlocal resistance for both y and z polarization of injected spins. Finally, in Figure 5.14 we compare the spin accumulations arising due to the spin Hall effect between the two phases at these two energies. The results indicate that the creation of spins along the sample width in 1T′-MoTe$_2$ is similar to that in 1T$_d$-MoTe$_2$. Although both phases present different symmetries which could lead to different spin transport properties, the distortion that drives 1T′-MoTe$_2$ to 1T$_d$-MoTe$_2$ is small [295], and therefore any difference in the spin dynamics between the two phases is expected to also be small.

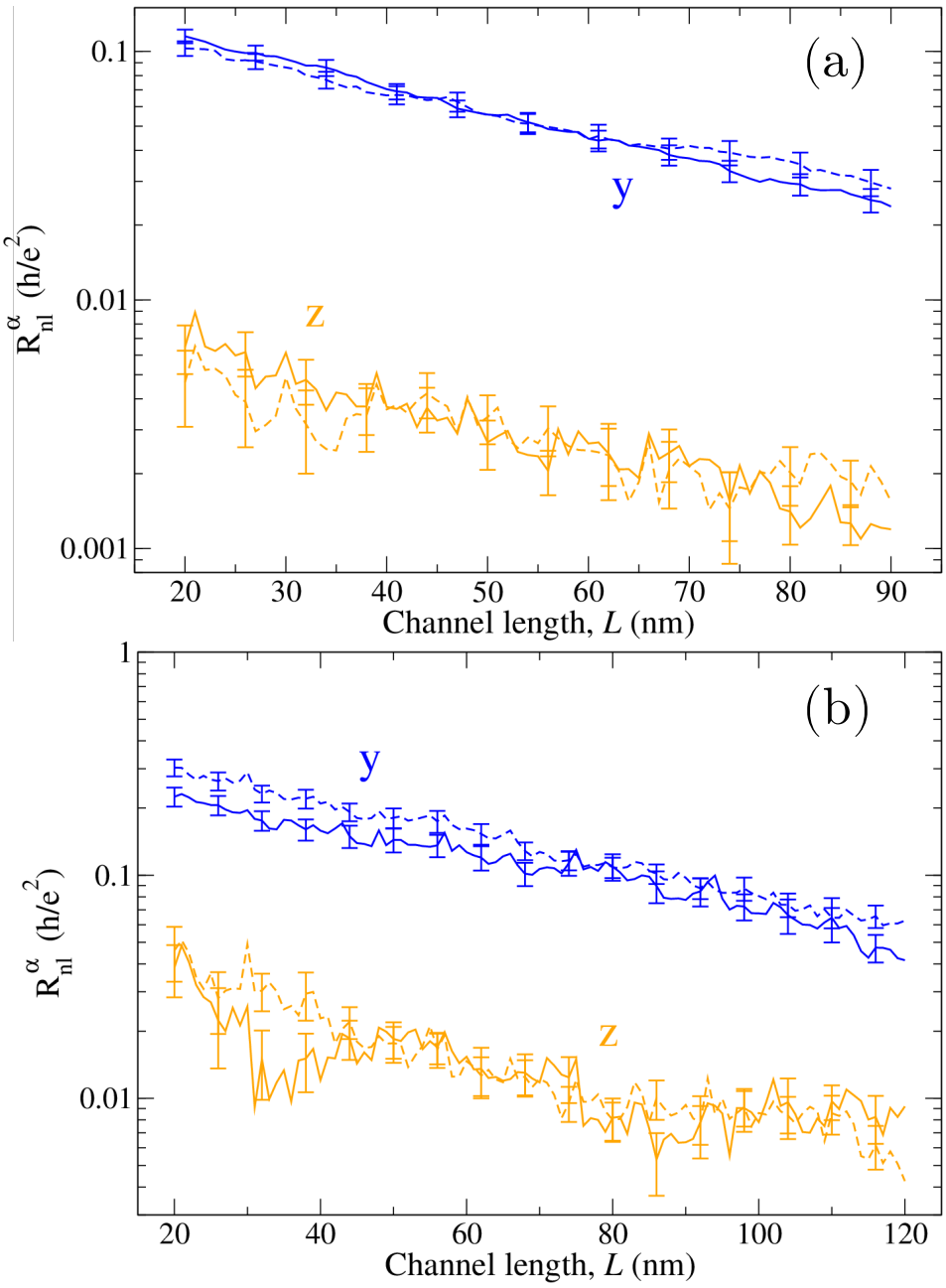

Figure 5.13: $R_{\rm nl}^{\alpha}$ as a function of channel length, L, for spins injected along y and z for (a) $E = 0$ and (b) $E = 105$ meV. Solid (dashed) lines correspond to a simulation of the $1{\rm T_d}$ ($1{\rm T}'$) phase. Error bars result from the averaging of 150 disorder configurations.

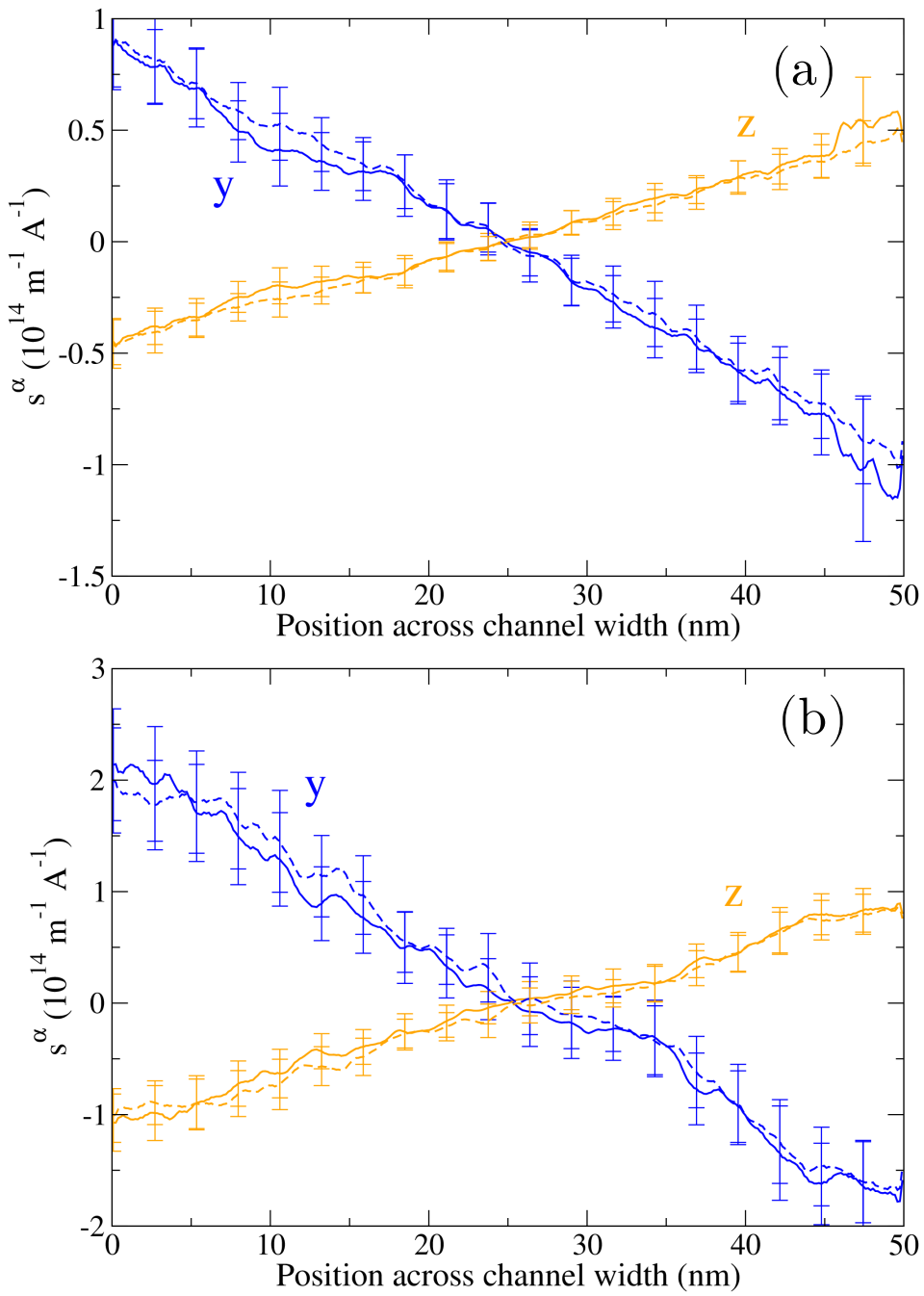

Figure 5.14: Spin accumulation as a function of position across the channel width of spins along y and z for (a) $E = 0$ and (b) $E = 105$ meV. Solid (dashed) lines correspond to a simulation of the $1T_d$ ($1T'$) phase. Error bars result from the averaging of 200 and 100 disorder configurations for (a) and (b), respectively.

5.6 Canted quantum spin Hall effect

From the results obtained in the previous sections, it is natural to ask what will happen to spin transport for energies in the gap, where the quantum spin Hall effect is expected. To address this question, we now focus on the model for WTe_2, as it is the TMD more studied in the quantum spin Hall regime.

Figure 5.15 shows a close-up of the band structure of $1T_d$-WTe_2 near the Fermi level, which is located closer to the bottom of the conduction band than the Fermi level of $MoTe_2$. As in $1T_d$-$MoTe_2$, each band presents a tiny spin splitting and features two charge pockets symmetrically located away from Γ at the point labeled Q and its time-reversal counterpart (not shown). In the inset, we compare the spin textures at E_F for one of the Q-centered electron pockets obtained by DFT with that arising from the model. The spin orientations in the yz plane are represented by the orange arrows (despite not strictly zero, the x component is omitted for clarity, as it was found comparatively much smaller in magnitude). In addition to the obvious agreement, it is noteworthy that the spin texture is uniform to a very good approximation. Hence, WTe_2 is also a material with a naturally present *persistent spin texture* which is invariant upon changing E_F within the range of energies shown (i.e low electronic densities). The spins cant at an angle $\theta \approx -56°$ with respect to t and $\theta \approx 34°$ with respect to $-z$.

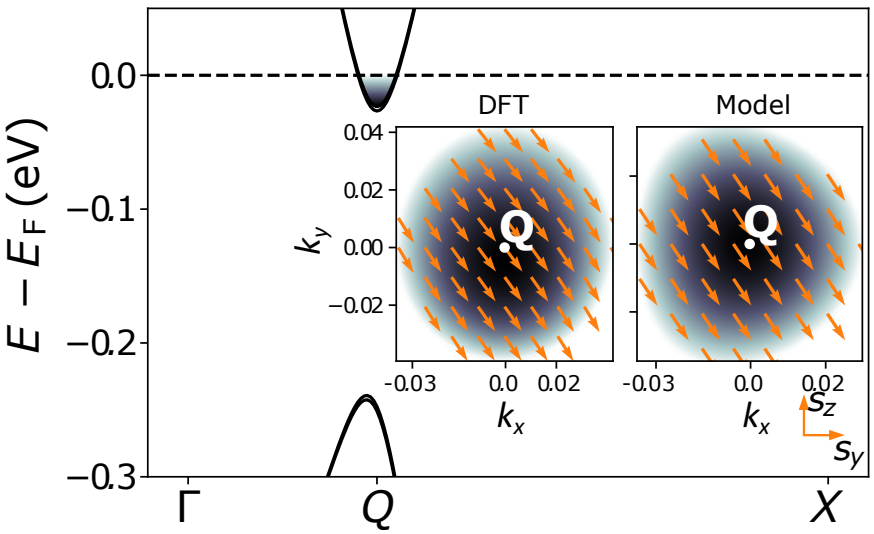

Figure 5.15: Band structure of WTe_2 around the charge pockets formed by the band inversion at Γ. The inset compares the spin textures computed from DFT and the effective model; the color represents the energy with respect to the Fermi level and the arrows the spin orientation in the yz plane (spin projection along x is negligible). The white dots marks the position of the Q point.

Spin Hall conductivity

We next explore the nature of spin transport as E_F is varied across the band gap by computing different elements of the spin Hall conductivity tensor ($\sigma_{ij}^{\alpha}, \alpha = x, y, z$) using the Kubo-Bastin formula implemented as described in section 3.2.2. Figure 5.16 shows the nonzero components of the transverse spin Hall conductivity tensor, σ_{xy}^{α}, $\alpha \in \{y, z\}$, as E_F is varied near and within the band gap. Although both σ_{xy}^{z} and σ_{xy}^{y} display a plateau in the gap region, their values are $-1.65\, e^2/h$ and $1.1\, e^2/h$, respectively. This is intriguing since usually, within a topological gap, quantized spin Hall conductivities are integer multiple of the conductance quantum, reflecting the existence of a definite (integer) number of helical edge channels [139, 159, 183, 234].

However we note that, by definition, each component α of σ_{xy}^{α} provides only a measure of the *projection* of the spin onto the Cartesian direction α, because $\sigma_{ij}^{\alpha} \propto J_{s,i}^{\alpha}/J_j$ where $\boldsymbol{J}_s^{\alpha}$ is the spin current density[2] carrying spins polarized parallel to α in response to a driving charge current $\boldsymbol{J}$. But the choice of Cartesian directions is arbitrary — in fact, the results in Figure 5.16 show that a Cartesian system fixed by the orthorhombic axes of the crystal obscures the adequate spin quantization axis in this problem. This is readily confirmed by the fact that, in the gap, $|\sigma_{xy}^{\alpha}| \equiv \sqrt{(\sigma_{xy}^{y})^2 + (\sigma_{xy}^{z})^2}$ is indeed quantized at $2e^2/h$ (Figure 5.16, solid curve), where the factor of 2 reflects the existence of two counter-propagating modes per edge.

This shows that the interdependence among the magnitudes of the spin Hall conductivity components seen in Figure 5.16 has a fundamental origin, namely the presence of *spin-canted topological edge states* which sustain a quantum spin Hall effect in WTe_2 monolayer. From the values of each plateau, we determine that the spin quantization axis is canted at $\theta = \arctan(\sigma_{xy}^{z}/\sigma_{xy}^{y}) \approx -56^{\circ}$ with respect to the y axis. Notably, this angle matches perfectly with the orientation of the persistent spin texture near the bottom of the conduction band, shown earlier in the inset of Figure 5.15.

The existence of a quantized plateau at $2e^2/h$ is an indication of spin conservation [138, 159, 183, 234]. To demonstrate this more explicitly, we unitarily transform the $\mathbf{k}\cdot\mathbf{p}$ Hamiltonian in equation (3.13) with a rotation in *spin space* about x, which is effected by the matrix $U(\theta) \equiv \cos[(2\theta - \pi)/4]\, s_0 - i \sin[(2\theta - \pi)/4]\, s_x$, where $\theta \equiv \arctan(\Lambda_z/\Lambda_y) \approx -56^{\circ}$ is an angle defined by the SOC parameters in equation (5.1). While the spin-independent part of the WTe_2 tight-binding model remains invariant, the SOC term transforms into

$$\mathcal{H}'_{\mathrm{SOC}} \equiv U^{\dagger}(\theta)\mathcal{H}U(\theta) = \Lambda_x k_y s_x + \Lambda_r k_x s_{z'} \tau_x, \tag{5.3}$$

[2]Here, $\boldsymbol{J}_s^{\alpha} = (J_{s,x}^{\alpha}, J_{s,y}^{\alpha}, J_{s,z}^{\alpha})$, in contrast to the definition given in equation (2.10). See List of Acronyms and useful Symbols for the different definitions of the spin current.

with $\Lambda_r \equiv \sqrt{\Lambda_z^2 + \Lambda_y^2}$ and $s_{z'} \equiv U^\dagger(\theta) s_z U(\theta)$. We now note that Λ_x is numerically smaller than Λ_r in WTe_2 and, more importantly, $|k_y| \ll |k_x|$ near the bottom of the Q-centered electronic pockets. The combined effect is that, over the range of energies shown in Figure 5.15, the first term in equation (5.3) is two orders of magnitude smaller than the second and thus *negligible in practice*. Consequently, $[\mathcal{H}', s_{z'}] \approx 0$ so that spin is preserved along the canted z' direction to a very good approximation, which has two physical consequences: (i) when E_F lies in the conduction band, the carriers have a persistent spin texture directed along z' over the entire Fermi contour; (ii) the canting angle is preserved in the quantum spin Hall regime (when E_F lies in the gap), which supports the quantization of the spin Hall conductivity and defines a canted QSHE. For completeness and further corroboration, we include in Figure 5.16 (open circles) the spin Hall conductivity $\sigma_{xy}^{z'}$ computed explicitly with the rotated Hamiltonian in equation (5.3), and also show in Figure 5.17 the explicit spin texture of the edge states in a WTe_2 ribbon.

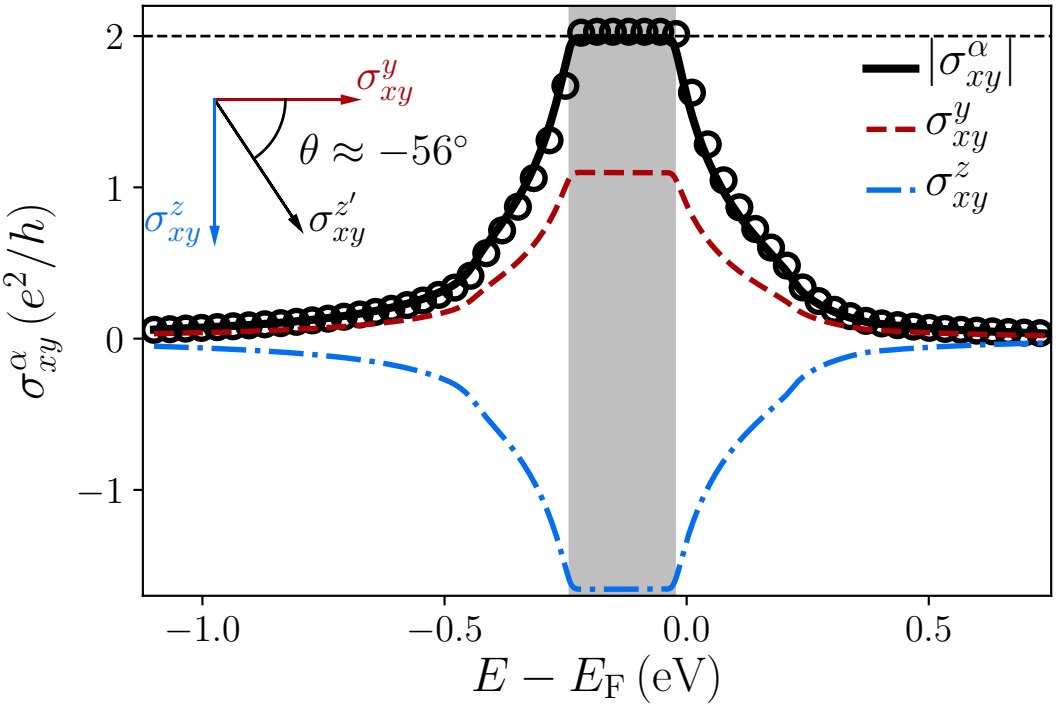

Figure 5.16: Spin Hall conductivities σ_{xy}^{y} and σ_{xy}^{z}. The solid line shows the norm of $|\sigma_{xy}^{\alpha}| \equiv \sqrt{(\sigma_{xy}^{y})^2 + (\sigma_{xy}^{z})^2}$, the grey area highlights the bandgap; the open black circles correspond to $\sigma_{xy}^{z'}$. Inset: orientation of the spin of the helical edge states. The calculations were done considering a broadening of 5 meV on a system with $1000 \times 1000 \times 4$ orbitals.

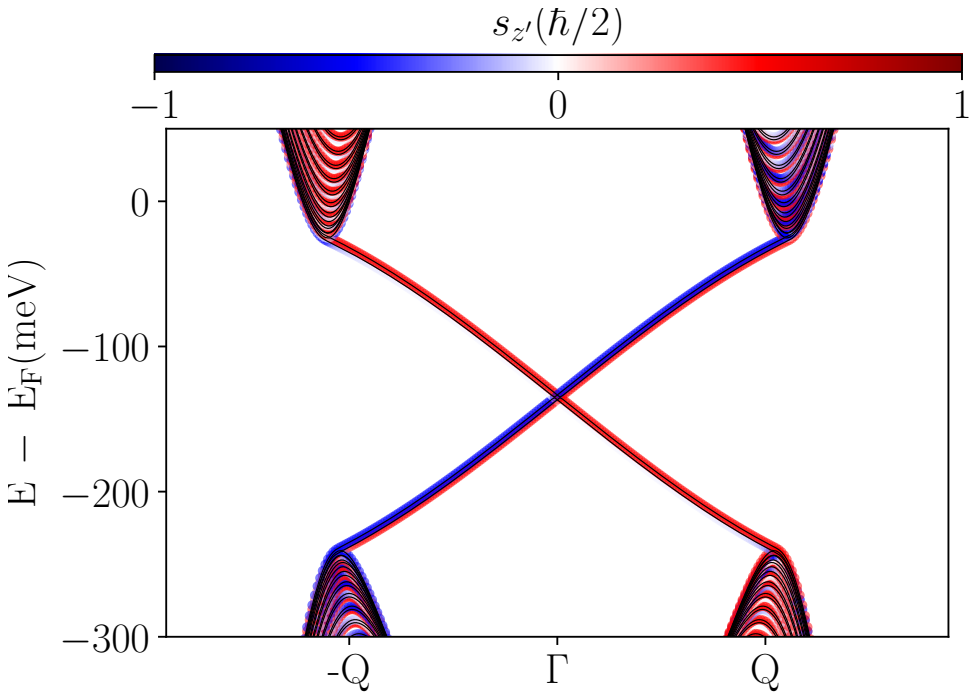

Figure 5.17: Band structure of a $1T_d$-WTe_2 ribbon with width of 63 nm where the color represents the spin texture along the canting direction, $s_{z'}$. The pair of helical states with canting spin polarization are readily visible.

Helical transport of spin at the edges

The topological nature of the electronic states can be unequivocally confirmed by probing nonlocal resistances, R_{nl}, in a Hall-bar geometry under different bias conditions: If the nonlocal signal is due only to helical edge states, R_{nl} should display plateau values uniquely determined by the specific combination of contacts chosen for current injection and nonlocal voltage detection [222]. We employ our effective tight-binding model to compute the nonlocal resistance using the device geometry illustrated in Figure 5.18(b). To obtain R_{nl}, we proceed in a similar faishon as we did for the nonlocal spin valve: from the transmission probabilities between each pair of leads and build the conductance matrix $\mathbf{G}$ and then require the current to flow from lead i to j by setting $I_i = -I_j$ and $I_k = 0, k \neq i, j$, and calculate the resulting voltages $\mathbf{V}$. The nonlocal resistance is defined as $R_{ij,kl} = (V_k - V_l)/I_{ij}$, i.e., current flows from lead i to j and voltage is measured between leads k and l. Furthermore, to test the robustness of the nonlocal signal, we include Anderson disorder with equation (3.16) in the tight-binding Hamiltonian.

The results are plotted in Fig 5.18(a), where solid (dashed) lines show R_{nl} for a system with (without) disorder. Each curve represents a different calculation of R_{nl}, that is, a different choice of current paths and probes used to calculate $R_{ij,kl}$. The quantized values obtained at the plateaus precisely correspond to those expected in the QSHE state for

the chosen injection and detection contacts, as explained in Appendix F. That different choices of electrical contacts yield distinct — yet precisely defined — plateau values stems from the equilibration of the chemical potential at the leads [222]; therefore, the chosen voltage probes and the current path uniquely determine the value of $R_{ij,kl}$. Note however that such nonlocal setup is unable to discern the y and z projections of the spin in the edge states; for that, one may need to use magnetic electrodes.

We also computed the bond-projected spin currents with equation (3.52) for spins polarized along the (rotated) z' and y' directions, i.e., $\boldsymbol{J}_s^{z'}$ and $\boldsymbol{J}_s^{y'}$. The former is shown in Figure 5.18(b) as horizontal arrows at the top/bottom edges, evidencing the fingerprint of helical transport in the QSH regime. In contrast, $\boldsymbol{J}_s^{y'}$ was found to be negligible, which is consistent with the form of $\mathcal{H}'_{\mathrm{SOC}}$ in equation (5.3). Finally, we also observe a strong resilience of the plateaus to nonmagnetic disorder in Figure 5.18(a), consistent with time-reversal topologically protected states ($U = 2$ eV, much larger than any other energy scale of the Hamiltonian). These nonlocal results clearly establish that the canted QSH effect, inferred above from a bulk Kubo-Bastin calculation, is characterized by robust helical spin transport at the edges, a fact fully consistent with the bulk-boundary correspondence [108].

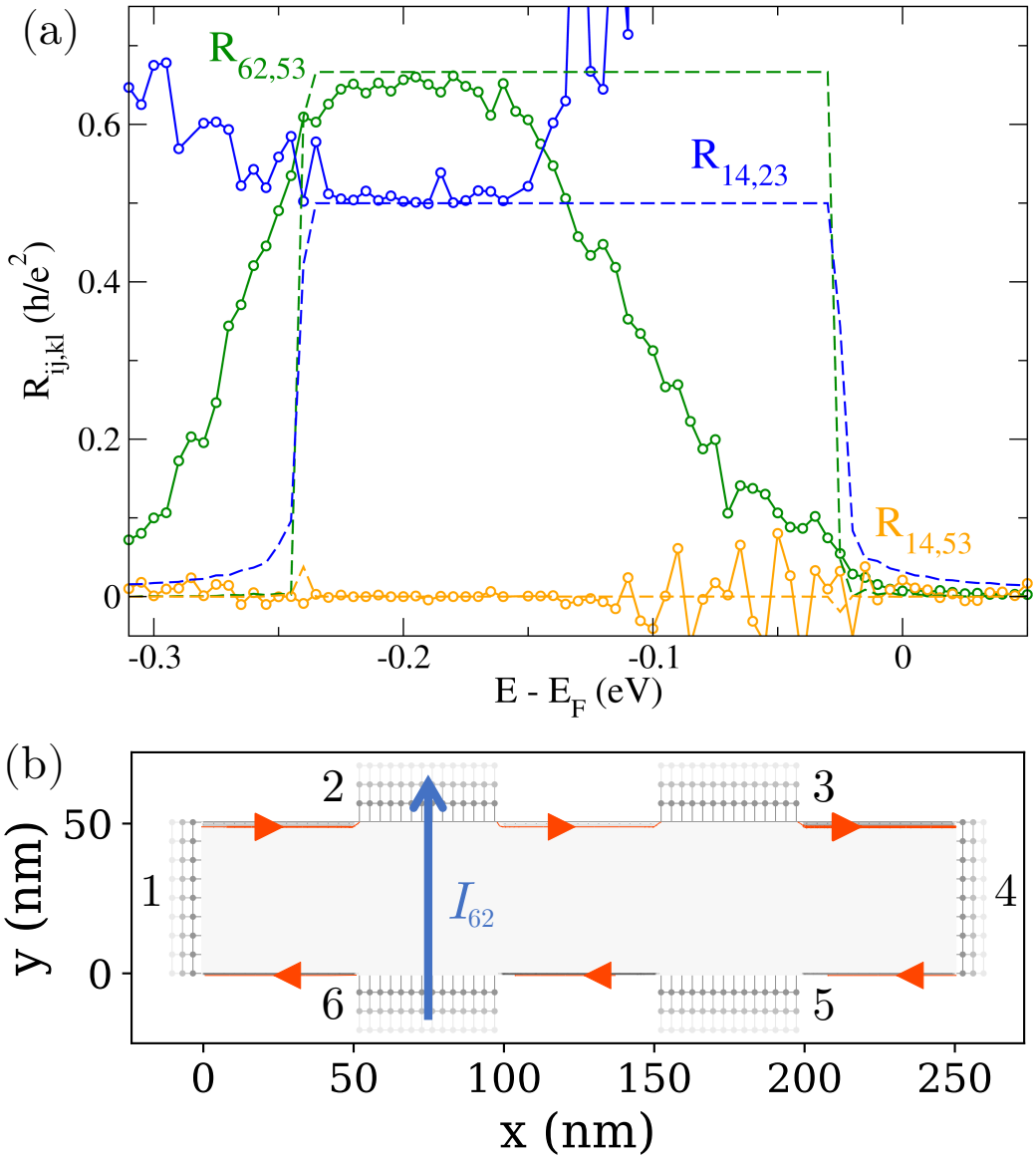

Figure 5.18: Nonlocal resistances $R_{ij,kl} = (V_k - V_l)/I_{ij}$ calculated in the 6-terminal Hall-bar device shown in the inset. The two plateau values $2h/3e^2$ and $h/2e^2$ seen here unequivocally attribute the nonlocal signal to QSH edge states (see Appendix F for details). Solid (dashed) lines correspond to simulations with (without) Anderson disorder (with strength $U = 2$ eV). In the inset, the solid (lattice) regions delineate the device (leads). The device is defined on a rectangular lattice (parameters $a_x = 3.4607$ Å and $a_y = 6.3066$ Å). The device width, inter-lead separations, and lead widths are all 50 nm. The small horizontal arrows along the top and bottom edges mark the direction of the local, bond-projected spin current density $\boldsymbol{J}_s^{z'}$ arising as the response to driving charge current from lead 6 to lead 2.

5.7 Conclusions

Numerical calculations for 1T′- and $1T_d$ TMD monolayers like $MoTe_2$ reveal a novel, oblique SHE which reflects the unconventional spin textures allowed by their reduced symmetry and strong SOC. The obtained CSI figure of merit $\lambda_s\theta_{xy} \sim$ 1–50 nm is up to two orders of magnitude superior than in traditional spintronic materials such as Pt, Au, W, and Ta [123, 244]. Furthermore, calculations of spin Hall conductivities and nonlocal resistances in multi-probe configurations of $1T_d$-WTe_2 revealed a so-far-unique quantum spin Hall effect defined by a canted spin quantization axis, fixed by the SOC symmetries. The oblique spin polarization of topological edge states in the QSHE continuously evolves into a persistent spin texture when E_F enters the conduction band.

Our findings also call for a careful analysis of both the SHE and QSHE measurements. The interpretation of all-electrical detection in Hall bars [1, 105, 222, 251] usually ignores the possibility of multiple nonzero components of the spin Hall conductivity tensor. As a result, erroneous values for the spin Hall angle may be estimated and non-integer quantization might be erroneously inferred. We show how the presence of oblique SHE can be experimentally identified by reciprocal SHE, and how the different SHC contributions may be isolated in a spin precession setup. A similar procedure and/or using magnetic contatcts in nonlocal measurements could disentangle as well the different spin contributions in the quantum spin Hall regime. Interestingly, such non-integer QSH plateaus associated to a single spin component of the SHC tensor were theoretically discussed for square and hexagonal lattices [183], suggesting the possible existence of a canted QSHE in those systems as well.

The low-symmetry phases of TMDs may thus provide fascinating avenues to design new topological nanodevices for spin transport beyond the current paradigm of the (quantum) spin Hall effect with z-polarized spins. In the context of spin-orbit torque, such canted spin polarization allows for torques with different symmetries, which could facilitate the current quest for magnetic-field-free switching of magnets with out-of-plane magnetic anisotropy, a feature that is forbidden using high-symmetry 2D materials. Finally, a QSHE whose canting angle depends on the ratio of SOC parameters could enable electrically tunable dissipationless spin currents with controllable spin orientation in the absence of magnetic fields.

CHAPTER 6

CONCLUSIONS AND OUTLOOK

In this thesis I explored the spin dynamics in two-dimensional quantum materials such as graphene and transition metal dichalcogenides (TMDs). To that end, I have adapted an existing quantum transport computational platform (the open source code Kwant [94]) to implement spin transport physics. The deployment of tight-binding models has allowed me to simulate realistic device geometries and explore the crossover from diffusive to ballistic spin transport in ultraclean graphene devices as well as charge-to-spin interconversion and the quantum spin Hall effect in low-symmetry TMDs.

In graphene, I discovered a new extrinsic source of spin relaxation which is driven by the nonlocal setup geometry of nonlocal spin valves. When the transport is diffusive and the spin diffusion length comparable to the device size, the nonmagnetic electrodes that are usually neglected in the analysis of nonlocal signals start limiting the spin current in the graphene channel. By extending the formulation of the spin diffusive equations, I derived a formula to capture this effect and correctly extract the values for the spin diffusion length. Such an effect occurs only when transport is diffusive and disappears in the absence of scattering. By varying the degree of disorder in the devices, I could follow the evolution of the Hanle spin precession curves from diffusive to quasiballistic and to purely ballistic. When the mean free path is only a few times shorter than the channel length, the spin diffusive equations used to interpret the Hanle curves in the diffusive regime fails dramatically. The nonlocal signal now presents several oscillations with magnetic field. The origin and period of these oscillations is traced back to the ballistic propagation of electrons and their Fermi velocity, respectively. While analytical formulas are derived to interpret the numerical simulations of both the diffusive and ballistic transport, they fail to fully capture the nonlocal resistance profiles in the quasiballistic regime, mainly due to the complex and unknown distribution of transit times of the

electrons propagating through the graphene channel.

It is interesting to compare our numerical results obtained in the ballistic transport for quasi-1D devices to the predictions made by 2D spin transport calculations, where spins relax due to an inhomogeneous precession from the Rashba SOC [51]. In our case, the dephasing process occurs because there are electron spins precessing with the same frequency but with different Fermi velocities, while in 2D, the Fermi velocity is constant but there is a well-defined distribution of precession frequencies. Such spread in frequencies originates from the Rashba SOC, likely present in experiments, and absent in our calculations due to its complex spin dynamics for quasi-1D systems. However, the bulk calculation lacks the quantization of the transverse momenta which is relevant in a ballistic scenario. Therefore, further studies should clarify whether the quasi-1D Rashba SOC can transition into a 2D-Rashba SOC for wide enough ribbons or in contrast the 2D picture of spin relaxation fails in the ballistic limit independently of the channel width. Finally, in the same lines as Ref. [262], it would be useful for experimental guidance to investigate ballistic spin transport but with scattering localized underneath the contacts, which mimics more realistic experimental conditions. However, it may be computationally too demanding to study this with the Landauer-Büttiker formalism since this would require to simulate wider ferromagnetic contacts than the ones modeled in this thesis.

In TMD monolayers, I found that the low-symmetry of the 1T′ and $1T_d$ crystal phases produces an approximate persistent spin texture in the conduction bands with a canting angle in a direction in the yz plane. The values of this angle with respect to the yz Cartesian axes are $\sim -29°$ for $MoTe_2$ and $\sim -56°$ for WTe_2, and is given by the ratio of the SOC parameters Λ_y and Λ_z from the model in equation (3.13). Such persistent spin texture can explain the spin relaxation anisotropy observed from the nonlocal spin valve simulations. Furthermore, I computed the spin accumulation at the edges of a $1T_d$-$MoTe_2$ device, which displays both out-of-plane and in-plane spin polarization, and from which the spin Hall angles can be determined by an analytical formula I derived. This is attributed to the extra components of the spin Hall conductivity tensor allowed by the reduced symmetry of the $1T_d$ monolayer. The presence of both spin polarizations implies an oblique spin Hall effect with spins lying in the yz plane. Importantly for technological applications, both the spin diffusion lengths and the spin Hall angles are large, reaching values of tens of nanometers and at least $\sim 10\%$, respectively, both y and z-polarized spins. The simulations revealed that both quantities are gate-tunable, being maximum near the minimum of the conduction band, leading to spin Hall angles up to $\sim 80\%$. Therefore, the charge-to-spin interconversion efficiency $\lambda_s^\alpha \theta_{xy}^\alpha$ reaches values as large as 50 nm, suggesting low-symmetry TMDs as an excellent class of materials for spin generation, manipulation and transport of spins. I also found similar results for the

1T′ phase of $MoTe_2$ for spin transport and charge-to-spin interconversion. The increased spin Hall conductivity near the band edge is reminiscent from the underlying nontrivial topology. Indeed, the spin Hall effect transitions into a quantum spin Hall effect, which I investigated for $1T_d$-WTe_2. I found that the canting angle of the persistent spin texture remains for the topological helical edge states, thus forming a canted quantum spin Hall effect. Moreover, I demonstrated that such canting of the spins is not incompatible with spin conservation, and therefore the norm of the spin Hall conductivity presents a well defined quantized integer value.

The results concerning the spin Hall effect in low-symmetry TMDs provide further guidance to the recent experimental results in few-layer $MoTe_2$ and WTe_2 [227, 251, 307, 308]. In these works, similar charge-to-spin interconversion efficiencies have been estimated. However, experimental control on layer thickness is complicated, which makes the investigation of spin relaxation and spin Hall effect down to the monolayer limit elusive. Here, I provide such information and importantly I show how the spintronic potential can be increased by proper tuning of the Fermi level. Further studies should investigate in more depth the specific spin relaxation mechanism and how the persistent spin texture can be utilized to enhance the spin diffusion lengths (e.g. by injecting spins along the canting direction). In regards of the quantum spin Hall phase, it is worth mentioning the very recent experimental findings of the canted quantum spin Hall effect in WTe_2 monolayer with canting angles of $\sim -60^\circ$ [260, 310]. This demonstrate that our calculations predict both qualitatively and quantitatively this topological effect and establishes the validity of our tight-binding model to be used in future studies, for example, in the interaction of the edge states with magnetic fields to realized other topological states of matter such as the quantum anomalous Hall effect.

LIST OF PUBLICATIONS

1. **Marc Vila**, Chuang-Han Hsu, Jose. H. Garcia, L. Antonio Benítez, Xavier Waintal, Sergio Valenzuela, Vitor M. Pereira, and Stephan Roche, Charge-to-Spin Interconversion in Low-Symmetry Topological Materials, arXiv:2007.02053, *Submitted to Phys. Rev. Lett.*, 2020.

2. Jose. H. Garcia, **Marc Vila**, Chuang-Han Hsu, Xavier Waintal, Vitor M. Pereira, and Stephan Roche, Canted Persistent Spin Texture and Quantum Spin Hall Effect in WTe_2, arXiv:2007.05626, *Submitted to Phys. Rev. Lett.*, 2020.

3. **Marc Vila**, Jose H. Garcia, Aron W. Cummings, Stephen R. Power, Christoph W. Groth, Xavier Waintal, and Stephan Roche, Nonlocal Spin Dynamics in the Crossover from Diffusive to Ballistic Transport, *Phys. Rev. Let.*, 124, 196602, 2020.

4. Bogdan Karpiak, Aron W. Cummings, Klaus Zollner, **Marc Vila**, Dmitrii Khokhriakov, Anamul Md. Hoque, André Dankert, Peter Svedlindh, Jaroslav Fabian, Stephan Roche, and Saroj P. Dash, Magnetic proximity in a van der Waals heterostructure of magnetic insulator and graphene, *2D Mater.*, 7, 015026, 2019.

5. **Marc Vila**, Nguyen Tuan Hung, Stephan Roche, and Riichiro Saito, Tunable circular dichroism and valley polarization in the modified Haldane model, *Phys. Rev. B*, 99, 161404(R), 2019.

6. C. K. Safeer, Josep Ingla-Aynés, Franz Herling, José H. Garcia, **Marc Vila**, Nerea Ontoso, M. Reyes Calvo, Stephan Roche, Luis E. Hueso, and Fèlix Casanova, Room-Temperature Spin Hall Effect in Graphene/MoS_2 van der Waals Heterostructures, *Nano Lett.*, 19, 1704, 2019.

7. Dmitrii Khokhriakov, Aron W. Cummings, Kenan Song, **Marc Vila**, Bogdan Karpiak, André Dankert, Stephan Roche, and Saroj P. Dash, Tailoring emergent spin phenomena in Dirac material heterostructures, *Sci. Adv.*, 4, eaat9349, 2018.

8. Jose H Garcia, **Marc Vila**, Aron W Cummings, and Stephan Roche, Spin transport in graphene/transition metal dichalcogenide heterostructures, *Chem. Soc. Rev.*, 47, 3359, 2018.

APPENDIX A

DERIVATION OF THE SPIN-DIFFUSION EQUATION IN NSVS INCLUDING THE DRAIN AND REFERENCE ELECTRODES

In this Appendix, we derive equation (4.3) from Chapter 4. We will start by solving the generalized form of the spin diffusion equations in a 1-dimensional (1D) channel (x direction) with a magnetic field in the z direction [209][1]:

$$\frac{\partial^2 \boldsymbol{s}}{\partial x^2} = \frac{1}{\lambda_s^2}\boldsymbol{s} - \frac{1}{l_{\mathrm{L}} l_{\mathrm{e}}}(\widehat{\mathbf{z}} \times \boldsymbol{s}). \tag{A.1}$$

Here, l_e is the mean free path, l_{L} is the Larmor precession length $l_{\mathrm{L}} = v_{\mathrm{F}}/\omega$ with v_{F} the Fermi velocity and ω the precession frequency and λ_s is the spin diffusion length. The spin accumulation is defined as $\boldsymbol{s} = \boldsymbol{s}_\uparrow - \boldsymbol{s}_\downarrow = (s^x, s^y, s^z)$. We are interested in the in-plane components of the spin accumulation since it is the one usually measured in the NSV. The above equation has solutions of the form:

$$s^x = -A\frac{i}{\kappa}e^{-\kappa x} + B\frac{i}{\kappa}e^{\kappa x} + C\frac{i}{\kappa^*}e^{-\kappa^* x} - D\frac{i}{\kappa^*}e^{\kappa^* x}$$

$$s^y = -A\frac{1}{\kappa}e^{-\kappa x} + B\frac{1}{\kappa}e^{\kappa x} - C\frac{i}{\kappa^*}e^{-\kappa^* x} + D\frac{i}{\kappa^*}e^{\kappa^* x} \tag{A.2}$$

$$\tag{A.3}$$

with $\kappa = \sqrt{\frac{1}{\lambda_s^2} - i\frac{\omega}{D_s}}$ where D_s is the spin diffusion coefficient. To describe the length-dependent nonlocal resistance or Hanle precession, one often assumes diffusion only to the

[1]Note that we are using here a different notation than that from equation (2.12).

right part of the injector and that the spin decays far away from it ($s^x(+\infty) = s^y(+\infty) = 0$) and that it is injected in the magnetization direction of the FM source electrode: $\partial s^x(0)/\partial x = 0$, $\partial s^y(0)/\partial x = -J_0/2D_s$, where $J_0 = I_0/w$ (w the channel width) and D_s are the the injected spin polarized current density and diffusion coefficient, respectively [67, 122, 125, 131, 132]. These conditions leads to equation (4.2), but fails to describe situations where λ_s becomes comparable with the device size ($\lambda_s \geq l_1, l$), which is the case of our simulations and possibly state-of-the-art graphene NSV [58,85,137]. Therefore, we need to consider the continuity of $\boldsymbol{s}$ and spin current density ($\boldsymbol{J}_s^\alpha$) conservation at *all* electrodes, leading to a more complicated set of equations. To simplify this, we want that the injector and detector do not perturb the system. Experimentally, one can achieve this by placing tunnel barriers between graphene and the FM contacts, thus avoiding spin absorption and relaxation [101]. This condition allows us to exclude the injector and detector from the equations and just have their polarization as a constant prefactor [257, 258]. In the simulation, the same effect can be obtained by setting the injector and detector to be fully spin polarized (i.e. only inject/detect one spin component), as seen in Figure 3.19. This, together with the condition of no net charge current at the detector, assures that there is no spin current being absorbed in these leads[2]. This keeps the set of equations simpler and let us focus on the main physics without loss of generality. Eventually, the conditions at the electrode-graphene interface are [209]:

$$s^\alpha(-l_1) = -\frac{eR_c}{2}\boldsymbol{J}_{s,1}^\alpha \tag{A.4}$$

$$eD_s\frac{\partial s^\alpha(-l_1)}{\partial x} = \boldsymbol{J}_{s,1}^\alpha \tag{A.5}$$

$$s^\alpha(0_-) = s^\alpha(0_+) \tag{A.6}$$

$$eD_s(-\frac{\partial s^x(0_-)}{\partial x} + \frac{\partial s^x(0_+)}{\partial x}) = 0 \tag{A.7}$$

$$eD_s(-\frac{\partial s^y(0_-)}{\partial x} + \frac{\partial s^y(0_+)}{\partial x}) = J_0 \tag{A.8}$$

$$eD_s\frac{\partial s^\alpha(l)}{\partial x} = \boldsymbol{J}_{s,4}^\alpha \tag{A.9}$$

$$s^\alpha(l) = -\frac{eR_c}{2}\boldsymbol{J}_{s,4}^\alpha \tag{A.10}$$

where $\boldsymbol{J}_{s,p}^\alpha$ is the spin current density at lead p with spin polarization $\alpha = x, y$[3] and R_c is the contact resistance between graphene and electrodes 1 and 4. Although R_c may be smaller than the system resistance in the diffusive regime, its inclusion in equations (A.5)

[2] If the total charge current is set to $I_c = I_\uparrow + I_\downarrow = 0$, and because of perfect FM polarization $I_\downarrow = 0$, it follows that $I_\uparrow = 0$ and consequently the spin current is $I_s = I_\uparrow - I_\downarrow = 0$

[3] Here we have dropped the subscript x indicating the direction of the spin current for clarity.

and (A.10) assures that the spin accumulation is not forced to be zero at $x = -l_1$ and $x = l$, avoiding in this way contact-induced spin relaxation [59]. As shown in Figure 5.3, lead 2 (injector) is placed at $x = 0$, while lead 1 (drain) and 4 (reference) are located at $x = -l_1$ and $x = l$, respectively. Since there is no spin current flowing in to or out from the detector, the nonlocal resistance becomes simply half of the spin accumulation divided by the incoming current I_0:

$$R_{\mathrm{nl}} = \frac{\mu^y}{-2eI_0} = \frac{P_i P_d}{2w\sigma}\mathrm{Re}\left\{\frac{[\beta\cosh(l_1\kappa) + 4\sinh(l_1\kappa)]\cdot[\beta\cosh(\kappa(L-l)) - 4\sinh(\kappa(L-l))]}{\kappa[4\beta\cosh((l_1+l)\kappa) + (8+\beta^2/2)\sinh((l_1+l)\kappa)]}\right\}, \tag{A.11}$$

where we used equation 2.8, P_i (P_s) is the injector (detector) polarization and $\beta = R_{\mathrm{c}} w\sigma\kappa$, with σ being the electrical conductivity. By taking the appropriate limits, we can restore equation (4.2). Namely, if $\lambda_s << l_1, l$ such that $s^y(-l_1) \to 0$ and $s^y(l) \to 0$, R_{nl} becomes

$$R_{\mathrm{nl}} = \frac{P_i P_i}{2w\sigma}\mathrm{Re}\left\{\frac{e^{-L\kappa}}{\kappa}\right\}. \tag{A.12}$$

Importantly, we can also take the limit in equation (4.3) of $\lambda_s \to \infty$ resulting in a linear scaling of the nonlocal resistance with the injector-detector distance:

$$R_{\mathrm{nl}} = \frac{P_i P_d}{2w\sigma}\frac{(4R_{l_1} + R_{\mathrm{c}})(-4L + 4l + R_{\mathrm{c}} w\sigma)}{8R_{l_1} + 8R_l + 4R_{\mathrm{c}}}, \tag{A.13}$$

with $R_{l_1} = l_1/(w\sigma)$ and $R_l = l/(w\sigma)$ being the sheet resistance of the left and right-handed device region, respectively. This limit allows as to treat the cases $\lambda_s \geq l_1, l$ and reveals that even when there is no sources of spin relaxation, the nonlocal resistance does decrease with length in the diffusive regime.

APPENDIX B

SPIN RELAXATION INDUCED BY RANDOM MAGNETIC FLUCTUATIONS

Here, we derive the scaling of the spin diffusion length with the magnetic disorder strength J. We start by considering an initial spin state in the y direction, whose relaxation rate $\frac{1}{\tau_s^y}$ induced by a fluctuating magnetic fields reads [67]

$$\frac{1}{\tau_s^y} = \overline{\omega_z^2}\tau_c + \overline{\omega_x^2}\frac{\tau_c}{\omega_0^2\tau_c^2 + 1}, \tag{B.1}$$

with $\overline{\omega}_\alpha$ being the time-averaged precession frequency in the $\alpha = x, y, z$ direction originating from the fluctuating field, ω_0 is the constant precession frequency from the external field (here in the z direction) and τ_c is the correlation time, that is, the time it takes for the spin to experience a change in the fluctuating field. In our case, the fluctuating field arises from each atom having an exchange term J with random orientation, thus $\overline{\omega_z^2} = \overline{\omega_x^2} = \overline{\omega^2} = \left(\frac{g|J|}{\hbar}\right)^2$. In addition, for the length dependence of R_{nl}, $\omega_0 = 0$. Our model is not actually time-dependent but length-dependent, with the correlation length being the carbon-carbon distance a_c. Therefore, we can express τ_c as $\tau_c = a_c/v_{\mathrm{F}}$. After these considerations, the spin relaxation rate can be simplified to:

$$\frac{1}{\tau_s^y} = \overline{\omega_z^2}\tau_c + \overline{\omega_x^2}\tau_c = 2\overline{\omega^2}\tau_c = 2\left(\frac{g|J|}{\hbar}\right)^2\frac{a_{\mathrm{c}}}{v_{\mathrm{F}}} \propto |J|^2. \tag{B.2}$$

This shows a dependence of $1/J^2$ in the spin lifetime. Since in the diffusive regime $\lambda_s = \sqrt{D\tau_s}$, we eventually obtain the $1/J$ trend showed in Figure 5.4.

APPENDIX C

SYMMETRY-ALLOWED SPIN HALL CONDUCTIVITY OF 1T′ AND $1T_D$ TMDS

A crystal symmetry is a transformation that leaves the electronic properties and observables invariant. Thus, to characterize the implications of the physical symmetries, it is sufficient to analyze under which conditions they leave the spin-orbit interaction and the trace above unaltered. To do this, let us define the yz-plane as M_x, the zx-plane as M_y, and the xy-plane as M_z. These three planes are mutually orthogonal. Now, suppose that the only symmetries of the system are reflections.

The charge current and momentum operators are polar vectors, while the spin is a pseudo-vector. These mathematical objects behave differently under symmetry operations. A polar vector subject to a reflection on a mirror plane changes the direction of the components that are perpendicular to it. Meanwhile, under the same operation, pseudo-vectors invert the direction of all components lying on the mirror plane only. From these properties, if p_α, J_α and s_α are the $\alpha = x, y, z$ component of the momentum, current and spin operators, respectively, we readily obtain how

$$\begin{aligned}
&(p_x, p_y) \xrightarrow{M_x} (-p_x, p_y), && (p_x, p_y) \xrightarrow{M_y} (p_x, -p_y),\\
&(J_x, J_y) \xrightarrow{M_x} (-J_x, J_y), && (J_x, J_y) \xrightarrow{M_y} (J_x, -J_y),\\
&(s_x, s_y, s_z) \xrightarrow{M_x} (s_x, -s_y, -s_z), && (s_x, s_y, s_z) \xrightarrow{M_y} (-s_x, s_y, -s_z)
\end{aligned} \tag{C.1}$$

These transformation properties imposed on crystals having the two orthogonal mirror planes constrain the spin-orbit interaction to, at most, have the form

$$\mathcal{H}_{\mathrm{SOC}} = \Lambda_y k_x s_y + \Lambda_x k_y s_x, \tag{C.2}$$

with Λ_α and k_α the SOC strength and the momentum, respectively. This Hamiltonian will give rise to a spin texture lying in xy-plane similar to the Rashba coupling. Additionally, it also imposes constraints on the spin Hall conductivity (SHC), namely, $\sigma^x_{xy} \xrightarrow{M_x} -\sigma^x_{xy}$, and $\sigma^y_{xy} \xrightarrow{M_y} -\sigma^y_{xy}$, which means that the presence of these two orthogonal mirror planes allows only for a finite σ^z_{xy}, i.e., an SHC tensor that generates only out-of-plane (along z) spin polarization. Repeating the procedure for all the SHC components shows that only the components σ^α_{ij} are allowed. Consequently, in such a system, the spin Hall effect can only generate mutually orthogonal charge current, spin current, and spin polarization.

Bulk multilayers of $1T_d$ TMDs contains the two mirror symmetries discussed above, M_x which is a true point symmetry, and M_y that is a glide-mirror symmetry. However, in the monolayer, the loss of translation symmetry along the layer-stacking z direction implies the concomitant loss of the glide mirror M_y. Repeating the above arguments without this symmetry element permits demonstrating that the spin-orbit coupling takes the generic form

$$\mathcal{H}_{\mathrm{SOC}} = \Lambda_y k_x s_y + \Lambda_x k_y \sigma_x + \Lambda_z k_x s_z \tag{C.3}$$

which allows for an spin texture with both in- and out-of-plane spin components and also enable the components of the SHC tensor with spins polarized in the y direction, σ^y_{xy}.

Overall, in a 2D crystal in the presence of both M_x and M_y, the only allowed components of the SHC are σ^z_{xy} and its cyclical permutations. Lowering the symmetry removes certain constraints that prohibit specific components, as in the monolayer (or few-layer) $1T_d$-$MoTe_2$ and $1T_d$-WTe_2 where only M_x is left, thus enabling unconventional directions of spin textures and SHC. On the other hand, the different symmetries of the $1T'$ phase with respect to $1T_d$ (see section 2.2.2) allows for unconventional terms of the SHC tensor even in the bulk. We summarize all the possible terms of the SHC tensor for both $1T_d$ and $1T'$ phases in the following tables[1]:

[1]Courtesy of C.-H. Hsu.

Table 1: SHC tensor form of Td-$MoTe_2$

	s_x	s_y	s_z
		Bulk	
Space Group $Pmn2_1$	$\begin{pmatrix} 0 & 0 & 0 \\ 0 & 0 & \sigma^x_{yz} \\ 0 & \sigma^x_{zy} & 0 \end{pmatrix}$	$\begin{pmatrix} 0 & 0 & \sigma^y_{xz} \\ 0 & 0 & 0 \\ \sigma^y_{zx} & 0 & 0 \end{pmatrix}$	$\begin{pmatrix} 0 & \sigma^z_{xy} & 0 \\ \sigma^z_{yx} & 0 & 0 \\ 0 & 0 & 0 \end{pmatrix}$
		Few-Layer	
Layer Group $Pm11$	$\begin{pmatrix} \sigma^x_{xx} & 0 & 0 \\ 0 & \sigma^x_{yy} & \sigma^x_{yz} \\ 0 & \sigma^x_{zy} & \sigma^x_{zz} \end{pmatrix}$	$\begin{pmatrix} 0 & \sigma^y_{xy} & \sigma^y_{xz} \\ \sigma^y_{yx} & 0 & 0 \\ \sigma^y_{zx} & 0 & 0 \end{pmatrix}$	$\begin{pmatrix} 0 & \sigma^z_{xy} & \sigma^z_{xz} \\ \sigma^z_{yx} & 0 & 0 \\ \sigma^z_{zx} & 0 & 0 \end{pmatrix}$

Table 2: SHC tensor form of 1T'-$MoTe_2$

	s_x	s_y	s_z
		Bulk	
Space Group $P2_1/m$	$\begin{pmatrix} \sigma^x_{xx} & 0 & 0 \\ 0 & \sigma^x_{yy} & \sigma^x_{yz} \\ 0 & \sigma^x_{zy} & \sigma^x_{zz} \end{pmatrix}$	$\begin{pmatrix} 0 & \sigma^y_{xy} & \sigma^y_{xz} \\ \sigma^y_{yx} & 0 & 0 \\ \sigma^y_{zx} & 0 & 0 \end{pmatrix}$	$\begin{pmatrix} 0 & \sigma^z_{xy} & \sigma^z_{xz} \\ \sigma^z_{yx} & 0 & 0 \\ \sigma^z_{zx} & \sigma & 0 \end{pmatrix}$
		Few-Layer	
Layer Group $P2/m11$	$\begin{pmatrix} \sigma^x_{xx} & 0 & 0 \\ 0 & \sigma^x_{yy} & \sigma^x_{yz} \\ 0 & \sigma^x_{zy} & \sigma^x_{zz} \end{pmatrix}$	$\begin{pmatrix} 0 & \sigma^y_{xy} & \sigma^y_{xz} \\ \sigma^y_{yx} & 0 & 0 \\ \sigma^y_{zx} & 0 & 0 \end{pmatrix}$	$\begin{pmatrix} 0 & \sigma^z_{xy} & \sigma^z_{xz} \\ \sigma^z_{yx} & 0 & 0 \\ \sigma^z_{zx} & 0 & 0 \end{pmatrix}$

APPENDIX D

DERIVATION THE SPIN HALL ANGLE FORMULA IN TWO-TERMINAL DEVICES

In this section we derive an expression connecting the spin accumulation at the edges ($x = 0$ and $x = w$) of the device described in Figure D.1(a), with the spin Hall angle; and then adapt it to fit the spin accumulation obtained in Kwant [94]. We note that in this case, we drive current along the y direction, in contrast to the previous calculations. This is because we want the spin transport to be along x, so the obtained spin diffusion lengths from the nonlocal spin valve can be taken into account. To start, let us cast the constitutive relations for the charge $\boldsymbol{J}_c$ and spin $\boldsymbol{J}_s^\alpha$ current densities

$$\begin{aligned} \boldsymbol{J}_c &= (\overline{\sigma} - \overline{\sigma}_{\mathrm{sH}}^{\alpha})\boldsymbol{E} - e\overline{D}_c \boldsymbol{\nabla} n \\ \boldsymbol{J}_s^\alpha &= \overline{\sigma}_{\mathrm{sH}}^{\alpha}\boldsymbol{E} - e\overline{D}_s^{\alpha} \boldsymbol{\nabla} s^\alpha, \end{aligned} \tag{D.1}$$

where $\boldsymbol{E}$ the electric field, $\overline{\sigma}$ the electrical conductivity tensor which due to time-reversal symmetry is diagonal

$$\overline{\sigma}_{ij} = \delta_{ij}\sigma_{ii}, \tag{D.2}$$

n the charge density in units of inverse of area, $\overline{D}_c$ the charge diffusion tensor which is proportional to the conductivity by the Einstein's relations, $\overline{D}_s^{\alpha}$ the spin diffusion tensor which we assume to be the same as the charge $\overline{D}_c$ because we consider diffusive transport (thus we drop the superscript α), and $\overline{\sigma}_{\mathrm{sH}}^{\alpha}$ the spin Hall conductivity tensor

$$\overline{\sigma}_{\mathrm{sH}}^{\alpha} = \begin{pmatrix} 0 & \sigma_{xy}^{\alpha} \\ \sigma_{yx}^{\alpha} & 0 \end{pmatrix} \tag{D.3}$$

where the matrix element σ_{ij}^{α} represents the formation of a spin current flowing along the $i = x, y$ direction with spins polarized in $\alpha = x, y, z$ due to a charge current flowing along $j = x, y$. The difference in the sign of the spin Hall conductivity in the charge and spin equations (equation (D.1)) is a consequence of Onsager's relations, while the absence of diagonal elements in the spin conductivity originates from time-reversal symmetry.

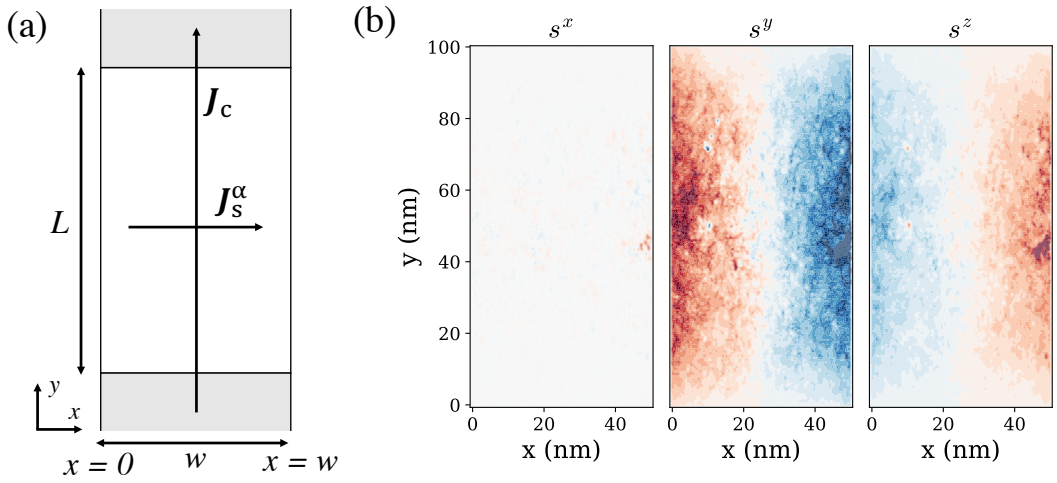

Figure D.1: (a) Schematics of the device geometry. Grey (white) regions depict the semiinfinite leads (scattering region). The positive convention for the spin Hall angle is taken when the spin current flows to the right with respect to the charge current. (b) Calculated spin accumulation $s^{\alpha=x,y,z}$ in a device with width 50 nm and length 100 nm. Red (blue) color denotes positive (negative) values of the spin accumulation.

In our device configuration, charge current is mostly driven by the electric field $J_{c,y} \approx \sigma_{yy} E_y$, and although there is an additional contribution coming from the inverse spin Hall effect, it is a second order effect which we will neglect. Since there is only charge current along the y direction, we will drop the y index henceforth. Likewise, the absence of diagonal terms in the spin Hall conductivity imposes that $\boldsymbol{J}_c$ and $\boldsymbol{J}_s^{\alpha}$ are perpendicular to each other. This allows us to focus only in a single element of the spin diffusion tensor $(\overline{D}_s)_{xx} \rightarrow D_s$ and the spin Hall conductivity $\overline{\sigma}_{\mathrm{sH}}^{\alpha} \rightarrow \sigma_{xy}^{\alpha}$. The spin density or accumulation, s^{α}, can be computed by combining equation (D.1) with the continuity equation

$$\boldsymbol{\nabla} \cdot \boldsymbol{J}_s^{\alpha} = -e \frac{s^{\alpha}}{\tau_s^{\alpha}}, \tag{D.4}$$

leading to the following diffusion equation

$$\nabla^2 s^{\alpha} = \frac{s^{\alpha}}{\lambda_s^{\alpha 2}}, \tag{D.5}$$

where we have introduced a spin relaxation time τ_s^α for describing the spin relaxation processes, which is related to the spin diffusion length by $\lambda_s^{\alpha 2} \equiv D_s \tau_s^\alpha$. In our case, the spin density varies only along the x direction, therefore, a general solution for the diffusion equation is

$$s^\alpha(x) = A\mathrm{e}^{-x/\lambda_s^\alpha} + B\mathrm{e}^{x/\lambda_s^\alpha}, \tag{D.6}$$

which stills needs to be supplemented by the boundary conditions

$$\boldsymbol{J}_s^\alpha(x=0) = 0, \quad \boldsymbol{J}_s^\alpha(x=w) = 0, \tag{D.7}$$

which by equation (D.1) implies

$$eD_s \frac{ds^\alpha}{dx}\bigg|_{0,w} = \theta_{xy}^\alpha J_c \tag{D.8}$$

at the edges, where we have introduced the spin Hall angle (SHA) $\theta_{xy}^\alpha \equiv \sigma_{xy}^\alpha/\sigma_{yy}$. Using these boundary conditions one finally finds the spin density

$$s^\alpha(x) = -\frac{\theta_{xy}^\alpha \lambda_s^\alpha J_c}{eD_s} \frac{\sinh\left(\frac{w-2x}{2\lambda_s^\alpha}\right)}{\cosh\left(\frac{w}{2\lambda_s^\alpha}\right)}. \tag{D.9}$$

This spin density has units of m^{-2} since J_c has units of A/m, λ_s^α has units of m, D_s has units of m^2/s, e has units of Coulomb and θ_{xy}^α is unitless. However, Kwant calculates the spin accumulation response function locally at site i per unit bias voltage V_b at energy E [94]:

$$s_{\mathrm{K},i}^\alpha(E) = \frac{\delta s_i^\alpha(E)}{\delta V_b} = \sum_j^M \psi_i^{j\dagger}(E)\sigma_\alpha \psi_i^j(E), \tag{D.10}$$

thus having units of V^{-1}. Here, $\psi_i^j(E)$ is the wave function at energy E at site i, originating from the incoming wave function of mode j of one of the leads; σ_α is the Pauli matrix and M is the total number of modes at energy E. We note that in equation (D.9), $\theta_{xy}^\alpha, \lambda_s^\alpha$ and D_s are also energy-dependent, but we drop the E dependence to keep the equations more compact.

In Figure D.1(b), we show $s_{\mathrm{K},i}^\alpha(E=0)$. We chose $w = 50$ nm and $L = 100$ nm so the transport was diffusive for the most part for all energies studied. It is clearly seen that a spin accumulation arises for spins in the y and z direction, but not in x. As commented in Appendix C, the appearance of an unconventional in-plane component of the spin Hall effect (s^y) is rooted in the low symmetry of the layer group of 1T′ and $1\mathrm{T}_\mathrm{d}$ TMDs [251]. Since equation (D.9) describes the spin accumulation along the x direction only, we now

need to average the y component of $s^{\alpha}_{\mathrm{K},i}(E)$:

$$s^{\alpha}_{\mathrm{K}}(x) = \frac{\sum_i^N s^{\alpha}_{\mathrm{K,i}}(x, y_i)}{N}, \tag{D.11}$$

where we have also dropped the E dependence for simplicity. Here, N is the number of sites i along the y direction.

We can finally equate equation (D.9), embodying the spin transport parameters we are interested in, with the averaged simulation output, $s^{\alpha}_{\mathrm{K}}(x)$. If A is the area of site i (corresponding to the area of the rectangular unit cell in our case), we have:

$$s^{\alpha}(x)A = s^{\alpha}_{\mathrm{K}}(x)\frac{V_b}{2\pi}, \tag{D.12}$$

with the factor 2π appearing naturally in the Landauer-Büttiker formalism [54, 84]. We can relate the bias voltage to the current in the linear response regime by $I_c = \frac{e^2}{h}\overline{T}V_b$, where $\overline{T} = MT$ is the two-terminal transmission function (with T the transmission probability per mode) obtained from the two-terminal conductance of the device in Figure D.1(a) ($G_{2textT} = \frac{e^2}{h}\overline{T}$). Together with $I_c = wJ_c$, we obtain:

$$s^{\alpha}(x)A = s^{\alpha}_{\mathrm{K}}(x)\frac{J_c\hbar w}{e^2\overline{T}}. \tag{D.13}$$

By rearranging the terms and using equation (D.9), we finally arrive at:

$$\frac{s^{\alpha}(x)}{J_c} = s^{\alpha}_{\mathrm{K}}(x)\frac{\hbar w}{e^2 A\overline{T}} = -\frac{\theta^{\alpha}_{xy}\lambda^{\alpha}_s}{eD_s}\frac{\sinh\left(\frac{w-2x}{2\lambda^{\alpha}_s}\right)}{\cosh\left(\frac{w}{2\lambda^{\alpha}_s}\right)}, \tag{D.14}$$

or alternatively:

$$s^{\alpha}_{\mathrm{K}}(x) = -\theta^{\alpha}_{xy}\lambda^{\alpha}_s\frac{eA\overline{T}}{D_s\hbar w}\frac{\sinh\left(\frac{w-2x}{2\lambda^{\alpha}_s}\right)}{\cosh\left(\frac{w}{2\lambda^{\alpha}_s}\right)}, \tag{D.15}$$

Hence, we find that we need to add the prefactor $\frac{\hbar w}{e^2 A\overline{T}}$ ($\hbar$ in units J·s) to the output of Kwant to fit it to the solution of the spin drift-diffusion equations. To fit the spin Hall angle, we also need the values of the spin diffusion coefficient and the spin diffusion lengths. The former is taken as the value of D_c obtained from the two-terminal conductance (see values in Table 5.1), as we consider diffusive transport, and the latter is taken from the nonlocal spin valve simulations by fitting the nonlocal resistance to equation (4.3).

APPENDIX E

EXPERIMENTAL SETUP FOR MEASURING THE OBLIQUE SPIN HALL EFFECT

In this section, we present the formulation to calculate the output voltage in a realistic nonlocal device, allowing in this way the measurement of the oblique SHE. The one-dimensional steady-state Bloch diffusion equation is used to calculate the spin density $\boldsymbol{s} = (s^x, s^y, s^z)$ over the graphene channel and reaching the TMD [21,22], according to the experimental setup described in the main text. In the presence of an external magnetic field $\boldsymbol{B}$, the diffusion equation reads:

$$D_s \frac{d^2\boldsymbol{s}}{dx^2} + \gamma\, \boldsymbol{s} \times \boldsymbol{B} - \overline{\tau_s^{-1}} \cdot \boldsymbol{s} = 0. \tag{E.1}$$

The three components of $\boldsymbol{s}$ describe the spin density projected along the corresponding Cartesian axes. $\gamma = 2\,\mu_B/\hbar$ is the electron gyromagnetic ratio with μ_B the Bohr magneton and $\overline{\tau_s^{-1}}$ is a 3×3 diagonal matrix containing the spin relaxation times in x, y and z.

Within this model, the spin transport in the device (schematic in Figure 5.12 in Chapter 5) is characterized by simultaneous diffusive and precessional motion under a magnetic field that is chosen to be either along the x or z direction. All the components of $\boldsymbol{s}$ are calculated at any position and, therefore, the spin-current densities that generate the SHE. The solution of equation (E.1) is adapted from Ref. [21]. When the TMD crystal is oriented in the configuration shown in Figure 5.12(a) (configuration a), the spin current density flowing in the x direction with spins in the yz plane, $J_{s,x}^{y,z}$, generates a transverse charge current density, $J_{c,y}$, that is detected as a $R_{\mathrm{ISHE}} = V_{\mathrm{ISHE}}/I_0^y$ due to the inverse SHE. Here, I_0^y is the injected current, which is polarized along the direction of the ferromagnetic injector (y in this case, see insets in Figure 5.12). If the TMD crystal is oriented in the configuration shown in Figure 5.12(b) (configuration b), $J_{c,y}$ is generated

by the spin current density with spins along z and x directions (y in the TMD's system of coordinates, which have been rotated with respect to those in Figure 5.12(a)). In general, $J^{\alpha}_{s,x}$ is [21],

$$J^{\alpha}_{s,x} = |\boldsymbol{J}_{s,x}| = \frac{1}{e\, l_{\rm w}\, R_{\square}} \int_{x_0}^{x_0+l_{\rm w}} \frac{d\, s^{\alpha}(x)}{dx} dx = \frac{\Delta s^{\alpha}}{e\, l_{\rm w}\, R_{\square}}, \tag{E.2}$$

where $s^{\alpha}(x)$ is given by equation (E.1) and $\Delta s^{\alpha} = s^{\alpha}(x_0 + l_{\rm w}) - s^{\alpha}(x_0)$. x_0, l_w, $R_{\square}$ are the distance of the TMD to the injector, the TMD width and its square resistance, respectively. In the simulations presented in Figure 4 of the main text, we use $x_0 = 3.9\,\mu$m, $l_w = 1.6\,\mu$m and $R_{\square} = 3.3$ kΩ, and a spin polarization of the FM injector of 10%. Once the spin current of each spin component is known, the generated charge current can be easily obtained given that $J_{c,x} = \theta^{\alpha}_{xy}\, J^{\alpha}_{s,y}$ and $R_{\rm SHE} = J_c\, l_{\rm w}\, R_a / I^{y}_{0}$. We note that here the relation between the charge and spin current densities is opposite to that of equation (D.8) since we are dealing with the inverse SHE, which is reciprocal to the SHE. In this way,

$$R_{\rm SHE} = \theta^{\alpha}_{xy}\, c\, \Delta s^{\alpha};\ \text{with}\, c = \frac{R_a}{e R_{\square} I^{y}_{0}}, \tag{E.3}$$

with R_a the resistance of the TMD channel. The conversion efficiency is related to the spin Hall angle, θ^{α}_{xy} , which depends on the spin orientation, α. The total charge current density is calculated from the independent contributions of $J^{z,y}_{s}$.

In the configuration (a) with B_z, $R_{\rm SHE} = -\theta^{y}_{xy}\, c\, \Delta s^{y}$, $\theta^{y}_{xy} = 0.8$. In an experiment the sign depends on the voltage polarity. Here we choose that $R_{\rm SHE} = |\theta^{y}_{xy}|\, c\, \Delta s^{y}$, which switches the sign for θ^{z}_{xy}. For B_x, $R_{\rm SHE} = |\theta^{y}_{xy}|\, c\, \Delta s^{y} - |\theta^{z}_{xy}|\, c\, \Delta s^{z}$, with $\theta^{z}_{xy} = 0.5$ and according to the chosen polarity convention. For the configuration (b) with B_z, $R_{\rm SHE} = |\theta^{y}_{xy}|\, c\, \Delta s^{y}$, and with B_y, $R_{\rm SHE} = -|\theta^{z}_{xy}|\, c\, \Delta s^{z}$. Note that here we are referring according to the TMD system of coordinates (see Fig 4 (b) in the main text).

Finally, we present arguments that show that the spin current flowing in the graphene channel will be absorbed by the TMD. The spin resistance of a material is defined as $R_s = \rho\lambda_s/A$, ρ is the resistivity and A the cross area in which the spins flow. An alternative to this definition in terms of the square resistance, is $R_s = R_{\square}\lambda_s/w_N$, where w_N is the width of the nonmagnetic material. In the device proposed, the cross width where spins propagate is the same for graphene (g) and TMD. The ratio of the graphene's spin resistance and the TMD's spin resistance reads as,

$$\frac{R^{\rm TMD}_{s}}{R^{\rm g}_{s}} = \frac{R^{\rm TMD}_{\square}}{R^{\rm g}_{\square}} \frac{\lambda^{\rm TMD}_{s}}{\lambda^{\rm g}_{s}} \tag{E.4}$$

Using reported values of $R^{\rm g}_{\square} \approx 2$ kΩ [22] and $R^{\rm TMD}_{\square} \approx 3.3$ kΩ for 1T' $MoTe_2$ [312]

$$\frac{R_s^{\mathrm{TMD}}}{R_s^{\mathrm{g}}} \sim \frac{\lambda_s^{\mathrm{TMD}}}{\lambda_s^{\mathrm{g}}} \tag{E.5}$$

Comparing the calculated $\lambda_s^y \approx 30$ nm with the typical $\lambda_s^{\mathrm{g}} \approx 1.6\,\mu$m [22], we have that $R_s^{\mathrm{TMD}} \sim 0.01 R_s^{\mathrm{g}}$, and of the same order for λ_s^z.

APPENDIX F

NONLOCAL RESISTANCE QUANTIZATION IN THE QUANTUM SPIN HALL EFFECT

In the following, we calculate the analytical values of the expected nonlocal resistances in a 6-terminal Hall bar geometry, as shown in Figure F.1, where it is assumed that the only conducting channels are the topological helical states of the quantum spin Hall effect. The results are the same obtained in the pioneering work of Roth *et. al.* [222].

We begin by writing the relationship between the current and voltage $\mathbf{I} = \mathbf{G} \cdot \mathbf{V}$ in the QSHE regime. In such a case, we can distinguish at least 2 counterpropagating states located at the sample edge, as drawn in Figure F.1, with opposite spin polarization. Because the conduction is solely along the edge, a spin-up state injected by lead $p = i$ will be transmitted only to lead $p = i + 1$ and a spin-down mode will go to $p = i - 1$. Furthermore, because of the topological protection, the transport in these channels is

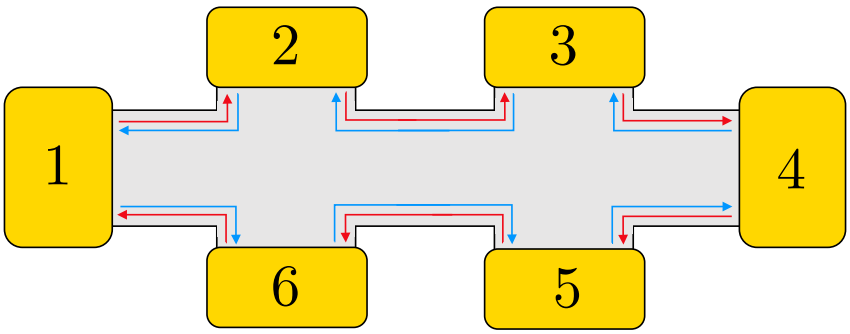

Figure F.1: Sketch of a 6-terminal Hall bar device with the leads numerated from 1 to 6. Red and blue arrows represent opposite spin polarization of the topological states of the QSHE.

assumed ballistic and hence the transmission is unity. In this way, we can write:

$$\begin{pmatrix} I_1 \\ I_2 \\ I_3 \\ I_4 \\ I_5 \\ I_6 \end{pmatrix} = \begin{pmatrix} 2 & -1 & 0 & 0 & 0 & -1 \\ -1 & 2 & -1 & 0 & 0 & 0 \\ 0 & -1 & 2 & -1 & 0 & 0 \\ 0 & 0 & -1 & 2 & -1 & 0 \\ 0 & 0 & 0 & -1 & 2 & -1 \\ -1 & 0 & 0 & 0 & -1 & 2 \end{pmatrix} \begin{pmatrix} V_1 \\ V_2 \\ V_3 \\ V_4 \\ V_5 \\ V_6 \end{pmatrix}. \tag{F.1}$$

By applying the current and voltage conditions, we can now obtain the values of the nonlocal resistances showed in Figure 5.18 in Chapter 5. When the current is applied between leads 1 and 4, and we ground lead 4, we have the equations (after removing the 4^{th} row and column):

$$\begin{pmatrix} I \\ 0 \\ 0 \\ 0 \\ 0 \end{pmatrix} = \begin{pmatrix} 2 & -1 & 0 & 0 & -1 \\ -1 & 2 & -1 & 0 & 0 \\ 0 & -1 & 2 & 0 & 0 \\ 0 & 0 & 0 & 2 & -1 \\ -1 & 0 & 0 & -1 & 2 \end{pmatrix} \begin{pmatrix} V_1 \\ V_2 \\ V_3 \\ V_5 \\ V_6 \end{pmatrix}, \tag{F.2}$$

which result in the following voltages:

$$V_1 = \frac{3I}{2}, \quad V_2 = I, \quad V_3 = \frac{I}{2}, \quad V_4 = 0, \quad V_5 = \frac{I}{2}, \quad V_6 = I. \tag{F.3}$$

Consequently, the resistances plotted in Figure 5.18 are:

$$R_{14,23} = \frac{V_2 - V_3}{I} = \frac{1}{2} \tag{F.4}$$

$$R_{14,35} = \frac{V_3 - V_5}{I} = 0. \tag{F.5}$$

To obtain $R_{62,53}$, we need to construct again the system of equations $\mathbf{I} = \mathbf{G} \cdot \mathbf{V}$ with another condition for the currents, namely $\mathbf{I} = (0, -I, 0, 0, 0, I)$:

$$\begin{pmatrix} 0 \\ 0 \\ 0 \\ 0 \\ 0 \end{pmatrix} = \begin{pmatrix} 2 & 0 & 0 & 0 & -1 \\ 0 & 2 & -1 & 0 & 0 \\ 0 & -1 & 2 & -1 & 0 \\ 0 & 0 & -1 & 2 & -1 \\ -1 & 0 & 0 & -1 & 2 \end{pmatrix} \begin{pmatrix} V_1 \\ V_3 \\ V_4 \\ V_5 \\ V_6 \end{pmatrix}, \tag{F.6}$$

where now we have removed the 2^{nd} row and column. This gives the following voltages:

$$V_1 = \frac{2I}{3}, \quad V_2 = 0, \quad V_3 = \frac{I}{3}, \quad V_4 = \frac{2I}{3}, \quad V_5 = I, \quad V_6 = \frac{4I}{3}, \tag{F.7}$$

and the resistance is

$$R_{62,53} = \frac{V_5 - V_3}{I} = \frac{2}{3}. \tag{F.8}$$

LIST OF ACRONYMS AND USEFUL SYMBOLS

- DFT - Density functional theory
- SOC - Spin-orbit coupling
- NSV - Nonlocal spin valve
- TB - Tight-binding
- LB - Landauer-Büttiker
- QSH - Quantum spin Hall
- QSHE - Quantum spin Hall Effect
- 1D - One-dimensional
- 2D - Two-dimensional
- 3D - Three-dimensional
- 2DEG - Two-dimensional electron gas
- 2T - Two-terminal
- TMD - Transition metal dichalcogenide
- ECP - Electrochemical potential
- FM - Ferromagnetic
- ISGE - Inverse Spin galvanic effect
- (I)SHE - (Inverse) Spin Hall effect

- SHA - Spin Hall angle
- SHC - Spin Hall conductivity
- SHC - Spin Berry curvature
- SR - Scattering Region
- $\boldsymbol{s}_\sigma = (s_x, s_y, s_z)$ - vector of spin Pauli matrices
- s_α - spin-α Pauli matrix
- $\boldsymbol{s}$ - nonequilibrium spin accumulation or density
- s^α - nonequilibrium spin accumulation along α.
- $\langle s^\alpha_{(n)}(k)\rangle$ - spin texture of spin-α at k (implicit band n)
- $\langle s^\alpha_{(n)}\rangle_E$ - spin texture of spin-α at energy E (implicit band n)
- $\boldsymbol{J}_{s,\alpha}$ - Spin current vector in the α direction with components $(J^x_{s,\alpha}, J^y_{s,\alpha}, J^z_{s,\alpha})$
- $\boldsymbol{J}^\alpha_s$ - Spin current vector for α-spins with components $(J^\alpha_{s,x}, J^\alpha_{s,y}, J^\alpha_{s,z})$

LIST OF FIGURES

LIST OF TABLES

REFERENCES

[1] D. A. Abanin, A. V. Shytov, L. S. Levitov, and B. I. Halperin. Nonlocal charge transport mediated by spin diffusion in the spin hall effect regime. *Phys. Rev. B*, 79:035304, Jan 2009.

[2] E. Abrahams, P. W. Anderson, D. C. Licciardello, and T. V. Ramakrishnan. Scaling theory of localization: Absence of quantum diffusion in two dimensions. *Phys. Rev. Lett.*, 42:673–676, Mar 1979.

[3] S. Adam, E. H. Hwang, V. M. Galitski, and S. Das Sarma. A self-consistent theory for graphene transport. *Proceedings of the National Academy of Sciences*, 104(47):18392–18397, 2007.

[4] S. Adam, S. Jung, N. N. Klimov, N. B. Zhitenev, J. A. Stroscio, and M. D. Stiles. Mechanism for puddle formation in graphene. *Phys. Rev. B*, 84:235421, Dec 2011.

[5] E. C. Ahn. 2d materials for spintronic devices. *npj 2D Materials and Applications*, 4(1):17, Jun 2020.

[6] W. Amamou, Z. Lin, J. van Baren, S. Turkyilmaz, J. Shi, and R. K. Kawakami. Contact induced spin relaxation in graphene spin valves with al2o3 and mgo tunnel barriers. *APL Materials*, 4:032503, 2016.

[7] P. R. Amestoy, I. S. Duff, J.-Y. L'Excellent, and J. Koster. A fully asynchronous multifrontal solver using distributed dynamic scheduling. *SIAM Journal on Matrix Analysis and Applications*, 23(1):15–41, 2001.

[8] P. W. Anderson. Absence of diffusion in certain random lattices. *Phys. Rev.*, 109:1492–1505, Mar 1958.

[9] A. Arora, L.-k. Shi, and J. C. W. Song. Cooperative orbital moments and edge magnetoresistance in monolayer WTe_2. *Phys. Rev. B*, 102:161402, Oct 2020.

[10] A. Avsar, H. Ochoa, F. Guinea, B. Özyilmaz, B. J. van Wees, and I. J. Vera-Marun. Colloquium: Spintronics in graphene and other two-dimensional materials. *Rev. Mod. Phys.*, 92:021003, Jun 2020.

[11] A. Avsar, T.-Y. Yang, S. Bae, J. Balakrishnan, F. Volmer, M. Jaiswal, Z. Yi, S. R. Ali, G. Gntherodt, B. H. Hong, B. Beschoten, and B. zyilmaz. Toward wafer scale fabrication of graphene based spin valve devices. *Nano Lett.*, 11(6):2363–2368, 2011.

[12] S. Bader and S. Parkin. Spintronics. *Annual Review of Condensed Matter Physics*, 1(1):71–88, 2010.

[13] M. N. Baibich, J. M. Broto, A. Fert, F. N. Van Dau, F. Petroff, P. Etienne, G. Creuzet, A. Friederich, and J. Chazelas. Giant magnetoresistance of (001)fe/(001)cr magnetic superlattices. *Phys. Rev. Lett.*, 61:2472–2475, Nov 1988.

[14] V. Baltz, A. Manchon, M. Tsoi, T. Moriyama, T. Ono, and Y. Tserkovnyak. Antiferromagnetic spintronics. *Rev. Mod. Phys.*, 90:015005, Feb 2018.

[15] S. Bandyopadhyay and M. Cahay. *Introduction to Spintronics*. CRC Press, 2008.

[16] L. Banszerus, M. Schmitz, S. Engels, J. Dauber, M. Oellers, F. Haupt, K. Watanabe, T. Taniguchi, B. Beschoten, and C. Stampfer. Ultrahigh-mobility graphene devices from chemical vapor deposition on reusable copper. *Sci. Adv.*, 1(6):e1500222, 2015.

[17] L. Banszerus, M. Schmitz, S. Engels, M. Goldsche, K. Watanabe, T. Taniguchi, B. Beschoten, and C. Stampfer. Ballistic transport exceeding 28 μm in cvd grown graphene. *Nano Lett.*, 16(2):1387–1391, 2015.

[18] A. Bastin, C. Lewiner, O. Betbeder-matibet, and P. Nozieres. Quantum oscillations of the hall effect of a fermion gas with random impurity scattering. *Journal of Physics and Chemistry of Solids*, 32(8):1811 – 1824, 1971.

[19] C. W. J. Beenakker. Random-matrix theory of quantum transport. *Rev. Mod. Phys.*, 69:731–808, Jul 1997.

[20] C. Bena and G. Montambaux. Remarks on the tight-binding model of graphene. *New J. Phys.*, 11(9):095003, 2009.

[21] L. A. Benítez, W. Savero Torres, J. F. Sierra, M. Timmermans, J. H. Garcia, S. Roche, M. V. Costache, and S. O. Valenzuela. Tunable room-temperature spin

galvanic and spin Hall effects in van der Waals heterostructures. *Nature Materials*, 19(2):170–175, 2020.

[22] L. A. Benítez, J. F. Sierra, W. Savero Torres, M. Timmermans, M. V. Costache, and S. O. Valenzuela. Investigating the spin-orbit interaction in van der Waals heterostructures by means of the spin relaxation anisotropy. *APL Mater.*, 7:120701, 2019.

[23] L. Berger. Emission of spin waves by a magnetic multilayer traversed by a current. *Phys. Rev. B*, 54:9353–9358, Oct 1996.

[24] B. A. Bernevig, T. L. Hughes, and S.-C. Zhang. Quantum spin hall effect and topological phase transition in hgte quantum wells. *Science*, 314(5806):1757–1761, 2006.

[25] B. A. Bernevig, J. Orenstein, and S.-C. Zhang. Exact su(2) symmetry and persistent spin helix in a spin-orbit coupled system. *Phys. Rev. Lett.*, 97:236601, Dec 2006.

[26] B. A. Bernevig and S.-C. Zhang. Quantum spin hall effect. *Phys. Rev. Lett.*, 96:106802, Mar 2006.

[27] S. Bhatti, R. Sbiaa, A. Hirohata, H. Ohno, S. Fukami, and S. N. Piramanayagam. Spintronics based random access memory: a review. *Materials Today*, 20(9):530 – 548, 2017.

[28] G. Binasch, P. Grünberg, F. Saurenbach, and W. Zinn. Enhanced magnetoresistance in layered magnetic structures with antiferromagnetic interlayer exchange. *Phys. Rev. B*, 39:4828–4830, Mar 1989.

[29] S. Borlenghi, V. Rychkov, C. Petitjean, and X. Waintal. Multiscale approach to spin transport in magnetic multilayers. *Phys. Rev. B*, 84:035412, Jul 2011.

[30] A. Brataas, A. D. Kent, and H. Ohno. Current-induced torques in magnetic materials. *Nature Materials*, 11(5):372–381, May 2012.

[31] M. Buchner, T. Kuczmik, M. Oltscher, M. Ciorga, T. Korn, J. Loher, D. Schuh, C. Schüller, D. Bougeard, D. Weiss, and C. H. Back. Optical investigation of electrical spin injection into an inverted two-dimensional electron gas structure. *Phys. Rev. B*, 95:035304, Jan 2017.

[32] M. Büttiker. Four-terminal phase-coherent conductance. *Phys. Rev. Lett.*, 57:1761–1764, Oct 1986.

[33] M. Büttiker, Y. Imry, R. Landauer, and S. Pinhas. Generalized many-channel conductance formula with application to small rings. *Phys. Rev. B*, 31:6207–6215, May 1985.

[34] Y. A. Bychkov and É. I. Rashba. Properties of a 2D electron gas with lifted spectral degeneracy. *Soviet Journal of Experimental and Theoretical Physics Letters*, 39:78, Jan. 1984.

[35] T. Cao, G. Wang, W. Han, H. Ye, C. Zhu, J. Shi, Q. Niu, P. Tan, E. Wang, B. Liu, and J. Feng. Valley-selective circular dichroism of monolayer molybdenum disulphide. *Nature Communications*, 3:885–887, 2012.

[36] A. H. Castro Neto, F. Guinea, N. M. R. Peres, K. S. Novoselov, and A. K. Geim. The electronic properties of graphene. *Rev. Mod. Phys.*, 81:109–162, Jan 2009.

[37] S. A. Cavill, C. Huang, M. Offidani, Y.-H. Lin, M. A. Cazalilla, and A. Ferreira. Proposal for unambiguous electrical detection of spin-charge conversion in lateral spin valves. *Phys. Rev. Lett.*, 124:236803, Jun 2020.

[38] T.-R. Chang, S.-Y. Xu, G. Chang, C.-C. Lee, S.-M. Huang, B. Wang, G. Bian, H. Zheng, D. S. Sanchez, I. Belopolski, N. Alidoust, M. Neupane, A. Bansil, H.-T. Jeng, H. Lin, and M. Zahid Hasan. Prediction of an arc-tunable Weyl fermion metallic state in $Mo_xW_{1-x}Te_2$. *Nature Communications*, 7(1):10639, Feb 2016.

[39] C. Chappert, A. Fert, and F. N. Van Dau. The emergence of spin electronics in data storage. *Nature Materials*, 6(11):813–823, Nov 2007.

[40] K. Chen and S. Zhang. Enhancement of spin accumulation in ballistic transport regime. *Phys. Rev. B*, 92:214402, Dec 2015.

[41] P. Chen, W. W. Pai, Y.-H. Chan, W.-L. Sun, C.-Z. Xu, D.-S. Lin, M. Y. Chou, A.-V. Fedorov, and T.-C. Chiang. Large quantum-spin-Hall gap in single-layer. *Nature Communications*, 9(1):1–7, May 2018.

[42] A. Chernyshov, M. Overby, X. Liu, J. K. Furdyna, Y. Lyanda-Geller, and L. P. Rokhinson. Evidence for reversible control of magnetization in a ferromagnetic material by means of spin–orbit magnetic field. *Nature Physics*, 5(9):656–659, Sep 2009.

[43] M. Chhowalla, H. S. Shin, G. Eda, L.-J. Li, K. P. Loh, and H. Zhang. The chemistry of two-dimensional layered transition metal dichalcogenide nanosheets. *Nature Chemistry*, 5(4):263–275, Apr 2013.

[44] C. Ciccarelli, K. M. D. Hals, A. Irvine, V. Novak, Y. Tserkovnyak, H. Kurebayashi, A. Brataas, and A. Ferguson. Magnonic charge pumping via spin–orbit coupling. *Nature Nanotechnology*, 10(1):50–54, Jan 2015.

[45] L. J. Cornelissen, J. Liu, R. A. Duine, J. B. Youssef, and B. J. van Wees. Long-distance transport of magnon spin information in a magnetic insulator at room temperature. *Nature Physics*, 11(12):1022–1026, Dec 2015.

[46] E. Coronado and A. J. Epsetin. Molecular spintronics and quantum computing. *J. Mater. Chem.*, 19:1670–1671, 2009.

[47] M. V. Costache, M. Sladkov, S. M. Watts, C. H. van der Wal, and B. J. van Wees. Electrical detection of spin pumping due to the precessing magnetization of a single ferromagnet. *Phys. Rev. Lett.*, 97:216603, Nov 2006.

[48] C. J. Cramer. *Essentials of Computational Chemistry: Theories and Models*. Wiley, New York, 2005.

[49] A. Cresti, N. Nemec, B. Biel, G. Niebler, F. Triozon, G. Cuniberti, and S. Roche. Charge transport in disordered graphene-based low dimensional materials. *Nano Research*, 1(5):361–394, Nov 2008.

[50] A. Cresti, B. K. Nikolić, J. H. García, and S. Roche. Charge, spin and valley Hall effects in disordered graphene. *Riv. Nuovo Cimento*, 39:587, 2016.

[51] A. W. Cummings and S. Roche. Effects of dephasing on spin lifetime in ballistic spin-orbit materials. *Phys. Rev. Lett.*, 116:086602, 2016.

[52] T. P. Cysne, A. Ferreira, and T. G. Rappoport. Crystal-field effects in graphene with interface-induced spin-orbit coupling. *Phys. Rev. B*, 98(4):045407, jul 2018.

[53] S. Das Sarma, S. Adam, E. H. Hwang, and E. Rossi. Electronic transport in two-dimensional graphene. *Rev. Mod. Phys.*, 83:407–470, May 2011.

[54] S. Datta. *Electronic transport in mesoscopic systems*. Cambridge University Press, 1997.

[55] S. Datta and B. Das. Electronic analog of the electrooptic modulator. *Applied Physics Letters*, 56(7):665–667, 1990.

[56] M. DC, R. Grassi, J.-Y. Chen, M. Jamali, D. Reifsnyder Hickey, D. Zhang, Z. Zhao, H. Li, P. Quarterman, Y. Lv, M. Li, A. Manchon, K. A. Mkhoyan, T. Low, and J.-P. Wang. Room-temperature high spin–orbit torque due to quantum confinement in sputtered bixse(1–x) films. *Nature Materials*, 17(9):800–807, Sep 2018.

[57] G. Dresselhaus. Spin-orbit coupling effects in zinc blende structures. *Phys. Rev.*, 100:580–586, Oct 1955.

[58] M. Drögeler, C. Franzen, F. Volmer, T. Pohlmann, L. Banszerus, M. Wolter, K. Watanabe, T. Taniguchi, C. Stampfer, and B. Beschoten. Spin lifetimes exceeding 12 nanoseconds in graphene non-local spin valve devices. *Nano Lett.*, 16(6):3533, 2016.

[59] M. Drögeler, F. Volmer, C. Stampfer, and B. Beschoten. Simulations on the influence of spatially varying spin transport parameters on the measured spin lifetime in graphene non-local spin valves. *Phys. Status Solidi*, 254(11):1700293, 2017.

[60] M. Drögeler, F. Volmer, M. Wolter, B. Terrés, K. Watanabe, T. Taniguchi, G. Guntherodt, C. Stampfer, and B. Beschoten. Nanosecond spin lifetimes in single- and few-layer graphene–hBN heterostructures at room temperature. *Nano Lett.*, 14(11):6050–6055, 2014.

[61] M. D'Yakonov and V. Perel'. Current-induced spin orientation of electrons in semiconductors. *Physics Letters A*, 35(6):459–460, jul 1971.

[62] M. I. D'Yakonov and V. I. Perel'. Possibility of Orienting Electron Spins with Current. *Soviet Journal of Experimental and Theoretical Physics Letters*, 13:467, June 1971.

[63] M. I. D'Yakonov and V. I. Perel'. Spin Orientation of Electrons Associated with the Interband Absorption of Light in Semiconductors. *Soviet Journal of Experimental and Theoretical Physics*, 33:1053, Jan. 1971.

[64] V. Edelstein. Spin polarization of conduction electrons induced by electric current in two-dimensional asymmetric electron systems. *Solid State Communications*, 73(3):233 – 235, 1990.

[65] R. J. Elliott. Theory of the effect of spin-orbit coupling on magnetic resonance in some semiconductors. *Phys. Rev.*, 96:266–279, Oct 1954.

[66] C. Ertler, S. Konschuh, M. Gmitra, and J. Fabian. Electron spin relaxation in graphene: The role of the substrate. *Phys. Rev. B*, 80:041405, 2009.

[67] J. Fabian, A. Matos-Abiaguea, P. Ertler, C. snd Stano, and I. Žutić. Semiconductor spintronics. *Acta Phys. Slovaca*, 57(4-5):565–907, 2007.

[68] Y. Fan, P. Upadhyaya, X. Kou, M. Lang, S. Takei, Z. Wang, J. Tang, L. He, L.-T. Chang, M. Montazeri, G. Yu, W. Jiang, T. Nie, R. N. Schwartz, Y. Tserkovnyak, and K. L. Wang. Magnetization switching through giant spin–orbit torque in a magnetically doped topological insulator heterostructure. *Nature Materials*, 13(7):699–704, Jul 2014.

[69] Z. Fan, J. Garcia, A. Cummings, J. Barrios-Vargas, M. Panhans, A. Harju, F. Ortmann, and S. Roche. Linear scaling quantum transport methodologies. *arXiv:1811.07387*, 2019.

[70] Z. Fan, A. Uppstu, and A. Harju. Anderson localization in two-dimensional graphene with short-range disorder: One-parameter scaling and finite-size effects. *Phys. Rev. B*, 89:245422, Jun 2014.

[71] V. Fatemi, S. Wu, Y. Cao, L. Bretheau, Q. D. Gibson, K. Watanabe, T. Taniguchi, R. J. Cava, and P. Jarillo-Herrero. Electrically tunable low-density superconductivity in a monolayer topological insulator. *Science*, 362(6417):926–929, 2018.

[72] Z. Fei, T. Palomaki, S. Wu, W. Zhao, X. Cai, B. Sun, P. Nguyen, J. Finney, X. Xu, and D. H. Cobden. Edge conduction in monolayer wte2. *Nature Physics*, 13(7):677–682, 2017.

[73] W. Feng, Y. Yao, W. Zhu, J. Zhou, W. Yao, and D. Xiao. Intrinsic spin hall effect in monolayers of group-vi dichalcogenides: A first-principles study. *Phys. Rev. B*, 86:165108, Oct 2012.

[74] A. Fert. Nobel lecture: Origin, development, and future of spintronics. *Rev. Mod. Phys.*, 80:1517–1530, Dec 2008.

[75] A. Fert, V. Cros, and J. Sampaio. Skyrmions on the track. *Nature Nanotechnology*, 8(3):152–156, Mar 2013.

[76] A. Fert and H. Jaffrès. Conditions for efficient spin injection from a ferromagnetic metal into a semiconductor. *Phys. Rev. B*, 64:184420, Oct 2001.

[77] D. S. Fisher and P. A. Lee. Relation between conductivity and transmission matrix. *Phys. Rev. B*, 23:6851–6854, Jun 1981.

[78] L. E. F. Foa Torres, S. Roche, and J. C. Charlier. *Introduction to Graphene-Based Nanomaterials: FromElectronic Structure to QuantumTransport*. Cambridge University Press, 2014.

[79] S. Fratini, D. Gosálbez-Martínez, P. Merodio Cámara, and J. Fernández-Rossier. Anisotropic intrinsic spin relaxation in graphene due to flexural distortions. *Phys. Rev. B*, 88:115426, Sep 2013.

[80] L. Fu and C. L. Kane. Topological insulators with inversion symmetry. *Phys. Rev. B*, 76:045302, Jul 2007.

[81] S. D. Ganichev, E. L. Ivchenko, V. V. Bel'kov, S. A. Tarasenko, M. Sollinger, D. Weiss, W. Wegscheider, and W. Prettl. Spin-galvanic effect. *Nature*, 417(6885):153–156, May 2002.

[82] J. H. García, L. Covaci, and T. G. Rappoport. Real-space calculation of the conductivity tensor for disordered topological matter. *Phys. Rev. Lett.*, 114:116602, Mar 2015.

[83] J. H. Garcia, M. Vila, A. W. Cummings, and S. Roche. Spin transport in graphene/transition metal dichalcogenide heterostructures. *Chem. Soc. Rev.*, 47:3359–3379, 2018.

[84] B. Gaury, J. Weston, M. Santin, M. Houzet, C. Groth, and X. Waintal. Numerical simulations of time-resolved quantum electronics. *Physics Reports*, 534(1):1–37, Jan 2014.

[85] Z. M. Gebeyehu, S. Parui, J. F. Sierra, M. Timmermans, M. J. Esplandiu, S. Brems, C. Huyghebaert, K. Garello, M. V. Costache, and S. O. Valenzuela. Spin communication over 30 μm long channels of chemical vapor deposited graphene on SiO2. *2D Mater.*, 6(3):034003, may 2019.

[86] A. K. Geim and I. V. Grigorieva. Van der Waals heterostructures. *Nature*, 499(7459):419–425, Jul 2013.

[87] A. K. Geim and K. S. Novoselov. The rise of graphene. *Nature Materials*, 6(3):183–191, Mar 2007.

[88] I. Georgescu. Trapped ion quantum computing turns 25. *Nature Reviews Physics*, 2(6):278–278, Jun 2020.

[89] T. S. Ghiasi, A. A. Kaverzin, P. J. Blah, and B. J. van Wees. Charge-to-Spin Conversion by the Rashba-Edelstein Effect in Two-Dimensional van der Waals Heterostructures up to Room Temperature. *Nano Lett.*, 19:5959–5966, 2019.

[90] F. Giustino, M. Bibes, J. H. Lee, F. Trier, R. Valent, S. M. Winter, Y.-W. Son, L. Taillefer, C. Heil, A. I. Figueroa, B. Plaais, Q. Wu, O. V. Yazyev, E. P. A. M. Bakkers, J. Nygrd, P. Forn-Daz, S. de Franceschi, L. E. F. F. Torres, J. McIver, A. Kumar, T. Low, R. Galceran, S. O. Valenzuela, M. V. Costache, A. Manchon, E.-A. Kim, G. R. Schleder, A. Fazzio, and S. Roche. The 2020 quantum materials roadmap. *Journal of Physics: Materials*, 2020.

[91] M. Gmitra, D. Kochan, P. Högl, and J. Fabian. Trivial and inverted Dirac bands and the emergence of quantum spin Hall states in graphene on transition-metal dichalcogenides. *Phys. Rev. B*, 93:155104, 2016.

[92] M. Gmitra, S. Konschuh, C. Ertler, C. Ambrosch-Draxl, and J. Fabian. Band-structure topologies of graphene: Spin-orbit coupling effects from first principles. *Phys. Rev. B*, 80:235431, 2009.

[93] M. O. Goerbig. Electronic properties of graphene in a strong magnetic field. *Rev. Mod. Phys.*, 83:1193–1243, Nov 2011.

[94] C. W. Groth, M. Wimmer, A. R. Akhmerov, and X. Waintal. Kwant: a software package for quantum transport. *New J. Phys.*, 16(6):063065, 2014.

[95] M. H. D. Guimarães, P. J. Zomer, J. Ingla-Aynés, J. C. Brant, N. Tombros, and B. J. van Wees. Controlling spin relaxation in hexagonal bn-encapsulated graphene with a transverse electric field. *Phys. Rev. Lett.*, 113:086602, 2014.

[96] M. H. D. Guimares, A. Veligura, P. J. Zomer, T. Maassen, I. J. Vera-Marun, N. Tombros, and B. J. van Wees. Spin transport in high-quality suspended graphene devices. *Nano Lett.*, 12(7):3512–3517, 2012.

[97] M. Gurram, S. Omar, and B. J. van Wees. Bias induced up to 100% spin-injection and detection polarizations in ferromagnet/bilayer-hBN/graphene/hBN heterostructures. *Nature Communication*, 8(248):1, 2017.

[98] F. D. M. Haldane. Model for a quantum hall effect without landau levels: Condensed-matter realization of the "parity anomaly". *Phys. Rev. Lett.*, 61:2015–2018, 1988.

[99] A. Hallal, F. Ibrahim, H. Yang, S. Roche, and M. Chshiev. Tailoring magnetic insulator proximity effects in graphene: first-principles calculations. *2D Mater.*, 4(2):025074, 2017.

[100] B. I. Halperin. Quantized hall conductance, current-carrying edge states, and the existence of extended states in a two-dimensional disordered potential. *Phys. Rev. B*, 25:2185–2190, Feb 1982.

[101] W. Han, R. K. Kawakami, M. Gmitra, and J. Fabian. Graphene spintronics. *Nature Nanotechnology*, 9(10):794–807, 2014.

[102] W. Han, K. Pi, W. Bao, K. M. McCreary, Y. Li, W. H. Wang, C. N. Lau, and R. K. Kawakami. Electrical detection of spin precession in single layer graphene spin valves with transparent contacts. *Applied Physics Letters*, 94(22):222109, Jun 2009.

[103] W. Han, K. Pi, K. M. McCreary, Y. Li, J. J. I. Wong, A. G. Swartz, and R. K. Kawakami. Tunneling spin injection into single layer graphene. *Phys. Rev. Lett.*, 105:167202, Oct 2010.

[104] Y. Hancock, A. Uppstu, K. Saloriutta, A. Harju, and M. J. Puska. Generalized tight-binding transport model for graphene nanoribbon-based systems. *Phys. Rev. B*, 81:245402, 2010.

[105] E. M. Hankiewicz, L. W. Molenkamp, T. Jungwirth, and J. Sinova. Manifestation of the spin hall effect through charge-transport in the mesoscopic regime. *Phys. Rev. B*, 70:241301, Dec 2004.

[106] W. Hanle. Über magnetische beeinflussung der polarisation der resonanzfluoreszenz. *Zeitschrift für Physik*, 30(1):93–105, Dec 1924.

[107] M. Z. Hasan and C. L. Kane. Colloquium: Topological insulators. *Rev. Mod. Phys.*, 82:3045–3067, 2010.

[108] Y. Hatsugai. Chern number and edge states in the integer quantum hall effect. *Phys. Rev. Lett.*, 71:3697–3700, Nov 1993.

[109] M. He, H. Sun, and Q. L. He. Topological insulator: Spintronics and quantum computations. *Frontiers of Physics*, 14(4):43401, May 2019.

[110] J. R. Heath and M. A. Ratner. Molecular electronics. *Physics Today*, 56(5):43–49, 2003.

[111] F. Herling, C. K. Safeer, J. Ingla-Ayns, N. Ontoso, L. E. Hueso, and F. Casanova. Gate tunability of highly efficient spin-to-charge conversion by spin hall effect in graphene proximitized with WSe_2. *APL Materials*, 8(7):071103, 2020.

[112] J. E. Hirsch. Spin Hall Effect. *Phys. Rev. Lett.*, 83(9):1834–1837, aug 1999.

[113] A. Hoffmann. Spin hall effects in metals. *IEEE Transactions on Magnetics*, 49(10):5172–5193, 2013.

[114] P. Högl, T. Frank, K. Zollner, D. Kochan, M. Gmitra, and J. Fabian. Quantum anomalous hall effects in graphene from proximity-induced uniform and staggered spin-orbit and exchange coupling. *Phys. Rev. Lett.*, 124:136403, Mar 2020.

[115] D. Huertas-Hernando, F. Guinea, and A. Brataas. Spin-orbit coupling in curved graphene, fullerenes, nanotubes, and nanotube caps. *Phys. Rev. B*, 74:155426, Oct 2006.

[116] D. Huertas-Hernando, F. Guinea, and A. Brataas. Spin-orbit coupling in curved graphene, fullerenes, nanotubes, and nanotube caps. *Phys. Rev. B*, 74:155426, Oct 2006.

[117] D. Huertas-Hernando, F. Guinea, and A. Brataas. Spin-orbit-mediated spin relaxation in graphene. *Phys. Rev. Lett.*, 103:146801, 2009.

[118] D. Huertas-Hernando, F. Guinea, and A. Brataas. Spin-orbit-mediated spin relaxation in graphene. *Phys. Rev. Lett.*, 103:146801, Sep 2009.

[119] E. H. Hwang, S. Adam, and S. D. Sarma. Carrier transport in two-dimensional graphene layers. *Phys. Rev. Lett.*, 98:186806, May 2007.

[120] H. Idzuchi, A. Fert, and Y. Otani. Revisiting the measurement of the spin relaxation time in graphene-based devices. *Phys. Rev. B*, 91:241407, Jun 2015.

[121] H. Idzuchi, Y. Fukuma, S. Takahashi, S. Maekawa, and Y. Otani. Effect of anisotropic spin absorption on the hanle effect in lateral spin valves. *Phys. Rev. B*, 89:081308, 2014.

[122] I. Žutić, J. Fabian, and S. Das Sarma. Spintronics: Fundamentals and applications. *Rev. Mod. Phys.*, 76:323–410, 2004.

[123] M. Isasa, E. Villamor, L. E. Hueso, M. Gradhand, and F. Casanova. Temperature dependence of spin diffusion length and spin hall angle in au and pt. *Phys. Rev. B*, 91:024402, 2015.

[124] M. Istas, C. Groth, A. R. Akhmerov, M. Wimmer, and X. Waintal. A general algorithm for computing bound states in infinite tight-binding systems. *SciPost Phys.*, 4:26, 2018.

[125] F. Jedema, H. Heersche, A. Filip, J. Baselmans, and B. Van Wees. Electrical detection of spin precession in a metallic mesoscopic spin valve. *Nature*, 416(6882):713–716, 2002.

[126] F. J. Jedema, M. S. Nijboer, A. T. Filip, and B. J. van Wees. Spin injection and spin accumulation in all-metal mesoscopic spin valves. *Phys. Rev. B*, 67:085319, Feb 2003.

[127] F. Jensen. *Introduction to Computational Chemistry*. Wiley, Chichester, 2007.

[128] J.-S. Jeong and H.-W. Lee. Ballistic spin field-effect transistors: Multichannel effects. *Phys. Rev. B*, 74:195311, Nov 2006.

[129] Z.-Y. Jia, Y.-H. Song, X.-B. Li, K. Ran, P. Lu, H.-J. Zheng, X.-Y. Zhu, Z.-Q. Shi, J. Sun, J. Wen, D. Xing, and S.-C. Li. Direct visualization of a two-dimensional topological insulator in the single-layer $1T^{'} - WTe_2$. *Phys. Rev. B*, 96:041108, 2017.

[130] J. Jiang, Z. K. Liu, Y. Sun, H. F. Yang, C. R. Rajamathi, Y. P. Qi, L. X. Yang, C. Chen, H. Peng, C.-C. Hwang, S. Z. Sun, S.-K. Mo, I. Vobornik, J. Fujii, S. S. P. Parkin, C. Felser, B. H. Yan, and Y. L. Chen. Signature of type-II Weyl semimetal phase in $MoTe_2$. *Nature Communications*, 8(1):13973, 2017.

[131] M. Johnson and R. H. Silsbee. Interfacial charge-spin coupling: Injection and detection of spin magnetization in metals. *Phys. Rev. Lett.*, 55:1790–1793, Oct 1985.

[132] M. Johnson and R. H. Silsbee. Coupling of electronic charge and spin at a ferromagnetic-paramagnetic metal interface. *Phys. Rev. B*, 37:5312–5325, Apr 1988.

[133] E. Jones, T. Oliphant, P. Peterson, et al. SciPy: Open source scientific tools for Python, 2001–.

[134] C. Józsa, T. Maassen, M. Popinciuc, P. J. Zomer, A. Veligura, H. T. Jonkman, and B. J. van Wees. Linear scaling between momentum and spin scattering in graphene. *Phys. Rev. B*, 80:241403, Dec 2009.

[135] T. Jungwirth, X. Marti, P. Wadley, and J. Wunderlich. Antiferromagnetic spintronics. *Nature Nanotechnology*, 11(3):231–241, Mar 2016.

[136] Y. Kajiwara, K. Harii, S. Takahashi, J. Ohe, K. Uchida, M. Mizuguchi, H. Umezawa, H. Kawai, K. Ando, K. Takanashi, S. Maekawa, and E. Saitoh. Transmission of electrical signals by spin-wave interconversion in a magnetic insulator. *Nature*, 464(7286):262–266, Mar 2010.

[137] M. V. Kamalakar, C. Groenveld, A. Dankert, and S. P. Dash. Long distance spin communication in chemical vapour deposited graphene. *Nature Communication*, 6:6766, 2015.

[138] C. L. Kane and E. J. Mele. Quantum spin hall effect in graphene. *Phys. Rev. Lett.*, 95:226801, Nov 2005.

[139] C. L. Kane and E. J. Mele. Z_2 topological order and the quantum spin hall effect. *Phys. Rev. Lett.*, 95:146802, Sep 2005.

[140] K. Kang, T. Li, E. Sohn, J. Shan, and K. F. Mak. Nonlinear anomalous Hall effect in few-layer WTe_2. *Nature Materials*, 18(4):324–328, 2019.

[141] M. A. Kastner. The single-electron transistor. *Rev. Mod. Phys.*, 64:849–858, Jul 1992.

[142] Y. K. Kato, R. C. Myers, A. C. Gossard, and D. D. Awschalom. Current-induced spin polarization in strained semiconductors. *Phys. Rev. Lett.*, 93:176601, Oct 2004.

[143] Y. K. Kato, R. C. Myers, A. C. Gossard, and D. D. Awschalom. Observation of the spin hall effect in semiconductors. *Science*, 306(5703):1910–1913, 2004.

[144] M. I. Katsnelson, K. S. Novoselov, and A. K. Geim. Chiral tunnelling and the klein paradox in graphene. *Nature Physics*, 2(9):620–625, Sep 2006.

[145] D. H. Keum, S. Cho, J. H. Kim, D.-H. Choe, H.-J. Sung, M. Kan, H. Kang, J.-Y. Hwang, S. W. Kim, H. Yang, K. J. Chang, and Y. H. Lee. Bandgap opening in few-layered monoclinic $MoTe_2$. *Nature Physics*, 11(6):482–486, Jun 2015.

[146] N. H. D. Khang, Y. Ueda, and P. N. Hai. A conductive topological insulator with large spin hall effect for ultralow power spin–orbit torque switching. *Nature Materials*, 17(9):808–813, Sep 2018.

[147] H.-J. Kim, S.-H. Kang, I. Hamada, and Y.-W. Son. Origins of the structural phase transitions in $MoTe_2$ and WTe_2. *Phys. Rev. B*, 95:180101, May 2017.

[148] K. v. Klitzing, G. Dorda, and M. Pepper. New method for high-accuracy determination of the fine-structure constant based on quantized hall resistance. *Phys. Rev. Lett.*, 45:494–497, Aug 1980.

[149] D. Kochan, M. Gmitra, and J. Fabian. Spin relaxation mechanism in graphene: Resonant scattering by magnetic impurities. *Phys. Rev. Lett.*, 112:116602, 2014.

[150] D. Kochan, S. Irmer, and J. Fabian. Model spin-orbit coupling hamiltonians for graphene systems. *Phys. Rev. B*, 95:165415, Apr 2017.

[151] M. Kohmoto. Topological invariant and the quantization of the hall conductance. *Annals of Physics*, 160(2):343 – 354, 1985.

[152] M. König, S. Wiedmann, C. Brüne, A. Roth, H. Buhmann, L. W. Molenkamp, X.-L. Qi, and S.-C. Zhang. Quantum spin hall insulator state in HgTe quantum wells. *Science*, 318(5851):766–770, 2007.

[153] S. Konschuh, M. Gmitra, and J. Fabian. Tight-binding theory of the spin-orbit coupling in graphene. *Phys. Rev. B*, 82:245412, 2010.

[154] H. C. Koo, J. H. Kwon, J. Eom, J. Chang, S. H. Han, and M. Johnson. Control of spin precession in a spin-injected field effect transistor. *Science*, 325(5947):1515–1518, 2009.

[155] V. Y. Kravchenko and E. I. Rashba. Spin injection into a ballistic semiconductor microstructure. *Phys. Rev. B*, 67:121310, Mar 2003.

[156] G. Kresse and J. Furthmüller. Efficiency of ab-initio total energy calculations for metals and semiconductors using a plane-wave basis set. *Computational Materials Science*, 6(1):15–50, July 1996.

[157] G. Kresse and J. Furthmüller. Efficient iterative schemes for *ab initio* total-energy calculations using a plane-wave basis set. *Phys. Rev. B*, 54(16):11169–11186, Oct. 1996.

[158] G. Kresse and J. Hafner. *Ab Initio* molecular dynamics for open-shell transition metals. *Phys. Rev. B*, 48(17):13115–13118, Nov. 1993.

[159] L. Matthes, S. Küfner, J. Furthmüller and F. Bechstedt. Intrinsic spin Hall conductivity in one-, two-, and three-dimensional trivial and topological systems. *Phys. Rev. B*, 94(8):085410, 2016.

[160] P. Laczkowski, Y. Fu, H. Yang, J.-C. Rojas-Sánchez, P. Noel, V. T. Pham, G. Zahnd, C. Deranlot, S. Collin, C. Bouard, P. Warin, V. Maurel, M. Chshiev, A. Marty, J.-P. Attané, A. Fert, H. Jaffrès, L. Vila, and J.-M. George. Large enhancement of the spin hall effect in au by side-jump scattering on ta impurities. *Phys. Rev. B*, 96:140405, Oct 2017.

[161] T. D. Ladd, F. Jelezko, R. Laflamme, Y. Nakamura, C. Monroe, and J. L. O'Brien. Quantum computers. *Nature*, 464(7285):45–53, Mar 2010.

[162] R. Landauer. Spatial variation of currents and fields due to localized scatterers in metallic conduction. *IBM Journal of Research and Development*, 1(3):223–231, July 1957.

[163] R. Landauer. Electrical resistance of disordered one-dimensional lattices. *The Philosophical Magazine: A Journal of Theoretical Experimental and Applied Physics*, 21(172):863–867, 1970.

[164] A. Lau, R. Ray, D. Varjas, and A. R. Akhmerov. Influence of lattice termination on the edge states of the quantum spin hall insulator monolayer 1T′-WTe_2. *Phys. Rev. Materials*, 3:054206, May 2019.

[165] H.-W. Lee, S. Çalışkan, and H. Park. Mesoscopic effects in a single-mode datta-das spin field-effect transistor. *Phys. Rev. B*, 72:153305, Oct 2005.

[166] A. Lherbier, B. Biel, Y.-M. Niquet, and S. Roche. Transport length scales in disordered graphene-based materials: Strong localization regimes and dimensionality effects. *Phys. Rev. Lett.*, 100:036803, Jan 2008.

[167] A. Lherbier, S. M.-M. Dubois, X. Declerck, Y.-M. Niquet, S. Roche, and J.-C. Charlier. Transport properties of graphene containing structural defects. *Phys. Rev. B*, 86:075402, Aug 2012.

[168] P. Li, Y. Wen, X. He, Q. Zhang, C. Xia, Z.-M. Yu, S. A. Yang, Z. Zhu, H. N. Alshareef, and X.-X. Zhang. Evidence for topological type-ii weyl semimetal wte2. *Nature Communications*, 8(1):2150, Dec 2017.

[169] L.-K. Liefeith, R. Tholapi, T. Ishikura, M. Hänze, R. Hartmann, T. Slobodskyy, and W. Hansen. Spin injection beyond the diffusive limit in the presence of spin-orbit coupling. *Phys. Rev. B*, 95:081303, 2017.

[170] X. Lin, W. Yang, K. L. Wang, and W. Zhao. Two-dimensional spintronics for low-power electronics. *Nature Electronics*, 2(7):274–283, Jul 2019.

[171] J. Linder and J. W. A. Robinson. Superconducting spintronics. *Nature Physics*, 11(4):307–315, Apr 2015.

[172] M. B. Lundeberg, R. Yang, J. Renard, and J. A. Folk. Defect-mediated spin relaxation and dephasing in graphene. *Phys. Rev. Lett.*, 110:156601, Apr 2013.

[173] Q. Ma, S.-Y. Xu, H. Shen, D. MacNeill, V. Fatemi, T.-R. Chang, A. M. Mier Valdivia, S. Wu, Z. Du, C.-H. Hsu, S. Fang, Q. D. Gibson, K. Watanabe, T. Taniguchi,

R. J. Cava, E. Kaxiras, H.-Z. Lu, H. Lin, L. Fu, N. Gedik, and P. Jarillo-Herrero. Observation of the nonlinear hall effect under time-reversal-symmetric conditions. *Nature*, 565(7739):337–342, 2019.

[174] T. Maassen, I. J. Vera-Marun, M. H. D. Guimarães, and B. J. van Wees. Contact-induced spin relaxation in hanle spin precession measurements. *Phys. Rev. B*, 86:235408, Dec 2012.

[175] D. MacNeill, G. M. Stiehl, M. H. D. Guimaraes, R. A. Buhrman, J. Park, and D. C. Ralph. Control of spin-orbit torques through crystal symmetry in WTe_2/ferromagnet bilayers. *Nature Physics*, 13(3):300–305, 2017.

[176] K. F. Mak, K. He, J. Shan, and T. F. Heinz. Control of valley polarization in monolayer mos2 by optical helicity. *Nature Nanotechnology*, 7:494–498, 6 2012.

[177] A. Manchon, J. Železný, I. M. Miron, T. Jungwirth, J. Sinova, A. Thiaville, K. Garello, and P. Gambardella. Current-induced spin-orbit torques in ferromagnetic and antiferromagnetic systems. *Rev. Mod. Phys.*, 91:035004, Sep 2019.

[178] A. Manchon, H. C. Koo, J. Nitta, S. M. Frolov, and R. A. Duine. New perspectives for rashba spin–orbit coupling. *Nature Materials*, 14(9):871–882, Sep 2015.

[179] S. Manipatruni, D. E. Nikonov, and I. A. Young. Beyond cmos computing with spin and polarization. *Nature Physics*, 14(4):338–343, Apr 2018.

[180] S. Manzeli, D. Ovchinnikov, D. Pasquier, O. V. Yazyev, and A. Kis. 2d transition metal dichalcogenides. *Nature Reviews Materials*, 2(8):17033, Jun 2017.

[181] J. Martin, N. Akerman, G. Ulbricht, T. Lohmann, J. H. Smet, K. von Klitzing, and A. Yacoby. Observation of electron–hole puddles in graphene using a scanning single-electron transistor. *Nature Physics*, 4(2):144–148, Feb 2008.

[182] P. T. Mathew and F. Fang. Advances in molecular electronics: A brief review. *Engineering*, 4(6):760 – 771, 2018.

[183] F. Matusalem, M. Marques, L. K. Teles, L. Matthes, J. Furthmüller, and F. Bechstedt. Quantization of spin hall conductivity in two-dimensional topological insulators versus symmetry and spin-orbit interaction. *Phys. Rev. B*, 100:245430, Dec 2019.

[184] A. R. Mellnik, J. S. Lee, A. Richardella, J. L. Grab, P. J. Mintun, M. H. Fischer, A. Vaezi, A. Manchon, E.-A. Kim, N. Samarth, and D. C. Ralph. Spin-transfer torque generated by a topological insulator. *Nature*, 511(7510):449–451, Jul 2014.

[185] I. Mihai Miron, G. Gaudin, S. Auffret, B. Rodmacq, A. Schuhl, S. Pizzini, J. Vogel, and P. Gambardella. Current-driven spin torque induced by the rashba effect in a ferromagnetic metal layer. *Nature Materials*, 9(3):230–234, Mar 2010.

[186] H. Min, J. E. Hill, N. A. Sinitsyn, B. R. Sahu, L. Kleinman, and A. H. MacDonald. Intrinsic and rashba spin-orbit interactions in graphene sheets. *Phys. Rev. B*, 74:165310, Oct 2006.

[187] F. Mireles and G. Kirczenow. Ballistic spin-polarized transport and rashba spin precession in semiconductor nanowires. *Phys. Rev. B*, 64:024426, Jun 2001.

[188] A. A. Mostofi, J. R. Yates, G. Pizzi, Y.-S. Lee, I. Souza, D. Vanderbilt, and N. Marzari. An updated version of wannier90: A tool for obtaining maximally-localised Wannier functions. *Computer Physics Communications*, 185(8):2309–2310, Aug. 2014.

[189] N. F. Mott and R. H. Fowler. The electrical conductivity of transition metals. *Proceedings of the Royal Society of London. Series A - Mathematical and Physical Sciences*, 153(880):699–717, 1936.

[190] L. Muechler, A. Alexandradinata, T. Neupert, and R. Car. Topological nonsymmorphic metals from band inversion. *Phys. Rev. X*, 6:041069, Dec 2016.

[191] S. Murakami. Quantum spin hall effect and enhanced magnetic response by spin-orbit coupling. *Phys. Rev. Lett.*, 97:236805, Dec 2006.

[192] S. Murakami, N. Nagaosa, and S.-C. Zhang. Dissipationless quantum spin current at room temperature. *Science*, 301(5638):1348–1351, 2003.

[193] N. Nagaosa and Y. Tokura. Topological properties and dynamics of magnetic skyrmions. *Nature Nanotechnology*, 8(12):899–911, Dec 2013.

[194] I. Neumann, J. Van de Vondel, G. Bridoux, M. V. Costache, F. Alzina, C. M. S. Torres, and S. O. Valenzuela. Electrical detection of spin precession in freely suspended graphene spin valves on cross-linked poly (methyl methacrylate). *Small*, 9(1):156–160, 2013.

[195] D. E. Nikonov and I. A. Young. Overview of beyond-cmos devices and a uniform methodology for their benchmarking. *Proceedings of the IEEE*, 101(12):2498–2533, 2013.

[196] K. S. Novoselov, V. I. Falko, L. Colombo, P. R. Gellert, M. G. Schwab, and K. Kim. A roadmap for graphene. *Nature*, 490(7419):192–200, Oct 2012.

[197] K. S. Novoselov, A. K. Geim, S. V. Morozov, D. Jiang, M. I. Katsnelson, I. V. Grigorieva, S. V. Dubonos, and A. A. Firsov. Two-dimensional gas of massless dirac fermions in graphene. *Nature*, 438(7065):197–200, Nov 2005.

[198] K. S. Novoselov, A. K. Geim, S. V. Morozov, D. Jiang, Y. Zhang, S. V. Dubonos, I. V. Grigorieva, and A. A. Firsov. Electric field effect in atomically thin carbon films. *Science*, 306:666, 2004.

[199] K. S. Novoselov, D. Jiang, F. Schedin, T. J. Booth, V. V. Khotkevich, S. V. Morozov, and A. K. Geim. Two-dimensional atomic crystals. *Proceedings of the National Academy of Sciences*, 102(30):10451–10453, 2005.

[200] K. S. Novoselov, A. Mishchenko, A. Carvalho, and A. H. Castro Neto. 2D materials and van der Waals heterostructures. *Science*, 353(6298), 2016.

[201] L. O'Brien, D. Spivak, N. Krueger, T. A. Peterson, M. J. Erickson, B. Bolon, C. C. Geppert, C. Leighton, and P. A. Crowell. Observation and modelling of ferromagnetic contact-induced spin relaxation in hanle spin precession measurements. *Phys. Rev. B*, 94:094431, Sep 2016.

[202] H. Ochoa, A. H. Castro Neto, V. I. Fal'ko, and F. Guinea. Spin-orbit coupling assisted by flexural phonons in graphene. *Phys. Rev. B*, 86:245411, Dec 2012.

[203] S. Ok, L. Muechler, D. Di Sante, G. Sangiovanni, R. Thomale, and T. Neupert. Custodial glide symmetry of quantum spin hall edge modes in monolayer WTe_2. *Phys. Rev. B*, 99:121105, Mar 2019.

[204] T. E. Oliphant. Python for scientific computing. *Computing in Science Engineering*, 9(3):10–20, 2007.

[205] M. Oltscher, M. Ciorga, M. Utz, D. Schuh, D. Bougeard, and D. Weiss. Electrical spin injection into high mobility 2d systems. *Phys. Rev. Lett.*, 113:236602, Dec 2014.

[206] F. Ortmann, S. Roche, and S. Valenzuela. *Topological Insulators: Fundamentals and Perspectives*. Wiley-VCH, 2015.

[207] A.-S. Pawlik, S. Aswartham, I. Morozov, M. Knupfer, B. Büchner, D. V. Efremov, and A. Koitzsch. Thickness dependent electronic structure of exfoliated mono- and few-layer 1T′-$MoTe_2$. *Phys. Rev. Materials*, 2:104004, Oct 2018.

[208] J. P. Perdew, K. Burke, and M. Ernzerhof. Generalized gradient approximation made simple. *Phys. Rev. Lett.*, 77:3865–3868, Oct 1996.

[209] C. Petitjean, D. Luc, and X. Waintal. Unified drift-diffusion theory for transverse spin currents in spin valves, domain walls, and other textured magnets. *Phys. Rev. Lett.*, 109:117204, Sep 2012.

[210] M. D. Petrović, B. S. Popescu, U. Bajpai, P. Plecháč, and B. K. Nikolić. Spin and charge pumping by a steady or pulse-current-driven magnetic domain wall: A self-consistent multiscale time-dependent quantum-classical hybrid approach. *Phys. Rev. Applied*, 10:054038, Nov 2018.

[211] M. Popinciuc, C. Józsa, P. J. Zomer, N. Tombros, A. Veligura, H. T. Jonkman, and B. J. van Wees. Electronic spin transport in graphene field-effect transistors. *Phys. Rev. B*, 80:214427, Dec 2009.

[212] X.-L. Qi and S.-C. Zhang. Topological insulators and superconductors. *Rev. Mod. Phys.*, 83:1057–1110, Oct 2011.

[213] Y. Qi, P. G. Naumov, M. N. Ali, C. R. Rajamathi, W. Schnelle, O. Barkalov, M. Hanfland, S.-C. Wu, C. Shekhar, Y. Sun, V. Süß, M. Schmidt, U. Schwarz, E. Pippel, P. Werner, R. Hillebrand, T. Förster, E. Kampert, S. Parkin, R. J. Cava, C. Felser, B. Yan, and S. A. Medvedev. Superconductivity in Weyl semimetal candidate $MoTe_2$. *Nature Communications*, 7(1):11038, 2016.

[214] X. Qian, J. Liu, L. Fu, and J. Li. Quantum spin hall effect in two-dimensional transition metal dichalcogenides. *Science*, 346(6215):1344–1347, 2014.

[215] Z. Qiao, W. Ren, H. Chen, L. Bellaiche, Z. Zhang, A. H. MacDonald, and Q. Niu. Quantum anomalous hall effect in graphene proximity coupled to an antiferromagnetic insulator. *Phys. Rev. Lett.*, 112:116404, 2014.

[216] B. Raes, J. E. Scheerder, M. V. Costache, F. Bonell, J. F. Sierra, J. Cuppens, J. Van de Vondel, and S. O. Valenzuela. Determination of the spin-lifetime anisotropy in graphene using oblique spin precession. *Nature communications*, 7, 2016.

[217] D. Ralph and M. Stiles. Spin transfer torques. *Journal of Magnetism and Magnetic Materials*, 320(7):1190 – 1216, 2008.

[218] E. I. Rashba. Theory of electrical spin injection: Tunnel contacts as a solution of the conductivity mismatch problem. *Phys. Rev. B*, 62:R16267–R16270, Dec 2000.

[219] S. Roche, J. Åkerman, B. Beschoten, J.-C. Charlier, M. Chshiev, S. P. Dash, B. Dlubak, J. Fabian, A. Fert, M. Guimarães, et al. Graphene spintronics: the european flagship perspective. *2D Mater.*, 2:030202, 2015.

[220] S. Roche and S. O. Valenzuela. Graphene spintronics: puzzling controversies and challenges for spin manipulation. *Journal of Physics D: Applied Physics*, 47(9):094011, feb 2014.

[221] J.-C. Rojas-Sánchez, S. Oyarzún, Y. Fu, A. Marty, C. Vergnaud, S. Gambarelli, L. Vila, M. Jamet, Y. Ohtsubo, A. Taleb-Ibrahimi, P. Le Fèvre, F. Bertran, N. Reyren, J.-M. George, and A. Fert. Spin to charge conversion at room temperature by spin pumping into a new type of topological insulator: α-Sn films. *Phys. Rev. Lett.*, 116:096602, Mar 2016.

[222] A. Roth, C. Brüne, H. Buhmann, L. W. Molenkamp, J. Maciejko, X.-L. Qi, and S.-C. Zhang. Nonlocal transport in the quantum spin hall state. *Science*, 325(5938):294–297, 2009.

[223] K. Roy. Estimating the spin diffusion length and the spin hall angle from spin pumping induced inverse spin hall voltages. *Phys. Rev. B*, 96:174432, 2017.

[224] K. Roy, A. Jaiswal, and P. Panda. Towards spike-based machine intelligence with neuromorphic computing. *Nature*, 575(7784):607–617, Nov 2019.

[225] V. S. Rychkov, S. Borlenghi, H. Jaffres, A. Fert, and X. Waintal. Spin torque and waviness in magnetic multilayers: A bridge between Valet-Fert theory and quantum approaches. *Phys. Rev. Lett.*, 103:066602, Aug 2009.

[226] C. K. Safeer, J. Ingla-Aynés, F. Herling, J. H. Garcia, M. Vila, N. Ontoso, M. R. Calvo, S. Roche, L. E. Hueso, and F. Casanova. Room-temperature spin hall effect in graphene/MoS_2 van der Waals heterostructures. *Nano Lett.*, 19(2):1074–1082, Feb 2019.

[227] C. K. Safeer, N. Ontoso, J. Ingla-Aynés, F. Herling, V. T. Pham, A. Kurzmann, K. Ensslin, A. Chuvilin, I. Robredo, M. G. Vergniory, F. de Juan, L. E. Hueso, M. R. Calvo, and F. Casanova. Large multidirectional spin-to-charge conversion in low-symmetry semimetal $MoTe_2$ at room temperature. *Nano Lett.*, 19(12):8758–8766, Dec 2019.

[228] E. Sagasta, Y. Omori, S. Vélez, R. Llopis, C. Tollan, A. Chuvilin, L. E. Hueso, M. Gradhand, Y. Otani, and F. Casanova. Unveiling the mechanisms of the spin hall effect in ta. *Phys. Rev. B*, 98:060410, Aug 2018.

[229] E. Sajadi, T. Palomaki, Z. Fei, W. Zhao, P. Bement, C. Olsen, S. Luescher, X. Xu, J. A. Folk, and D. H. Cobden. Gate-induced superconductivity in a monolayer topological insulator. *Science*, 362(6417):922–925, 2018.

[230] W. Savero Torres, J. F. Sierra, L. A. Benítez, F. Bonell, M. V. Costache, and S. O. Valenzuela. Spin precession and spin Hall effect in monolayer graphene/Pt nanostructures. *2D Mater.*, 4:041008, 2017.

[231] F. Schindler, A. M. Cook, M. G. Vergniory, Z. Wang, S. S. P. Parkin, B. A. Bernevig, and T. Neupert. Higher-order topological insulators. *Sci. Adv.*, 4(6), 2018.

[232] J. Schliemann. Colloquium: Persistent spin textures in semiconductor nanostructures. *Rev. Mod. Phys.*, 89:011001, Jan 2017.

[233] J. Schliemann, J. C. Egues, and D. Loss. Nonballistic spin-field-effect transistor. *Phys. Rev. Lett.*, 90:146801, Apr 2003.

[234] D. N. Sheng, Z. Y. Weng, L. Sheng, and F. D. Haldane. Quantum spin-hall effect and topologically invariant chern numbers. *Phys. Rev. Lett.*, 97(3):1–4, 2006.

[235] L. Sheng, D. N. Sheng, C. S. Ting, and F. D. Haldane. Nondissipative spin hall effect via quantized edge transport. *Phys. Rev. Lett.*, 95(13):95–98, 2005.

[236] L.-k. Shi and J. C. W. Song. Symmetry, spin-texture, and tunable quantum geometry in a WTe_2 monolayer. *Phys. Rev. B*, 99:035403, Jan 2019.

[237] Y. Shi, J. Kahn, B. Niu, Z. Fei, B. Sun, X. Cai, B. A. Francisco, D. Wu, Z.-X. Shen, X. Xu, D. H. Cobden, and Y.-T. Cui. Imaging quantum spin hall edges in monolayer WTe_2. *Sci. Adv.*, 5(2), 2019.

[238] V. Sih, R. C. Myers, Y. K. Kato, W. H. Lau, A. C. Gossard, and D. D. Awschalom. Spatial imaging of the spin hall effect and current-induced polarization in two-dimensional electron gases. *Nature Physics*, 1(1):31–35, Oct 2005.

[239] A. Y. Silov, P. A. Blajnov, J. H. Wolter, R. Hey, K. H. Ploog, and N. S. Averkiev. Current-induced spin polarization at a single heterojunction. *Applied Physics Letters*, 85(24):5929–5931, 2004.

[240] R. H. Silsbee. Novel method for the study of spin transport in conductors. *Bull. Magn. Reson.*, 2:284–285, 1980.

[241] S. Singh, J. Katoch, J. Xu, C. Tan, T. Zhu, W. Amamou, J. Hone, and R. Kawakami. Nanosecond spin relaxation times in single layer graphene spin valves with hexagonal boron nitride tunnel barriers. *Applied Physics Letters*, 109(12):122411, 2016.

[242] S. Singh, J. Kim, K. M. Rabe, and D. Vanderbilt. Engineering Weyl phases and nonlinear Hall effects in t_d-$MoTe_2$. *Phys. Rev. Lett.*, 125:046402, Jul 2020.

[243] J. Sinova, D. Culcer, Q. Niu, N. A. Sinitsyn, T. Jungwirth, and A. H. MacDonald. Universal Intrinsic Spin Hall Effect. *Phys. Rev. Lett.*, 92:126603, 2004.

[244] J. Sinova, S. O. Valenzuela, J. Wunderlich, C. H. Back, and T. Jungwirth. Spin Hall effects. *Rev. Mod. Phys.*, 87(4):1213–1260, oct 2015.

[245] J. Slonczewski. Current-driven excitation of magnetic multilayers. *Journal of Magnetism and Magnetic Materials*, 159(1):L1 – L7, 1996.

[246] L. Šmejkal, T. Jungwirth, and J. Sinova. Route towards dirac and weyl antiferromagnetic spintronics. *physica status solidi (RRL) Rapid Research Letters*, 11(4):1700044, 2017.

[247] L. Šmejkal, Y. Mokrousov, B. Yan, and A. H. MacDonald. Topological antiferromagnetic spintronics. *Nature Physics*, 14(3):242–251, Mar 2018.

[248] R. Sokolewicz, S. Ghosh, D. Yudin, A. Manchon, and M. Titov. Spin-orbit torques in a rashba honeycomb antiferromagnet. *Phys. Rev. B*, 100:214403, Dec 2019.

[249] A. A. Soluyanov, D. Gresch, Z. Wang, Q. Wu, M. Troyer, X. Dai, and B. A. Bernevig. Type-ii weyl semimetals. *Nature*, 527(7579):495–498, 2015.

[250] P. Song, C. Hsu, M. Zhao, X. Zhao, T.-R. Chang, J. Teng, H. Lin, and K. P. Loh. Few-layer 1T′ $MoTe_2$ as gapless semimetal with thickness dependent carrier transport. *2D Mater.*, 5(3):031010, jun 2018.

[251] P. Song, C.-H. Hsu, G. Vignale, M. Zhao, J. Liu, Y. Deng, W. Fu, Y. Liu, Y. Zhang, H. Lin, V. M. Pereira, and K. P. Loh. Coexistence of large conventional and planar spin Hall effect with long spin diffusion length in a low-symmetry semimetal at room temperature. *Nature Materials*, 19(3):292–298, 2020.

[252] D. Soriano, D. Van Tuan, S. M. Dubois, M. Gmitra, A. W. Cummings, D. Kochan, F. Ortmann, J.-C. Charlier, J. Fabian, and S. Roche. Spin transport in hydrogenated graphene. *2D Mater.*, 2(2):022002, 2015.

[253] E. Sosenko, H. Wei, and V. Aji. Effect of contacts on spin lifetime measurements in graphene. *Phys. Rev. B*, 89:245436, Jun 2014.

[254] G. Stecklein, P. A. Crowell, J. Li, Y. Anugrah, Q. Su, and S. J. Koester. Contact-induced spin relaxation in graphene nonlocal spin valves. *Phys. Rev. Applied*, 6:054015, Nov 2016.

[255] Y. Sun, S.-C. Wu, M. N. Ali, C. Felser, and B. Yan. Prediction of Weyl semimetal in orthorhombic $MoTe_2$. *Phys. Rev. B*, 92:161107, 2015.

[256] Y. Sun, Y. Zhang, C. Felser, and B. Yan. Strong intrinsic spin hall effect in the taas family of weyl semimetals. *Phys. Rev. Lett.*, 117:146403, Sep 2016.

[257] S. Takahashi and S. Maekawa. Spin injection and detection in magnetic nanostructures. *Phys. Rev. B*, 67:052409, Feb 2003.

[258] S. Takahashi and S. Maekawa. Spin current, spin accumulation and spin hall effect. *Sci. Technol. Adv. Mater.*, 9(1):014105, 2008.

[259] A. Tamai, Q. S. Wu, I. Cucchi, F. Y. Bruno, S. Riccò, T. K. Kim, M. Hoesch, C. Barreteau, E. Giannini, C. Besnard, A. A. Soluyanov, and F. Baumberger. Fermi arcs and their topological character in the candidate type-II Weyl semimetal $MoTe_2$. *Phys. Rev. X*, 6:031021, Aug 2016.

[260] C. Tan, M.-X. Deng, F. Xiang, G. Zheng, S. Albarakati, M. Algarni, J. Partridge, A. R. Hamilton, R.-Q. Wang, and L. Wang. Determination of the spin orientation of helical electrons in monolayer WTe_2. *arXiv:2010.15717*, 2020.

[261] T. Tanaka, H. Kontani, M. Naito, T. Naito, D. S. Hirashima, K. Yamada, and J. Inoue. Intrinsic spin Hall effect and orbital Hall effect in in 4d and 5d transition metals. *Phys. Rev. B*, 77:165117, 2008.

[262] H. X. Tang, F. G. Monzon, R. Lifshitz, M. C. Cross, and M. L. Roukes. Ballistic spin transport in a two-dimensional electron gas. *Phys. Rev. B*, 61:4437–4440, Feb 2000.

[263] S. Tang, C. Zhang, C. Jia, H. Ryu, C. Hwang, M. Hashimoto, D. Lu, Z. Liu, T. P. Devereaux, Z.-X. Shen, and S.-K. Mo. Electronic structure of monolayer 1T′-$MoTe_2$ grown by molecular beam epitaxy. *APL Materials*, 6(2):026601, 2018.

[264] S. Tang, C. Zhang, D. Wong, Z. Pedramrazi, H.-Z. Tsai, C. Jia, B. Moritz, M. Claassen, H. Ryu, S. Kahn, J. Jiang, H. Yan, M. Hashimoto, D. Lu, R. G. Moore, C.-C. Hwang, C. Hwang, Z. Hussain, Y. Chen, M. M. Ugeda, Z. Liu, X. Xie, T. P. Devereaux, M. F. Crommie, S.-K. Mo, and Z.-X. Shen. Quantum spin hall state in monolayer 1T′-WTe_2. *Nature Physics*, 13(7):683–687, 2017.

[265] G. Tatara, H. Kohno, and J. Shibata. Microscopic approach to current-driven domain wall dynamics. *Physics Reports*, 468(6):213 – 301, 2008.

[266] S. E. Thompson and S. Parthasarathy. Moore's law: the future of si microelectronics. *Materials Today*, 9(6):20 – 25, 2006.

[267] D. J. Thouless, M. Kohmoto, M. P. Nightingale, and M. den Nijs. Quantized hall conductance in a two-dimensional periodic potential. *Phys. Rev. Lett.*, 49:405–408, Aug 1982.

[268] N. Tombros, C. Jozsa, M. Popinciuc, H. T. Jonkman, and B. J. van Wees. Electronic spin transport and spin precession in single graphene layers at room temperature. *Nature*, 448(7153):571–574, 2007.

[269] N. Tombros, S. Tanabe, A. Veligura, C. Jozsa, M. Popinciuc, H. T. Jonkman, and B. J. van Wees. Anisotropic spin relaxation in graphene. *Phys. Rev. Lett.*, 101:046601, 2008.

[270] Y. Tserkovnyak, A. Brataas, and G. E. W. Bauer. Enhanced gilbert damping in thin ferromagnetic films. *Phys. Rev. Lett.*, 88:117601, Feb 2002.

[271] D. V. Tuan, F. Ortmann, D. Soriano, S. O. Valenzuela, and S. Roche. Pseudospin-driven spin relaxation mechanism in graphene. *Nature Physics*, 10(11):857–863, Nov 2014.

[272] K. Uchida, S. Takahashi, K. Harii, J. Ieda, W. Koshibae, K. Ando, S. Maekawa, and E. Saitoh. Observation of the spin seebeck effect. *Nature*, 455(7214):778–781, Oct 2008.

[273] S. O. VALENZUELA. Nonlocal electronic spin detection, spin accumulation and the spin hall effect. *International Journal of Modern Physics B*, 23(11):2413–2438, 2009.

[274] S. O. Valenzuela and M. Tinkham. Direct electronic measurement of the spin hall effect. *Nature*, 442(7099):176–179, Jul 2006.

[275] D. Van Tuan, J. M. Marmolejo-Tejada, X. Waintal, B. K. Nikolić, S. O. Valenzuela, and S. Roche. Spin hall effect and origins of nonlocal resistance in adatom-decorated graphene. *Phys. Rev. Lett.*, 117:176602, 2016.

[276] D. Van Tuan, F. Ortmann, A. W. Cummings, D. Soriano, and S. Roche. Spin dynamics and relaxation in graphene dictated by electron-hole puddles. *Scientific reports*, 6, 2016.

[277] I. M. Vicent, H. Ochoa, and F. Guinea. Spin relaxation in corrugated graphene. *Phys. Rev. B*, 95:195402, May 2017.

[278] G. Vignale. Ten years of spin hall effect. *Journal of Superconductivity and Novel Magnetism*, 23(1):3, Oct 2009.

[279] M. Vila, J. H. Garcia, A. W. Cummings, S. R. Power, C. W. Groth, X. Waintal, and S. Roche. Nonlocal spin dynamics in the crossover from diffusive to ballistic transport. *Phys. Rev. Lett.*, 124:196602, May 2020.

[280] F. Volmer, M. Drögeler, E. Maynicke, N. von den Driesch, M. L. Boschen, G. Güntherodt, and B. Beschoten. Role of MgO barriers for spin and charge transport in Co/MgO/graphene nonlocal spin-valve devices. *Phys. Rev. B*, 88:161405, 2013.

[281] F. Volmer, M. Drögeler, E. Maynicke, N. von den Driesch, M. L. Boschen, G. Güntherodt, C. Stampfer, and B. Beschoten. Suppression of contact-induced spin dephasing in graphene/MgO/Co spin-valve devices by successive oxygen treatments. *Phys. Rev. B*, 90:165403, Oct 2014.

[282] M. M. Waldrop. The chips are down for moores law. *Nature*, 530:144147, 2016.

[283] L. Wang, I. Meric, P. Y. Huang, Q. Gao, Y. Gao, H. Tran, T. Taniguchi, K. Watanabe, L. M. Campos, D. A. Muller, J. Guo, P. Kim, J. Hone, K. L. Shepard, and C. R. Dean. One-dimensional electrical contact to a two-dimensional material. *Science*, 342(6158):614–617, 2013.

[284] Z. Wang, D. Gresch, A. A. Soluyanov, W. Xie, S. Kushwaha, X. Dai, M. Troyer, R. J. Cava, and B. A. Bernevig. $MoTe_2$: A type-II Weyl topological metal. *Phys. Rev. Lett.*, 117:056805, Jul 2016.

[285] A. Weiße, G. Wellein, A. Alvermann, and H. Fehske. The kernel polynomial method. *Rev. Mod. Phys.*, 78:275–306, Mar 2006.

[286] M. Wojtaszek, I. J. Vera-Marun, and B. J. van Wees. Transition between one-dimensional and zero-dimensional spin transport studied by hanle precession. *Phys. Rev. B*, 89:245427, Jun 2014.

[287] S. A. Wolf, D. D. Awschalom, R. A. Buhrman, J. M. Daughton, S. von Molnár, M. L. Roukes, A. Y. Chtchelkanova, and D. M. Treger. Spintronics: A spin-based electronics vision for the future. *Science*, 294(5546):1488–1495, 2001.

[288] M. Wu, J. Jiang, and M. Weng. Spin dynamics in semiconductors. *Phys. Rep.*, 493(2):61 – 236, 2010.

[289] S. Wu, V. Fatemi, Q. D. Gibson, K. Watanabe, T. Taniguchi, R. J. Cava, and P. Jarillo-Herrero. Observation of the quantum spin hall effect up to 100 kelvin in a monolayer crystal. *Science*, 359(6371):76–79, 2018.

[290] J. Wunderlich, B. Kaestner, J. Sinova, and T. Jungwirth. Experimental observation of the spin-hall effect in a two-dimensional spin-orbit coupled semiconductor system. *Phys. Rev. Lett.*, 94:047204, Feb 2005.

[291] D. Xiao, M.-C. Chang, and Q. Niu. Berry phase effects on electronic properties. *Rev. Mod. Phys.*, 82:1959–2007, Jul 2010.

[292] D. Xiao, G.-B. Liu, W. Feng, X. Xu, and W. Yao. Coupled spin and valley physics in monolayers of MoS_2 and other group-VI dichalcogenides. *Phys. Rev. Lett.*, 108:196802, May 2012.

[293] Y.-M. Xie, B. T. Zhou, and K. T. Law. Spin-orbit-parity-coupled superconductivity in topological monolayer WTe_2. *Phys. Rev. Lett.*, 125:107001, Sep 2020.

[294] S.-Y. Xu, I. Belopolski, N. Alidoust, M. Neupane, G. Bian, C. Zhang, R. Sankar, G. Chang, Z. Yuan, C.-C. Lee, S.-M. Huang, H. Zheng, J. Ma, D. S. Sanchez, B. Wang, A. Bansil, F. Chou, P. P. Shibayev, H. Lin, S. Jia, and M. Z. Hasan. Discovery of a weyl fermion semimetal and topological fermi arcs. *Science*, 349(6248):613–617, 2015.

[295] S.-Y. Xu, Q. Ma, H. Shen, V. Fatemi, S. Wu, T.-R. Chang, G. Chang, A. M. M. Valdivia, C.-K. Chan, Q. D. Gibson, J. Zhou, Z. Liu, K. Watanabe, T. Taniguchi, H. Lin, R. J. Cava, L. Fu, N. Gedik, and P. Jarillo-Herrero. Electrically switchable berry curvature dipole in the monolayer topological insulator WTe_2. *Nature Physics*, 14(9):900–906, 2018.

[296] Y. Yafet. g factors and spin-lattice relaxation of conduction electrons. volume 14 of *Solid State Physics*, pages 1 – 98. Academic Press, 1963.

[297] A. Yamaguchi, T. Ono, S. Nasu, K. Miyake, K. Mibu, and T. Shinjo. Real-space observation of current-driven domain wall motion in submicron magnetic wires. *Phys. Rev. Lett.*, 92:077205, Feb 2004.

[298] H. X. Yang, A. Hallal, D. Terrade, X. Waintal, S. Roche, and M. Chshiev. Proximity effects induced in graphene by magnetic insulators: First-principles calculations on spin filtering and exchange-splitting gaps. *Phys. Rev. Lett.*, 110:046603, Jan 2013.

[299] Y. Yao, L. Kleinman, A. H. MacDonald, J. Sinova, T. Jungwirth, D.-s. Wang, E. Wang, and Q. Niu. First principles calculation of anomalous hall conductivity in ferromagnetic bcc fe. *Phys. Rev. Lett.*, 92:037204, Jan 2004.

[300] Y. Yao, F. Ye, X.-L. Qi, S.-C. Zhang, and Z. Fang. Spin-orbit gap of graphene: First-principles calculations. *Phys. Rev. B*, 75:041401, Jan 2007.

[301] A. N. M. Zainuddin, S. Hong, L. Siddiqui, S. Srinivasan, and S. Datta. Voltage-controlled spin precession. *Phys. Rev. B*, 84:165306, Oct 2011.

[302] H. Zeng, J. Dai, W. Yao, D. Xiao, and X. Cui. Valley polarization in mos2 monolayers by optical pumping. *Nature Nanotechnology*, 7:490–493, 2012.

[303] S. Zhang. Spin hall effect in the presence of spin diffusion. *Phys. Rev. Lett.*, 85:393–396, Jul 2000.

[304] X. Zhang, Q. Liu, J.-W. Luo, A. J. Freeman, and A. Zunger. Hidden spin polarization in inversion-symmetric bulk crystals. *Nature Physics*, 10(5):387–393, May 2014.

[305] Y. Zhang, T.-T. Tang, C. Girit, Z. Hao, M. C. Martin, A. Zettl, M. F. Crommie, Y. R. Shen, and F. Wang. Direct observation of a widely tunable bandgap in bilayer graphene. *Nature*, 459(7248):820–823, 2009.

[306] Y. Zhang, J. van den Brink, C. Felser, and B. Yan. Electrically tuneable nonlinear anomalous hall effect in two-dimensional transition-metal dichalcogenides WTe_2 and $MoTe_2$. *2D Mater.*, 5(4):044001, jul 2018.

[307] B. Zhao, B. Karpiak, D. Khokhriakov, A. Johansson, A. M. Hoque, X. Xu, Y. Jiang, I. Mertig, and S. P. Dash. Unconventional charge-to-spin conversion in Weyl-semimetal WTe_2. *Advanced Materials*, 32(38):2000818, 2020.

[308] B. Zhao, D. Khokhriakov, Y. Zhang, H. Fu, B. Karpiak, A. M. Hoque, X. Xu, Y. Jiang, B. Yan, and S. P. Dash. Observation of charge to spin conversion in Weyl semimetal WTe_2 at room temperature. *Phys. Rev. Research*, 2:013286, Mar 2020.

[309] C. Zhao, M. Hu, J. Qin, B. Xia, C. Liu, S. Wang, D. Guan, Y. Li, H. Zheng, J. Liu, and J. Jia. Strain tunable semimetal–topological-insulator transition in monolayer $1t^{'}-wte_2$. *Phys. Rev. Lett.*, 125:046801, Jul 2020.

[310] W. Zhao, E. Runburg, Z. Fei, J. Mutch, P. Malinowski, B. Sun, X. Huang, D. Pesin, Y.-T. Cui, X. Xu, J.-H. Chu, and D. H. Cobden. Determination of the helical edge and bulk spin axis in quantum spin Hall insulator WTe_2. *arXiv:2010.09986*, 2020.

[311] J. Zhou, J. Qiao, A. Bournel, and W. Zhao. Intrinsic spin Hall conductivity of the semimetals. *Phys. Rev. B*, 99(6):60408, feb 2019.

[312] L. Zhou, A. Zubair, Z. Wang, X. Zhang, F. Ouyang, K. Xu, W. Fang, K. Ueno, J. Li, T. Palacios, J. Kong, and M. S. Dresselhaus. Synthesis of High-Quality Large-Area Homogenous 1T-$MoTe_2$ from Chemical Vapor Deposition. *Adv. Mater.*, 28:9526–9531, 2016.

[313] Y. Zhou and M. W. Wu. Electron spin relaxation in graphene from a microscopic approach: Role of electron-electron interaction. *Phys. Rev. B*, 82:085304, Aug 2010.

[314] J. Zhu, T. Zhang, Y. Yang, and R. Huang. A comprehensive review on emerging artificial neuromorphic devices. *Applied Physics Reviews*, 7(1):011312, 2020.

[315] Z. Y. Zhu, Y. C. Cheng, and U. Schwingenschlögl. Giant spin-orbit-induced spin splitting in two-dimensional transition-metal dichalcogenide semiconductors. *Phys. Rev. B*, 84:153402, 2011.

[316] P. J. Zomer, M. H. D. Guimarães, N. Tombros, and B. J. van Wees. Long-distance spin transport in high-mobility graphene on hexagonal boron nitride. *Phys. Rev. B*, 86:161416, 2012.

[317] I. Žutić, A. Matos-Abiague, B. Scharf, H. Dery, and K. Belashchenko. Proximitized materials. *Materials Today*, 22:85 – 107, 2019.